Leptonic Radiative Corrections to Lepton-Proton Scattering

Dissertation submitted
for the award of the title
"Doctor of Natural Sciences"
to the Faculty of Physics, Mathematics, and Computer Science
of Johannes Gutenberg University
in Mainz

Razvan-Daniel Bucoveanu,
born in Slobozia

Institut für Physik
Johannes Gutenberg-Universität Mainz
July 10, 2022

Abstract

Low energy precision experiments have become an important tool in the search for new physics beyond the Standar Model (SM). These experiments can exclude new physics at mass scales extending well into the TeV range and are complementary to searches at the Large Hadron Collider (LHC).

With polarized elastic electron proton scattering, one can determine the weak charge of the proton, which is related to the weak mixing angle in the SM. This can be achieved by measuring the asymmetry between leptons with positive and negative helicities. Deviations from the SM prediction for the weak mixing angle can provide important tests of models beyond the SM.

A future experiment that plans to measure the weak charge of the proton at low energies and with high precision is the P2 experiment that will take place at the new MESA facility in Mainz. The present work is mostly motivated by this experiment and shows results that are relevant for this particular measurement. In addition, a μp scattering experiment, called MUSE, has been also proposed at the PSI with the aim to study the proton radius puzzle.

In order to match the experimental precision of such experiments it is necessary not only to have an exhaustive treatment of first order radiative corrections, but also to go beyond first order and include a treatment of second order radiative corrections. In this work we aim to provide such a calculation for polarized and unpolarized lepton nucleon scattering, that includes both virtual and real corrections to the lepton lines.

We re-derive first order corrections, including also hadronic corrections, relying as little as possible on approximations. The main focus is however on second order corrections, including a new calculation of two photon bremsstrahlung. Photon radiation leads to a shift in the measured Q^2, that translates in a 5% correction to the parity violating asymmetry. For this reason we present the effects of first and second order photon radiation on the asymmetry. Finally we present a first order calculation of lepton carbon scattering which is also relevant for the MESA experiments.

All the calculations that were done in this work were included in a Monte Carlo event generator called POLARES, that can be used to simulate both unpolarized and polarized lepton nucleon scattering events for the aforementioned experiments and possibly other future low energy precision experiments.

Zusammenfassung

Niederenergie-Präzisionsexperimente sind zu einem wichtigen Instrument bei der Suche nach neuer Physik jenseits des Standardmodells (SM) geworden. Diese Experimente können neue Physik auf Massenskalen bis weit in den TeV-Bereich hinein ausschließen und ergänzen die Suche am Large Hadron Collider (LHC).

Mit der polarisierten elastischen Elektron-Proton-Streuung kann man die schwache Ladung des Protons bestimmen, die mit dem schwachen Mischungswinkel im SM zusammenhängt. Dies kann durch die Messung der Asymmetrie zwischen Leptonen mit positiven und negativen Helizitäten erreicht werden. Abweichungen von der SM-Vorhersage für den schwachen Mischungswinkel können wichtige Tests für Modelle jenseits des SM liefern.

Ein zukünftiges Experiment, mit dem auch die schwache Ladung des Protons bei niedrigen Energien und mit hoher Präzision gemessen werden soll, ist das P2-Experiment, das an der neuen MESA-Anlage in Mainz durchgeführt werden soll. Die vorliegende Arbeit ist hauptsächlich durch dieses Experiment motiviert und zeigt Ergebnisse, die für diese spezielle Messung relevant sind. Zusätzlich, wurde am PSI auch ein μp-Streuexperiment namens MUSE vorgeschlagen, um das Rätsel um den Protonenradius zu untersuchen.

Um die experimentelle Präzision solcher Experimente zu erreichen, ist nicht nur eine umfassende Behandlung der Strahlungskorrekturen erster Ordnung erforderlich, sondern auch eine Behandlung der Strahlungskorrekturen zweiter Ordnung. Ziel dieser Arbeit ist es, eine Berechnung zweiter Ordnung für polarisierte und unpolarisierte Lepton-Nukleon-Streuung bereitzustellen, die sowohl virtuelle als auch reelle Korrekturen an den Leptonenlinien beinhaltet.

Wir leiten die Korrekturen erster Ordnung, einschließlich der hadronischen Korrekturen, neu ab und stützen uns dabei so wenig wie möglich auf Näherungen. Das Hauptaugenmerk liegt jedoch auf den Korrekturen zweiter Ordnung, einschließlich einer neuen Berechnung der Zwei-Photonen-Bremsstrahlung. Die Photonenstrahlung führt zu einer Verschiebung des gemessenen Q^2, was sich in einer 5%-Korrektur der parität verletzende Asymmetrie niederschlägt. Aus diesem Grund stellen wir die Auswirkungen von Photonenstrahlung erster und zweiter Ordnung auf die Asymmetrie dar. Schließlich stellen wir auch eine Berechnung erster Ordnung für die Lepton-Kohlenstoff-Streuung vor, die auch für die MESA-Experimente relevant ist.

Alle in dieser Arbeit durchgeführten Berechnungen wurden in einen Monte Carlo Ereignisgenerator namens POLARES aufgenommen. Dieser Monte Carlo Ereignisgenerator kann zur Simulation von unpolarisierten und polarisierten Lepton-Nukleon-Streuereignissen für die oben genannten Experimente und möglicherweise für künftige Präzisionsexperimente verwendet werden.

Contents

Chapter 1

Introduction

1.1 Historical background

Early on our human species had an innate curiosity to understand the nature of the world in which it was living, a curiosity that was reflected in various ancient cosmogonic myths that survived to our day. For the first time (at least for what we have knowledge of from the texts that survived to our day), at the beginning of the 6th century BCE, some Greek philosophers, which we refer today collectively as Presocratic philosophers, started to engage in an inquiry about the laws ("causes and principles") of the natural world and natural phenomena. Among these, the first presocratic philosopher that we know of was Thales of Miletus (a city in Ionia, on the west coast of what is now Turkey), who, according to Aristotle (Metaphysics 983b24–25), claimed that there was only one fundamental principle, ἀρχή, as the origin of all things, which he identified with water. His disciple, Anaximandros, went even further and identified an abstract principle ἄπειρον (indefinite, unlimited) as the origin of the natural world (Simplicius, Commentary on Aristotle's Physics 24). With their reasoning they have started a fruitful tradition of questioning and understanding the laws of nature.

This type of inquiry was later revived during the Enlightenment period. An essential addition, that gave birth to the scientific method as we know it today, was the requirement that these laws make predictions that can be tested (or falsified) by performing an experiment. This type of method proved to be very successful and efficient in determining the nature of reality and helped us to push the limits of our understanding of the universe.

Lately, in the last 80 years or so, great advances have been made in the field of fundamental particle physics with the development of a new generation of accelerators and detectors, that increased the quantity and the quality of the collected data on various interaction processes. This data helped us discover the fundamental interactions that we know of today, among which are the strong, electromagnetic and weak interactions and to develop a quantum field theory that describes them.

The first quantum field theory, called quantum electrodynamics (QED), was developed for electromagnetic interactions and proved to be the most accurately verified theory in the history of physics. One of the most remarkable achievements was the prediction of the anomalous magnetic moment of the electron which agrees (according to the latest measurements) with the theoretical calculation to about one part in a trillion (see Ref. [2]). A key feature of this theory is that it is a gauge theory and more precisely a gauge theory having the Abelian

U(1) symmetry. This means that the electron field, $\psi(x)$ with charge e, has a local symmetry and is invariant under the transformation

$$\psi(x) \longrightarrow \psi(x)e^{ie\alpha(x)}, \tag{1.1}$$

provided that a corresponding transformation is applied to the electromagnetic potential

$$A_\mu(x) \longrightarrow A_\mu(x) - \partial_\mu\alpha(x). \tag{1.2}$$

The reason why this is important is that it makes the theory renormalizable. This is an essential aspect of a field theory because it shows that the divergent parts that appear in the calculation, which have puzzled theorists like Feynman and Dirac, can be absorbed by redefinition into a few measurable quantities by using only a finite set of parameters.

The success of QED brought again into attention the dream of the presocratic philosophers of an ἀρχή, an unified theory, that is the origin of everything we see in nature. A step in this direction was the unification of the weak and electromagnetic interaction which was first suggested by Schwinger in 1957 who proposed that the weak gauge bosons W^+ and W^- and the photon γ can be unified into a single theory (see Ref. [3] and Ref. [4] for more details of the history of electroweak unification). Two years later, Sheldon Glashow, the student of Schwinger, further extended his supervisor's work, but at this stage the theory was not renormalizable (see Ref. [5]). The complete unification in a renormalizable theory was later achieved in 1967 independently by Weinberg (see Refs. [6–8]) and Salam by extending the model into a larger SU(2) × U(1) symmetry group that predicted also a fourth gauge boson Z^0, which was discovered in 1983 at the Super Proton Synchroton at the European Organization for Nuclear Research (CERN). Moreover, a mechanism is required in order to break the SU(2) × U(1) symmetry by spontaneous symmetry breaking (SSB), giving mass to the W and Z bosons in the process. This mechanism, now called the Higgs mechanism, was initially proposed in 1964 by three groups of physicists (see Refs. [9–11]). The Higgs mechanism predicted the existence of the Higgs boson, which was also discovered at CERN by the ATLAS collaboration in 2012 (see Ref. [12]).

The electroweak symmetry group SU(2) × U(1) together with the non-Abelian SU(3) symmetry group that describes the strong interactions among quarks builds what we know today as the standard model (SM) of particle physics shown in Fig. 1.1. This model proved to be amazingly successful and its predictions have been verified with increasingly impressive accuracy. Albeit very successful, there are many reasons to believe there should exist an even more fundamental theory. It contains, for example, twenty arbitrary parameters such as mass ratios that we cannot predict and it is not truly a unified model, because the symmetry group has three factors, each with its own coupling strength. Moreover, there are a few things that the standard model does not explain. It cannot account for example for dark matter, which we know it exists from the rotation curves of galaxies, or the dark energy responsible for the accelerating expansion of the universe. It cannot also explain why the elementary particles come in three families with very similar structure but very different masses, or why the neutrinos have non-zero, though tiny, masses. And finally, of course, the standard model cannot explain gravity. There is hope that one day we will finally find a truly unified theory, an ἀρχή or "theory of eveything". For these reasons there are many experiments running today trying to search for physics "beyond the standard model" or "New Physics" that could give us a hint of what such a theory would look like.

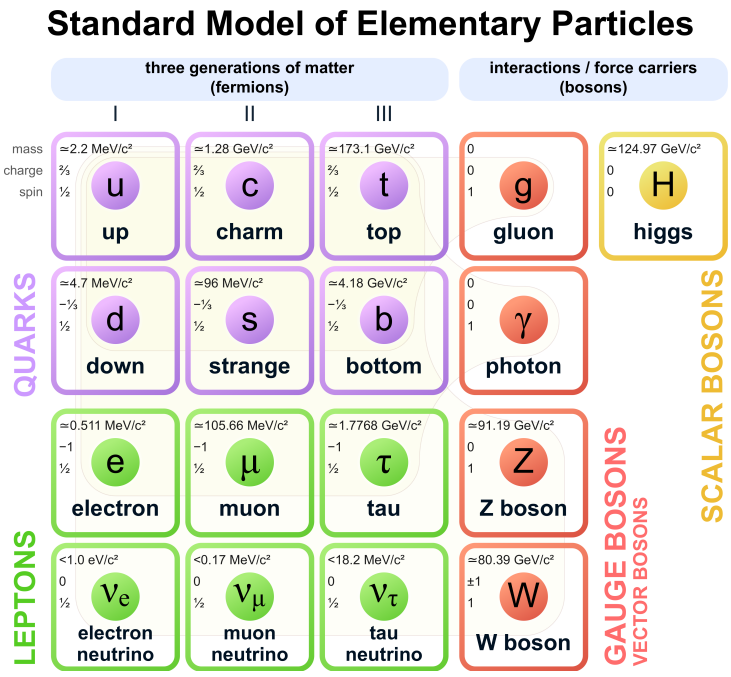

Figure 1.1: The Standard Model of particle physics consists of three generations of matter particles called fermions, grouped into quarks and leptons, and of force carriers called bosons. The are also two types of bosons, given by vector and a scalar bosons, called the Higgs boson (this figure was taken from the Wikipedia page of the Standard Model, see Ref. [13]).

1.2 The weak mixing angle

The weak mixing $\sin^2\theta_W$, also called the Weinberg angle, has a central role in the SM (see Ref. [8]), since it determines the angle by which the SSB rotates the 0 components of the vector bosons before SSB of the $SU(2)_L \times U(1)_Y$ producing as a result the Z^0 and the photon. Here the subscript Y stands for the weak hypercharge quantum number and it is used to differentiate from the symmetry of the electromagnetic interaction, which is also U(1). The subscript L reminds us that only the left components of the fermion fields transform under the SU(2) group, which leads to parity violation in the weak interaction. Parity violation of the weak interaction was, in fact, proposed as early as 1956 by Lee and Yang (see Ref. [14]) and observed shortly after in the Wu experiment (see Ref. [15]). In the following we describe in more detail the $SU(2)_L \times U(1)_Y$ unification, also called the Glashow-Weinberg-Salam (GWS) model and the role the weak mixing angle plays in this model (see Refs. [16] and [17]).

In the GWS model the fermion fields are massless, so they can be separated into right- and left-handed helicity doublets as

$$\psi_{R,L} = \frac{1}{2}(1 \pm \gamma_5)\psi, \tag{1.3}$$

where the positive (negative) sign corresponds to the right-handed (left-handed) helicity state and where we define $\gamma_5 \equiv \frac{i}{4!}\epsilon_{\mu\nu\alpha\beta}\gamma^\mu\gamma^\nu\gamma^\alpha\gamma^\beta$ [1]. ψ_L is a left-handed doublet that transforms under

[1] Here and the rest of the work we assume Einstein summation convention, such that i=1,2,3 and $\mu = 0, 1, 2, 3$.

$SU(2)_L \times U(1)_Y$ as

$$SU(2)_L \ : \ \psi_L \longrightarrow \psi'_L = e^{-i\alpha^i(x)T^i}\psi_L, \tag{1.4}$$

$$U(1)_Y \ : \ \psi_L \longrightarrow \psi'_L = e^{-iY_L\beta(x)}\psi_L \tag{1.5}$$

and ψ_R is right-handed singlet that transforms under $SU(2)_L \times U(1)_Y$ as

$$SU(2)_L \ : \ \psi_R \longrightarrow \psi'_R = \psi_R, \tag{1.6}$$

$$U(1)_Y \ : \ \psi_R \longrightarrow \psi'_R = e^{-iY_R\beta(x)}\psi_R. \tag{1.7}$$

Here α_i and β are group parameters for weak isospin and weak hypercharge operators, respectively. $T^i \equiv \tau^i/2$, with τ^i the Pauli matrices, are generators that satisfy the Lie algebra

$$[T^i, T^j] = i\epsilon_{ijk}T^k. \tag{1.8}$$

Finally, Y_L and Y_R are the hypercharge eigenvalues for left- and right-handed particles respectively. For leptons we have $Y_L = -1/2$ and $Y_R = -1$.

The Lagrangian for this model is composed of 4 parts as

$$\mathcal{L} = \mathcal{L}_{fermion} + \mathcal{L}_{gauge} + \mathcal{L}_{scalar} + \mathcal{L}_{Yukawa}. \tag{1.9}$$

The fermionic part of the Lagrangian is given by

$$\mathcal{L}_{fermion} = \bar{\psi}_L i\gamma^\mu \mathcal{D}_\mu \psi_L + \bar{\psi}_R i\gamma^\mu \mathcal{D}_\mu \psi_R. \tag{1.10}$$

The covariant derivative has the following general form

$$\mathcal{D}_\mu = \left(\partial_\mu - igT^iA^i_\mu - iYg'B_\mu\right), \tag{1.11}$$

where A^i_μ and B_μ are gauge boson fields associated with $SU(2)_L$ and $U(1)_Y$, respectively. Setting $Y = Y_L$ for ψ_L and $Y = Y_R$ for ψ_R we get the following covariant derivatives for left and right lepton fields, respectively:

$$\mathcal{D}_\mu \psi_L = \left(\partial_\mu - igT^iA^i_\mu + i\frac{g'}{2}B_\mu\right)\psi_L, \tag{1.12}$$

$$\mathcal{D}_\mu \psi_R = \left(\partial_\mu A^i_\mu + ig'B_\mu\right)\psi_R. \tag{1.13}$$

Since ψ_R is a singlet under $SU(2)_L$ it doesn't couple to A^i_μ.

The kinetic term of the gauge fields is given by

$$\mathcal{L}_{gauge} = -\frac{1}{4}A^i_{\mu\nu}A^{i\mu\nu} - \frac{1}{4}B_{\mu\nu}B^{\mu\nu}, \tag{1.14}$$

where $A^{i\mu\nu}$ and $B_{\mu\nu}$ are the field strength tensors of the gauge fields A^i_μ and B_μ, respectively.

There is one scalar field in this model, a complex doublet under SU(2) transformations with hypercharge 1/2, that is needed to realize the symmetry breaking $SU(2)_L \times U(1)_Y \longrightarrow U(1)_Q$, where Q stands for the electromagnetic charge. The Lagrangian for this scalar field is given by

$$\mathcal{L}_{scalar} = (\mathcal{D}_\mu\phi)^\dagger(\mathcal{D}^\mu\phi) + \mu^2\phi^\dagger\phi - \lambda(\phi^\dagger\phi)^2, \tag{1.15}$$

where the covariant derivative is given by

$$\mathcal{D}^{\mu}\phi = \left(\partial_{\mu} - igT^{i}A^{i}_{\mu} - i\frac{g'}{2}B_{\mu}\right)\phi \tag{1.16}$$

The last two terms in the scalar Lagrangian form the Higgs potential $V(\phi) = -\mu^2\phi^{\dagger}\phi + \lambda(\phi^{\dagger}\phi)^2$, where μ^2 and λ have to be real constant parameters. Finally, the Yukawa interaction terms provide the fermion masses after SSB and the Lagrangian that describes this in GWS model is given by

$$\mathcal{L}_{Yukawa} = -G_Y(\bar{\psi}_L\phi\psi_R + \bar{\psi}_R\phi^{\dagger}\psi_L) + h.c.\,, \tag{1.17}$$

where $h.c.$ stands for hermitian conjugate and G_Y is Yukawa coupling constant that cannot be determined in the model itself. In fact, the Yukawa couplings are the most arbitrary aspect of the SM since they introduce the most of the free parameters.

Strictly speaking, we have to add an additional contribution to the Lagrangian coming from gauge fixing and a term that cancels the remaining gauge dependence called $\mathcal{L}_{ghost}$, that are needed when higher order corrections are included (for more on this see Ref. [18] or [19]). These terms were included when was necessary.

The SSB occurs when the scalar doublet ϕ develops a vacuum expectation value (VEV) given by

$$\langle 0|\phi|0\rangle = \begin{pmatrix} 0 \\ v/\sqrt{2} \end{pmatrix}. \tag{1.18}$$

After the SSB there remains a symmetry $\mathrm{U}(1)_Q$ associated with the charge operator Q given by

$$Q = T^3 + Y. \tag{1.19}$$

In order to expand the scalar field around the minimum we use what is called the Kibble parametrization given by

$$\phi = e^{i\tau^i\xi_i/2v}\begin{pmatrix} 0 \\ (v+H)/\sqrt{2} \end{pmatrix}, \tag{1.20}$$

where ξ_i are the so-called Goldstone bosons that are absorbed into the longitudinal components of the $W^{\pm}$ and Z^0 bosons and H is the Higgs boson, such that the VEV of these fields becomes 0, i.e. $\langle 0|\xi_i|0\rangle = \langle 0|H|0\rangle = 0$.

By applying the unitary SU(2) transformation

$$U(\xi) = e^{-i\tau^i\xi_i/2v} \tag{1.21}$$

we arrive at the fields after SSB, which we define with a prime to distinguish them from the ones before SSB. The Lagrangian for the scalar field after SSB then becomes

$$\mathcal{L}_{scalar} = (\mathcal{D}_{\mu}\phi)'^{\dagger}(\mathcal{D}^{\mu}\phi)' - V(\phi'^{\dagger}\phi'), \tag{1.22}$$

with

$$(\mathcal{D}^{\mu}\phi)' = \left(\partial_{\mu} - igT^{i}A'^{i}_{\mu} - i\frac{g'}{2}B'_{\mu}\right)\frac{1}{\sqrt{2}}(v+H)\chi, \tag{1.23}$$

where $\chi = \begin{pmatrix} 0 \\ 1 \end{pmatrix}$. The mass of the weak gauge bosons originate from the first term of Eq. 1.22, which after some rearrangements is given by the Lagrangian

$$\mathcal{L}_{mass} = \frac{v^2}{8}\left[g^2 A'^1_\mu A'^{1\mu} + g^2 A'^2_\mu A'^{2\mu} + (g A'^3_\mu - g' B'_\mu)^2\right]. \tag{1.24}$$

By defining the charged boson fields $W^\pm$ as

$$W^\pm_\mu = \frac{A'^1_\mu \mp i A'^2_\mu}{\sqrt{2}} \tag{1.25}$$

we can rewrite the mass Lagrangian as

$$\mathcal{L}_{mass} = \frac{1}{4} g^2 v^2 W^+_\mu W^{-\mu} + \frac{v^2}{8}(g^2 + g'^2) Z_\mu Z^\mu, \tag{1.26}$$

where in order to arrive at the last term we have applied an orthogonal transformation given by

$$\begin{pmatrix} Z_\mu \\ A_\mu \end{pmatrix} = \begin{pmatrix} \cos\theta_W & -\sin\theta_W \\ \sin\theta_W & \cos\theta_W \end{pmatrix} \begin{pmatrix} A'^3_\mu \\ B'_\mu \end{pmatrix}, \tag{1.27}$$

where θ_W is called the weak mixing angle or the Weinberg angle. The diagonalization leads to a definition of θ_W in terms of the coupling constants g and g' as

$$\sin^2\theta_W = \frac{g'^2}{g^2 + g'^2}. \tag{1.28}$$

From Eq. 1.26 we see that the charged bosons $W^\pm$ are massive with mass given by

$$M_W = \frac{1}{2} g v \tag{1.29}$$

and the neutral boson Z^0 becomes massive with the mass given by

$$M_Z = \frac{1}{2} v \sqrt{g^2 + g'^2}, \tag{1.30}$$

while the other neutral boson A_μ is massless and can be identified with the photon. Moreover, at leading order, the mass of the Z^0 boson is related with the mass of the $W^\pm$ boson by

$$M_Z = \frac{M_W}{\cos\theta_W}, \tag{1.31}$$

from which we can express the weak mixing angle as

$$\sin^2\theta_W = 1 - \frac{M_W^2}{M_Z^2}. \tag{1.32}$$

At tree level this definition is identical with the definition from Eq. 1.28. However, when radiative corrections are included these two definitions differ.

Both definitions have their advantages and disadvantages and can be useful in different contexts. For example, by defining the weak mixing angle as the ratio of weak boson pole masses, also called the on-shell definition, we get a clear definition that is directly related to a physical observable, but has the disadvantage of large radiative corrections, enhanced by the mass of the top quark, $\mathcal{O}(\propto m_t^2/m_W^2)$. By using Eq. 1.28 and working in the $\overline{\text{MS}}$ renormalization scheme (for which reason is called the $\overline{\text{MS}}$ definition), we get a definition in terms of coupling constants that is scale dependent and is running with the energy. This provides us with a well-defined subtraction of singular terms arising in dimensional regularization, giving rise to expressions with a logarithmic μ dependence governed by a renormalization group equation (RGE). To make the energy dependence explicit we write the weak mixing angle as

$$\sin^2 \hat{\theta}_W(\mu) = \hat{\kappa}(\mu) \sin^2 \hat{\theta}_W(M_Z), \tag{1.33}$$

where the radiative corrections that are responsible for the running are included in the κ form factor. Such a definition has the disadvantage however that is not directly related to a physical observable.

There are a handful of calculations of the running of the weak mixing angle in the literature (see for example the calculation of Czarnecki and Marciano Refs. [21–23]). A more recent calculation, that includes also hadronic corrections was done by Jegerlehner and implemented in his code called alphaQED (see Ref. [20]). The expression for the κ form factor that is used in this work was extracted from the code alphaQED by A. Weber for his master thesis. With this expression and by setting $\sin^2 \hat{\theta}_W(M_Z) = 0.23156$ and $\mu = Q$, as was done in Ref. [20] we obtain the result of Fig. 1.2.

Another recent evaluation of the running of the weak mixing angle was done in Ref. [24] by using an RGE analysis. This calculation was used also for the most recent PDG review on electroweak physics (see Ref. [2]) which includes the result from Fig. 1.3. In this figure we can see also past measurements of the weak mixing angle marked with red and future proposed measurements marked with green. One recent measurement at low energies was done by the Qweak collaboration (see Ref. [26]). In order to obtain the weak mixing angle the Qweak

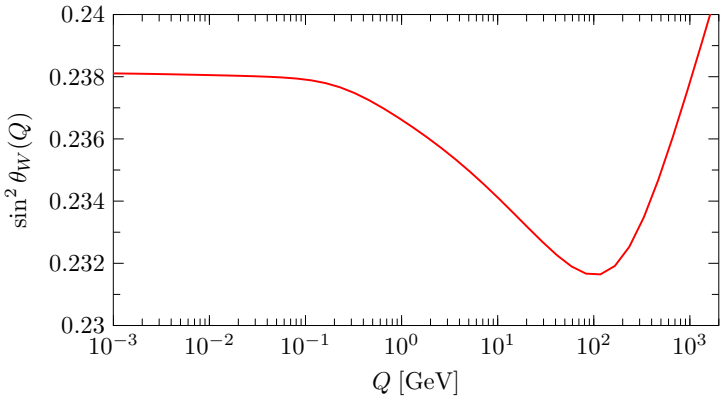

Figure 1.2: The running of the weak mixing angle as was calculated in Ref. [20]. The expressions that have been used to get this result were extracted for a master thesis from the code alphaQED by A. Weber.

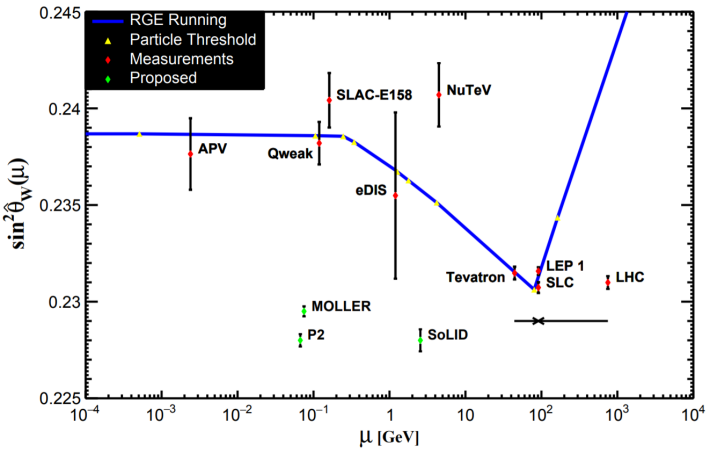

Figure 1.3: The running of the weak mixing angle as obtained in Ref. [24] from a RGE analysis in the $\overline{\text{MS}}$ renormalization scheme.

collaboration extracted the weak charge of the proton, defined as

$$Q_W^p = 1 - 4\sin^2\theta_W, \tag{1.34}$$

from the parity violating asymmetry A_{PV} that was measured in an electron-proton scattering experiment. As can be seen from Fig. 1.3 this latest measurement is in very good agreement with the SM prediction. Another future experiment that plans to measure the weak charge of the proton at even lower energies and with increased precision is the P2 experiment that will take place at the new MESA facility in Mainz (see Ref. [27]). The present work is mostly motivated by this experiment and shows results that are relevant for this measurement.

1.3 Overview of this work and motivation [2]

Low energy precision experiments have become an important tool in the search for new physics beyond the SM. These experiments can exclude new physics at mass scales extending well into the TeV range and are complementary to searches at the Large Hadron Collider (LHC). In particular, lepton nucleon scattering at low energies is an important example. With polarized elastic electron proton scattering, one can determine the weak charge of the proton, which is related to the weak mixing angle in the SM, as was explained in the previous section. Deviations from the SM prediction for the weak mixing angle can provide important tests of models beyond the SM. In addition to the P2 experiment, a μp scattering experiment, called MUSE (see Ref. [1]), has been proposed at the PSI with the aim to study the proton radius puzzle. By extracting the weak charge of heavier nuclei can give us also valuable information about the neutron densities (also called the "neutron skin"), since the weak charge of the neutron is much larger than the weak charge of the proton (see for example Ref. [29]).

Moreover, there has been a continued interest in the determination of the proton's form factors, notably the electric and magnetic ones, G_E and G_M, contributing to the unpolarized

[2] In this introduction some of the text is taken from Ref. [28]

scattering cross section (see for example Ref. [30]). Their precise knowledge is an important ingredient in the determination of the proton radius from electron proton scattering. With polarized scattering also axial and strangeness form factors contribute. Accurate data for them are needed for a better understanding of how matter is formed from quarks and gluons.

In order to match the precision of recent and future lepton nucleon scattering experiments it is important to include the full set of radiative corrections at first and second order in perturbation theory. Higher-order corrections, in particular QED radiative effects, can not be taken from the classical work of Mo and Tsai [31] (see also Ref. [32]) without carefully revisiting the underlying assumptions and improving approximations which had been acceptable in previous experiments. Since then, quite a number of articles have been published that put focus on more precise determinations (see for example Refs. [33–37]). Also higher-order effects, like those due to multi-photon radiation in the soft-photon approximation, or re-summed leading logarithms can be found in the literature (see Ref. [38, 39]). In addition, corrections due to hard photon radiation depend strongly on details of the detector setup and on how kinematic variables, like energies and scattering angles are measured and can lead to a shift in the measured Q^2. Their calculation therefore requires a full Monte Carlo event simulation. Such Monte Carlo event generators already exist for elastic electron proton scattering (see for example Ref. [40]), but to this day there are none that include a complete and consistent treatment of radiative corrections at second order in perturbation theory. Radiative corrections for electron scattering can be separated into contributions due to real and virtual photon radiation from the lepton, from the nucleon, and its interference. Real radiation from the nucleon is suppressed due to the higher nucleon mass. One of the goals of the present work is to provide a Monte Carlo simulation that includes a complete (apart from few exceptions) and consistent set of second order corrections to the lepton line, that includes both virtual and real corrections.

At first order, photon emission from the proton, although it doesn't affect the shift in Q^2, can also have an important effect in some kinematic regions, especially through the interference with leptonic radiation. Apart from its role as part of radiative corrections, photon emission from the proton is interesting by itself. For large momentum transfer it is known as (deeply) virtual Compton scattering (DVCS). It is used to study properties of the nucleon, e.g. as encoded in generalized parton distributions (GPDs), see for example Refs. [41–43]. Radiative corrections for DVCS involve Feynman diagrams which are also part of the second-order radiative corrections studied in the present work. The interference of radiation from the lepton and from the nucleon is linked to two-photon exchange (TPE) graphs (or box graphs). Both contributions taken separately are infrared divergent, but the infrared divergent terms cancel when interference effects and box graphs are combined. In recent years there have been an increased interest in TPE corrections, see for example the review in Ref. [44], since they are expected to be important when data is analyzed with the aim to separate the electric and magnetic form factors of the proton. The observed discrepancy between different techniques, the Rosenbluth separation on the one hand and a technique based on polarization measurements on the other hand, is sensitive to the treatment of two-photon exchange corrections. Calculations of radiative effects connected to the nucleon are model-dependent and often depend on additional assumptions and approximations (see for example Refs. [45–47]). Soft radiation and virtual effects are, however, not observable and appear as a part of the observed, effective form factors. The separation of such corrections requires a well-defined theoretical definition

of bare form factors. Higher-order QED effects at the nucleon should be taken into account only if these corresponding corrections had been subtracted during data analysis to extract the form factors.

In a realistic experiment one has to impose a set of conditions which fix the observable part of the final-state phase space. For example, the scattering angle will be restricted by the acceptance of the detector, or the energy of final-state particles is limited. If the goal is to measure elastic form factors, one will try to reduce the impact of non-elastic processes, for example by imposing a cut-off on the missing energy. This would remove e.g. pion production, but also restrict the emission of hard photons. In experiments with very high luminosity like P2, it is impossible to realize cuts on individual scattering events and the feasibility to impose kinematic conditions may be restricted. Finally, the efficiency for the detection of a scattering event may depend on energies and scattering angles and vary considerably over the observed phase space. It is therefore obvious that a Monte Carlo simulation program of the process, ideally interfaced to the simulation code of the detector response, is indispensable. This approach has become the standard for deep-inelastic lepton scattering like at HERA (see Refs. [48–51]), but has also been discussed for elastic ep scattering (see Refs. [40, 52]). In addition, with nowadays computer resources, computer algebra systems and high-performance computing on multi-core systems, there is no need anymore to search for simplified, i.e. approximate expressions which are fast to evaluate.

In the first chapter of this work we re-derive the first-order radiative corrections for elastic unpolarized lepton nucleon scattering, including hadronic corrections (Secs. 2.2 and 2.3). The emphasis of this chapter is, however, on the description of second-order corrections, i.e. two-loop and two-photon bremsstrahlung for unpolarized lepton proton elastic scattering. As explained above, we restrict ourselves to purely leptonic corrections at second order, i.e. not including for example 3-photon exchange or second order hadronic radiation. The corrections are implemented in a new Monte Carlo simulation program for numerical calculations. In Sec. 2.4 we describe our new calculation of second-order corrections, including non-radiative parts and corrections due to the radiation of one or two photons. Then, in Sec. 2.5 we describe some tests of the numerical evaluations, while, in Sec. 2.6 we present some numerical results, first of all for applications at the forthcoming P2 experiment in Mainz.

The second chapter is about polarized lepton nucleon scattering and the determination of the parity violating asymmetry between cross sections for incident leptons with positive and negative helicities, respectively. The structure of this chapter is similar with the previous one. In Sec. 3.2 we re-derive first order corrections for polarized leptons, while in Sec. 3.3 we describe our calculation of second-order corrections. Here we include only photonic corrections to the lepton line, i.e. only corrections that involve photon loops. The calculations for the polarized leptons are therefore similar with the ones for unpolarized leptons. Finally, in Sec. 3.4 we show some tests and results of the numerical evaluation of first and second order corrections and their effects in the shift of Q^2 and the asymmetry.

In chapter three we briefly present the effects of first order corrections for both unpolarized and polarized lepton carbon scattering, while chapter four describes the event generator POLARES that includes all corrections which are described in this work.

Chapter 2

Unpolarized Lepton-Proton Scattering [1]

2.1 Definitions and general remarks

We choose a coordinate frame where the target nucleon is at rest and the z axis is directed along the momentum of the incident lepton. We denote the 4-momenta of the incoming and scattered lepton (nucleon) by l^μ and l'^μ (p^μ and p'^μ). The notations for energies and angles of the particles that are involved in this scattering process can be found in Fig. 2.1.

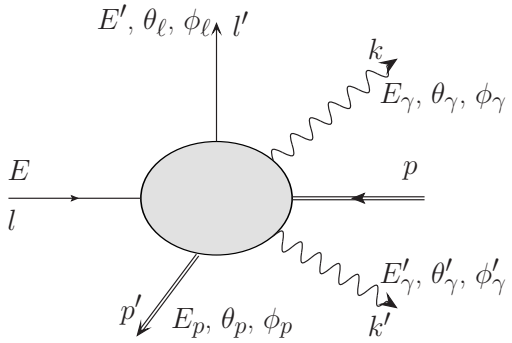

Figure 2.1: A schematic definition of kinematic variables for lepton nucleon scattering. Angles are defined with respect to the direction of the incoming lepton with 4-momentum l^μ. In the reference frame considered here the proton is at rest, i.e. with 4-momentum $p^\mu = (M, 0, 0, 0)$.

At lowest order, lepton nucleon scattering is described by the exchange of a virtual photon. The electromagnetic current for a spin-1/2 nucleon is given by

$$\mathcal{P}^\mu = e\bar{u}(p',\, s)\Gamma^\mu u(p,\, s), \tag{2.1}$$

where u is a Dirac spinor and $\bar{u}$ its hermitian conjugate. Here s denotes the spin of the particle [2]. The spin-averaged matrix element of the electromagnetic current can be decomposed into two form factors, F_1 and F_2, called the Pauli and the Dirac form factors. They are normalized

[1] This chapter follows the structure of Ref. [28]. Some parts are directly taken from this reference and are indicated by "see Ref. [28]".

[2] In the rest of the work we omit writing the spin s explictly.

by $F_1^p(0) = 1$ and $F_1^p(0) = \kappa_p - 1$ with $\kappa_p = 2.7928$ the proton's magnetic moment in units of the nuclear magneton. We also define the negative of the momentum transfer squared as

$$Q^2 = -q^2. \tag{2.2}$$

The proton vertex is determined by

$$\Gamma^\mu = \gamma^\mu (F_1^p(Q^2) + F_2^p(Q^2)) - \frac{(p+p')^\mu}{2M} F_2^p(Q^2), \tag{2.3}$$

where M is the nucleon mass. Using this vertex rule we can obtain the tree-level cross section for the scattering of unpolarized leptons with mass m_ℓ off unpolarized nucleons. In the lowest order, without the emission of a photon, it is given by

$$\frac{\mathrm{d}\sigma^{(0)}}{\mathrm{d}Q^2} = \frac{\overline{|\mathcal{M}_{\mathrm{Born}}|^2}}{16\pi\left[(s - m_\ell^2 - M^2)^2 - 4m_\ell^2 M^2\right]}. \tag{2.4}$$

This cross section is also called Born cross section (see Ref. [53]). The Born matrix element $\mathcal{M}_{\mathrm{Born}}$ is given by

$$\mathcal{M}_{\mathrm{Born}} = \frac{1}{q^2}\mathcal{L}_\mu \mathcal{P}^\mu = -\frac{e^2}{q^2}\bar{u}(l')\gamma_\mu u(l)\bar{u}(p')\Gamma_p^\mu u(p), \tag{2.5}$$

where $\mathcal{L}_\mu = -e\bar{u}(l')\gamma_\mu u(l)$ is the lepton current, while the proton current $\mathcal{P}^\mu$ was given in Eq. (2.1). The bar in Eq. (2.4) indicates that we need to average over initial state polarizations and sum over the final ones, after squaring of the matrix element. For the unpolarized cross section, this is achieved by

$$\overline{|\mathcal{M}|^2} = \frac{1}{4}\sum_{\text{spins}} |\mathcal{M}|^2, \tag{2.6}$$

where the sum over final state polarizations leads to the calculation of a trace. For the calculation of the trace the conventions from Ref. [19] are used. This leads to the following formula for the Born cross section:

$$\begin{aligned}\frac{\mathrm{d}\sigma^{(0)}}{\mathrm{d}Q^2} = & \frac{\pi\alpha^2}{Q^4\left((s - m_\ell^2 - M^2)^2 - 4m_\ell^2 M^2\right)} \\ & \Big[2\left(F_1^p\right)^2\left((s - m_\ell^2 - M^2)^2 + (s - Q^2)^2 - 2s(m_\ell^2 + M^2) + (M^2 + m_\ell^2)^2\right) \\ & + 4F_1^p F_2^p Q^2\left(Q^2 - 2m_\ell^2\right) \\ & + \left(F_2^p\right)^2 \frac{Q^2}{M^2}\left((s - m_\ell^2 - M^2)(s - Q^2) - (s - Q^2)M^2 - sm_\ell^2 + (M^2 - m_\ell^2)^2\right)\Big].\end{aligned} \tag{2.7}$$

Here, s is the square of the energy in the center-of-mass reference frame, $s = (l + p)^2$ and α the fine structure constant. An alternative compact expression for the Born cross section including all mass terms is given in App. A.

For the applications that we are considering here (P2 and Qweak experiments), the energies of the incoming and scattered electrons, E and E', are large in comparison with the electron's mass, $E, E' \gg m_\ell$. For lepton scattering angles that are not too small, i.e. $\theta_\ell \gtrapprox 5^\circ$, one can also assume that $m_\ell^2 \ll Q^2$. Using the Sachs electric and magnetic form factors defined

as $G_E = F_1^p - \tau F_2^p$ and $G_M = F_1^p + F_2^p$ with $\tau = Q^2/(4M^2)$, the cross section can be written in a more compact form, neglecting terms proportional to the lepton mass, as

$$\frac{d\sigma^{(0)}}{d\Omega_\ell} = \frac{d\sigma_{\text{Mott}}}{d\Omega_\ell} \frac{1}{\epsilon(1+\tau)} \left[\epsilon G_E^2(Q^2) + \tau G_M^2(Q^2)\right] \tag{2.8}$$

with

$$\frac{d\sigma_{\text{Mott}}}{d\Omega_\ell} = \frac{\alpha^2}{4E^2} \frac{\cos^2(\theta_\ell/2)}{\sin^4(\theta_\ell/2)} \frac{E'}{E} \tag{2.9}$$

and

$$\epsilon = \left[1 + 2(1+\tau)\tan^2(\theta_\ell/2)\right]^{-1} . \tag{2.10}$$

The program that was developed for the numerical evaluation of the cross sections (see chapter 5) includes however all lepton mass terms (except for the two-loop correction terms, see the discussion below in Sec. 2.4.1) and is applicable also for the case of muon scattering.

The proton form factors are considered as external input and are given by the data extracted from measurements. We have implemented into our numerical program three different types of parametrizations existing in the literature (see App. C), including the simple dipole parametrization. All our results given in this work are obtained with a simple dipole form factor parametrization, $G_E = \left(1 + Q^2/\Lambda^2\right)^{-2}$ and $G_M = \kappa_p G_E$ with $\Lambda^2 = 0.71$ GeV^2.

At leading order, the momentum transfer to the nucleon can be determined from the energy and scattering angle of the outgoing lepton. However, emission of a photon can lead to a shift of Q^2 (see Sec. 3.4 for more details) and we have to distinguish the value determined from the scattered lepton from its true value transferred to the nucleon. For this reason, we use an additional notation Q_ℓ^2, defined by

$$Q_\ell^2 = -(l - l')^2 . \tag{2.11}$$

As explained in chapter 1, it is important to include higher-order corrections in order to match the precision that recent and planned low energy experiments can achieve. These higher-order corrections are due to additional photon emission and absorption, either virtual, described by loop diagrams, or real, described by bremsstrahlung diagrams (see Ref. [28]). Both parts are infra-red (IR) divergent taken separately, but give an IR finite result when combined at the level of the cross-section. In our approach we use the phase-space slicing method to separate soft-photon radiation from hard-photon contributions. This method was used also by Mo and Tsai in their classical paper [31] and has the advantage that it is suitable for an event generator, which can be used for the analysis of the experiments. This separation is implemented by using a cut-off Δ on the energy of the radiated photon. Δ is chosen small, below the detection threshold for the observation of a photon in the detector, but not too small, so that it doesn't affect the numerical evaluation (see Sec. 2.2.2). The photons that are emitted with energies above the cut-off Δ are called hard-photons and the corrections that take this effect into account are called hard-photon corrections, while photons with energies below the cut-off Δ are called soft-photons. The soft-photon effects combined with loop diagrams are called non-radiative. The cross section with first order corrections, which includes $\mathcal{O}(\alpha)$ radiative corrections, is given by

$$\sigma^{(1)} = \sigma^{(1)}_{\text{non-rad}} + \sigma^{(1)}_{1h\gamma} , \tag{2.12}$$

where the non-radiative part is split between one loop and one soft-photon corrections as

$$\sigma^{(1)}_{\text{non-rad}} = \sigma^{(1)}_{1\text{–loop}} + \sigma^{(1)}_{1s\gamma}\,. \tag{2.13}$$

At second relative order $\mathcal{O}(\alpha^2)$, we have to include contributions with both one or two radiated photons and we have to distinguish the cases where only one or both photons are either soft or hard. The second-order contribution to the cross section, $\sigma^{(2)}$ is therefore split into three parts:

$$\sigma^{(2)} = \sigma^{(2)}_{\text{non-rad}} + \sigma^{(2)}_{1h\gamma} + \sigma^{(2)}_{2h\gamma}, \tag{2.14}$$

where the first part $\sigma^{(2)}_{\text{non-rad}}$ is the non-radiative cross section that includes two-loop, one-loop combined with one soft-photon and two soft-photons corrections given by

$$\sigma^{(2)}_{\text{non-rad}} = \sigma^{(2)}_{2\text{–loop}} + \sigma^{(2)}_{1\text{–loop}+1s\gamma} + \sigma^{(2)}_{2s\gamma}. \tag{2.15}$$

The second part is the cross section with one hard-photon in the final state combined with one-loop and one soft-photon which is given by

$$\sigma^{(2)}_{1h\gamma} = \sigma^{(2)}_{1\text{–loop}+1h\gamma} + \sigma^{(2)}_{1s\gamma+1h\gamma}\,. \tag{2.16}$$

Both $\sigma^{(2)}_{\text{non-rad}}$ and $\sigma^{(2)}_{1h\gamma}$ contain loop and soft photon corrections which are IR divergent. However the IR parts cancel when combined at the level of the cross-section and leaves us with an IR finite result. The third part here is the cross-section with two hard-photons in the final state which is IR finite.

In addition we will use correction factors defined relative to the differential Born-level cross section defined as $\mathrm{d}\sigma^{(0)}$,

$$\sigma^{(1)}_{\text{non-rad}} = \int \mathrm{d}\sigma^{(0)} \left[\delta^{(1)}_{1\text{–loop}} + \delta^{(1)}_{1s\gamma}(\Delta)\right], \tag{2.17}$$

$$\sigma^{(2)}_{\text{non-rad}} = \int \mathrm{d}\sigma^{(0)} \left[\delta^{(2)}_{2\text{–loop}} + \delta^{(2)}_{1\text{–loop}+1s\gamma}(\Delta) + \delta^{(2)}_{2s\gamma}(\Delta)\right], \tag{2.18}$$

where each δ is labeled with indices which correspond with the ones defined above for the cross sections. Additionally we show explicitly the dependence of the soft-photon parts on the IR cut-off Δ. The soft-photon part can be calculated analytically, integrating up to the cut-off Δ, by using a soft-photon approximation as described in Sec. 2.4.1

Contributions with a hard photon, i.e. with energy above the cut-off Δ, as already mentioned, are infrared finite and the phase space integration can be performed numerically. For one hard-photon at tree level we define the cross section with a hard-photon in the final state as

$$\sigma^{(1)}_{1h\gamma} = \int_{E_\gamma > \Delta} \mathrm{d}^4\sigma^{(1)}_{1\gamma}\,, \tag{2.19}$$

while at second order we define relative correction factors for the one-loop and soft photon contributions as

$$\sigma^{(2)}_{1h\gamma} = \int_{E_\gamma > \Delta} \mathrm{d}^4\sigma^{(1)}_{1\gamma} \left[\delta^{(1)}_{1\text{–loop}+1h\gamma} + \delta^{(1)}_{1s\gamma+1h\gamma}(\Delta)\right], \tag{2.20}$$

where $\mathrm{d}^4\sigma^{(1)}_{1\gamma}$ is the differential cross section for one radiated hard photon at tree-level. The calculation of $\sigma^{(2)}_{1h\gamma}$ is treated in Sec. 2.4.2. Finally, the cross section for two hard photons is given by

$$\sigma^{(2)}_{2h\gamma} = \int_{E_\gamma,\, E'_\gamma > \Delta} \mathrm{d}^7\sigma^{(2)}_{2\gamma} \,. \tag{2.21}$$

This cross-section is IR finite and can be calculated numerically as described in Sec. 2.4.4. We emphasize here that the cut-off parameter Δ is introduced only for a technical reason: it allows us to separate the IR singularities (see Ref. [28]). Only separate parts contributing to the cross section carry a Δ-dependence as shown in the a formulas given above. The sum of non-radiative and hard-photon contributions has to be independent of Δ. However, when we use the soft-photon approximation to calculate the non-radiative contributions, and due to numerical uncertainties we don't expect the result to be exactly Δ-independent. We will study this at more detail below. Our choice to use the phase-space slicing technique is dictated by our goal to develop a full Monte Carlo event simulation program where individual non-radiative and one- or two-photon radiative events can be generated. For the calculation of inclusive cross sections, a subtraction method is an alternative approach which may be preferable if numerical stability is otherwise difficult to achieve. At first-order such an approach was described in Ref. [54] and tested in Refs. [55, 56].

Explicit simple expressions for Feynman diagrams with loops can be found in the literature (see for example Ref. [42]). Where necessary, we used the Mathematica package Feyncalc (see Ref. [57]) to perform the calculations, including a reduction to the conventional scalar one-loop Passarino-Veltman integrals B_0, C_0 and D_0. The final result is obtained in terms of scalar integrals and kinematic invariants. The scalar integrals have simple explicit expressions that are given in App. D.

2.2 First order corrections

2.2.1 Non-radiative cross section

One-loop corrections

This section deals with one-loop corrections to the lepton line for the unpolarized cross section. These corrections consist of self energy diagrams and the vertex graph. The matrix element squared for one-loop corrections at order $\mathcal{O}(\alpha)$ is given by

$$2\Re(\mathcal{M}^\dagger_{\mathrm{Born}}\mathcal{M}_{\mathrm{se1+se2}}) + 2\Re(\mathcal{M}^\dagger_{\mathrm{Born}}\mathcal{M}_{\mathrm{vert}}) \tag{2.22}$$

where the meaning of the labels corresponds to the diagrams shown in Fig. 2.2.

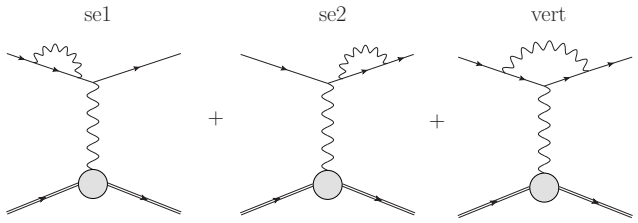

Figure 2.2: Feynman diagrams for the one-loop corrections at the lepton line.

Self-energy corrections

The free electron propagator for an electron with four-momentum l, which is given by

$$S^{(0)}(l) = \frac{\not{l} + m_\ell}{l^2 - m_\ell^2 + i\epsilon}, \tag{2.23}$$

is modified by the self-energy $\Sigma(l)$ as

$$S(l) = S^{(0)}(l) + S^{(0)}(l)\Sigma(l)S(l). \tag{2.24}$$

The self-energy diagram is UV and IR divergent. To regularize the UV divergence we use dimensional regularization, while to regularize the IR divergence we introduce a small fictitious mass λ for the virtual photon that goes in the loop (see App. B). In the lowest order the self-energy diagram in D dimensions is given by

$$\Sigma(l)^{(1)} = (-ie^2)\mu^{D-4}\int \frac{d^d k_l}{(2\pi)^d}\frac{\gamma_\alpha(\not{l} + \not{k}_l + m_\ell)\gamma^\alpha}{(k_l^2 - \lambda^2)\left[(k_l + l)^2 - m_\ell^2\right]}, \tag{2.25}$$

where k_l is the loop momentum and (1) indicates that it is of order α. Performing the loop integral using the method described in App. D we obtain the following structure for the self-energy

$$\Sigma(l)^{(1)} = m_\ell A(l^2) + B(l^2)\not{l}, \tag{2.26}$$

where

$$A(l^2) = \frac{\alpha}{2\pi}\left[1 - 2B_0(l^2, m_\ell^2, \lambda^2)\right]$$
$$B(l^2) = \frac{\alpha}{4\pi}\left[\frac{(m_\ell^2 - \lambda^2)}{l^2}\left(B_0(l^2, m_\ell^2, \lambda^2) - B_0(0, m_\ell^2, \lambda^2)\right) + B_0(l^2, m_\ell^2, \lambda^2) - 1\right].$$

The bare quantities, as the mass, charge and wave-function, that enter the Lagrangian are UV divergent and they are renormalized by adding a counter-term Lagrangian given in App. B. In the on-shell renormalization scheme the self-energy is renormalized by

$$\Sigma^R(l) = \Sigma(l) - (\not{l} - m_\ell)\delta Z_2 - \delta m_\ell, \tag{2.27}$$

where the counter-terms δZ_2 and δm_ℓ contain the ultra-violet (UV) divergences and enter the counter-term Lagrangian as is described in App. B. Inserting the renormalized self-energy given in Eq. (2.27) and in Eq. (2.24) and inverting the total lepton propagator we get

$$S^{-1} = \not{l} - m_\ell - \Sigma^R(l) \tag{2.28}$$

Expanding the inverse lepton propagator around $l - m_\ell = 0$ and truncating the series at $\mathcal{O}\left[(l - m_\ell)^2\right]$ to get one-loop accuracy we obtain the following expression

$$S^{-1} = (l - m_\ell)\left(1 - \left.\frac{\partial \Sigma}{\partial l}\right|_{l=m_\ell} + \delta Z_2\right) + \left[\delta m_\ell - \Sigma(l = m_\ell)\right] + \mathcal{O}\left[(l - m_\ell)^2\right]. \tag{2.29}$$

Requiring that the propagator S has a pole at $l = m_\ell$ with residue 1, allows us to determine the renormalization constants. In dimensional regularization and in the on-shell scheme they are given by

$$\delta Z_2 = -\frac{\alpha}{4\pi}\left[B_0(0, 0, m_\ell^2) - 4m_\ell^2 B_0'(m_\ell^2, \lambda^2, m_\ell^2) - 1\right], \tag{2.30}$$

$$\delta m_\ell = \frac{\alpha}{4\pi} m_\ell \left[B_0(0, 0, m_\ell^2) + 2B_0(m_\ell^2, 0, m_\ell^2) - 1\right]. \tag{2.31}$$

Using the expressions of the scalar integrals given in App. D, the renormalization constants can be expressed also as

$$\delta Z_2 = -\frac{\alpha}{4\pi}\left(\Delta_\epsilon - \ln\frac{m_\ell^2}{\mu^2} + 2\ln\frac{\lambda^2}{m_\ell^2} + 4\right), \tag{2.32}$$

$$\delta m_\ell = \frac{\alpha}{4\pi} m_\ell \left(3\Delta_\epsilon - 3\ln\frac{m_\ell^2}{\mu^2} + 4\right). \tag{2.33}$$

$\Delta_\epsilon = \frac{2}{\epsilon} - \gamma_E + \ln 4\pi$ contains the $1/\epsilon$-poles of the UV divergences, μ is the mass scale parameter of dimensional regularization and λ is a finite photon-mass used to regularize the IR divergence. Inserting Eq. (2.32) into Eq. (2.27) we get

$$\Sigma^{(1),R}(l) = -\frac{\alpha}{2\pi}(l - m_\ell)\left[-B_0(0, 0, m_\ell^2) + B_0(m_\ell^2, 0, m_\ell^2) + 2m_\ell^2 B_0'(m_\ell^2, \lambda^2, m_\ell^2)\right], \tag{2.34}$$

As it can be seen from Eq. (2.34), the self-energy diagrams vanish after renormalization and after contraction of a Dirac spinor of the external lepton, if the external leptons are on-shell. For this reason we only need to include the vertex diagram.

Vertex correction

Since the self-energy correction vanishes for on-shell leptons, the relative one-loop correction is given therefore only by the vertex correction

$$\delta^{(1)}_{1\text{-loop}} = \frac{2\Re(\mathcal{M}^\dagger_{\text{Born}}\mathcal{M}_{\text{vert}})}{|\mathcal{M}_{\text{Born}}|^2}, \tag{2.35}$$

where the matrix element for the $\mathcal{O}(\alpha)$ vertex corrections is given by

$$\mathcal{M}_{\text{vert}} = -\frac{e^2}{q^2}\bar{u}(l')\Gamma^\mu_{\text{vert}}u(l)\bar{u}(p')\Gamma^p_\mu u(p), \tag{2.36}$$

with

$$\Gamma^\mu_{\text{vert}} = (-ie^2)\mu^{4-D}\int \frac{\mathrm{d}^D k_l}{(2\pi)^D}\frac{\gamma^\alpha(\not{l}' - \not{k}_l + m_\ell)\gamma^\mu(\not{l} - \not{k}_l + m_\ell)\gamma_\alpha}{(k_l^2 - \lambda^2)\left[(l' - k_l)^2 - m_\ell^2\right]\left[(l - k_l)^2 - m_\ell^2\right]}, \tag{2.37}$$

where a small fictitious mass λ for the virtual photon was introduced in order to regularize the IR divergence. For on-shell leptons, the vertex correction can be separated into two form factors, in a similar way as was done for the nucleon vertex in 1. The vertex correction can be taken therefore into account by replacing the tree-level on-shell vertex by

$$\gamma^\mu \longrightarrow \Gamma^\mu_{\text{vert}} \equiv F_1^\ell(Q_\ell^2)\gamma^\mu + \frac{i}{2m_\ell}\sigma^{\mu\nu}q_\nu F_2^\ell(Q_\ell^2)\,. \tag{2.38}$$

F_2^ℓ from this expression is UV and IR finite. The other form factor, F_1^ℓ, is both UV and IR divergent. The UV divergence is regularized using dimensional regularization and removed by renormalization by adding a counterterm Lagrangian (see App. B). In the on-shell renormalization scheme the normalization constant that removes the UV divergence is found by requiring that in the limit $Q^2 \longrightarrow 0$ the vertex reproduces the tree level vertex. Therefore at first order the renormalized form factor $F_1^{\ell\,(1,R)}(Q_\ell^2)$ is given by

$$F_1^{\ell\,(1,R)}(Q_\ell^2) = F_1^{\ell\,(1)}(Q_\ell^2) - F_1^{\ell\,(1)}(0) = F_1^{\ell\,(1)}(Q_\ell^2) + \delta Z_1\,, \tag{2.39}$$

where we introduced additional upper indices to display the loop-order and distinguish renormalized (with index R) from unrenormalized quantities. Performing the loop integral from Eq. (2.37) by using the methods described in App. D we get the following expression for the renormalized $F_1^{\ell\,(1,R)}$ form factor

$$\begin{aligned} F_1^{\ell\,(1)}(Q_\ell^2) =& \frac{\alpha}{4\pi}\Big[2(2m_\ell^2 + Q_\ell^2)C_0(m_\ell^2, m_\ell^2, -Q_\ell^2, m_\ell^2, \lambda^2, m_\ell^2) \\ &- 4m_\ell^2 C_0(m_\ell^2, m_\ell^2, 0, m_\ell^2, \lambda^2, m_\ell^2) + \frac{1}{4m_\ell^2 + Q_\ell^2}\Big(Q_\ell^2 B_0(m_\ell^2, 0, m_\ell^2) \\ &- (8m_\ell^2 + 3Q_\ell^2)B_0(-Q_\ell^2, m_\ell^2, m_\ell^2)\Big) + 2B_0(0, m_\ell^2, m_\ell^2)\Big]. \end{aligned} \tag{2.40}$$

The counter-term δZ_1, that removes the UV divergence, is given in the on-shell prescription by

$$\delta Z_1 = -\frac{\alpha}{4\pi}\left[4m_\ell^2 C_0(m_\ell^2, m_\ell^2, 0, m_\ell^2, \lambda^2, m_\ell^2) - 2B_0(0, m_\ell^2, m_\ell^2) + 3B_0(m_\ell^2, 0, m_\ell^2) - 2\right]. \tag{2.41}$$

Inserting the expressions of the scalar integrals found in App. D we get

$$\delta Z_1 = -\frac{\alpha}{4\pi}\left(\Delta_\epsilon - \ln\frac{m_\ell^2}{\mu^2} + 2\ln\frac{\lambda^2}{m_\ell^2} + 4\right). \tag{2.42}$$

δZ_1 is identical with δZ_2, Eq. (2.32), as a consequence of the Ward identity (see for example Refs. [19] or [58]). For $Q^2 \gg m_\ell^2$, ignoring terms suppressed by the lepton mass, the renormalized $F_1^{\ell\,(1)}$ form factor is given by

$$F_1^{\ell\,(1,R)}(Q_\ell^2) = \frac{\alpha}{4\pi}\left[-L^2 + 3L - 4 + \frac{\pi^2}{3} + 4\ln\frac{\lambda}{m_\ell}(L-1)\right], \tag{2.43}$$

where $L = \ln\left(Q^2/m_\ell^2\right)$. The relative vertex correction is therefore given by,

$$\delta^{(1)}_{1-\text{loop}} = 2F_1^{\ell\,(1,R)}\,. \tag{2.44}$$

The result of the loop integration can be found in the literature, including the exact lepton mass dependence (see for example Ref. [42]) and is given by

$$\delta^{(1)}_{1-\text{loop}} = \frac{\alpha}{\pi}\left[\frac{v^2+1}{4v}\ln\left(\frac{v+1}{v-1}\right)\ln\left(\frac{v^2-1}{4v^2}\right) + \frac{2v^2+1}{2v}\ln\left(\frac{v+1}{v-1}\right) - 2 + \frac{v^2+1}{2v}\left(\text{Li}_2\left(\frac{v+1}{2v}\right) - \text{Li}_2\left(\frac{v-1}{2v}\right)\right)\right] + \delta^{(1)}_{\text{IR}}, \tag{2.45}$$

where $v = \sqrt{1+4m_\ell^2/Q_\ell^2}$ and $\delta^{(1)}_{\text{IR}}$ is the term that contains the IR divergence, given by

$$\delta^{(1)}_{\text{IR}} = \frac{\alpha}{\pi}\ln\frac{\lambda^2}{m_\ell^2}\left[\frac{v^2+1}{2v}\ln\left(\frac{v+1}{v-1}\right) - 1\right]. \tag{2.46}$$

This term will cancel at the level of the cross section when one-photon radiation is included, as will be seen below. The exact expression for the second form factor can also be found in Ref. [42] and is given, at first order, by

$$F_2^{\ell(1)} = \frac{\alpha}{4\pi}\frac{v^2-1}{v}\ln\left(\frac{v+1}{v-1}\right). \tag{2.47}$$

It can be seen that this form factor is suppressed by m_ℓ^2/Q^2 and can be ignored for P2 and Qweak kinematics. However we include it in our calculation, since it might become important in some regions of the phase space or for the case of μ scattering.

One radiated photon in the soft-photon approximation

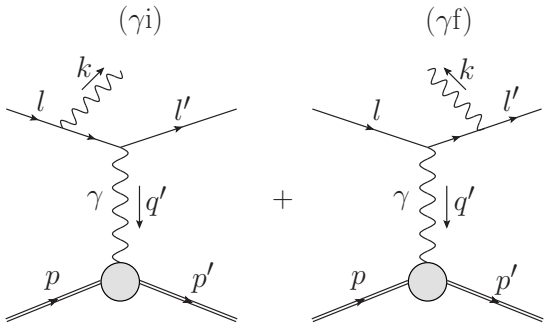

Figure 2.3: Feynman diagrams for first-order leptonic bremsstrahlung corrections.

The diagrams that contribute to the leptonic radiative process $\ell p \longrightarrow \ell p\gamma$ can be found in Fig. 2.3. As can be seen from this figure, we indicate by labels i and f when the photon is emitted from the initial or the final lepton, respectively. The 4-momentum of the final state photon is denoted by k^μ and its energy by E_γ. The matrix element that corresponds for the diagrams of radiative scattering is given by

$$\mathcal{M}^\ell_{1\gamma} = \mathcal{M}^\ell_{1\gamma\text{i}} + \mathcal{M}^\ell_{1\gamma\text{f}}, \tag{2.48}$$

where the matrix element for initial state radiation is given by

$$\mathcal{M}^{\ell}_{1\gamma \mathrm{i}} = i\frac{e^3}{q'^2}\bar{u}(l')\gamma_\mu \frac{\not{l} - \not{k} + m_\ell}{-2lk}\not{\epsilon}^* u(l)\bar{u}(p')\Gamma^\mu_p u(p), \tag{2.49}$$

while the matrix element for final state radiation by

$$\mathcal{M}^{\ell}_{1\gamma \mathrm{f}} = i\frac{e^3}{q'^2}\bar{u}(l')\not{\epsilon}^* \frac{\not{l}' + \not{k} + m_\ell}{2l'k}\gamma_\mu u(l)\bar{u}(p')\Gamma^\mu_p u(p), \tag{2.50}$$

where ϵ^μ is the photon polarization vector. Note that the momentum transfer is shifted by the emission of a photon, $q^\mu \longrightarrow q'^\mu = l^\mu - l'^\mu - k^\mu$, and the matrix element is proportional to $1/Q^2$, not $1/Q^2_\ell$ (see Sec. 3.4 for more details). In the soft-photon approximation it is assumed that the photon 4-momentum $\not{k}$ is neglected in the numerator. The off-shell electron propagators in Eq. (2.49) and Eq. (2.50) are therefore replaced by

$$\frac{\not{l} - \not{k} + m_\ell}{-2lk} \longrightarrow \frac{\not{l} + m_\ell}{-2lk} \qquad \text{and} \qquad \frac{\not{l}' + \not{k} + m_\ell}{2l'k} \longrightarrow \frac{\not{l}' + m_\ell}{2l'k}. \tag{2.51}$$

Making use of the relation $\not{l}\not{\epsilon}^* = -\not{\epsilon}^*\not{l} + 2l\epsilon^*$ and of the Dirac equation to get rid of the $-\not{\epsilon}^*\not{l}$ term, we obtain the following result, known as the eikonal factor,

$$\mathcal{M}^{\ell}_{1\gamma} \longrightarrow \mathcal{M}^{\ell}_{1s\gamma} = -e\mathcal{M}_{0\gamma}\left(\frac{l\epsilon^*}{lk} - \frac{l'\epsilon^*}{l'k}\right). \tag{2.52}$$

Integration over the photon 4-momentum up to a cut-off Δ in the soft-photon approximation leads to

$$\int_{E_\gamma<\Delta} \mathrm{d}^4\sigma^{(1)}_{1s\gamma} = \mathrm{d}\sigma^{(0)}\left(-\frac{\alpha}{4\pi^2}\right)\int_{E_\gamma<\Delta}\frac{\mathrm{d}^3k}{E_\gamma}\left|\frac{l\epsilon^*}{lk} - \frac{l'\epsilon^*}{l'k}\right|^2. \tag{2.53}$$

The sum over photon polarizations amounts to the replacement

$$\sum_{\text{polarizations}} \epsilon^*_\mu\epsilon_\nu \longrightarrow -g_{\mu\nu}. \tag{2.54}$$

Performing the integral of Eq. (2.53) we obtain the following

$$\delta^{(1)}_{1s\gamma}(\Delta) = \left(-\frac{\alpha}{2\pi^2}\right)\int_{E_\gamma<\Delta}\frac{\mathrm{d}^3k}{2E_\gamma}\left|\frac{l\epsilon^*}{lk} - \frac{l'\epsilon^*}{l'k}\right|^2 = -\frac{\alpha}{\pi}\left(B_{ll} - B_{ll'} + B_{l'l'}\right) - \delta^{(1)}_{\mathrm{IR}}, \tag{2.55}$$

where the result has been written as a contribution from initial state radiation, B_{ll}, final state radiation, $B_{l'l'}$ and the interference between the two, $B_{ll'}$. The IR divergence is contained in $\delta^{(1)}_{\mathrm{IR}}$ and cancels exactly against the IR divergent part of Eq. (2.45). The calculation of B_{ll} and $B_{l'l'}$ is straightforward and leads to

$$B_{ll} = \ln\left(\frac{2\Delta}{m_\ell}\right) + \frac{E}{|\vec{l}|}\ln\left(\frac{m_\ell}{E + |\vec{l}|}\right), \tag{2.56}$$

$$B_{l'l'} = \ln\left(\frac{2\Delta}{m_\ell}\right) + \frac{E'}{|\vec{l'}|}\ln\left(\frac{m_\ell}{E' + |\vec{l'}|}\right). \tag{2.57}$$

The calculation of the interference term $B_{ll'}$ is more involved and can be done following Refs. [59] and [34]. The final result is given by [3]

$$\begin{aligned} B_{ll'} = &\ln\left(\frac{4\Delta^2}{m_\ell^2}\right)\frac{v^2+1}{v}\ln\left(\frac{v+1}{v-1}\right) + \frac{\beta l l'}{\xi(\beta E - E')}\left[\frac{1}{4}\ln^2\left(\frac{E-|\vec{l}|}{E+|\vec{l}|}\right) - \frac{1}{4}\ln^2\left(\frac{E'-|\vec{l}'|}{E'+|\vec{l}'|}\right)\right. \\ &+ \mathrm{Li}_2\left(1-\frac{\beta(E-|\vec{l}|)}{\xi}\right) - \mathrm{Li}_2\left(1-\frac{\beta(E'-|\vec{l}'|)}{\xi}\right) \\ &\left.+ \mathrm{Li}_2\left(1-\frac{\beta(E+|\vec{l}|)}{\xi}\right) - \mathrm{Li}_2\left(1-\frac{\beta(E'+|\vec{l}'|)}{\xi}\right)\right], \end{aligned} \tag{2.58}$$

where $ll' = m_\ell^2 + Q_\ell^2/2$ is the product of the 4-momenta of the incident and scattered lepton. The following abbreviations have been used:

$$\begin{aligned} \beta &= \frac{ll' + \sqrt{(ll')^2 - m_\ell^4}}{m_\ell^2}, \\ \xi &= \frac{\beta l l' - m_\ell^2}{\beta E - E'}. \end{aligned}$$

For $Q^2 \gg m_\ell^2$, ignoring terms suppressed by the lepton mass, we get the following result for the first order soft photon correction

$$\delta_{1s\gamma}^{(1)}(\Delta) = \frac{\alpha}{\pi}\left[\ln\left(\frac{\Delta^2}{EE'}\right)(L-1) + \frac{1}{2}L^2 - \frac{1}{2}\ln^2\frac{E}{E'} - \frac{\pi^2}{3} + \mathrm{Li}_2\left(\cos^2\frac{\theta_l}{2}\right)\right] - \delta_{\mathrm{IR}}^{(1)}. \tag{2.59}$$

This expression agrees for example with the one given in Ref. [42]. In our calculations, however, we use the exact expression given in Eq. (2.55). The non-radiative relative correction at first order for the cross section with no observed photon is IR finite and is given by

$$\delta_{\text{non-rad}}^{(1)}(\Delta) = \delta_{\text{1-loop}}^{(1)} + \delta_{1s\gamma}^{(1)}(\Delta). \tag{2.60}$$

In can be seen here that by combining the virtual correction with the real one in the soft photon approximation, not only the IR term $\delta_{\mathrm{IR}}^{(1)}$ cancels, but also the L^2 term. It is a well known result in perturbation theory, called the Kinoshita-Lee-Nauenberg theorem (see Refs. [60], [61] and Ref. [62] for a more recent review), that large logarithms can be considered as mass singularities, since they diverge in the limit $m_\ell \longrightarrow 0$, and they cancel at the level of the cross section in the same way as the IR singularities, when virtual and real corrections are combined. Because of this property the order of logarithms is never higher than the order of the coupling constant, such that the relative cross section has the following structure

$$\delta^{(n)} \equiv \mathrm{d}\sigma^{(n)}/\mathrm{d}\sigma^{(0)} = \sum_{k=0}^{n}\sum_{\ell=0}^{k} c_k \alpha^k L^{k-\ell}\Big|_{n\geq 1} = \sum_{k=0}^{n}\left[c_k\alpha^k L^k + \mathcal{O}(\alpha^k L^{k-1})\Big|_{n\geq 1}\right], \tag{2.61}$$

where L^k are called leading logs.

[3] We have corrected here a typo that appears in our publication (see Ref. [28]).

2.2.2 One hard photon cross section

The diagrams for the radiative process were given in Fig. 2.3. The cross-section for this process with one hard photon in the final state is given by

$$\mathrm{d}^4\sigma^{(1)}_{1h\gamma} = \frac{\mathrm{d}^4\Gamma_{1\gamma}}{4M|\vec{l}\,|}\overline{|\mathcal{M}^{\ell}_{1\gamma}|^2}, \tag{2.62}$$

where the flux factor is given for the fixed-target frame and the bar indicates that one has to average and sum over the polarization degrees of freedom in the initial and final state, respectively (see Ref. [28]). The differential phase-space is given by

$$\mathrm{d}^4\Gamma_{1\gamma} = \int \frac{1}{(2\pi)^5}\,\mathrm{d}^4l'\,\mathrm{d}^4k\,\mathrm{d}^4p'\,\delta(l'^2 - m_\ell^2)\delta(k^2)\delta(p'^2 - M^2)\delta^4\left(l + p - l' - p' - k\right). \tag{2.63}$$

We choose a phase space parametrization in terms of energies and polar angles of the lepton and emitted photon as described in detail in App. E.1. The advantage of such a parametrization is that it allows the implementation of a direct cut on the energy of the scattered lepton, which is required for the applications we are considering here (P2 and Qweak experiments). An alternative choice is to replace the photon energy in favor of its azimuthal angle, see e.g. Ref. [40]. We have implemented also this option in our program for numerical evaluations. We found excellent agreement between the different phase space parametrizations, but one or the other may be preferable for the implementation of kinematic cuts depending on the experimental situation. Using the notation defined there, the cross-section for one hard radiated photon becomes

$$\begin{aligned}\sigma^{(1)}_{1h\gamma} = {} & \frac{1}{32(2\pi)^4 M|\vec{l}\,|}\int_{E'_{\min}}^{E'_{\max}}\mathrm{d}E'\int_{\theta_\ell^{\min}}^{\theta_\ell^{\max}}\mathrm{d}\cos\theta_\ell\int_{\Delta}^{E_\gamma^{\max}}\mathrm{d}E_\gamma\int_{\theta_\gamma^{\min}}^{\theta_\gamma^{\max}}\mathrm{d}\cos\theta_\gamma \\ & \times\frac{\overline{|\mathcal{M}^{\ell}_{1\gamma}|^2}}{\sin\theta_\ell\sin\theta_\gamma\sin\phi_\gamma}\Theta\left(1 - \frac{A^2}{B^2}\right),\end{aligned} \tag{2.64}$$

where $\sin\phi_\gamma = \sqrt{1 - A^2/B^2}$. Explicit expressions for $A = A(E', \theta_\ell, E_\gamma, \theta_\gamma)$, $B = B(E', \theta_\ell, E_\gamma, \theta_\gamma)$ and the integration limits are given in App. E.1, (see Eqs. (E.3) and (E.6)). The matrix element for this process is given by the sum of the matrix elements for initial state and final state radiation as it can be seen from Eq. (2.48). Averaging over initial polarization states and summing over final ones, the matrix element squared reads

$$\begin{aligned}\overline{|\mathcal{M}^{\ell}_{1\gamma}|^2} = -\frac{e^6}{4q'^4}\sum_{\text{spins}}\Bigg|\bar{u}(l')\left[\gamma_\mu\frac{\not{l} - \not{k} + m_\ell}{-2lk}\not{\epsilon}^* + \not{\epsilon}^*\frac{\not{l}' + \not{k} + m_\ell}{2l'k}\gamma_\mu\right]u(l) \\ \times\,\bar{u}(p')\left(\gamma^\mu(F_1^p + F_2^p) - \frac{(p' + p)^\mu}{2M}F_2^p\right)u(p)\Bigg|^2.\end{aligned} \tag{2.65}$$

The sum over final state electron spins leads to a calculation of a trace, which is calculated with the help of `FeynCalc` package and the final result is expressed in terms invariant products of 4-momenta. A compact expression is given in App. A. The numerical integration is performed with the help of `Cuba` package [63].

2.2.3 Vacuum polarization

In general, in an arbitrary ξ gauge, the photon propagator can be separated into a longitudinal and a transversal component as

$$G_{\mu\nu} = G^T_{\mu\nu} + G^L_{\mu\nu}. \tag{2.66}$$

The transversal part satisfies the relation

$$G^T_{\mu\nu} = \mathcal{P}^T_{\mu\nu} G^T_{\mu\nu}, \tag{2.67}$$

where $\mathcal{P}^T_{\mu\nu}$ is a projection operator given by

$$\mathcal{P}^T_{\mu\nu} = g_{\mu\nu} - \frac{k_\mu k_\nu}{k^2}. \tag{2.68}$$

In the Feynman gauge (the gauge used in this work) $\xi = 0$ and the longitudinal part drops out. The vacuum polarization, re-summed to all orders, leads to the replacement of the photon propagator, in the Feynman gauge, by (see Ref. [28])

$$G_{\mu\nu} = \frac{-ig_{\mu\nu}}{q^2\,[1 - \Pi(q^2)]}, \tag{2.69}$$

where $\Pi(q^2)$ is the vacuum polarization function, given below. The correction can be absorbed in the fine-structure constant as

$$\alpha_{\text{eff}}(q^2) = \frac{\alpha}{1 - \Pi(q^2)}. \tag{2.70}$$

The vacuum polarization tensor $\Pi_{\mu\nu}$ at first order, for lepton and anti-lepton loops is given by integrating over the loop momentum, k_l, the Feynman diagram given in Fig. 2.5 as

$$\Pi_{\mu\nu} = (-ie^2)\mu^{4-D} \int \frac{\mathrm{d}^D k_l}{(2\pi)^D} \frac{\mathrm{Tr}\left[\gamma_\mu(\not{k}_l + m_\ell)\gamma_\nu(\not{k}_l + \not{q})\right]}{(k_l^2 - m_\ell^2)\,[(k_l + q)^2 - m_\ell^2]}. \tag{2.71}$$

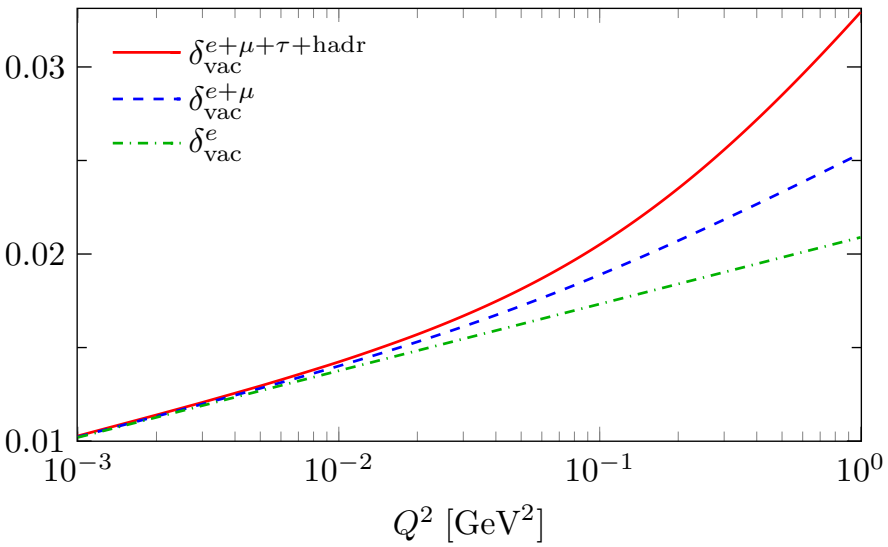

Figure 2.4: Leptonic and hadronic contributions to the vacuum polarization in the Q^2 range relevant for the P2 experiment.

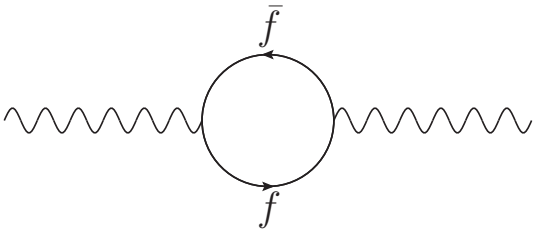

Figure 2.5: Feynman diagram for one-loop vacuum polarization correction.

As a consequence of the Ward-Takahashi identities (see Ref. [19] for example), it can be shown that the vacuum polarization tensor $\Pi_{\mu\nu}$ is transversal to all orders of perturbation theory, i. e.

$$\Pi_{\mu\nu} = -q^2 \mathcal{P}^T_{\mu\nu} \Pi(q^2), \tag{2.72}$$

where $\Pi(q^2)$ is the vacuum polarization function. Performing the loop integral of Eq. (2.71) using the methods of App. D we obtain for the vacuum polarization function the following expression

$$\Pi(q^2) = \frac{\alpha}{9\pi}\left[\frac{6m_\ell^2}{q^2}\left(B_0(q^2, m_\ell^2, m_\ell^2) - B_0(0, m_\ell^2, m_\ell^2)\right) + 3B_0(q^2, m_\ell^2, m_\ell^2) - 1\right]. \tag{2.73}$$

The expression for the vacuum polarization function was regularized by using dimensional regularization and it is UV divergent for $D \longrightarrow 4$. The renormalized vacuum polarization is obtained by adding a counterterm Lagrangian as is described in App. B. In the on-shell renormalization scheme the counterterm is found by normalizing the photon field, such that the experimental value of the electric charge is found in the limit $q \longrightarrow 0$ of Coulomb scattering, i. e.

$$\lim_{k\longrightarrow 0} q^2 G^{(R)T}_{\mu\nu} = -i\mathcal{P}^T_{\mu\nu}, \tag{2.74}$$

where the upper index (R) stands for renormalized. To satisfy the above condition we need to replace the vacuum polarization function from Eq. (2.69) by

$$\Pi(q^2) \longrightarrow \Pi^R(q^2) = \Pi(q^2) - \Pi(0) = \Pi(q^2) + \delta Z_3. \tag{2.75}$$

In the limit $q^2 \longrightarrow 0$ the vacuum polarization function becomes

$$\Pi(q^2 \longrightarrow 0) = \frac{\alpha}{9\pi}\left[6m_\ell^2 B_0'(0, m_\ell^2, m_\ell^2) + 3B_0(0, m_\ell^2, m_\ell^2) - 1\right]. \tag{2.76}$$

Since $B_0'(0, m_\ell^2, m_\ell^2) = 1/6m_\ell^2$ (see App. D) we find

$$\delta Z_3 = -\Pi(0) = -\frac{\alpha}{3\pi} B_0(0, m_\ell^2, m_\ell^2) = -\frac{\alpha}{3\pi}\left(\Delta_\epsilon - \ln\frac{m_\ell^2}{\mu^2}\right). \tag{2.77}$$

The renormalized vacuum polarization is given therefore by

$$\Pi^R(q^2) = \frac{\alpha}{9\pi}\left[\frac{3(2m_\ell^2 + q^2)}{q^2}\left(B_0(q^2, m_\ell^2, m_\ell^2) - B_0(0, m_\ell^2, m_\ell^2)\right) - 1\right]. \tag{2.78}$$

The contribution from lepton loops is given at first order by

$$\delta^{\text{leptons}}_{\text{vac-pol}} = 2\Pi_{e+\mu+\tau}(q^2) = \delta^{e}_{\text{vac-pol}} + \delta^{\mu}_{\text{vac-pol}} + \delta^{\tau}_{\text{vac-pol}} \tag{2.79}$$

and can be written, for space-like momentum transfer $-q^2 = Q^2 > 0$, in a compact form by replacing the expressions for the scalar integrals in Eq. (2.78) with the expressions found in App D as

$$\delta^{\ell}_{\text{vac-pol}} = \frac{2\alpha}{3\pi}\left[\left(v^2 - \frac{8}{3}\right) + v\frac{(3-v^2)}{2}\ln\left(\frac{v+1}{v-1}\right)\right], \tag{2.80}$$

where $v = \sqrt{1+4m_\ell^2/Q^2}$ with m_ℓ the mass of the lepton in the loop. At large Q^2, relative to the lepton mass, one may use [64] [4]:

$$\delta^{\ell}_{\text{vac-pol}} = 2\frac{\alpha}{\pi}\left(\frac{1}{3}\ln\frac{Q^2}{m_\ell^2} - \frac{5}{9}\right) + 2\left(\frac{\alpha}{\pi}\right)^2\left(\frac{1}{4}\ln\frac{Q^2}{m_\ell^2} + \zeta(3) - \frac{5}{24}\right) + O(\alpha^3), \tag{2.81}$$

which includes the two-loop contribution.

The hadronic part of $\Pi(q^2)$ can be extracted from experimental data for the cross section of e^+e^- annihilation into hadrons. We use three different parametrisations for the hadronic contributions. The first one is a table provided by F. Ignatov [65] (see also Ref. [66]). A second one is taken from the work of Jegerlehner (see Ref. [20]). The last one is used by the KNT18 collaboration (see Ref. [67]). In Fig. 2.6 we show a comparison between the different parametrisations. As one can see, for P2 kinematics, the difference between Ignatov and Jegerlehner is negligible. The difference between the Ignatov and the KNT18 parametrizations is larger, but still small, about 0.3%. In Fig. 2.4 we show numerical results for $\delta_{\text{vac-pol}}$. We conclude that one has to include the vacuum polarization effect in a high-precision calculation of the cross section and contributions from other than electron loops should not be neglected for Q^2 values above a few times 10^{-2} GeV^2.

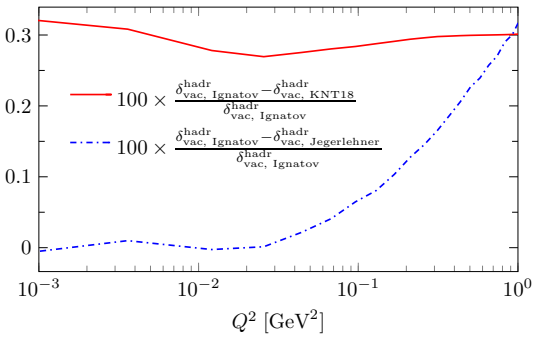

Figure 2.6: Comparison of different parametrizations for the hadronic contributions to the vacuum polarization correction.

2.3 Hadronic corrections

This section deals with $\mathcal{O}(\alpha)$ corrections to the proton line (hadronic corrections) of the unpolarized electron-proton scattering process. These corrections are either purely hadronic, like

[4] For energies at the P2 experiment this expression is valid only for electron and muon loops

self-energies and the vertex correction, or mixed, like the two-photon exchange correction. Hadronic radiation is composed also of a purely hadronic part, coming from the square of the diagrams shown in Fig. 2.14, and the interference between hadronic and leptonic radiation. Hadrons and implicitly protons are composite systems and their constituents are strongly interacting particles, called quarks and gluons, which are described by Quantum Chromodynamics (QCD). This theory can be treated perturbatively for large values of Q^2, in the region where the coupling constant α_s is small, a property called asymptotic freedom. However, α_s becomes increasingly strong for lower values of Q^2. (see Ref. [68] for a review on this topic). In particular, the strong coupling constant $\alpha_s(Q^2)$ is expected to diverge if Q^2 approaches the Landau pole, at $\Lambda^2_{\text{QCD}} \approx (250\ \text{MeV})^2$. Therefore, at low Q^2, QCD breaks down and one has to use an alternative approach in order to calculate these hadronic corrections and effects. One such approach is a theory based on effective Lagrangians, called chiral perturbation theory (ChPT), first developed by Weinberg [69]. However, an effective field theory is not renormalizable and the infinities that appear in the calculations have to be removed order by order. This procedure gives rise to a growing number of low energy constants that have to be fitted to data (see Refs. [70] and [71] for some reviews on this topic). Another approach, which made considerable progress in recent years, is lattice gauge theory or lattice QCD. This theory works by discretizing QCD on a four-dimensional space-time lattice and approaches the physical world in the continuum limit of vanishing lattice constants. A disadvantage of this method is the requirement of considerable computing power. Recently, important progress have been made by improved algorithms and increased computing power (for the recent developments see the most recent PDG review [72]). Both ChPT and lattice QCD cannot make yet precise predictions and therefore we will use a third approach which makes use of experimental data to calculate these corrections. In fact, is possible to make use of experimental data to calculate these effects. One such approach, which was already discussed in the calculation of hadronic contributions to the vacuum polarization in the previous section, is to make use of the optical theorem to relate the experimental data to the imaginary part of the amplitude and dispersion relations to obtain the real part from the imaginary part. Finally, by using a specific model for the internal structure of the nucleon we can rely on the available experimental to determine the nucleon form factors, which in turn can be used in higher order calculations. Following Refs. [42] and [34] this is done in our work by using the on-shell proton vertex function given in Eq. (2.3). This is explained in more detail in the section that deals with hadronic radiation (see Sec. 2.3.3).

2.3.1 Two-photon exchange correction

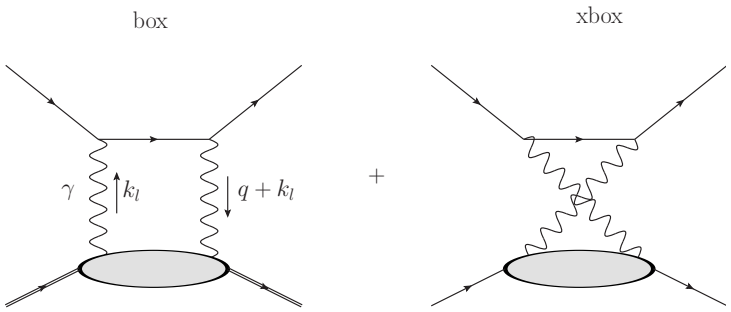

Figure 2.7: Feynman diagrams for first-order two-photon exchange corrections.

The two-photon exchange (TPE) correction has an importance by itself even at low energies, since it becomes important for the extraction of proton form factors (see Ref. [30]) and thus can have indirectly a significant contribution to the electromagnetic radii. For this reason several improved calculations, which take into account different intermediate states, were performed (see for example Refs. [73–76]). Additionally, the TPE correction is important in view of 4-7 standard deviations discrepancy between measurements of the proton charge radius performed using muonic hydrogen spectroscopy and electron scattering experiments (see Ref. [44] and Ref. [77] for some reviews on this topic). The most recent experiment using spectroscopy experiment that was performed on electronic hydrogen (see Ref. [78]) is in good agreement with the recommended CODATA-2014 value, which doesn't include the spectroscopy measurements done with muonic hydrogen. Recently, a new elastic electron-proton scattering experiment has been performed (see Ref. [79]) that agrees with the muonic hydrogen spectroscopy experiment. Thus, this measurement seems to tip the scales in favour of a smaller proton radius, in agreement with the highly accurate results from muonic-hydrogen experiments. Moreover, the MUSE collaboration (see Ref. [1]) plans to make a high precision measurement of the proton radius using both ep and μp elastic scattering. Also the imaginary part of two-photon exchange can be directly accessed through the analysis of single-spin asymmetry in lepton-nucleon scattering (see Ref. [80] for a recent measurement of this observable by the Qweak collaboration using electron proton scattering and Ref. [81] for a recent theoretical calculation), which in turn can be related to the real part via dispersion relations.

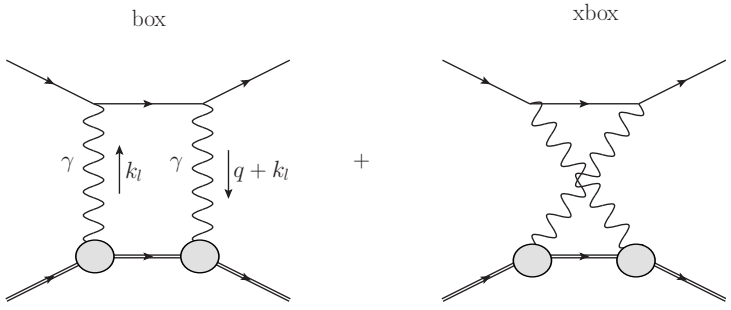

Figure 2.8: Feynman diagrams for first-order two-photon exchange corrections, that describes only the elastic contribution.

At $\mathcal{O}(\alpha)$ the TPE correction is given by the interference between the Born matrix element and box and crossed box matrix elements as

$$2\Re(\mathcal{M}_{\text{Born}}^{\dagger}\mathcal{M}_{\text{box}}) + 2\Re(\mathcal{M}_{\text{Born}}^{\dagger}\mathcal{M}_{\text{xbox}})\,. \tag{2.82}$$

The relative TPE corrections is given then by

$$\delta_{\text{TPE}}^{(1)} = \frac{2\Re(\mathcal{M}_{\text{Born}}^{\dagger}\mathcal{M}_{\text{box}}) + 2\Re(\mathcal{M}_{\text{Born}}^{\dagger}\mathcal{M}_{\text{xbox}})}{|\mathcal{M}_{\text{Born}}|^2}\,, \tag{2.83}$$

where the box and crossed box matrix elements correspond to the diagrams from Fig. 2.7 and are given by

$$\mathcal{M}_{\text{box (xbox)}} = (-ie^4)\int \frac{\mathrm{d}^4k_l}{(2\pi)^4}\frac{\mathcal{L}_{\mu\nu}^{\text{box (xbox)}}\mathcal{P}^{\mu\nu}}{(k_l^2-\lambda^2)\,[(k_l+q)^2-\lambda^2]}\,, \tag{2.84}$$

where a small photon mass λ has been introduced to regularize the IR divergence as in the case of the vertex and soft-photon corrections. The leptonic tensor corresponding to box and cross-box diagrams are given by

$$\mathcal{L}_{\mu\nu}^{\text{box}} = \bar{u}_\ell(l')\gamma_\mu\frac{(\not{l}+\not{k}_l+m_\ell)}{(l+k_\ell)^2-m_\ell^2}\gamma_\nu u_\ell(l)\,, \qquad \mathcal{L}_{\mu\nu}^{\text{xbox}} = \bar{u}_\ell(l')\gamma_\nu\frac{(\not{l}'-\not{k}_l+m_\ell)}{(l'-k_\ell)^2-m_\ell^2}\gamma_\mu u_\ell(l)\,, \tag{2.85}$$

while the proton tensor is given by (see Refs. [44] and [77])

$$\mathcal{P}^{\mu\nu} = \bar{u}_p(p')\Gamma_{\mu\alpha}^{R\to\gamma N}(p+k_l,q+k_l)S^{\alpha\beta}(p-k_\ell,M_R)\Gamma_{\nu\beta}^{\gamma N\to R}(p+k_l,k_l)u_p(p)\,, \tag{2.86}$$

where $S^{\alpha\beta}(p-k_\ell,M_R)$ is the hadronic state propagator and the hadronic transition current operator is written in the general form $\Gamma_{\mu\alpha}^{R\to\gamma N}$, such that it allows for a possible dependence of the incoming momentum q of the virtual photon and the outgoing momentum p_R of the hadron. This definition allows the inclusion of intermediate states and inelastic contributions. Neglecting inelastic intermediate states and assuming only the elastic contribution to the TPE correction (see Fig. 2.8), the proton tensor is given by

$$\mathcal{P}^{\mu\nu} = \bar{u}_p(p')\Gamma_p^{\mu}(q+k_l)\frac{(\not{p}-\not{k}_l+m_\ell)}{(p-k_\ell)^2-M^2}\Gamma_p^{\nu}(k_l)u_p(p)\,. \tag{2.87}$$

Furthermore, we assume that the proton vertex function Γ_p^{μ} has the on-shell form given in Eq. (2.3). The TPE diagrams are UV finite, but IR divergent. The IR-divergent part can be obtained by analyzing the structure of the photon propagators in the integrand. The two poles occur when the four momentum of either of the virtual photons becomes 0. This can happen when $k_l = 0$ or when $q = -k_l$. Applying the soft photon approximation (SPA), which implies the evaluation of the numerator in the integral at either value we get for the box diagram (see Ref. [44])

$$\mathcal{M}_{\text{box}} = -\frac{zZ\alpha}{2\pi}(s-M^2)Q^2\mathcal{M}_{\text{Born}}D_0(s;\lambda^2,\lambda^2,m_\ell^2,M^2)\,, \tag{2.88}$$

where Z is the proton charge and $z = -1$ for negatively charged leptons. In the case of positively charged leptons, the Dirac spinor $u(l)$ in Eq. (2.85) gets replaced by $v(l)$ and this

leads in this expression to $z = 1$. Furthermore, s the Mandelstam variable, given by $s = M^2 + 2ME$ in the laboratory frame, while $D_0(s; \lambda^2, \lambda^2, m_\ell^2, M^2)$ is the four-point Passarino-Veltman function, for which the real part is given in the limit $s - M^2 \gg m_\ell^2, m_\ell M$ by (see Ref. [82])

$$D_0(s; \lambda^2, \lambda^2, m_\ell^2, M^2) = -\frac{2}{(s - M^2)} Q^2 \ln\left(\frac{M^2 - s}{m_\ell M}\right) \ln\left(\frac{Q^2}{\lambda^2}\right) . \tag{2.89}$$

To obtain the expression for the crossed-box diagram we can make use of crossing symmetry to get

$$\mathcal{M}_{\text{xbox}}(u, t) = \mathcal{M}_{\text{box}}(s, t)|_{s \to u} , \tag{2.90}$$

where $t = -Q^2$ and $u = M^2 + 2ME'$ are the other two Mandelstam variables in the laboratory frame. Combining the two expressions we get the same result for the IR contribution that was obtained by Maximon and Tjon in Ref. [34]

$$\delta_{\text{IR}}^{\text{int}} = -2zZ\frac{\alpha}{\pi} \ln\frac{E}{E'} \ln\frac{Q^2}{\lambda^2} . \tag{2.91}$$

In contrast, in the earlier treatment of Mo and Tsai (see Ref. [31]), the SPA is also applied to the denominator. In this case the result for the box diagram is

$$\mathcal{M}_{\text{box}} = zZ\frac{\alpha}{2\pi}(s - M^2)Q^2 \mathcal{M}_{\text{Born}} C_0(s; m_\ell^2, \lambda^2, M^2) , \tag{2.92}$$

where the C_0 is the three-point Passarino-Veltman function and the extra factor of two accounts for the contribution from both poles. Therefore the total contribution from box and crossed-box diagrams in this approximation, as obtained by Mo and Tsai, is given by

$$\delta_{\text{IR}}(\text{MoT}) = -2zZ\frac{\alpha}{\pi} \left[(s - M^2)C_0(s; m_\ell^2, \lambda^2, M^2) - (u - M^2)C_0(u; m_\ell^2, \lambda^2, M^2)\right] . \tag{2.93}$$

To calculate this expression, Mo and Tsai make an additional approximation for the C_0 function by replacing $p \longrightarrow -p$ in the box contribution, or equivalently $s \longrightarrow M^2 - 2ME$. This approximation eliminates the complex term that appears in the calculation of the C_0 function. We this approximation they arrive at

$$\delta_{\text{IR}}(\text{MoT}) = -2zZ\frac{\alpha}{\pi} \left[\text{Li}_2\left(1 + \frac{M}{2E}\right) - \text{Li}_2\left(1 + \frac{M}{2E'}\right) - \frac{1}{2}\ln\frac{E}{E'}\ln\frac{4M^2EE'}{\lambda^4}\right] . \tag{2.94}$$

This expression differs from the one obtained in Eq. (2.91), obtained by Maximon and Tjon. Neither of these two expressions is an exact calculation of the two-photon exchange contribution, but Maximon and Tjon Eq. (2.91) uses a less drastic approximation than Mo and Tsai (see Ref. [83] for the exact expressions of the C_0 functions). The IR pole, however, is the same in both cases and the difference $\delta_{\text{IR}}^{\text{diff}} = \delta_{\text{IR}}^{\text{int}} - \delta_{\text{IR}}(\text{MoT})$ is finite and given by

$$\delta_{\text{IR}}^{\text{diff}} = zZ\frac{\alpha}{\pi} \left[\ln\frac{E}{E'}\ln\frac{Q^4}{4M^2EE'} + 2\text{Li}_2\left(1 + \frac{M}{2E}\right) - 2\text{Li}_2\left(1 + \frac{M}{2E'}\right)\right] . \tag{2.95}$$

For electron-proton scattering at P2 kinematics, as can be seen from Fig. 2.9, the difference $\delta_{\text{IR}}^{\text{diff}}$ between the two approaches is smaller than 10^{-3}. The IR term, $\delta_{\text{IR}}^{\text{int}}$, cancels exactly at the level

of the cross section by including the interference between leptonic and hadronic radiation in the soft-photon limit.

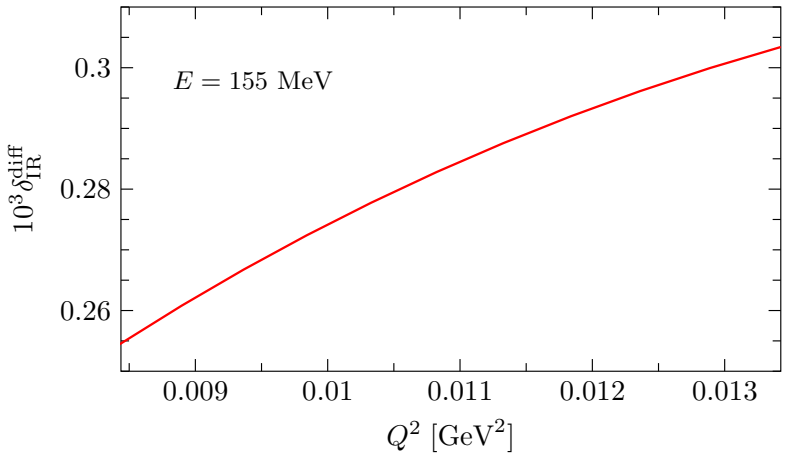

Figure 2.9: The difference between the calculations of Maximon and Tjon and Mo and Tsai for P2 kinematics. Since both have the same IR structure, the difference between them is finite.

A recent calculation at forward angles and at low Q^2, that includes both the elastic and inelastic contributions was performed by Tomalak and Vanderhaeghen (see Ref. [74]). In this work, the TPE contribution is expressed as an integral over the double Compton amplitudes. The double virtual Compton scattering tensor is approximated by two unpolarized virtual Compton scattering amplitudes in the forward limit (see Fig. 2.10), which are obtained as a dispersion integral over the unpolarized proton structure functions. The results of this calculation are available in POLARES (see Sec. 5.1) only for P2 kinematics, i.e. for a beam energy of $E = 155$ MeV and scattering angle $25^\circ < \theta_\ell < 45^\circ$. For this reason we provide also alternatives for this calculation that can be used also for different kinematics.

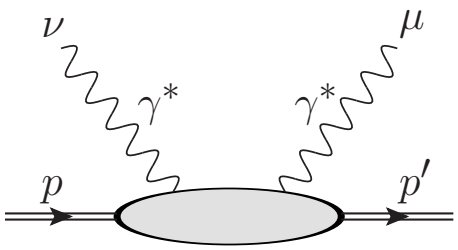

Figure 2.10: Diagram that describes the double virtual Compton scattering.

One of the earlier treatments of this correction was done in the Dirac theory by McKinley and Feshbach in Ref. [84] and is valid at forward limit for $Q^2 \longrightarrow 0$ and $\epsilon \longrightarrow 1$, where ϵ is the virtual photon polarization parameter and was given in Eq.(2.10). This correction, called the Feshbach term δ_F, can be expressed as a function of the scattering angle as

$$\delta_F = \pi\alpha \frac{\sin\frac{\theta_\ell}{2} - \sin^2\frac{\theta_\ell}{2}}{\cos^2\frac{\theta_\ell}{2}}. \tag{2.96}$$

At high momentum transfer, the evaluation of this correction was done in Ref. [85] by using a quark-parton representation of virtual Compton scattering. In the forward limit, for $Q^2 \longrightarrow 0$ and $\epsilon \longrightarrow 1$, the finite part of $\delta^{(1)}_{\rm TPE}$ reduces to the Feshbach term and an additional large logarithmic terms in $(1-\epsilon)$ (see Ref. [73]). We will call this expression the improved Feshbach correction given by

$$\delta^{(1)}_{\rm TPE} - \delta^{\rm int}_{\rm IR} \approx \delta_F + \frac{\alpha}{\pi}\sqrt{\frac{1-\epsilon}{2}}\ln\left[2(1-\epsilon)\right]\left[\frac{1}{2}\ln\left[2(1-\epsilon)\right]+1\right]. \tag{2.97}$$

A more direct way to perform this calculation is to treat the proton as a point-like fermion, i.e. by setting $F_1 = 1$ and $F_2 = 0$. This amounts to the replacement of the proton vertex functions in Eq. (2.87) with corresponding γ-matrices as $\Gamma^\mu_p \longrightarrow \gamma^\mu$ and $\Gamma^\nu_p \longrightarrow \gamma^\nu$. However, this calculation has the disadvantage that it ignores any effect that comes from the proton structure. In this calculation, before performing the integral over the loop momentum k_l, we evaluate the traces that result from summing over final state polarizations after contracting the Born matrix element with the box (xbox) matrix element given in Eq. (2.84). The calculation of the traces and of the loop momentum was performed with the help of `Mathematica` package `FeynCalc` using the methods of App. D, such that the resulting expression is given in terms of products of four momenta and B_0, C_0 and D_0 scalar integrals. The resulting expression is too large to be given here. To evaluate numerically the more complicated four-point functions the package `LoopTools` was used. We call the finite part of this expression the point-like calculation.

Another model dependent way to obtain both the elastic and inelastic contributions to this correction is via dispersion relations. The dispersive approach consists in relating the imaginary part of the TPE amplitude to the real part. The imaginary part can then be obtained from experimental data by using the unitarity condition of the scattering matrix. In general, the S matrix element $S_{fi} = \langle f|S|i\rangle$, between the initial state i, with momentum p_i and final state f, with momentum p_f can be written as

$$S_{fi} = \delta_{fi} + i(2\pi)^4\delta^4(p_f - p_i)\mathcal{M}_{fi}, \tag{2.98}$$

where $\mathcal{M}_{fi}$ is the invariant amplitude. Unitarity requires that

$$2\Im\mathcal{M}_{fi} = \int \mathrm{d}\rho \sum_h \mathcal{M}^*_{nf}\mathcal{M}_{ni}, \tag{2.99}$$

where $\mathrm{d}\rho$ is the covariant phase-space factor for a set of intermediate states h. See Fig. 2.11 for a graphical representation of this relation.

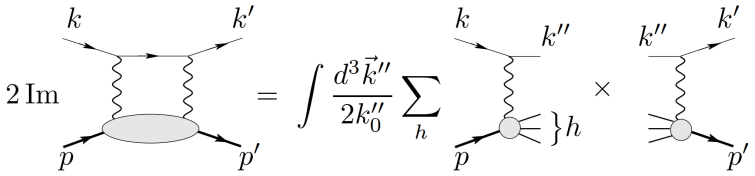

Figure 2.11: A graphical representation of Eq. (2.99) (see Ref. [86]).

In the limit of forward elastic scattering, $i = f$, the product of amplitudes in Eq. (2.99) can be expressed as an observable and allows loop integrations to be evaluated in terms of on-shell states, such that empirical data can be used as input in the calculation of the imaginary part. The Cauchy integral formula allows the real and imaginary parts of $\mathcal{M}_{fi}$ to be related by

$$\Re\mathcal{M}_{fi}(s) = \frac{1}{\pi}\mathcal{P}\int_{-\inf}^{\inf} \mathrm{d}s' \frac{\Im\mathcal{M}_{fi}(s')}{s' - s}\,, \tag{2.100}$$

where $\mathcal{P}$ denotes the principal value of the integral. To relate the two parts it is convenient to decompose the hadronic tensor, as in the case of one photon exchange (OPE) into form factors as (see Ref. [87])

$$\mathcal{P}^{\mu\nu} = \bar{u}_p(p')\left(\tilde{F}_1\gamma_\mu + \tilde{F}_2\frac{i\sigma^{\mu\nu}q_\nu}{2M} + \tilde{F}_3\frac{\gamma\cdot(l+l')\,(p+p')^\mu}{4M^2}\right)u_p(p)\,, \tag{2.101}$$

where $\sigma^{\mu\nu} = \frac{i}{2}[\gamma^\mu,\ \gamma^\nu]$ and the form factors $\tilde{F}_1$, $\tilde{F}_2$ and $\tilde{F}_3$ are functions of Q^2 and ϵ. In the OPE limit $\tilde{F}_1$ and $\tilde{F}_2$ reduce to the usual Dirac and Pauli form factors, while $\tilde{F}_3$ vanishes. As in the OPE limit it is convenient to introduce generalized Sachs form factors, which are given by the ones from the OPE limit and a correction factor, as $\tilde{G}_E = G_E + \delta G_E$ and $\tilde{G}_M = G_M + \delta G_M$. The correction factors δG_E and δG_M have both a real and an imaginary part and are functions of Q^2 and ϵ. In this approach the correction factors δG_E and δG_M, plus the extra form factor $\tilde{F}_3$ can then be calculated via dispersion relations. In Ref. [86] the contribution to the TPE amplitudes arising from nucleon elastic intermediate states was calculated in terms of elastic on-shell nucleon form factors parametrized as a sum of monopoles. The prescription of taking on-shell values for the half off-shell form factors in the direct calculations is an approximation, that seems to works well however at low energies ($Q^2 \leq 6GeV^2$) This calculation can therefore also be used as an alternative to the already mentioned ones and has the advantage that it was implemented in a C++ program called `TPEcalc` (see Ref. [76]) and it is readily available. Furthermore, the program allows the inclusion of various intermediate states. The TPE relative correction can be expressed in terms of the correction factors δG_E and δG_M as

$$\delta^{(1)}_{\mathrm{TPE}} \approx \frac{2}{\epsilon R^2 + \tau}\Re\left(\epsilon R^2\frac{\delta G_E}{G_E} + \tau\frac{\delta G_M}{G_M}\right), \tag{2.102}$$

where $R = G_E/G_M$. The ratios $\delta G_E/G_E$ and $\delta G_M/G_M$ can be obtained with the program `TPEcalc`. In Fig. 2.12 the result obtained with `TPEcalc`, with a proton in the intermediate state is shown, which corresponds to the elastic contribution of TPE. Note, however, that the authors of `TPEcalc` use the approach of Mo and Tsai to regularize the IR divergences. Therefore, for the comparison to be meaningful, we have added the finite difference $\delta^{\mathrm{diff}}_{\mathrm{IR}}$ from Eq.(2.95) to the result obtained with `TPEcalc`. A comparison between the different calculations can also be found in Fig. 2.12 for P2 kinematics. As can be seen from this figure all other calculations are in good agreement with the result obtained by Tomalak and Vanderhaeghen, that includes both elastic and inelastic contributions. For the purpose of the P2 experiment, which aims at per mile precision any of this calculations can be used. In particular, the Feshbach expression is useful, since it has a simple form and can be easily implemented.

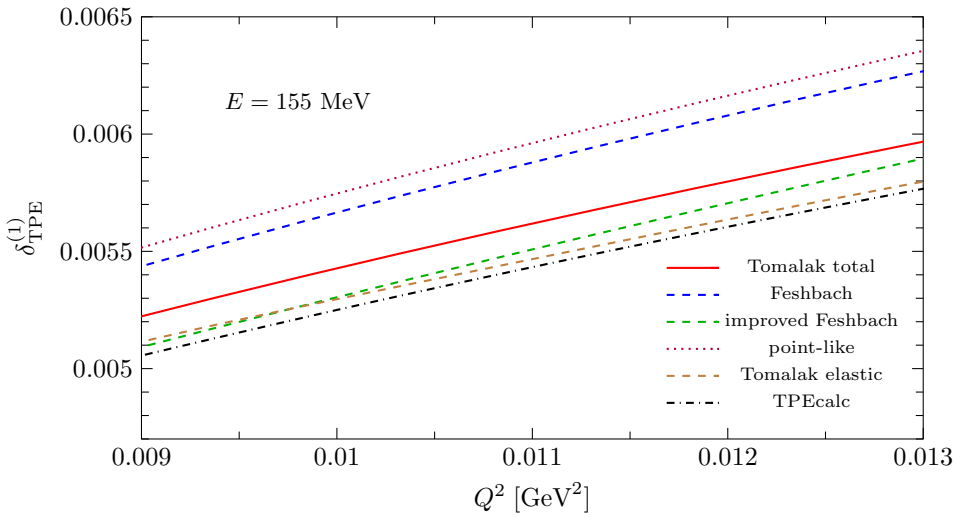

Figure 2.12: A comparison between different calculations of two photon exchange for P2 kinematics. The results called Tomalak total and Tomalak elastic are based on the work of Tomalak and Vanderhaeghen. The Feshbach term was given in Eq. (2.96), while the improved Feshbach expression was given in Eq. (2.97). The point-like result was obtained by treating the proton as a point-like fermion, while the TPEcalc result was obtained with the program of Borisyuk and Kobushkin to which the finite contribution $\delta^{\rm diff}_{\rm IR}$ was added.

We conclude this section by saying that the result for the total TPE correction, as was calculated in Ref. [74] is made available in the program POLARES only for P2 kinematics, i.e. for a beam energy of 155 MeV and scattering angles between 25° and 45° in the laboratory frame. However, as we have seen here, there are many other alternatives at low energies that are a very good approximation of this result, that can be used also for different kinematics. In particular, the Feshbach, the improved Feshbach and the results obtained with TPEcalc were also included in POLARES (see 5.1).

2.3.2 Hadronic self-energy and vertex corrections

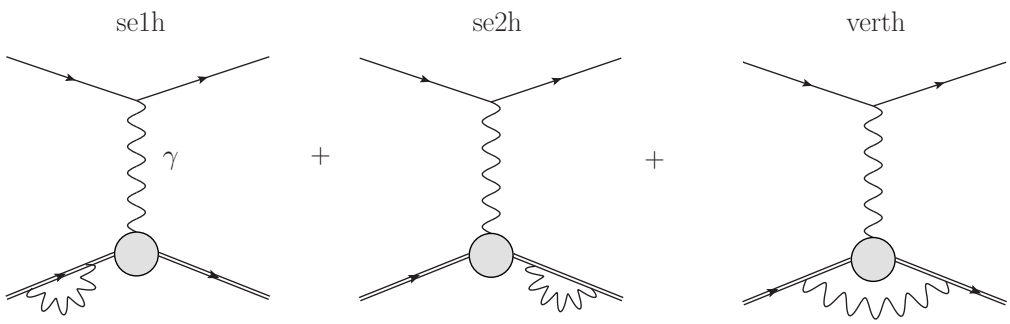

Figure 2.13: Feynman diagrams for first-order hadronic self-energy and vertex corrections.

The interference between the Born matrix element and the matrix elements for the hadronic self-energy and vertex corrections is given by

$$2\Re(\mathcal{M}^{\dagger}_{\text{Born}}\mathcal{M}_{\text{se1h+se2h}}) + 2\Re(\mathcal{M}^{\dagger}_{\text{Born}}\mathcal{M}_{\text{verth}}), \tag{2.103}$$

where the matrix elements correspond to the diagrams from Fig. 2.13. The relative correction is then given by

$$\delta^{(1h)}_{\text{1loop}} = \frac{2\Re(\mathcal{M}^{\dagger}_{\text{Born}}\mathcal{M}_{\text{verth}})}{|\mathcal{M}_{\text{Born}}|^2} + \frac{2\Re(\mathcal{M}^{\dagger}_{\text{Born}}\mathcal{M}_{\text{se1h+se2h}})}{|\mathcal{M}_{\text{Born}}|^2}. \tag{2.104}$$

In Ref. [34] the effects of these corrections are calculated by taking the proton form factors to have a dipole form as

$$F_1^p = F_2^p = \left(\frac{\Lambda^2}{Q^2+\Lambda^2}\right)^2. \tag{2.105}$$

In their calculation, the authors of Ref. [34] split the result into a part which is form factor independent (denoted by $\delta^{(0)}_{el}$), and a form factor dependent part (denoted by $\delta^{(1)}_{el}$). The IR divergence, that cancels when we include soft-photon hadronic radiation (see next section for more details), is entirely contained in the form factor independent part, which is given by

$$\delta^{(0)}_{el} = Z^2\frac{\alpha}{\pi}\frac{E_p}{|\vec{p}_2|}\left[-\ln x \ln\left(\frac{\rho^2}{M^2}\right) + \frac{1}{2}\ln^2 x + 2\text{Li}_2\left(-\frac{1}{x}\right) + \frac{\pi^2}{6}\right] + \delta^{(1h)}_{\text{IR}}, \tag{2.106}$$

where $x = (Q+\rho)^2/4M^2$ with $\rho^2 = Q^2 + 4M^2$. The IR term $\delta^{(1h)}_{\text{IR}}$ is given by

$$\delta^{(1h)}_{\text{IR}} = -Z^2\frac{\alpha}{\pi}\left(\frac{E_p}{|\vec{p}_2|}\ln x - 1\right)\ln\frac{M^2}{\lambda^2}. \tag{2.107}$$

For the expression of $\delta^{(1)}_{el}$, originating from the inclusion of form factors in the calculation of the self-energy and vertex corrections, we refer to Ref. [34]. We mention here that $\delta^{(1)}_{el}$ gives a small contribution of approximately 0.2% for $Q^2 = 6$ GeV^2 and a beam energy of $E = 4.4GeV$ in the study of Ref. [34]. Even at these higher energies this contribution is very small, at per mile level. Since at lower energies we expect this contribution to be even smaller, we can conclude that $\delta^{(1)}_{el}$ can be safely ignored for P2 kinematics. As an alternative to this calculation we present another way of calculating this contribution by ignoring the structure of the proton and treating it as a fermion particle, i.e. setting the form factors to $F_1 = 1$ and $F_2 = 0$. By doing so, the self-energies vanish for on-shell protons, as they do for on-shell leptons (see Sec.2.2.1), such that the 1-loop correction to the proton side is given only by the vertex correction as

$$\delta^{(1h)}_{\text{1loop}} = \frac{2\Re(\mathcal{M}^{\dagger}_{\text{Born}}\mathcal{M}_{\text{verth}})}{|\mathcal{M}_{\text{Born}}|^2}, \tag{2.108}$$

where the matrix element for the vertex correction is given by

$$\mathcal{M}_{\text{vert}} = -\frac{e^2}{q^2}\bar{u}(l')\gamma^{\mu}u(l)\bar{u}(p')\Gamma^{\text{vert},p}_{\mu}u(p), \tag{2.109}$$

with

$$\Gamma^{\text{vert},p}_{\mu} = (-ie^2)\mu^{4-D}\int\frac{\mathrm{d}^D k_l}{(2\pi)^D}\frac{\gamma^{\alpha}(\not{p}-\not{k}_l+M)\gamma_{\mu}(\not{p}'-\not{k}_l+M)\gamma_{\alpha}}{(k_l^2-\lambda^2)\left[(p-k_l)^2-M^2\right]\left[(p'-k_l)^2-M^2\right]}, \tag{2.110}$$

where a small fictitious mass λ for the virtual photon was introduced in order to regularize the IR divergence. To perform the integration over the loop momentum we have used the `Mathematica` package `FeynCalc`. The resulting tensor functions that result from this integration are reduced to B_0 and C_0 scalar integrals, such that we obtain the following expression for the vertex correction factor

$$\begin{aligned}\delta_{\text{vert}}^{(1h)} = &-2\delta Z_1^p + \frac{\alpha}{4\pi}\Bigg[2\Big(3B_0(-Q^2,M^2,M^2) - 4B_0(M^2,0,M^2) \\ &- 2(2M^2+Q^2)C_0(M^2,M^2,-Q^2,M^2,\lambda^2,M^2)\Big) \\ &- \frac{Q^2(Q^2-4S)^2\left(B_0(-Q^2,M^2,M^2) - B_0(0,M^2,M^2) - 2\right)}{(4M^2+Q^2)(Q^2(2(m_\ell^2+M^2)-Q^2)+4Q^2S-8S^2)} \\ &- \frac{\left(4M^2Q^2-(Q^2-4S)^2\right)\left(B_0(-Q^2,M^2,M^2) - B_0(0,M^2,M^2) - 2\right)}{Q^2\left(2(m_\ell^2+M^2)-Q^2\right)+4Q^2S-8S^2}\Bigg],\end{aligned} \tag{2.111}$$

where $S = l\cdot p$ and δZ_1^p is the counter-term that removes the UV divergence and is given in the on-shell prescription by

$$\delta Z_1^p = -\frac{\alpha}{4\pi}\left[B_0(0,M^2,M^2) + 4 + 4M^2C_0(M^2,M^2,0,M^2,\lambda^2,M^2)\right]. \tag{2.112}$$

The expression of scalar integrals, B_0 and C_0 are given in App. D. The IR divergence is contained in the expression of the C_0 scalar integral and cancels exactly at the level of the cross section when we include the square of the hadronic radiation Feynman diagrams, given in Fig. 2.14, in the soft-photon limit (see next section for more details). The expression of $\delta_{\text{vert}}^{(1h)}$ is similar in size with $\delta_{el}^{(0)}$ from Eq. (2.106) and gives a very small contribution, of the order of 10^{-7} for P2 kinematics.

2.3.3 Hadronic radiation

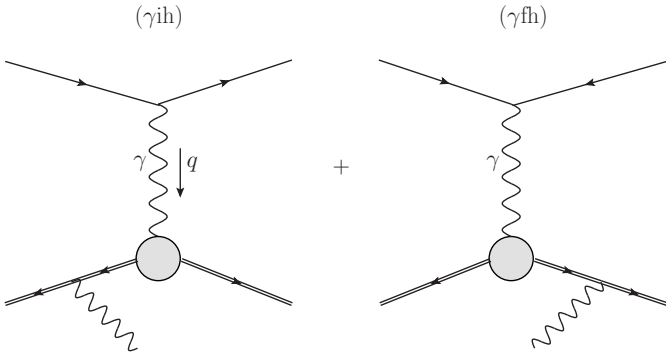

Figure 2.14: Feynman diagrams for first-order hadronic bremsstrahlung corrections.

The matrix element for the radiative process $\ell p \longrightarrow \ell p\gamma$ includes leptonic and hadronic radiation and it is given by

$$\mathcal{M}_{1\gamma} = \mathcal{M}_{1\gamma}^{\ell} + \mathcal{M}_{1\gamma}^{h}. \tag{2.113}$$

The diagrams that describe the leptonic radiative process were given in Fig. 2.3, while the ones that describe the hadronic radiative process are given in Fig. 2.14. As in the case of leptonic radiation, we indicate with i and f, initial and final state hadronic radiation. The matrix element that corresponds to these diagrams is given by

$$\mathcal{M}^h_{1\gamma} = \mathcal{M}^h_{1\gamma i} + \mathcal{M}^h_{1\gamma f}\,. \tag{2.114}$$

We assume that the intermediate hadronic states are virtual proton ones and that the vertices of the photon-proton interaction are described by the on-shell vertex operator Γ^μ, given in Eq. (2.3). With these assumptions the matrix elements for hadronic initial and final state radiation are given by

$$\mathcal{M}^h_{1\gamma \mathrm{i}} = i\frac{e^3}{q^2}\bar{u}(l')\gamma_\mu u(l)\bar{u}(p')\Gamma^\mu_p \frac{\not{p} - \not{k} + m_\ell}{-2pk}\not{\epsilon}^* u(p) \tag{2.115}$$

and

$$\mathcal{M}^h_{1\gamma \mathrm{f}} = i\frac{e^3}{q^2}\bar{u}(l)\gamma_\mu u(l)\bar{u}(p')\not{\epsilon}^* \frac{\not{p}' + \not{k} + m_\ell}{2p'k}\Gamma^\mu_p u(p). \tag{2.116}$$

As in the case of TPE, the intermediate hadronic states can be given by higher resonances. From these intermediate states, $\Delta(1232)$ is the lowest resonance and is expected to give the leading contribution (see Ref. [47]). Although, a simple estimate of the $\Delta(1232)$ correction, that doesn't take into account experimental cuts, leads to a significant contribution to the hadronic radiation process, the authors of Ref. [47] show that an accurate calculation at low energies, by taking into account experimental cuts, leads to a small effect, smaller than 0.01%. Note that in the case of hadronic radiation the momentum transfer squared is not shifted as in the case of leptonic radiation, such that the momentum transfer squared that is being measured is the real momentum transfer squared, denoted by Q^2_ℓ. In the soft-photon approximation, neglecting the 4-momentum of the photon in the numerator we obtain the eikonal factor for the total matrix element, which is given by

$$\mathcal{M}_{1\gamma} \longrightarrow \mathcal{M}_{1s\gamma} = -e\mathcal{M}_{0\gamma}\left(z\frac{l\epsilon^*}{lk} - z\frac{l'\epsilon^*}{l'k} + Z\frac{p\epsilon^*}{pk} - Z\frac{p'\epsilon^*}{p'k}\right), \tag{2.117}$$

where $z = -1$ in the case of negatively charged leptons. In the case of positively charged lepton, the Dirac spinor $u(l)$ is replaced by $v(l)$ and this leads to $z = 1$ in this expression. With this matrix element the cross section in the soft-photon approximation becomes

$$\int_{E_\gamma<\Delta} \mathrm{d}^4\sigma^{(1)}_{1s\gamma} = \mathrm{d}\sigma^{(0)}\left(-\frac{\alpha}{4\pi^2}\right)\int_{E_\gamma<\Delta}\frac{\mathrm{d}^3k}{E_\gamma}\left|z\frac{l\epsilon^*}{lk} - z\frac{l'\epsilon^*}{l'k} + Z\frac{p\epsilon^*}{pk} - Z\frac{p'\epsilon^*}{p'k}\right|^2. \tag{2.118}$$

Evaluating the integral we find terms coming form the square of leptonic radiation and from the hadronic radiation, but also terms from the interference between them. The total relative soft-photon correction becomes

$$\begin{aligned}\delta^{(1)}_{1s\gamma}(\Delta) = &\frac{\alpha}{\pi}\Big[z^2\left(B_{ll} - B_{ll'} + B_{l'l'}\right) + Z^2\left(B_{pp} - B_{pp'} + B_{p'p'}\right)\\ &+ zZ\left(B_{lp} - B_{lp'} - B_{l'p} + B_{l'p'}\right)\Big] - \delta^\ell_{\mathrm{IR}} - \delta^h_{\mathrm{IR}} - \delta^{\mathrm{int}}_{\mathrm{IR}}.\end{aligned} \tag{2.119}$$

The correction arising from the leptonic squared terms B_{ll}, $B_{ll'}$ and $B_{l'l'}$ was treated in Sec. 2.2.1. The hadronic squared terms are given collectively in Ref. [34] by

$$B_{pp} - B_{pp'} + B_{p'p'} = \ln\frac{4\Delta^2}{M^2}\left(\frac{E_p}{|\vec{p'}|}\ln x - 1\right) - \frac{E_p}{|\vec{p'}|}\left[-\frac{\ln^2 x}{2} - \ln x + \mathrm{Li}_2\left(1 - \frac{1}{x^2}\right)\right] - 1, \quad (2.120)$$

where x and ρ were defined in the previous section, while the interference terms are given by

$$B_{lp} - B_{lp'} - B_{l'p} + B_{l'p'} = 2\left[\ln\frac{4\Delta^2}{xQ^2}\ln\eta - \ln\eta\ln x + \mathrm{Li}_2\left(1 - \frac{\eta}{x}\right) - \mathrm{Li}_2\left(1 - \frac{1}{\eta x}\right)\right], \quad (2.121)$$

where $\eta = E/E'$. We separate the hadronic squared terms as

$$\delta^{(1h)}_{1s\gamma}(\Delta) = \frac{\alpha}{\pi}Z^2\left(B_{pp} - B_{pp'} + B_{p'p'}\right) - \delta^h_{\mathrm{IR}} \quad (2.122)$$

and the interference terms

$$\delta^{(1\mathrm{int})}_{1s\gamma}(\Delta) = \frac{\alpha}{\pi}zZ\left(B_{lp} - B_{lp'} - B_{l'p} + B_{l'p'}\right) - \delta^{\mathrm{int}}_{\mathrm{IR}}. \quad (2.123)$$

Combining the square of hadronic radiation with the hadronic vertex correction, the IR divergence cancels and we get a final result given by

$$\delta^{(1h)}_{\text{non-rad}}(\Delta) = \delta^{(1h)}_{1s\gamma}(\Delta) + \delta^{(1h)}_{\text{vert}}. \quad (2.124)$$

In a similar way, combining the interference between hadronic and leptonic radiation with the two-photon exchange correction we get a finite result given by

$$\delta^{(1\mathrm{int})}_{\text{non-rad}}(\Delta) = \delta^{(1\mathrm{int})}_{1s\gamma}(\Delta) + \delta^{(1)}_{\mathrm{TPE}}. \quad (2.125)$$

The cross section for the radiative process in which a photon can be emitted either from the lepton side or from the hadron side is given by

$$\mathrm{d}^4\sigma^{(1)}_{1h\gamma} = \frac{\mathrm{d}^4\Gamma_{1\gamma}}{4M|\vec{l}\,|}\overline{|\mathcal{M}_{1\gamma}|^2}. \quad (2.126)$$

The differential phase space $\mathrm{d}^4\Gamma_{1\gamma}$ for this cross section was given in Eq. (2.63) and a parametrization of it in App. E.1. Separating leptonic from hadronic radiation the averaged matrix element squared becomes

$$\overline{|\mathcal{M}_{1\gamma}|^2} = \overline{|\mathcal{M}^{\ell}_{1\gamma}|^2} + \overline{|\mathcal{M}^{h}_{1\gamma}|^2} + \overline{2\Re\left[\left(\mathcal{M}^{\ell}_{1\gamma}\right)^*\mathcal{M}^{h}_{1\gamma}\right]}. \quad (2.127)$$

The averaged matrix element squared for leptonic radiation was given in Eq. (2.65). Similarly, the averaged matrix element squared for hadronic radiation is given by

$$\begin{aligned}\overline{|\mathcal{M}^{h}_{1\gamma}|^2} = &\frac{e^6}{4q^4}\sum_{\text{spins}}\Big|\bar{u}(l_2)\gamma_\mu u(l_1)\\ &\times\bar{u}(p_2)\Big[\Gamma^\mu(p', p-k)\frac{\not{p}_1 - \not{k} + m_e}{-2p_1k}\Gamma^\alpha(p-k, p)\\ &+\Gamma^\alpha(p', p'+k)\frac{\not{p}_2 + \not{k} + m_e}{2p_2k}\Gamma^\mu(p'+k, p)\Big]u(p_1)\Big|^2,\end{aligned} \quad (2.128)$$

where the sum over the photon polarizations is implicit. The vertex operator Γ_μ is now evaluated for off mass-shell values of one of its arguments. Following Refs. [42] and [40], the on-shell vertex operator, given by

$$\Gamma^\mu(p',p) = F_1^p\left[(p'-p)^2\right]\gamma^\mu + F_2^p\left[(p'-p)^2\right]\frac{i}{2M}\sigma^{\mu\nu}(p'-p)_\nu\,, \tag{2.129}$$

is used when evaluating this matrix element. The averaged matrix element squared for the interference between leptonic and hadronic radiation is given by

$$\begin{aligned}\overline{2\Re\left[\left(\mathcal{M}^{\ell}_{1\gamma}\right)^*\mathcal{M}^{h}_{1\gamma}\right]} = -\,zZ\frac{e^6}{4q^2q'^2}\sum_{\text{spins}}\Re\Bigg[&\bar{u}(l_1)\left(\gamma_\alpha\frac{\not{l}_1-\not{k}+m_e}{-2l_1k}\gamma_\mu+\gamma_\mu\frac{\not{l}_2+\not{k}+m_e}{2l_2k}\gamma_\alpha\right)u(l_2)\\ &\times\bar{u}(p_1)\Gamma_\mu(p',p)u(p_2)\bar{u}(l_2)\gamma_\mu u(l_1)\\ &\times\bar{u}(p_2)\Big[\Gamma^\mu(p',p-k)\frac{\not{p}_1-\not{k}+m_e}{-2p_1k}\Gamma^\alpha(p-k,p)\\ &+\Gamma^\alpha(p',p'+k)\frac{\not{p}_2+\not{k}+m_e}{2p_2k}\Gamma^\mu(p'+k,p)\Big]u(p_1)\Bigg],\end{aligned} \tag{2.130}$$

where again the sum over photon polarizations is implicit. Also here the on-shell form of the vertex operator given in Eq. (2.129) is used in the evaluation. As in the previous case of leptonic radiation, the sum over final state electron and proton spins leads to an evaluation of a trace, which is performed with the help of the package `FeynCalc` and expressed in terms of invariant products of 4-momenta.

In Fig. 2.15 we show a comparison between first order non-radiative corrections for P2 kinematics. The purely hadronic correction $\delta^{(1h)}_{\text{non-rad}}$ is very small, with a contribution of approximately −0.01%, while the interference between hadronic and leptonic, $\delta^{(1\text{int})}_{\text{non-rad}}$ is smaller than 0.5% and is dominated by the two photon exchange correction. Adding also the hard photon correction we get the results shown in Fig. 2.16. We see that the leptonic first order correction becomes positive and it is still dominant at approximately 4%, while the change to the hadronic part is negligible, since the the contribution coming from hadronic radiation is very small.

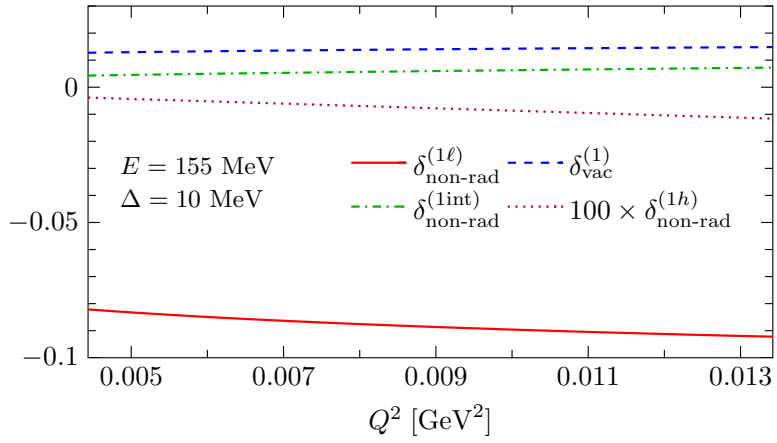

Figure 2.15: A comparison between hadronic and leptonic non-radiative corrections for P2 kinematics at forward angles, $25^\circ < \theta_\ell < 45^\circ$.

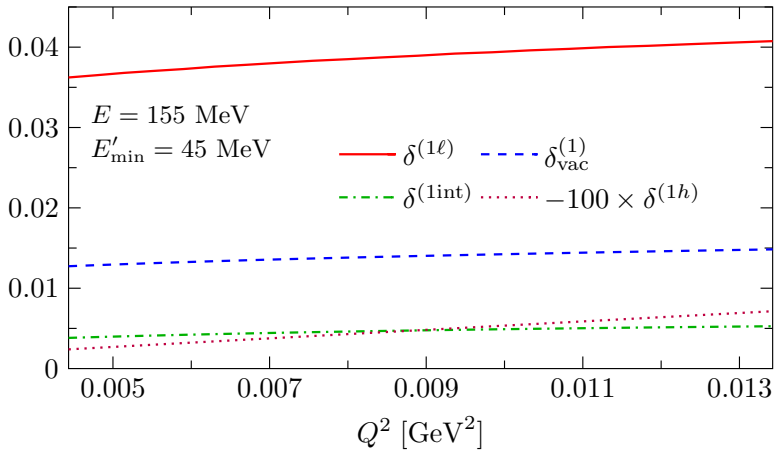

Figure 2.16: Same as Fig. 2.15, but including also hard-photon radiation with a cut on the final state electron energy of $E'_{\text{min}} = 45$ MeV. The relative corrections are defined as $\delta^{(1\ell)} = \sigma^{(1\ell)}/\sigma^{(0)} - 1$, $\delta^{(1\text{int})} = \sigma^{(1\text{int})}/\sigma^{(0)} - 1$ and $\delta^{(1h)} = \sigma^{(1h)}/\sigma^{(0)} - 1$.

We conclude this section by pointing out that the hadronic corrections, except for the TPE correction, don't have a significant contribution at energies relevant for the P2 experiment and they don't need in principle to be included. Moreover, since the form factors have to be extracted from data, if the hadronic corrections are not removed in this process, they are contained inside the form factors. This is also why a clear and transparent extraction method of the form factors has to be provided if one wants to isolate the hadronic corrections.

A more significant contribution comes however from second-order leptonic corrections and this is the topic of the next section.

2.4 Second-order corrections

2.4.1 Non-radiative corrections

The Feynman diagrams for two-loop corrections at the lepton line are shown in Fig. 2.17. Their contribution to the matrix element is denoted by $\mathcal{M}_{\text{2-loop}}$. The relative two-loop correction factor includes the square of the one-loop corrections and is given by

$$\delta^{(2)}_{\text{2-loop}} = \frac{|\mathcal{M}_{\text{vert}}|^2 + 2\Re(\mathcal{M}^{\dagger}_{\text{Born}}\mathcal{M}_{\text{2-loop}})}{|\mathcal{M}_{\text{Born}}|^2}\,. \tag{2.131}$$

For electron scattering, the Pauli form factor F_2^{ℓ} can be neglected at order α^2, since it doesn't contain order one logs. Then the two-loop correction reduces to

$$\delta^{(2)}_{\text{2-loop}} = \left(F_1^{\ell(1)}\right)^2 + 2F_1^{\ell(2)}. \tag{2.132}$$

A compact expression for the second order renormalized form factor $F_1^{\ell(2)}$, in the on-shell scheme, valid for $Q_\ell^2 \gg m_\ell^2$, can be extracted from Ref. [88] and is given by[5]

$$\begin{aligned} F_1^{\ell(2,R)} = \left(\frac{\alpha}{\pi}\right)^2 \Bigg[& \frac{1}{32}L^4 - \frac{31}{144}L^3 + \left(\frac{229}{288} - \frac{\pi^2}{48}\right)L^2 + \left(-\frac{1627}{864} - \frac{13\pi^2}{144} + \frac{3}{2}\zeta(3)\right)L \\ & + \frac{1171}{216} + \frac{13\pi^2}{32} - \frac{\pi^2\ln(2)}{2} - \frac{59\pi^4}{1440} - \frac{9}{4}\zeta(3) + \frac{1}{2}(L-1)^2\ln^2\frac{\lambda}{m_\ell} \\ & + \left(-\frac{L^3}{4} + L^2 + \frac{\pi^2}{12}L - \frac{7}{4}L - \frac{\pi^2}{12} + 1\right)\ln\frac{\lambda}{m_\ell} + \mathcal{O}\left(\frac{m_\ell^2}{Q_\ell^2}\right)\Bigg], \end{aligned} \tag{2.133}$$

where $L = \ln\left(Q_\ell^2/m_\ell^2\right)$. Eq. (2.133) agrees with the earlier calculations[6] of Refs. [92] and [93]. After removing the UV divergent parts the expression still contains IR divergences which

[5] We note that the diagram of Fig. 2.17c is taken into account with an electron loop only. In principle, there are also contributions with a heavy lepton or with hadronic states in the loop. These contributions can be calculated for example with the help of a dispersion relation technique. From similar calculations for other processes [89, 90], their numerical contribution can be estimated to be small.

[6] The two-loop electron form factor from a calculation where both UV and IR divergences are isolated in dimensional regularization can be found in Ref. [91].

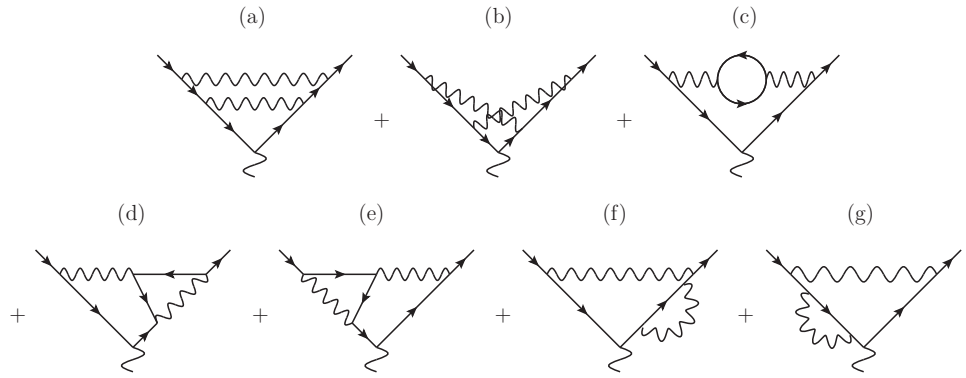

Figure 2.17: Feynman diagrams for two-loop vertex corrections.

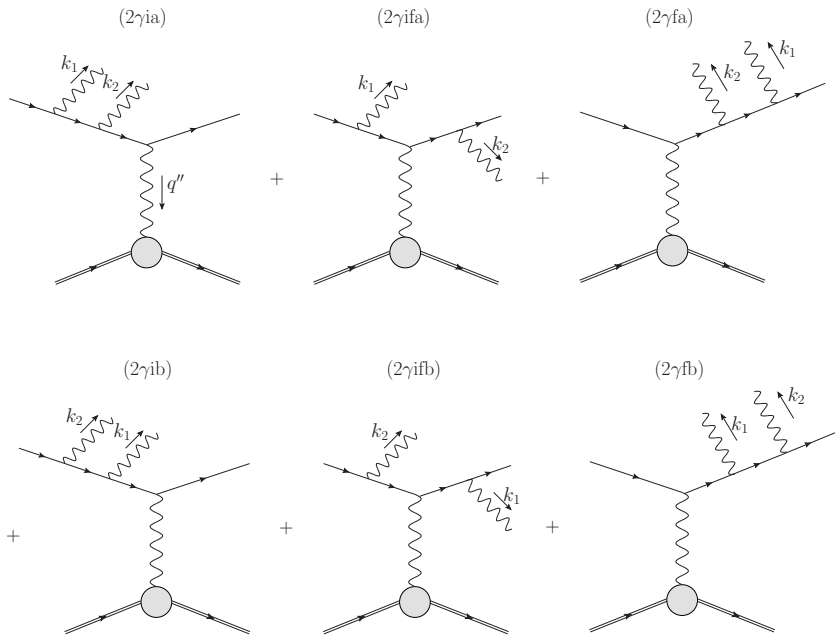

Figure 2.18: Feynman diagrams for two-photon bremsstrahlung.

cancel when soft-photon corrections are included at the level of the cross section. These soft-photon corrections at second order are corrections from two-soft-photon radiation and one-loop corrections for one-soft-photon radiation.

The diagrams for two-photon radiation are shown in Fig. 2.18. In the soft-photon approximation, the corresponding correction factor is given by

$$\delta^{(2)}_{2s\gamma} = \frac{1}{2!}\left(-\frac{\alpha}{4\pi^2}\right)^2 \int_{E_\gamma,\, E'_\gamma<\Delta} \frac{\mathrm{d}^3k_1}{E_\gamma}\frac{\mathrm{d}^3k_2}{E'_\gamma}\left(\frac{l}{lk_1}-\frac{l'}{l'k_1}\right)^2\left(\frac{l}{lk_2}-\frac{l'}{l'k_2}\right)^2 . \tag{2.134}$$

If both photon energies separately are taken smaller than the cut-off value Δ, as we assume here, the phase space integration factorizes and leads to

$$\delta^{(2)}_{2s\gamma} = \frac{1}{2!}\left(\delta^{(1)}_{1s\gamma}\right)^2 . \tag{2.135}$$

In contrast, if the integration is done by restricting the total unobserved energy, i.e., using $E_\gamma + E'_\gamma < \Delta$, as was done for example in Ref. [39], the soft-photon correction factor $\delta^{(2)}_{2s\gamma}$ contains an additional term $-\frac{\alpha^2}{3}(L-1)^2$, which comes from the phase-space overlap of the two photons [38]. In our approach we take account of this overlap region in the contribution from two hard photons. Of course, the final result has to be independent of the way the phase-space slicing is implemented.

The Feynman diagrams for one radiated photon at one-loop order are shown in Fig. 2.19. When treating the photon as soft, one can approximate their contribution by a factorized form in terms of the one-photon and one-loop correction factors:

$$\delta^{(2)}_{1\text{-loop}+1s\gamma}(\Delta) = \delta^{(1)}_{1\text{-loop}}\delta^{(1)}_{1s\gamma}(\Delta) . \tag{2.136}$$

Combining all non-radiative second order corrections at the level of the cross section we obtain an IR finite, but cut-off dependent result,

$$\delta^{(2)}_{\text{non-rad}}(\Delta) = \delta^{(2)}_{\text{2-loop}} + \delta^{(1)}_{\text{1-loop}}\delta^{(1)}_{1s\gamma}(\Delta) + \delta^{(2)}_{2s\gamma}(\Delta)\,. \tag{2.137}$$

Inserting the expressions of the different components we get the following expression:

$$\begin{aligned}\delta^{(2)}_{\text{non-rad}}(\Delta) =& \frac{1}{2}\left(\delta^{(1)}_{\text{non-rad}}(\Delta)\right)^2 \\ &+ \left(\frac{\alpha}{\pi}\right)^2\left[-\frac{1}{36}L^3 + \frac{19}{36}L^2 + \left(-\frac{979}{432} + \frac{132\pi^2}{432} + 3\zeta(3)\right)L + \mathcal{O}(1)\right]\end{aligned} \tag{2.138}$$

As was stated in Sec. 2.2 we don't expect to have terms of L with powers higher than the order of the coupling constant after combining virtual and real corrections, due to the Kinoshita-Lee-Nauenberg theorem. In this particular case, at second order, L^4 terms cancel when combining the two loop correction with the soft photon correction, as can be seen from Eq. (2.138). However, L^3 terms only partially cancel after combining these two corrections. The remaining L^3 term comes exclusively from the diagram 3.3(c), with a vacuum polarization insertion (VPI) in the propagator of the virtual photon. Up to terms of $\mathcal{O}(1)$ the renormalized result for this diagram is given by (see Ref. [62])

$$F_1^{(c)} = \left(\frac{\alpha}{\pi}\right)^2\left[-\frac{1}{36}L^3 + \frac{19}{72}L^2 - \left(\frac{265}{216} + \frac{\pi^2}{36}\right)L + \mathcal{O}(1)\right]. \tag{2.139}$$

A complete result for this diagram can be extracted from the calculation given in Ref. [91] or can be calculated with the methods given in Ref. [90]. The remaining L^3 term cancels exactly when the real pair production correction is also included (see Ref. [62] for more details). However, the real pair production correction has not been included yet in the present calculation. This is why, for consistency, the expression for diagram 3.3(c) given in the previous equation is subtracted from $F_1^{\ell(2,R)}$. In Ref. [62] the real electron-positron pair production is estimated to not exceed a 0.5% correction relative to the Born cross section.

2.4.2 One-loop corrections to radiative scattering

A complete second-order calculation of the cross section includes one-loop corrections for the process with one radiated photon. The corresponding Feynman diagrams are shown in Fig. 2.19. The renormalization of these diagrams is done in on-shell scheme, using dimensional regularization for the UV divergences and a small photon mass for the regularization of the IR divergences (see App. B for more details on the renormalization and regularization methods that were used). In this renormalization scheme the lepton self energy corrections at external legs vanish after renormalization as was described already in Sec.2.2.1.

First, there are two self-energy diagrams with a photon radiated from the off-shell line. Their contribution to the matrix element is denoted by

$$\mathcal{M}_{\text{se1}\gamma} = \mathcal{M}_{\text{se1}\gamma\text{i}} + \mathcal{M}_{\text{se1}\gamma\text{f}}\,. \tag{2.140}$$

The one-loop integral entering $\mathcal{M}_{\text{se1}\gamma}$ is IR finite. Its UV divergence is removed by adding the vertex counter-term proportional to δZ_1 (see Eq. (2.42)).

Next two diagrams are vertex corrections with a photon emitted from the off-shell line and their matrix element is denoted by

$$\mathcal{M}_{\mathrm{v1}\gamma} = \mathcal{M}_{\mathrm{v1}\gamma\mathrm{i}} + \mathcal{M}_{\mathrm{v1}\gamma\mathrm{f}}\,. \tag{2.141}$$

The 4-point one-loop integrals needed here are UV finite, but contain IR-divergent contributions.

The second row of diagrams in Fig. 2.19 have a photon attached to an external, on-shell lepton line; two of them are self energy insertions in the off-shell lepton line,

$$\mathcal{M}_{\mathrm{se2}\gamma} = \mathcal{M}_{\mathrm{se2}\gamma\mathrm{i}} + \mathcal{M}_{\mathrm{se2}\gamma\mathrm{f}}\,, \tag{2.142}$$

and two of them describe a one-loop vertex correction,

$$\mathcal{M}_{\mathrm{v2}\gamma} = \mathcal{M}_{\mathrm{v2}\gamma\mathrm{i}} + \mathcal{M}_{\mathrm{v2}\gamma\mathrm{f}}\,. \tag{2.143}$$

These diagrams are UV divergent and require renormalization by including counter-terms, either at the vertex (δZ_1) or at the lepton self energy (δZ_2 and δm_ℓ).

The second-order corrections due to these diagrams are obtained from the interference with the first-order diagrams. The relative correction that takes into account their contribution can be split into four parts,

$$\delta^{(1)}_{\text{1-loop+1}h\gamma} = \delta^{(1)}_{\mathrm{se1}\gamma} + \delta^{(1)}_{\mathrm{v1}\gamma} + \delta^{(1)}_{\mathrm{se2}\gamma} + \delta^{(1)}_{\mathrm{v2}\gamma}\,, \tag{2.144}$$

where the individual relative corrections are defined by

$$\delta^{(1)}_{\mathrm{se1}\gamma} = \frac{2\Re\left(\mathcal{M}^{\dagger}_{\mathrm{se1}\gamma}\mathcal{M}_{1\gamma}\right)}{\left|\mathcal{M}_{1\gamma}\right|^2}, \qquad \delta^{(1)}_{\mathrm{v1}\gamma} = \frac{2\Re\left(\mathcal{M}^{\dagger}_{\mathrm{v1}\gamma}\mathcal{M}_{1\gamma}\right)}{\left|\mathcal{M}_{1\gamma}\right|^2},$$
$$\delta^{(1)}_{\mathrm{v2}\gamma} = \frac{2\Re\left(\mathcal{M}^{\dagger}_{\mathrm{v2}\gamma}\mathcal{M}_{1\gamma}\right)}{\left|\mathcal{M}_{1\gamma}\right|^2}, \qquad \delta^{(1)}_{\mathrm{se2}\gamma} = \frac{2\Re\left(\mathcal{M}^{\dagger}_{\mathrm{se1}\gamma}\mathcal{M}_{1\gamma}\right)}{\left|\mathcal{M}_{1\gamma}\right|^2}.$$

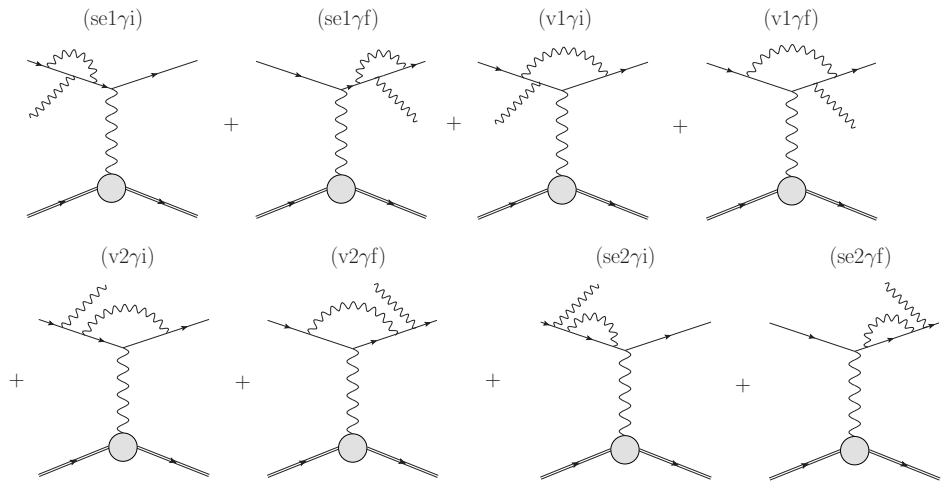

Figure 2.19: Feynman diagrams for one-loop corrections to one-photon bremsstrahlung.

The calculation of these diagrams was done by performing the Passarino-Veltman decomposition and reducing the tensor integrals to scalar integrals with the help of the `Mathematica` package `Feyncalc` (see App. D for details on how the calculation was performed). For the scalar integrals that result from the tensor decomposition we use analytical expressions that are given in App. D. However, after the reduction to scalar integrals is performed, we are left with huge expressions, that can take several mega bytes of hard disk space, which makes them unpractical for the purpose of a numerical calculation. To simplify these expressions we first used the `Mathematica` function `Simplify`. This function already reduces the size considerable of these expressions, but after this simplification we are still left with relatively large expressions and with large powers of masses and invariants in the numerator, which can create problems numerically in some regions of phase space. To further simplify and reduce the size considerably of these expressions (up to ten times) we used recently developed algorithms that make use of partial fractioning techniques. One such algorithm is based on Leinartas' multivariate partial fraction algorithm and it is implemented in the computer algebra system `Singular` (see Ref. [94]). Such a simplification has the advantage, not only that it reduces the size considerably, but also that it removes the higher order powers in the numerator that could create problems numerically otherwise. The algorithm we have used to simplify our expressions also makes sure not to introduce new spurious singularities (see Ref. [95]).

In the following we present the treatment of UV and IR divergences of each of these corrections.

Self-energy with a photon emitted from the off-shell line

The amplitude corresponding to the diagram se1γi from Fig. 2.19, with the correction for the initial state electron line, is given by

$$\mathcal{M}_{\text{se1}\gamma\text{i}} = i\frac{e^3}{q'^2}\bar{u}(l')\gamma_\mu\frac{\not{l}-\not{k}+m_e}{-2lk}\Lambda_{\text{se1}\gamma\text{i}}(l,k)u(l)\bar{u}(p_2)\Gamma_p^\mu u(p_1), \tag{2.145}$$

where $\Lambda_{\text{se1}\gamma\text{i}}$ is the loop correction and is given by

$$\Lambda_{\text{se1}\gamma\text{i}}(l,k) = (-ie^2)\mu^{4-D}\int\frac{\mathrm{d}^D k_l}{(2\pi)^D}\frac{\gamma^\alpha(\not{l}-\not{k}-\not{k}_l+m_e)\not{\epsilon}^*(\not{l}-\not{k}_l+m_e)\gamma_\alpha}{(k_l^2-\lambda^2)\left[(l-k-k_l)^2-m_e^2\right]\left[(l-k_l)^2-m_e^2\right]}. \tag{2.146}$$

$\Lambda_{\text{se1}\gamma\text{i}}$ is IR finite, but contains an UV divergence due to the term proportional with $\gamma^\alpha\not{k}_l\not{\epsilon}^*\not{k}_l\gamma_\alpha$. In order to remove the UV divergence, following Ref. [42], we need to add a counter-term to the matrix element as

$$\mathcal{M}_{\text{se1}\gamma\text{i}} \longrightarrow \mathcal{M}_{\text{se1}\gamma\text{i}} + (CT)_{\text{se1}\gamma\text{i}}, \tag{2.147}$$

where the counter-term is given by

$$(CT)_{\text{se1}\gamma\text{i}} = \mathcal{M}_{\gamma\text{i}}\frac{(-e^2)}{(4\pi)^2}\delta Z_1, \tag{2.148}$$

with

$$\delta Z_1 = -\frac{\alpha}{4\pi}\left(\Delta_\epsilon + \ln\left(\frac{\mu^2}{m_e^2}\right) + 2\ln\left(\frac{\lambda^2}{m_e^2}\right) + 4\right). \tag{2.149}$$

Due to the Ward identity the counter-term for the vertex correction δZ_1 is the same with the counter-term for self-energy correction δZ_2. Therefore δZ_2 is replaced everywhere with δZ_1.

In a similar way, the diagram se1γf from Fig. 2.19, corresponding to the final state correction is given by

$$\mathcal{M}_{\text{se1}\gamma\text{f}} = i\frac{e^3}{q'^2}\bar{u}(l')\Lambda_{\text{se1}\gamma\text{f}}(l',k)\frac{\not{l}'+\not{k}+m_e}{2l'k}\gamma_\mu u(l)\bar{u}(p_2)\Gamma_p^\mu u(p_1), \tag{2.150}$$

where $\Lambda_{\text{se1}\gamma\text{f}}$ is given by

$$\Lambda_{\text{se1}\gamma\text{f}}(l',k) = (-ie^2)\mu^{4-D}\int\frac{\mathrm{d}^D k_l}{(2\pi)^D}\frac{\gamma^\alpha(\not{l}'-\not{k}_l+m_e)\not{\epsilon}^*(\not{l}'+\not{k}-\not{k}_l+m_e)\gamma_\alpha}{(k_l^2-\lambda^2)\left[(l'-k_l)^2-m_e^2\right]\left[(l'+k-k_l)^2-m_e^2\right]}. \tag{2.151}$$

To remove the UV divergence we need to add the following counter-term

$$\mathcal{M}_{\text{se1}\gamma\text{f}} \longrightarrow \mathcal{M}_{\text{se1}\gamma\text{f}} + (CT)_{\text{se1}\gamma\text{f}}, \tag{2.152}$$

where

$$(CT)_{\text{se1}\gamma\text{f}} = \mathcal{M}_{\gamma\text{f}}\frac{(-e^2)}{(4\pi)^2}\delta Z_1. \tag{2.153}$$

Vertex with a photon emitted from the off-shell line

The amplitude corresponding to the diagram v1γi from Fig. 2.19, with a photon emitted from the off-shell initial state line is given by

$$\mathcal{M}_{\text{v1}\gamma\text{i}} = i\frac{e^3}{q'^2}\bar{u}(l')\Lambda_{\text{v1}\gamma\text{i}}(l,l',k)u(l)\bar{u}(p_2)\Gamma_p^\mu u(p_1), \tag{2.154}$$

where the loop correction is given by

$$\begin{aligned}\Lambda_{\text{v1}\gamma\text{i}}(l,l',k) =& (-ie^2)\mu^{4-D} \\ &\times\int\frac{\mathrm{d}^D k_l}{(2\pi)^D}\frac{\gamma^\alpha(\not{l}'-\not{k}_l+m_e)\gamma_\mu(\not{l}-\not{k}-\not{k}_l+m_e)\not{\epsilon}^*(\not{l}-\not{k}_l+m_e)\gamma_\alpha}{(k_l^2-\lambda^2)\left[(l'-k_l)^2-m_e^2\right]\left[(l-k-k_l)^2-m_e^2\right]\left[(l-k_l)^2-m_e^2\right]}.\end{aligned} \tag{2.155}$$

For the final state we get

$$\mathcal{M}_{\text{v1}\gamma\text{f}} = i\frac{e^3}{q'^2}\bar{u}(l')\Lambda_{\text{v1}\gamma\text{f}}(l,l',k)u(l)\bar{u}(p_2)\Gamma_p^\mu u(p_1), \tag{2.156}$$

where the loop correction is given by

$$\begin{aligned}\Lambda_{\text{v1}\gamma\text{f}}(l,l',k) =& (-ie^2)\mu^{4-D} \\ &\times\int\frac{\mathrm{d}^D k_l}{(2\pi)^D}\frac{\gamma^\alpha(\not{l}'-\not{k}_l+m_e)\not{\epsilon}^*(\not{l}'+\not{k}-\not{k}_l+m_e)\gamma_\mu(\not{l}-\not{k}_l+m_e)\gamma_\alpha}{(k_l^2-\lambda^2)\left[(l'-k_l)^2-m_e^2\right]\left[(l-k-k_l)^2-m_e^2\right]\left[(l-k_l)^2-m_e^2\right]}.\end{aligned} \tag{2.157}$$

$\Lambda_{\text{v1}\gamma\text{i}}(l,l',k)$ and $\Lambda_{\text{v1}\gamma\text{f}}(l,l',k)$ are UV finite, but contain an IR divergence. The IR divergences cancel out exactly at the level of the cross section where the result for one hard-photon and one loop is combined with the result for two emitted photons, in which one is a soft-photon. The treatment of the cross section for one-hard photon and one soft-photon is done in Sec. 2.4.3. In Sec. 2.5 we provide a test of the cancellation of IR divergences.

Vertex with a photon emitted from the on-shell line

The amplitude corresponding to the initial state diagram v2γi from Fig. 2.19 is given by

$$\mathcal{M}_{\mathrm{v2}\gamma\mathrm{i}} = i\frac{e^3}{q'^2}\bar{u}(l')\Lambda_{\mathrm{v2}\gamma\mathrm{i}}(l,l',k)\frac{\not{l}-\not{k}+m_e}{-2lk}\not{\epsilon}^* u(l)\bar{u}(p_2)\Gamma^\mu_p u(p_1), \tag{2.158}$$

where $\Lambda_{\mathrm{v2}\gamma\mathrm{i}}$ is the loop correction and is given by

$$\Lambda_{\mathrm{v2}\gamma\mathrm{i}}(l,l',k) = (-ie^2)\mu^{4-D}\int\frac{\mathrm{d}^D k_l}{(2\pi)^D}\frac{\gamma^\alpha(\not{l}'-\not{k}_l+m_e)\gamma_\mu(\not{l}-\not{k}-\not{k}_l+m_e)\gamma_\alpha}{(k_l^2-\lambda^2)\left[(l'-k_l)^2-m_e^2\right]\left[(l-k-k_l)^2-m_e^2\right]}, \tag{2.159}$$

For the final state diagram v2γf we get

$$\mathcal{M}_{\mathrm{v2}\gamma\mathrm{f}} = i\frac{e^3}{q'^2}\bar{u}(l')\not{\epsilon}^*\frac{\not{l}'+\not{k}+m_e}{2l'k}\Lambda_{\mathrm{v2}\gamma\mathrm{f}}(l,l',k)u(l)\bar{u}(p_2)\Gamma^\mu_p u(p_1), \tag{2.160}$$

where $\Lambda_{\mathrm{v2}\gamma\mathrm{i}}$ is the loop correction and is given by

$$\Lambda_{\mathrm{v2}\gamma\mathrm{f}}(l,l',k) = (-ie^2)\mu^{4-D}\int\frac{\mathrm{d}^D k_l}{(2\pi)^D}\frac{\gamma^\alpha(\not{l}'+\not{k}-\not{k}_l+m_e)\gamma_\mu(\not{l}-\not{k}_l+m_e)\gamma_\alpha}{(k_l^2-\lambda^2)\left[(l'-k_l)^2-m_e^2\right]\left[(l-k-k_l)^2-m_e^2\right]}. \tag{2.161}$$

These diagrams contain UV divergences due to the terms in the numerator proportional with $\gamma^\alpha\not{k}_l\gamma_\mu\not{k}_l\gamma_\alpha$. As before, in order to remove the UV divergence we need to add a counter-term to the matrix elements as

$$\begin{aligned}\mathcal{M}_{\mathrm{v2}\gamma\mathrm{i}} &\longrightarrow \mathcal{M}_{\mathrm{v2}\gamma\mathrm{i}} + (CT)_{\mathrm{v2}\gamma\mathrm{i}},\\ \mathcal{M}_{\mathrm{v2}\gamma\mathrm{f}} &\longrightarrow \mathcal{M}_{\mathrm{v2}\gamma\mathrm{f}} + (CT)_{\mathrm{v2}\gamma\mathrm{f}},\end{aligned}$$

where the counter-terms are the same as in the previous case, i.e.

$$\begin{aligned}(CT)_{\mathrm{v2}\gamma\mathrm{i}} &= \mathcal{M}_{\gamma\mathrm{i}}\frac{(-e^2)}{(4\pi)^2}\delta Z_1,\\ (CT)_{\mathrm{v2}\gamma\mathrm{f}} &= \mathcal{M}_{\gamma\mathrm{f}}\frac{(-e^2)}{(4\pi)^2}\delta Z_1.\end{aligned}$$

Self-energy with a photon emitted from the on-shell line

The amplitude corresponding to the initial state diagram se2γi from Fig. 2.19 is given by

$$\mathcal{M}_{\mathrm{se2}\gamma\mathrm{i}} = i\frac{e^3}{q'^2}\bar{u}(l')\gamma_\mu\frac{\not{l}-\not{k}+m_e}{-2lk}\Lambda_{\mathrm{se2}\gamma\mathrm{i}}(l,k)\frac{\not{l}-\not{k}+m_e}{-2lk}\not{\epsilon}^* u(l)\bar{u}(p_2)\Gamma^\mu_p u(p_1), \tag{2.162}$$

where the initial state self energy correction is given by

$$\Lambda_{\mathrm{se2}\gamma\mathrm{i}}(l,k) = (-ie^2)\mu^{4-D}\int\frac{\mathrm{d}^D k_l}{(2\pi)^D}\frac{\gamma^\alpha(\not{l}-\not{k}-\not{k}_l+m_e)\gamma_\alpha}{(k_l^2-\lambda^2)\left[(l-k-k_l)^2-m_e^2\right]}. \tag{2.163}$$

The UV divergence from the self-energy loop integral is removed through renormalization of the electron field and electron mass. The renormalized self-energy is given then by

$$\Lambda_{\mathrm{se2}\gamma\mathrm{i}} \longrightarrow \Lambda^R_{\mathrm{se2}\gamma\mathrm{i}} = \Lambda_{\mathrm{se2}\gamma\mathrm{i}} - \delta Z_1(\not{l}-\not{k}-m_e) - \delta_m, \tag{2.164}$$

where the counter-term that renormalizes the electron mass was given in Sec. 2.2.1. The amplitude for the final state is given by

$$\mathcal{M}_{\mathrm{se2\gamma f}} = i\frac{e^3}{q'^2}\bar{u}(l')\not{\epsilon}^*\frac{\not{l}' + \not{k} + m_e}{2l'k}\Lambda_{\mathrm{se2\gamma f}}(l',k)\frac{\not{l}' + \not{k} + m_e}{2l'k}\gamma_\mu u(l)\bar{u}(p_2)\Gamma_p^\mu u(p_1), \tag{2.165}$$

where the final state self-energy correction is

$$\Lambda_{\mathrm{se2\gamma f}}(l',k) = (-ie^2)\mu^{4-D}\int\frac{\mathrm{d}^D k_l}{(2\pi)^D}\frac{\gamma^\alpha(\not{l}' + \not{k} - \not{k}_l + m_e)\gamma_\alpha}{(k_l^2 - \lambda^2)\left[(l' + k - k_l)^2 - m_e^2\right]}. \tag{2.166}$$

The renormalized final self-energy is given therefore by

$$\Lambda_{\mathrm{se2\gamma f}} \longrightarrow \Lambda^R_{\mathrm{se2\gamma f}} = \Lambda_{\mathrm{se2\gamma f}} - \delta Z_1(\not{l}' + \not{k} - m_e) - \delta_m. \tag{2.167}$$

2.4.3 One hard and one soft photon

The diagrams that contribute to the $ep \longrightarrow ep\gamma\gamma$ process are given in Fig. 2.18. The matrix element for these diagrams is denoted by

$$\mathcal{M}_{2\gamma} = \mathcal{M}_{2\gamma\mathrm{ia}} + \mathcal{M}_{2\gamma\mathrm{ifa}} + \mathcal{M}_{2\gamma\mathrm{fa}} + \mathcal{M}_{2\gamma\mathrm{ib}} + \mathcal{M}_{2\gamma\mathrm{ifb}} + \mathcal{M}_{2\gamma\mathrm{ifb}}. \tag{2.168}$$

Assuming one photon is soft and the other one is hard, it is possible to separate the IR divergent part from the IR finite one. Making use of the Dirac equation we can split $\mathcal{M}_{2\gamma}$ into two parts as

$$\mathcal{M}_{2\gamma} = E(k_1)\mathcal{M}_{1\gamma}(k_2) + R, \tag{2.169}$$

where $\mathcal{M}_{1\gamma}$ is the matrix element for the process $ep \longrightarrow ep\gamma$ given by the diagrams from Fig. 2.3 with photon k_2 in the final state. The IR divergence is contained in $E(k_1)$, called the eikonal factor, which is given by

$$E(k_1) = \left(-\frac{l_1\epsilon_1}{l_1k_1} + \frac{l_2\epsilon_1}{l_2k_1}\right). \tag{2.170}$$

The remainder $R = R_1 + R_2$ can be separated in two parts as

$$\begin{aligned} R_1 &= \mathcal{M}_{2\gamma\mathrm{ib}} + \mathcal{M}_{2\gamma\mathrm{fb}}\,, \\ R_2 &= \left(\mathcal{M}_{2\gamma\mathrm{ia}} + \mathcal{M}_{2\gamma\mathrm{ifa}} + \mathcal{M}_{2\gamma\mathrm{fa}} + \mathcal{M}_{2\gamma\mathrm{ifb}}\right) - E(k_1)\mathcal{M}_{1\gamma}\,, \end{aligned} \tag{2.171}$$

where the different contributions $\mathcal{M}_i$ correspond to the Feynman diagrams shown in Fig. 2.18. The first part, R_1, is given by those diagrams that have the soft-photon emitted from an off-shell line and are thus IR finite. The second part, R_2, is given by the sum of the rest of the diagrams, with the soft-photon emitted from the on-shell line, from which the IR divergent part, contained in the eikonal factor, is subtracted.

The cross section for two photons in the final state is given by

$$\mathrm{d}^7\sigma^{(2)}_{2\gamma} = \frac{\mathrm{d}^7\Gamma_{2\gamma}}{2\cdot 4M|\vec{l}|}\overline{|\mathcal{M}_{2\gamma}|^2}\,, \tag{2.172}$$

where a symmetrization factor of one-half is applied to take into account the fact that there are two identical particles in the final state. Making the integration over the photon energies explicit and taking into account that the cross section is symmetric with respect to interchanging $k_1 \leftrightarrow k_2$, the separation between soft- and hard-photon phase space regions is done as (see Ref. [28])

$$\int_0^{E_\gamma^{\max}} \mathrm{d}E_\gamma \int_0^{E_\gamma^{\max}} \mathrm{d}E'_\gamma = \int_0^{\Delta} \mathrm{d}E_\gamma \int_0^{\Delta} \mathrm{d}E'_\gamma + 2\int_\Delta^{E_\gamma^{\max}} \mathrm{d}E_\gamma \int_0^{\Delta} \mathrm{d}E'_\gamma + \int_\Delta^{E_\gamma^{\max}} \mathrm{d}E_\gamma \int_\Delta^{E_\gamma^{\max}} \mathrm{d}E'_\gamma \,. \quad (2.173)$$

Only the second term on the right-hand side of Eq. (2.173) contributes to the part of the total cross section considered here, where we require one hard and one soft photon. The first part is purely soft-photon and contributes to the non-radiative cross section, combined with the 2-loop contribution, as was described in Sec. 2.4.1, while the last term for two hard photons is described in the next sub-section.

Inserting Eq. (2.169) in Eq. (2.172) we get

$$\sigma_{2\gamma}^{(2)} = \int \frac{\mathrm{d}^7\Gamma_{2\gamma}}{2\cdot 4M|\vec{l}|} \left[\left| E(k_1)\mathcal{M}_{1\gamma}(k_2) \right|^2 + |R|^2 + 2\Re\left(E(k_1)\mathcal{M}_{1\gamma}(k_2)R^\dagger \right) \right] , \quad (2.174)$$

where the over line that denotes the fact we have to sum over final states and average over the initial states is implicit. When integrating from 0 up to a cut-off Δ, the first term of Eq. (2.174) is IR-divergent and must be combined with one-loop diagrams. The IR divergences contained in the one-loop corrections to the radiative process described in the previous sub-section are canceled by corresponding IR divergences from 2-photon bremsstrahlung with one soft-photon. Using the soft-photon approximation, this part can be integrated analytically with the methods presented in Sec. 2.2.1 and it is given by

$$\sigma_{1h\gamma+1s\gamma}^{(2)} = \int_0^{\Delta} \frac{\mathrm{d}^7\Gamma_{2\gamma}}{4M|\vec{l}|} |E(k_1)\mathcal{M}_{1\gamma}|^2 = \int \delta_{1s\gamma}(\Delta)\mathrm{d}^4\sigma_{1\gamma}(k_2). \quad (2.175)$$

The second and third terms of Eq. (2.172) are finite and proportional to Δ. We denote the cross section that includes these two terms by

$$\sigma_{1h\gamma+1s\gamma}^{R} = \int_0^{\Delta} \frac{\mathrm{d}^7\Gamma_{2\gamma}}{4M|\vec{l}|} \left[|R|^2 + 2\Re\left(E(k_1)\mathcal{M}_{1\gamma}(k_2)R^\dagger \right) \right] . \quad (2.176)$$

Since the cross section is proportional to Δ, it vanishes as $\Delta \longrightarrow 0$. This behavior can be seen also from Fig. 2.20, where $\sigma_{1h\gamma+1s\gamma}^{R}$ is plotted as a function of Δ. As Δ becomes smaller it can be seen that the value of the cross section decreases, but also the numerical uncertainties become larger.

The last part of Eq. (2.174) can be safely integrated numerically, since both photon energies are bigger than the cut-off Δ. This last term is described in the next sub-section.

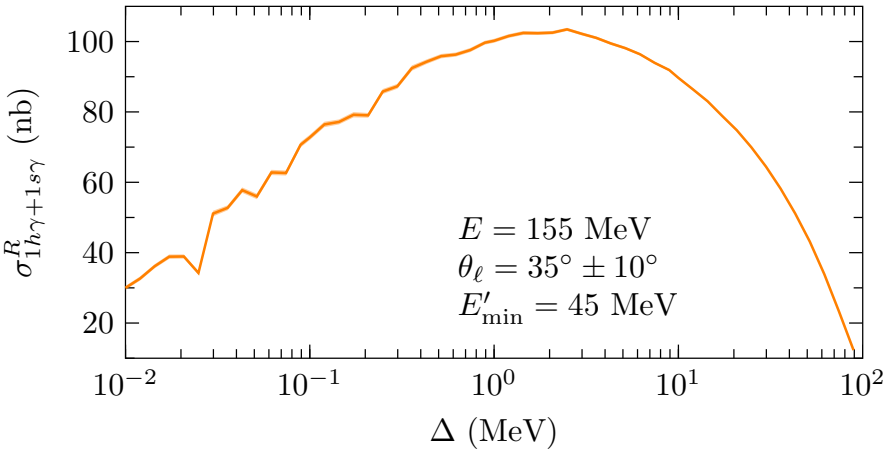

Figure 2.20: The finite part of the cross section with one hard-photon and one soft-photon in the final state plotted as a function of Δ.

2.4.4 Two hard photons cross section

The cross section for $\ell p \longrightarrow \ell p \gamma \gamma$ is given by Eq. (2.172), while the matrix element is given by Eq. (2.168) . The differential phase-space for this process is given by

$$\begin{aligned} \mathrm{d}^7\Gamma = \int \frac{1}{(2\pi)^8}\, \mathrm{d}^4 l'\, \mathrm{d}^4 p'\, \mathrm{d}^4 k_1\, \mathrm{d}^4 k_2\, \delta(l'^2 - m_\ell^2)\delta(p'^2 - M^2)\delta(k_1^2)\delta(k_2^2) \\ \times\, \delta^4\left(l + p - l' - p' - k_1 - k_2\right) . \end{aligned} \tag{2.177}$$

The treatment of the delta-functions and the derivation of integration limits is described in App. E.2. Using the notation defined in App. E.2, the cross section for two-hard-photon radiation is expressed as

$$\begin{aligned} \sigma^{(2)}_{2h\gamma} = \frac{E_\gamma E'_\gamma |\vec{l}\,'|}{128(2\pi)^7 M |\vec{l}|} \int_{E'_{\min}}^{E'_{\max}} \mathrm{d}E' \int_{\cos\theta_{\ell,\min}}^{\cos\theta_{\ell,\max}} \mathrm{d}\cos\theta_\ell \int_{\Delta}^{E_{\gamma,\max}} \mathrm{d}E_\gamma \int_{\Delta}^{E'_{\gamma,\max}} \mathrm{d}E'_\gamma \\ \times \int_{\cos\theta'_{\gamma,\min}}^{\cos\theta'_{\gamma,\max}} \mathrm{d}\cos\theta'_\gamma \int_{\phi'_{\gamma,\min}}^{\phi'_{\gamma,\max}} \mathrm{d}\phi'_\gamma \int_{\cos\theta_{\gamma,\min}}^{\cos\theta_{\gamma,\max}} \mathrm{d}\cos\theta_\gamma \frac{\overline{|\mathcal{M}_{2\gamma}|^2}}{|\alpha_1 \cos\phi_\gamma - \alpha_2 \sin\phi_\gamma|} \Theta\left(1 - \frac{\alpha_3^2}{\alpha_1^2 + \alpha_2^2}\right) , \end{aligned} \tag{2.178}$$

where the integration limits and the definition of the quantities α_i are given in App. E.2.

Taking the complex conjugate squared of the matrix element, averaging over initial spin

states and summing over the final state we get

$$\begin{aligned}\overline{|\mathcal{M}_{2\gamma}|^2} =& \frac{e^8}{4q''^4}\sum_{\text{spins}}\Big|\bar{u}(l')\Big[\gamma_\mu\frac{\not{l}-\not{k}_1-\not{k}_2+m_e}{-2lk_1-2lk_2+2k_1k_2}\not{\epsilon}_2^*\frac{\not{l}-\not{k}_1+m_e}{-2lk_1}\not{\epsilon}_1^* \\ &+\not{\epsilon}_2^*\frac{\not{l}'+\not{k}_2+m_e}{2l'k_2}\gamma_\mu\frac{\not{l}-\not{k}_1+m_e}{-2lk_1}\not{\epsilon}_1^* \\ &+\not{\epsilon}_1^*\frac{\not{l}'+\not{k}_1+m_e}{2l'k_1}\not{\epsilon}_2^*\frac{\not{l}'+\not{k}_1+\not{k}_2+m_e}{2l'k_1+2l'k_2+2k_1k_2}\gamma_\mu + k_1\leftrightarrow k_2\Big]u(l) \\ &\times\bar{u}(p')\left(\gamma^\mu(F_1+F_2)-\frac{(p_2+p_1)^\mu}{2M}F_2\right)u(p)\Big|^2. \end{aligned} \tag{2.179}$$

The sum over the final state electron spins leads to a calculation of a trace. For calculating the trace the function `Tr` from `FeynCalc` package is used. The final result is expressed in term of invariants and consists of a lengthy expression, which is not given here. To simplify and reduce the size considerably of this expression we used a recently developed algorithm that makes use of a partial fraction method called the Leinartas decomposition (see Ref. [95]). A useful feature of this decomposition is that it avoids the introduction of new spurious denominators, by separating the denominators which don't share common zeros or are algebraically dependent. The advantage of the algorithm that we have used over other algorithms, based also on this method (see for example Ref. [94]), is that it allows for deviations from Leinartas' form to allow for lower denominator degrees. Such a simplification has the advantage, not only that it reduces the size considerably, but also that it removes higher order terms in the numerator and denominator that could create problems numerically otherwise.

Since the IR poles are cut-off by integration limits on the photon energies, it is possible to use standard integration packages for numerical calculations. However, there are another type of poles in the differential cross section that could create problems numerically. These type of poles appear whenever a photon is emitted collinear to the direction of either initial or final state electron, for which reason they are called collinear poles. These poles are regularized naturally by the electron mass, but since the electron mass is very small, a naive approach will be numerically unstable. From Eq. (2.168) we find there are collinear poles due to initial, final state radiation and a combination between the two. The poles for initial state radiation are given by the 4-momenta products lk_1 and lk_2, while the poles for final state radiation are given by $l'k_1$ and $l'k_2$. These 4-momenta products reduce in the laboratory frame to $E_\gamma(E-|\vec{l}|)$ and $E_\gamma(E'-|\vec{l}'|)$ whenever the photon k_1 is emitted collinear to the initial state electron or final state electron and to $E'_\gamma(E-|\vec{l}|)$ and $E'_\gamma(E'-|\vec{l}'|)$ whenever the photon k_2 is emitted collinear to the initial state electron or final state electron. Expanding for example the first of the 4-momenta products we get

$$lk_1 \approx \frac{E_\gamma}{E}m_\ell^2\,, \tag{2.180}$$

which tells us that the collinear poles are of the order of $1/m_\ell^2$ if the emitted photon is hard, i.e. $E_\gamma > \Delta$. In order to deal with this problem we have used a partial fractioning technique to separate the collinear poles. First, by multiplying the matrix element squared with $D_1D_2D_3D_4$, where $D_1 = lk_1$, $D_2 = l'k_1$, $D_3 = lk_2$ and $D_4 = l'k_2$, we make sure that none of the 4-momenta products appear anymore in the denominator. Then, since we have to divide back

by $D_1D_2D_3D_4$, we split this denominator as

$$\begin{aligned}\frac{1}{D_1D_2D_3D_4} =& \frac{1}{D_1D_2 + D_1D_3 + D_1D_4 + D_2D_3 + D_2D_4 + D_3D_4} \\ &\left[\frac{1}{D_1}\left(\frac{1}{D_1+D_2}+\frac{1}{D_1+D_3}+\frac{1}{D_1+D_4}\right)\right. \\ &+\frac{1}{D_2}\left(\frac{1}{D_2+D_1}+\frac{1}{D_2+D_3}+\frac{1}{D_2+D_4}\right) \\ &+\frac{1}{D_3}\left(\frac{1}{D_3+D_1}+\frac{1}{D_3+D_2}+\frac{1}{D_3+D_4}\right) \\ &\left.+\frac{1}{D_4}\left(\frac{1}{D_4+D_1}+\frac{1}{D_4+D_2}+\frac{1}{D_4+D_3}\right)\right].\end{aligned} \tag{2.181}$$

Splitting the denominator using this partial fractioning method we make sure that for each part there is only one collinear pole, while the others appear as sums of terms that don't create additional singularities and numerical problems, since we are left only with sums of denominators, $D_i + D_j$, and all 4-momenta products are real numbers, greater than 0. The cross section and implicitly the numerical integration is separated therefore into four parts, for each collinear pole. For each term in the sum, after partial fractioning, we find a specific change of integration variables which allows us to obtain an efficient and numerically stable integration. Since the cross section is symmetric under the interchange $k_1 \leftrightarrow k_2$, we make use of this property to interchange the order of variables in Eq. (2.178). This allows us to deal with the change of variables for denominators D_1 and D_3. Therefore, for the first denominator D_1 we replace the integration of θ_γ by $\ln\left(lk_1/\mu^2\right)$ as

$$\int\limits_{\cos\theta_{\gamma,\min}}^{\cos\theta_{\gamma,\max}} \mathrm{d}\cos\theta_\gamma = \int\limits_{\ln(lk_1/\mu^2)_{\min}}^{\ln\left(lk_1/\mu^2\right)_{\max}} \mathrm{d}\ln\left(lk_1/\mu^2\right)\mathcal{J}_{lk_1}\,, \tag{2.182}$$

with the Jacobian given by $\mathcal{J}_{lk_1} = lk_1/|\vec{l}|E_\gamma$. We have introduced an arbitrary parameter μ^2, which can be chosen with the same dimension of the logarithm, such that the numerical value is not changed, but the argument becomes dimensionless. For D_2 we replace θ'_γ by $\ln\left(lk_2/\mu^2\right)$ as

$$\int\limits_{\cos\theta'_{\gamma,\min}}^{\cos\theta'_{\gamma,\max}} \mathrm{d}\cos\theta'_\gamma = \int\limits_{\ln(lk_2/\mu^2)_{\min}}^{\ln\left(lk_2/\mu^2\right)_{\max}} \mathrm{d}\ln\left(lk_2/\mu^2\right)\mathcal{J}_{lk_2}\,, \tag{2.183}$$

with the Jacobian given by $\mathcal{J}_{lk_2} = lk_2/|\vec{l}|E'_\gamma$; For D_3 we replace ϕ_γ by $\ln\left(l'k_1/\mu^2\right)$ as

$$\int\limits_{\phi_{\gamma,\min}}^{\phi_{\gamma,\max}} \mathrm{d}\phi_\gamma = \int\limits_{\ln(l'k_1/\mu^2)_{\min}}^{\ln\left(l'k_1/\mu^2\right)_{\max}} \mathrm{d}\ln\left(l'k_1/\mu^2\right)\mathcal{J}_{l'k_1}\,, \tag{2.184}$$

with the Jacobian $\mathcal{J}_{l'k_1} = l'k_1/\vec{l}'E_\gamma \sin(\theta_\ell)\sin\left(\theta_\gamma\right)\sin\left(\phi_\gamma\right)$ and finally for D_4 we replace ϕ'_γ by $\ln\left(l'k_2/\mu^2\right)$ as

$$\int\limits_{\phi'_{\gamma,\min}}^{\phi'_{\gamma,\max}} \mathrm{d}\phi'_\gamma = \int\limits_{\ln(l'k_2/\mu^2)_{\min}}^{\ln\left(l'k_2/\mu^2\right)_{\max}} \mathrm{d}\ln\left(l'k_2/\mu^2\right)\mathcal{J}_{l'k_2}\,, \tag{2.185}$$

with the Jacobian $\mathcal{J}_{l'k_2} = l'k_2/\vec{l}'E'_\gamma \sin(\theta_\ell)\sin\left(\theta'_\gamma\right)\sin\left(\phi'_\gamma\right)$. The phase space limits for the new variables can be directly obtained from the limits of the old variables. For example, for D_1 the new limits are given by

$$\begin{aligned}
\ln\left(lk_1/\mu^2\right)_{\min} &= \ln\left[\left(EE_\gamma - |\vec{l}|E_\gamma\cos\left(\theta_\gamma\right)_{\max}\right)/\mu^2\right]\,,\\
\ln\left(lk_1/\mu^2\right)_{\max} &= \ln\left[\left(EE_\gamma - |\vec{l}|E_\gamma\cos\left(\theta_\gamma\right)_{\min}\right)/\mu^2\right]\,.
\end{aligned} \tag{2.186}$$

We note here that Eq. (2.168) contains two additional denominators, given by $lk_1 + lk_2 - k_1k_2$ and $l'k_1 + l'k_2 + k_1k_2$ that become problematic when both photons are emitted either collinear to the initial state electron or to the final state electron. However, since they appear as a sum in the denominator, it turns out that they don't require a special treatment.

2.5 Numerical tests

In this section we present some numerical tests that can be used to check the consistency and the accuracy of our results. Since we know that the bremsstrahlung cross section contains narrow peaks that can create problems numerically, we first show some tests for the numerical integration of these cross sections by varying the number of evaluations, to make sure they reach a point for which the variations of the results are relatively small and they are within the uncertainties predicted by the numerical integration. In the second part we use the fact that we have introduced some unphysical parameters in our calculations in order to deal with the divergent behavior of our expressions. The final result should be of course independent of these parameters and we can vary them to check if the result stays, in fact, constant.

As can be seen from Eq. (2.62) the cross section with one hard radiated photon is proportional to the following 4-momenta products

$$\sigma^{(1)}_{1h\gamma} \propto \frac{1}{(lk)(l'k)}\,, \tag{2.187}$$

or the square of any of them. Because of this property the cross section is divergent if the photon energy goes to 0, i.e. for $E_\gamma \longrightarrow 0$. Using the phase-space slicing method allowed us to separate the integration of this cross section into two parts, by defining a cut-off, Δ, on the photon energy. However, as was explained in the previous section, the cross section contains also collinear peaks that can create problems numerically due to the smallness of the electron mass and we want to make sure that the methods we are using for numerical integration overcome this difficulty. At first order, as can be seen from Fig. 2.21 the integration is stable and for a number of evaluations bigger than 10^7 has very small fluctuations, that lie within the uncertainties predicted by the algorithm. As was mentioned in Sec. 2.2.2 we have used also two

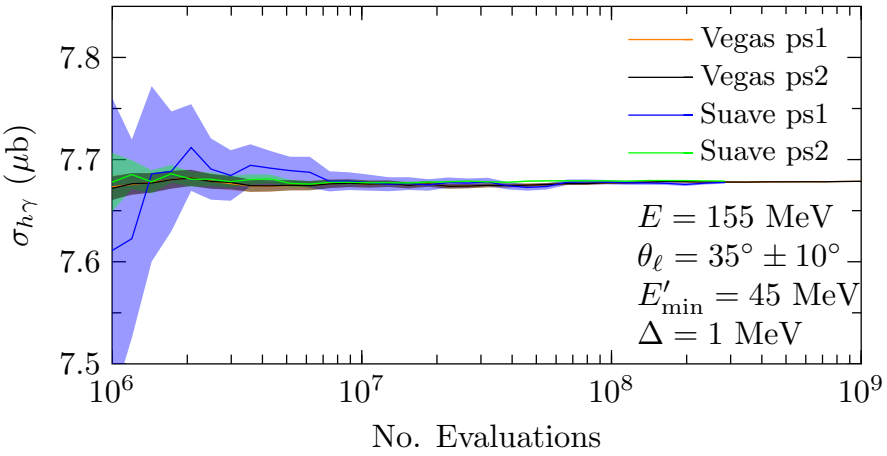

Figure 2.21: The dependence of the bremsstrahlung cross-section with one photon in the final state on the number of evaluations used for the numerical integration. In this figure we also compare the results obtained with two different numerical integration algorithms, Vegas and Suave, and with two different phase-space parametrizations, given in App. E.1. The kinematics are chosen for the P2 experiment.

different phase-space parametrizations (see App. E.1), which allows us to make an additional consistency check by comparing the results obtained in two different ways. Additionally, we compare in this figure also the results obtained with two different algorithms. For the Vegas algorithm, we perform beforehand an additional run with 10^7 evaluations, in order to train the grid. As can be seen from this figure, all integrations agree for a number of evaluations bigger than 10^7 and have small fluctuations, from which we conclude that the numerical integration is stable at first order, despite the collinear poles.

At second order, the cross section with two hard radiated photons is proportional, for example, to the following 4-momenta products

$$\sigma^{(1)}_{1h\gamma} \propto \frac{1}{(lk_1)(lk_2)(l'k_1)(l'k_2)}\,, \tag{2.188}$$

that contain four different collinear poles which can create problems numerically and affect the efficiency of the integration. To deal with this problem we have used a partial fractioning technique, as was shown in Sec. 2.4.4, that makes the numerical integration more stable. As can be seen from Fig. 2.22 the partial fractioning method is enough to make the cross section for two hard photons to become stable at above approximately 10^9 evaluations, with the Vegas algorithms, for $\Delta = 10$ MeV and P2 kinematics. Above 10^9 the result changes very little with changes that lie within the uncertainties predicted by the algorithm. The fact that the result at higher number of evaluations is not inside the errors predicted at lower number of evaluations is a feature of the Vegas algorithm that tends to underestimate the errors for integrands with higher peaks such as this one. For lower values of the cut-off Δ we need increasingly more evaluations to reach a stable point, above which the changes lie within the uncertainties. For example, for $\Delta = 1$ MeV this point is reached only above approximately 10^{10} evaluations as can be seen from Fig. 2.23.

As was mentioned earlier, the presence of divergences forces us to introduce various reg-

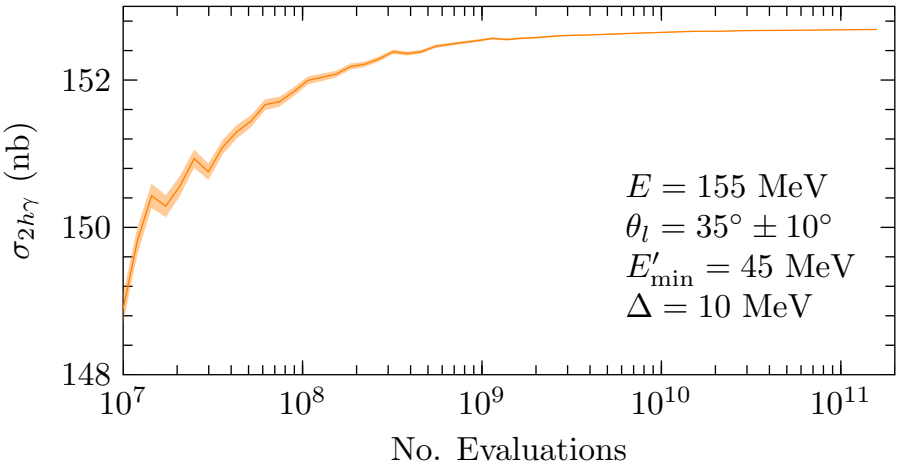

Figure 2.22: The dependence of the second order bremsstrahlung cross-section on the number of evaluations used for the numerical integration at P2 kinematics and with the cut-off of 10 MeV.

ularization parameters which must cancel in the final result (see App. B). The cancellation of these parameters can then be used as a numerical test, since by varying these parameters the result has to remain constant. There are essentially two types of divergences that appear in our calculations, for which we use different approaches as:

- UV divergences are treated in dimensional regularization where pole terms in Δ_ϵ appear (Δ_ϵ is defined in App. B). They are accompanied by logarithms of a mass scale parameter μ introduced to keep the mass dimension of loop integrals homogeneous. Both the Δ_ϵ- and μ-dependence cancel by including corresponding counter-terms;
- IR divergences are regularized by a finite photon mass λ. Logarithms of the photon mass have to cancel exactly between loop contributions and corrections from soft-photon radiation at the level of the cross section.
- The phase space slicing parameter Δ was introduced to separate soft-photon from hard-photon contributions. The part with $E_\gamma, E'_\gamma < \Delta$ is calculated in the soft-photon approximation. Therefore the Δ-dependence disappears only in the limit $\Delta \longrightarrow 0$. A residual Δ-dependence may be visible if Δ is chosen too large (see Ref. [28]).

The analytical expressions of the scalar integrals (see App. D) allows us to keep the parameters Δ_ϵ, μ and λ in separate parts of the calculation. Their cancellation can therefore be tested numerically. As an example, we show numerical results for the $O(\alpha)$ corrected one-photon bremsstrahlung cross section, given in Eq. (2.20) for P2 kinematics, i.e. for electron scattering with $E = 155$ MeV, $\theta_\ell = 35^\circ \pm 10^\circ$ and $E'_{\text{min}} = 45$ MeV and with a cut-off for the photon energy of $\Delta = 10$ MeV. We take default values for the three regularization parameters as $\lambda^2 = m_e^2$, $\Delta_\epsilon = 0$ and $\mu^2 = 1$. For these values the terms that contain the IR and UV divergences vanish and we can use this result as a reference. From Tab. 2.1 we conclude that these unphysical parameters can be varied over a very large range of values without leading to a significant numerical variation of the correction factor. The observed behaviour constitutes a test of an important part of the calculation.

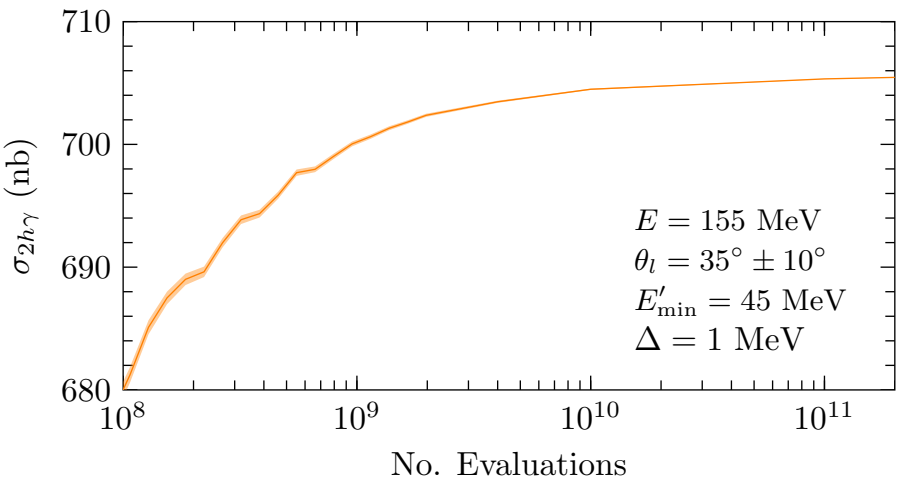

Figure 2.23: The dependence of the bremsstrahlung cross-section with two photons in the final state on the number of evaluations used for the numerical integration at P2 kinematics and with the cut-off of 1 MeV.

The non-radiative parts of the cross section depend logarithmically on the phase space slicing parameter Δ. At first order we have $\delta^{(1)}_{\text{non-rad}} \propto \ln \Delta$, while at second order $\delta^{(2)}_{\text{non-rad}} \propto \ln^2 \Delta$. An example of numerical results of the Δ-dependence for the case of the P2 experiment is shown in Fig. 2.24. This Δ-dependence is canceled by the hard-photon contribution. In Fig. 2.25 we show an example of how the Δ-dependence cancels when we include both contributions, again for the kinematics of the P2 experiment. At large values of the soft-photon cut-off, when Δ reaches some 10 percent of the beam energy, the break-down of the soft-photon approximation is visible. Below $\Delta \simeq 10$ MeV, there is a nice plateau where the total result is independent of the cut-off. At first order, the cancellation looks perfect while for the second-order calculation one can observe that the numerical cancellation becomes less and less stable for decreasing Δ. However, the choice $1\text{ MeV} \lesssim \Delta \lesssim 10\text{ MeV}$ is appropriate for the P2 experiment and guarantees that the soft-photon approximation used for the calculation of the non-radiative part of the total correction does not lead to a significant distortion of the total result (see Ref. [28]).

It is also interesting to study an approximation for the calculation of $\delta^{(1)}_{1\text{-loop}+1h\gamma}$, Eq. (2.144). The approximation consists in assuming that the one hard-photon correction and the loop correction factorize also for finite values of the photon energy. This approximation allows us to replace the loop correction for the process with one radiated photon with the loop correction for the Born process as

$$\delta^{(1)}_{1\text{-loop}+1h\gamma} \longrightarrow \delta^{(1)}_{1\text{-loop}}. \tag{2.189}$$

Figure 2.25 shows an example of numerical results based on this approximation (green, dash-dotted line). We find good agreement between the exact calculation and the approximation, at the level of 10^{-4} and better for the energy and angle range shown in this figure. The differences, however, are larger in the vicinity of the final-state radiation peak, as can be seen in Fig. 2.29.

The results of this cross section were compared also with a recent calculation, implemented in the code `mcmule` (see Refs. [96] and [97]), which uses a subtraction method to deal with soft singularities. We have compared all intermediate results, both at the matrix

λ^2 [GeV^2]	m_e^2	10^{-4}	10^{-8}	10^{-12}
$\sigma_{1h\gamma}^{(2)}$	4034.10 ± 0.92	4033.33 ± 0.92	4033.89 ± 0.87	4033.79 ± 0.88

Δ_ϵ	0	10^2	10^4	10^6
$\sigma_{1h\gamma}^{(2)}$	4034.10 ± 0.92	4033.84 ± 0.91	4033.41 ± 0.90	4031.11 ± 0.92

μ^2	1	10^4	10^8	10^{12}
$\sigma_{1h\gamma}^{(2)}$	4034.10 ± 0.92	4033.03 ± 0.90	4034.04 ± 0.94	4033.41 ± 0.92

Table 2.1: Test of the independence of $\sigma_{1h\gamma}^{(2)}$ for electron scattering (see Eq. (2.20)) on the unphysical regularization parameters λ^2, Δ_ϵ and μ^2. The uncertainty estimates are due to the finite statistics of the Monte Carlo integration.

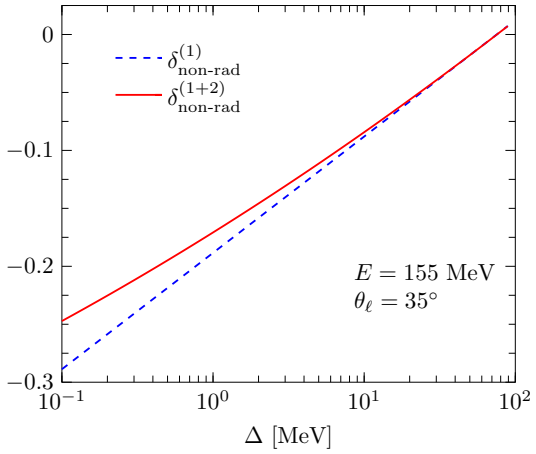

Figure 2.24: The dependence of the non-radiative parts of the correction factors for electron scattering at first and second order on the phase space slicing cut-off Δ.

level and at the cross section level, except for the R contribution, which was presented in Sec. 2.4.2, that couldn't be isolated in their approach, and found very good agreement. The results for the two hard-photon cross section also agree very well, within the uncertainties, with `mcmule`, as long as we take care we have enough number of evaluations, such that the integration reaches the convergence point. However, in the final result we found that our results disagree by approximately 8%, which translates to a difference smaller than 0.003% relative to the Born cross section. The results seem to agree well, within the uncertainties of the numerical integration without the R contribution, which lead us to believe that the source of disagreement is this contribution. However, we haven't yet reach a final conclusion about the source of disagreement. For the purpose of the P2 experiment this disagreement is irrelevant, since the difference between the results is much smaller than the precision the experiment can reach. Until this disagreement is solved we recommend to use the R contribution with care and not include it, unless really necessary.

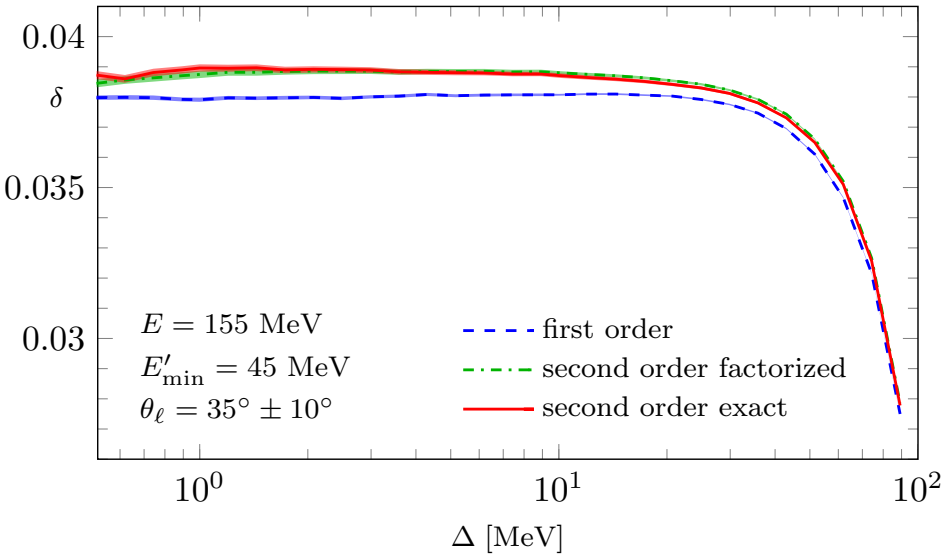

Figure 2.25: Test of the Δ-independence of the complete correction factors when non-radiative contributions and hard-photon radiative effects are added, at first order $\delta = \sigma^{(1)}/\sigma^{(0)} - 1$ and at second order $\delta = \sigma^{(2)}/\sigma^{(0)} - 1$. Beam energy and the range of the scattering angle is chosen for electron scattering at the P2 experiment. The meaning of the labels "factorized" and "exact" is explained in the text.

2.6 Numerical results [7]

We start this section with the discussion of a few numerical results for leptonic radiative corrections which are relevant for electron scattering at the P2 experiment at the MESA facility in Mainz [27]. The P2 experiment plans to measure the parity-violating asymmetry in elastic electron proton scattering with a polarized electron beam of energy $E = 155$ MeV. The P2 spectrometer covers an angular acceptance range of $35 \pm 10^\circ$ and for simplicity we assume that only scattered electrons with a fixed energy of at least $E'_{\rm min} = 45$ MeV are detected. The average momentum transfer squared is $\langle Q^2 \rangle = 6 \cdot 10^{-3}$ GeV^2. An ancillary measurement for the determination of the axial and strange magnetic form factors at backward angles is also possible. Such a measurement could cover the angular range $135^\circ \le \theta_\ell \le 155^\circ$. We repeat that we have used a simple dipole parametrization for the proton form factors, $G_E = \left(1 + Q^2/\Lambda^2\right)^{-2}$ and $G_M = \kappa_p G_E$ with $\Lambda = 0.71$ GeV^2 and we have checked that, while the cross sections can change by a few per mill when using a different form factor parametrization, the correction factors are insensitive to this choice at the level well below one per mill.

The non-radiative part of the corrections is shown in Fig. 2.26. In this case, soft-photon radiation is included with the cut-off $\Delta = 10$ MeV. The corrections reach the level of some $-8.5\,\%$ and exhibit a moderate Q^2 dependence. Second-order corrections are small, but are relevant at the level of 0.3 to 0.5 %. The layout of the P2 spectrometer with a solenoidal magnetic field is constructed in such a way that no bremsstrahlung photon emitted in the target volume can reach the detector. Therefore, radiative scattering will contribute to the measured cross section as long as the scattered electrons fulfil the condition $E' > E'_{\rm min}$. The complete

[7] The text of this subsection is taken entirely from Ref. [28].

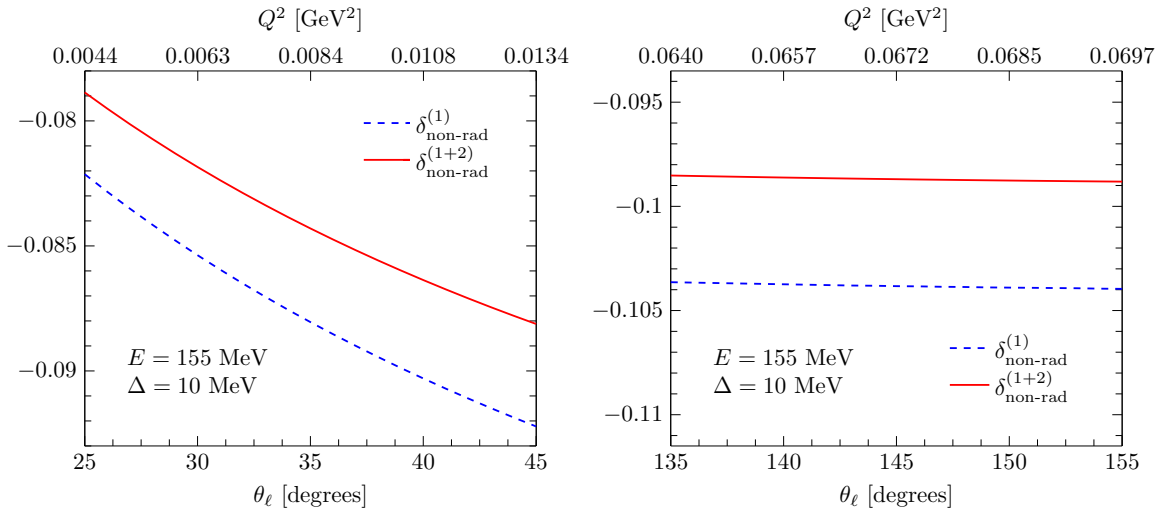

Figure 2.26: The non-radiative part of the correction factors at first (dashed, blue curve) and second order (full, red curve) in the range of scattering angles relevant for electron scattering at the P2 experiment: forward scattering with $25^\circ < \theta_\ell < 45^\circ$ (left) and backward scattering with $135^\circ < \theta_\ell < 155^\circ$ (right). Soft-photon corrections are included with the cut-off fixed at $\Delta = 10$ MeV.

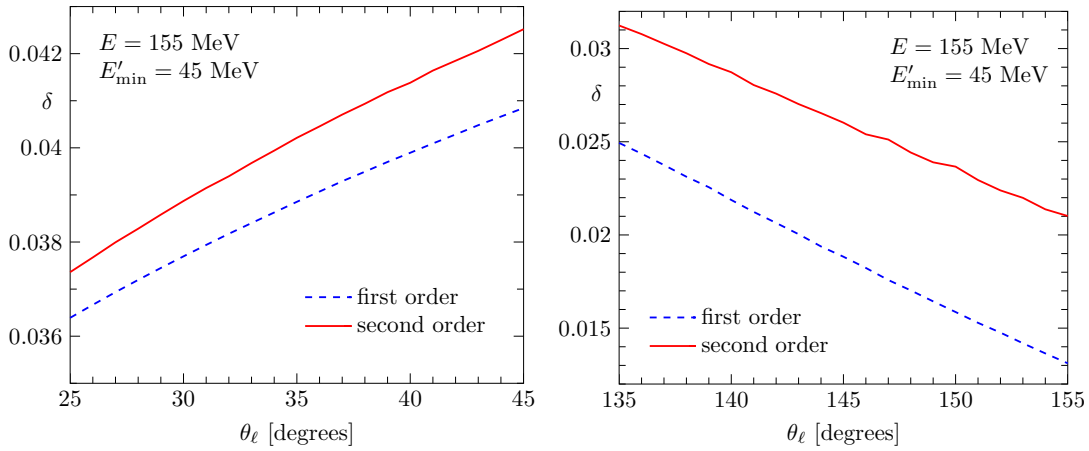

Figure 2.27: The complete radiative correction factors at first (dashed, blue curve) and second order (full, red curve) in the range of scattering angles relevant for electron scattering at the P2 experiment: forward scattering with $25^\circ < \theta_\ell < 45^\circ$ (left) and backward scattering with $135^\circ < \theta_\ell < 155^\circ$ (right). Hard-photon radiation is included with the restriction that the final state electron has an energy above $E'_{\text{min}} = 45$ MeV.

radiative correction factor including hard-photon radiation is shown in Fig. 2.27. We find that the cross section is increased significantly by the inclusion of radiative processes. The corrections are now positive, at the level of a few percent. The difference between the first- and second-order calculations turns out to be slightly smaller in the forward region, but can still reach somewhat more than half a percent in the backward region.

While it is not possible at the P2 experiment to impose a veto on hard radiated photons

directly, the requirement of a minimum energy E'_{min} for the scattered electrons restricts the phase space for photon emission indirectly. This introduces a strong dependence on E'_{min}. Numerical results are shown in Fig. 2.28 (left), again both at first and at second order. In the P2 experiment energy loss can also occur when the incoming electron passes through the liquid hydrogen target. It is therefore also important to know how the cross section depends on the energy E of the incoming electrons. Results for the first- and second-order radiative correction factors are shown in the right part of Fig. 2.28. For reduced E while keeping $E'_{\text{min}} = 45$ MeV fixed, hard-photon radiation will be suppressed and the corrections become negative. The observed strong dependence on E and E'_{min} highlights the necessity to include radiative effects in a full Monte-Carlo simulation of the experiment where the acceptance for electron detection may be a complicated function of the scattering angle.

For a better understanding and for completeness we also show results for the cross section of radiative ep scattering in Fig. 2.29. This process is, in fact, not measurable at P2. The plot of this figure shows that bremsstrahlung is dominated by far by the emission of photons collinear with the incoming electrons, but there is also a peak in the angular distribution where photons are emitted in the direction of the scattered electron. The one-loop and soft-photon corrections for radiative scattering are negative on the collinear peaks (−7 % for $\theta_\gamma = \theta_\ell = 35^\circ$) and positive for photon emission angles far away from the peaks (+11.4 % for $\theta_\gamma \simeq 15^\circ$). A particularly interesting feature is a dip on top of the final-state radiation peak, shown in more detail in the upper right corner of Fig. 2.29. The final-state peak is determined by terms proportional to $1/(l'k)$ in the soft-photon eikonal factor, see Eq. (2.53),

$$\frac{1}{l'k} = \frac{1}{E_\gamma \left(E' - |\vec{l}'| \cos\psi \right)}, \tag{2.190}$$

where ψ is the angle between the scattered lepton and the emitted photon. It is obvious that for a photon emitted collinearly with the final-state electron, i.e. for $\psi \longrightarrow 0$, and for $m_\ell \longrightarrow 0$

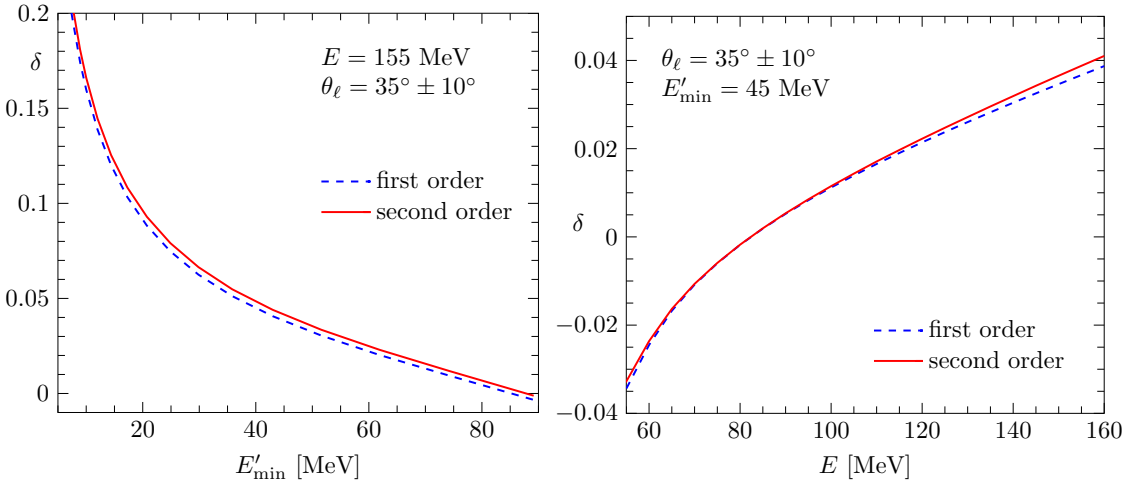

Figure 2.28: The complete radiative correction factors at first (dashed, blue curve) and second order (full, red curve) for electron scattering at the P2 experiment as a function of the cut-off on the energy of the scattered electron E'_{min} (left) and as a function of the beam energy with fixed E'_{min} (right). The scattering angle was integrated over the range $25^\circ \leq \theta_\ell \leq 45^\circ$.

this term diverges. One can show that for a finite value of the electron mass the dominating terms in the eikonal factor vanish for zero emission angle,

$$\frac{2l'l}{(l'k)(lk)} - \frac{m_\ell^2}{(l'k)^2} \longrightarrow \frac{1}{E_\gamma^2}\frac{4E'^4}{m_\ell^4}\psi^2 \tag{2.191}$$

for $\psi \ll m_\ell/E' \ll 1$, which explains the local minimum in the angular distribution of Fig. 2.29. The details of this feature depend on the value of the lepton mass and will be particularly important for muon scattering. Effects due to lepton-mass dependent terms in the cross section have been discussed in detail also in Refs. [98, 99]. Our results agree with these references.

In Figure 2.30 we show an example of results for the radiative correction factor relevant for the Qweak experiment. Here the beam energy is $E = 1.16$ GeV and the experiment covers scattering angles between 5.8° and 11.6°. The corrections are similar to the case of P2 and reach the level of roughly 5 %. The corrections at second order are smaller than at first order by an order of magnitude.

Finally we conclude the discussion with a few results for the planned MUSE experiment where also the scattering of muons off protons will be measured. The beam momentum is fixed at $|\vec{l}| = 210$ MeV and we do not impose a restriction on the energy of the final-state muon. Results are shown in Fig. 2.31. The corrections are rather small and vary between

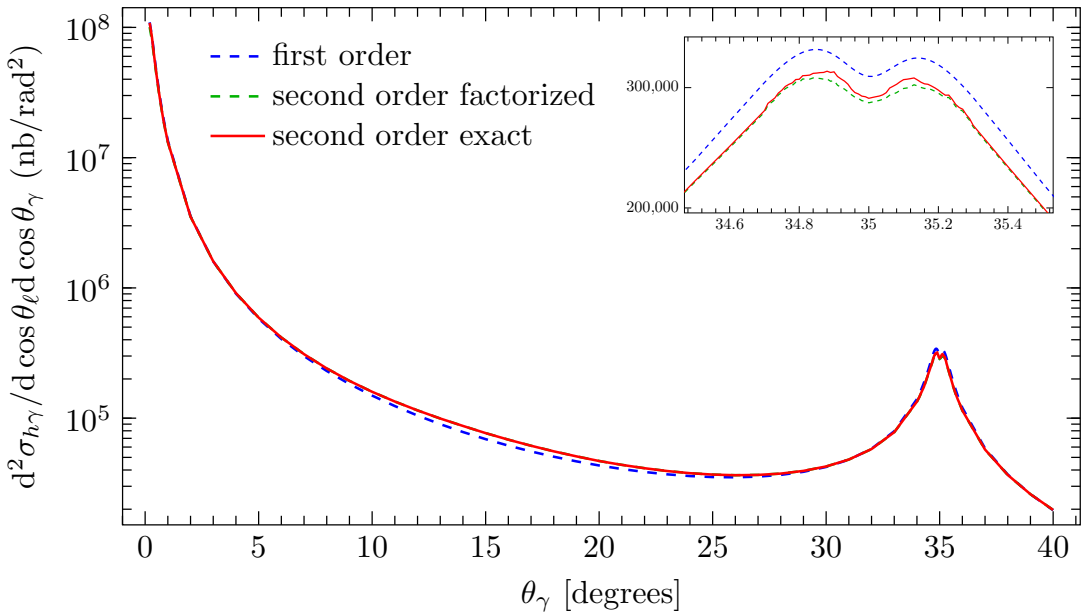

Figure 2.29: Cross section for radiative electron scattering with an observed photon of energy $E_\gamma \geq \Delta = 10$ MeV at tree level (first order, blue dashed line) and including the effect due one-loop corrections and a second unobserved soft photon with energy below the cut-off $\Delta = 10$ MeV (second order exact, full red line). Additionally an approximation of this result is included, described in the previous subsection (second order factorized, green dash dotted line). The beam energy is $E = 155$ MeV and the scattering angle of the electron fixed at $\theta_\ell = 35°$. The energy of the scattered electron is integrated over the range $E' > 45$ MeV.

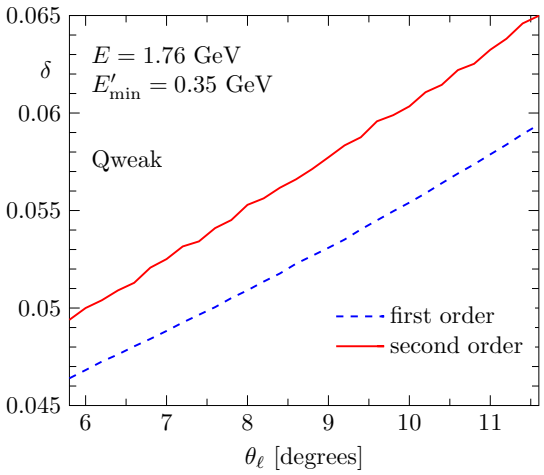

Figure 2.30: The complete radiative correction factors at first (dashed, blue curve) and second order (full, red curve) in the range of electron scattering angles relevant for Qweak at E = 1.165 GeV. Hard-photon radiation is included with the restriction $E'_{\rm min}$ = 0.35 GeV.

−0.1 % and −0.9 %. For the calculation of the second-order corrections in this figure we have used the expression Eq. (2.133) taken from Ref. [39].

We note that the ultra-relativistic approximation, where lepton mass terms suppressed by powers of m_ℓ^2/Q^2 are neglected, is not suitable in this case. Our calculation includes the full lepton-mass dependence at leading order and for the first-order corrections. In the second-order corrections, our calculation includes lepton-mass dependent terms for the radiative parts, but the two-loop diagrams are known only in the ultra-relativistic approximation or in the limit of vanishing momentum transfer. For electron scattering the expression Eq. (2.133) for the two-loop corrections, valid for large momentum transfer, is an excellent approximation for our applications; however, for muon scattering this may not be applicable in the full range of scattering angles covered by the MUSE experiment.

As a test we show in Fig. 2.32 the non-radiative correction factor over a larger range of Q^2 values and using two alternative expressions taken from Ref. [88]. The one denoted "Mastrolia $Q^2 \longrightarrow \infty$" contains additional lepton mass dependent terms up to and including 4th powers of $\mu = \left(m_\ell^2/Q^2\right)$ and the option denoted "Mastrolia $Q^2 \longrightarrow 0$" includes terms up to μ^{-4}. Our expression derived from Hill's result, Eq. (2.133), agrees with Ref. [88] at large Q^2, as expected, and seems to provide a nice interpolation between the large-Q^2 and small-Q^2 limits of Ref. [88], but this may be accidental. For a conclusive interpretation of a high-precision measurement of muon scattering, a calculation of 2-loop and 2-photon corrections taking into account the full mass dependence will be needed. We mention that radiative corrections for the MUSE experiment based on an alternative approach have also been studied recently in Ref. [100].

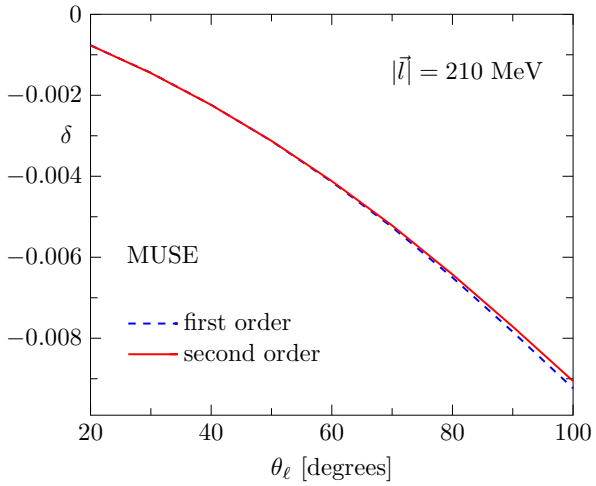

Figure 2.31: The complete radiative correction factors at first (dashed, blue curve) and second order (full, red curve) in the range of scattering angles relevant for muon scattering at the planned MUSE experiment. Hard-photon radiation is included without an additional restriction, i.e. $E'_{\text{min}} = m_\mu$. The soft-photon cut-off is fixed at $\Delta = 0.01$ MeV and we have used Eq. (2.133) for the 2-loop corrections [39].

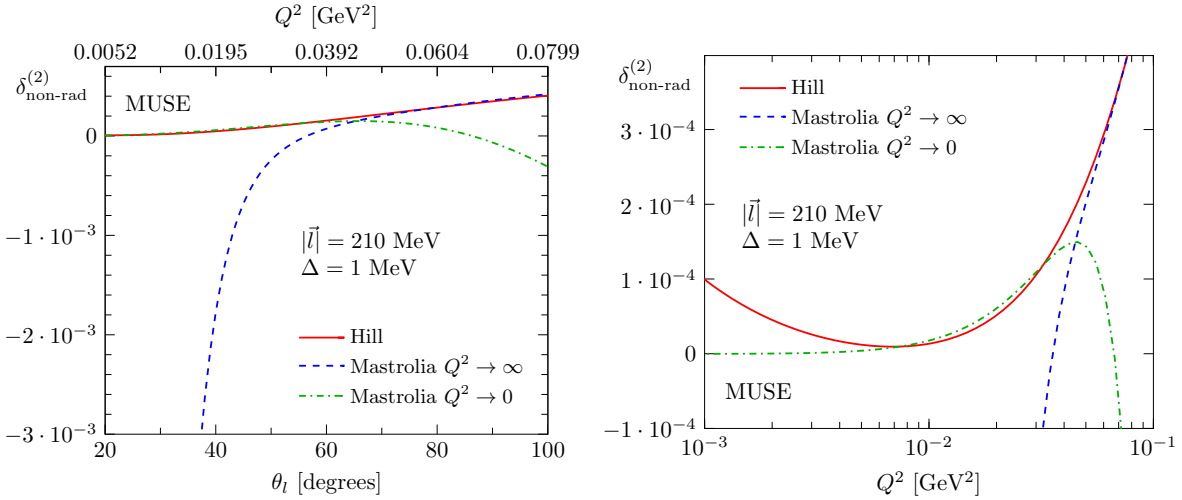

Figure 2.32: The second-order non-radiative part of the corrections for muon scattering at the MUSE experiment using different approximations from Refs. [39, 88] as described in the text.

Chapter 3

Polarized Lepton-Proton Scattering

3.1 Definitions and general remarks

The asymmetry between cross sections for incident leptons with positive and negative helicities, $\sigma_{\pm}$, is defined as

$$A_{\mathrm{PV}} = \frac{\sigma_+ - \sigma_-}{\sigma_+ + \sigma_-} = \frac{\sigma_P}{\sigma}, \tag{3.1}$$

where the polarization-dependent part of the cross section $\sigma_P = (\sigma_+ - \sigma_-)/2$ is obtained from the difference between cross sections for leptons with positive and negative helicities. The helicity spinors $u(l, \lambda)$ satisfy the Dirac equation, i.e. $\not{l} u(l, \lambda) = m u(l, \lambda)$, and are eigenstates of $\gamma_5 \not{\zeta}$, i.e. $\gamma_5 \not{\zeta} u(l, \lambda) = u(l, \lambda)$, where ζ^μ is the spin four-vector (see App. F for more details). In the limit $m_\ell \longrightarrow$ the helicity operators reduce to the chirality operators. However, unless stated, in our work we use explicitly the helicity operators to derive the expressions for polarized cross sections.

In a real experiment it is impossible to achieve a totally polarized beam. Therefore we need to introduce a degree of polarization P and make the replacement $\sigma_P \longrightarrow P\sigma_P$.

The leading order asymmetry, at low momentum transfer and for $E \gg m_\ell$, is given by

$$A_{PV}^{(0)} = \frac{\sigma_+^{(0)} - \sigma_-^{(0)}}{\sigma_+^{(0)} + \sigma_-^{(0)}} = -\frac{G_F Q^2}{4\sqrt{2}\pi\alpha}\left[Q_W^p - F(Q^2)\right], \tag{3.2}$$

where G_F is the Fermi constant and Q_W^p is the weak charge of the proton, which at leading order is given by $Q_W^p = 1 - 4\sin^2\theta_W$. $F(Q^2)$ comprises form factors describing the proton structure and are expected to be small at Q^2 values relevant for the P2 experiment (see Ref. [27]).

At lowest order, polarized lepton nucleon scattering is described by the exchange of a virtual Z^0 boson. The weak current for a spin-1/2 nucleon is given by

$$\mathcal{P}_Z^\mu = g_Z \bar{u}(p')\Gamma_Z^\mu u(p), \tag{3.3}$$

where g_Z can be related to the Fermi constant G_F as

$$g_Z^2 = \frac{e^2}{16\cos^2\theta_W \sin^2\theta_W} = \frac{G_F M_Z^2}{2\sqrt{2}}. \tag{3.4}$$

The weak current, as the electromagnetic current, can be decomposed into Pauli and Dirac form factors, F_1^Z and F_2^Z, and an additional axial form factor G_A^Z. The weak charge of the proton Q_w^p is absorbed in the definition of the form factors F_1^Z and F_2^Z. For the sake of completeness we note here that Lorentz invariance allows an extra pseudo-scalar form factor G_P as $\frac{q_\mu}{M}\gamma_5 G_P$, but this will have no contribution on the parity-violating electron scattering. The proton vertex in the case of Z^0 exchange is given therefore by

$$\Gamma_Z^\mu = \gamma^\mu F_1^Z + \frac{i\sigma^{\mu\nu}q_\nu}{2M}F_2^Z + \gamma^\mu\gamma_5 G_A^Z. \tag{3.5}$$

As in the case of the electromagnetic form factors we can define Sachs form factors as

$$G_E^Z(Q^2) = F_1^Z - \tau F_2^Z \quad \text{and} \quad G_M^Z(Q^2) = F_1^Z + F_2^Z. \tag{3.6}$$

The weak Sachs form factors can be related to the electromagnetic Sachs form factors of the proton and neutron as is shown in App. G. Using this vertex rule we can obtain the tree-level cross section for scattering of polarized leptons with mass m_ℓ off unpolarized nucleons. We note here that since we need to take the difference between cross sections with positive and negative helicities, the polarized cross section is proportional to the following matrix elements:

$$2\frac{\mathrm{d}\sigma_P^{(0)}}{\mathrm{d}Q^2} \propto |\mathcal{M}_{Z,+}|^2 + |\mathcal{M}_{Z,-}|^2 + 2\Re\left[\mathcal{M}_\gamma^\dagger(\mathcal{M}_{Z,+} - \mathcal{M}_{Z,-})\right], \tag{3.7}$$

where $|\mathcal{M}_{Z,+(-)}|^2$ are proportional to G_F^2 and therefore approximately 10^{-5} smaller than the interference term, which allows us to safely ignore them. We are left therefore with

$$\frac{\mathrm{d}\sigma_P^{(0)}}{\mathrm{d}Q^2} \propto \Re\left[\mathcal{M}_\gamma^\dagger(\mathcal{M}_{Z,+} - \mathcal{M}_{Z,-})\right] \equiv \Re\left(\mathcal{M}_\gamma^\dagger \mathcal{M}_Z^P\right). \tag{3.8}$$

The differential Born polarized cross section is given then by

$$\frac{\mathrm{d}\sigma_P^{(0)}}{\mathrm{d}Q^2} = \frac{\overline{\Re\left(\mathcal{M}_{\mathrm{Born},\gamma}^\dagger \mathcal{M}_{\mathrm{Born},Z}^P\right)}}{16\pi\left[(s - m_\ell^2 - M^2)^2 - 4m_\ell^2 M^2\right]}. \tag{3.9}$$

The Born matrix element for γ exchange denoted here by $\mathcal{M}_{\mathrm{Born},\gamma}$ was given in Eq. (2.5). The Born matrix element for Z^0 exchange is given by

$$\mathcal{M}_{\mathrm{Born,Z}} = \frac{1}{M_Z^2 - q^2}\mathcal{L}_{\mu,Z}\mathcal{P}_Z^\mu, \tag{3.10}$$

where $\mathcal{L}_{\mu,Z} = -g_Z\bar{u}(l')\gamma_\mu(g_V + g_A\gamma_5)u(l,\lambda)$ is the lepton current for Z^0 exchange, for initial leptons with helicity λ. Here g_V and g_A stand for the vector and the axial couplings respectively, given in table 3.1. Since $Q^2 \ll M_Z^2$, we can ignore Q^2 in the denominator and the Born matrix element for Z^0 exchange becomes

$$\mathcal{M}_{\mathrm{Born,Z}} = -\frac{G_F}{2\sqrt{2}}\bar{u}(l')\gamma_\mu(g_V + g_A\gamma_5)u(l,\lambda)\bar{u}(p')\Gamma_Z^\mu u(p). \tag{3.11}$$

Fermion	e	g_V	g_A
e, μ, τ	-1	$-1 + 4\sin^2\theta_W$	1
u, c, t	$\frac{2}{3}$	$1 - \frac{8}{3}\sin^2\theta_W$	-1
d, s, b	$-\frac{1}{3}$	$-1 + \frac{4}{3}\sin^2\theta_W$	1

Table 3.1: Standard Model values for the elementary electromagnetic and weak charges of the fermions (see Ref. [101]).

The bar in Eq. (3.9) indicates that we need to average over initial state polarizations and sum over the final ones. Since the initial state lepton is polarized we only need to average over the initial state of the nucleon, which leads to

$$\overline{\Re\left(\mathcal{M}^{\dagger}_{\text{Born},\gamma}\mathcal{M}^{P}_{\text{Born},Z}\right)} = \frac{1}{2}\sum_{\text{spins}}\Re\left(\mathcal{M}^{\dagger}_{\text{Born},\gamma}\mathcal{M}^{P}_{\text{Born},Z}\right), \tag{3.12}$$

where the sum over final state polarizations leads to the calculation of a trace. Using the helicity projection operators from Eq. F.3 defined in App. F and assuming $E \gg m_\ell$ [1], we obtain the following expression for the averaged interference term after performing the trace

$$\begin{aligned}\overline{\Re\left(\mathcal{M}^{\dagger}_{\text{Born},\gamma}\mathcal{M}^{P}_{\text{Born},Z}\right)} = -\frac{4\pi\alpha G_F}{\sqrt{2}Q^2}\Big[&2F_1F_1^Z g_A\left(2M^2Q^2 - Q^4 + 2Q^2S - 2S^2\right)\\ &- 2F_1F_2^Z g_A Q^4 + 2F_1G_A^Z g_V(Q^2 - 2S)\\ &- F_2F_2^Z g_A\frac{Q^2}{M^2}(M^2Q^2 - Q^2S + S^2)\\ &- 2F_2Q^2\left(F_1^Z g_A Q^2 - G_A^Z g_V(Q^2 - 2S)\right)\Big],\end{aligned} \tag{3.13}$$

where $S = 2l\cdot p$. For fixed Q^2 the asymmetry is given by the ratio of the differential cross sections

$$A_{PV}^{(0)} = \frac{\mathrm{d}\sigma_P/\mathrm{d}Q^2}{\mathrm{d}\sigma/\mathrm{d}Q^2} = \frac{\overline{\Re\left(\mathcal{M}^{\dagger}_{\text{Born},\gamma}\mathcal{M}^{P}_{\text{Born},Z}\right)}}{\overline{\left|\mathcal{M}_{\text{Born},\gamma}\right|^2}}. \tag{3.14}$$

The last expression can be written in a compact form using the definitions of the Sachs form factors as

$$A_{\text{PV}}^{(0)} = -\frac{G_F Q^2}{4\pi\alpha\sqrt{2}}\frac{\epsilon G_E G_E^Z + \tau G_M G_M^Z - (1 - 4\sin^2\theta_W)\epsilon' G_M G_A^Z}{\epsilon G_E^2 + \tau G_M^2}, \tag{3.15}$$

where ϵ and τ were defined in Sec. 2.1 and $\epsilon' = \sqrt{(1-\epsilon^2)\tau(1+\tau)}$. This expression further simplifies if we assume $E \gg m_\ell$ and a low momentum transfer squared and reduces to Eq. (3.2). We note here that the integration over Q^2 leads to important effects that cannot be ignored (see Sec. 3.4 for more details).

For the definitions of the polarized cross sections, at leading order, first order and second order, we import again the definitions from Sec. 2.1, to which we add an additional symbol P, to denote they are polarized, as $\sigma \longrightarrow \sigma_P$ or $\sigma^{(0)} \longrightarrow \sigma^{(0P)}$. Furthermore we note that the corrections for the polarized cross-section σ_P can be separated between photonic corrections,

[1] We note here that in our program the exact expression of the polarized cross section is used.

i.e. corrections that involve virtual photons, and weak corrections, i.e. corrections that involve virtual weak bosons. In this work we treat only photonic corrections.

In Eq. (3.2) we see that the parity violating asymmetry is proportional to Q^2. Even though the QED corrections are parity conserving and do not affect the weak charge of the proton directly, they lead to a shift of the momentum transfer. If an experimental event-by-event determination of Q^2 is not possible, QED corrections have to be applied in the analysis to extract Q_W^p from the measured asymmetry. Therefore, these corrections have to be calculated from theory with high precision.

From the measurement of the scattering angle one can only obtain information about what is called leptonic momentum transfer (see Ref. [28]) defined as

$$Q_l^2 = -(l - l')^2 \,, \tag{3.16}$$

where l and l' are the 4-momenta of the initial and final electrons. However, taking into account bremsstrahlung effects (see Fig. 3.2), a photon with momentum k will shift the momentum transfer to the true value given by

$$Q^2 = -(l - l' - k)^2 \,. \tag{3.17}$$

See Sec. 3.4 for the definition and calculation of the shift in momentum transfer squared. This is why is important to include the full set of QED radiative corrections to the asymmetry. In the next section we start with the treatment of first order photonic corrections to the polarized cross section.

3.2 First order corrections

The asymmetry with $\mathcal{O}(\alpha)$ corrections is defined as

$$A_{PV}^{(0+1)} = \frac{\sigma_+^{(0+1)} - \sigma_-^{(0+1)}}{\sigma_+^{(0+1)} + \sigma_-^{(0+1)}} = \frac{\sigma_P^{(0+1)}}{\sigma^{(0+1)}} \,. \tag{3.18}$$

We separate $\mathcal{O}(\alpha)$ photonic corrections into non-radiative corrections, i.e. one-loop and one soft photon corrections to the lepton line, and radiative corrections, i.e. corrections with a hard-photon in the final state. At the level of the matrix element, the one-loop corrections are given by

$$\Re\left(\mathcal{M}_{1-\text{loop},\gamma}^{\dagger}\mathcal{M}_Z^p\right) + \Re\left(\mathcal{M}_\gamma^{\dagger}\mathcal{M}_{1-\text{loop},Z}^P\right) \,, \tag{3.19}$$

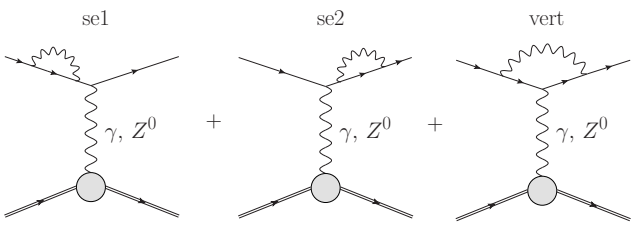

Figure 3.1: Feynman diagrams for the one-loop corrections at the lepton line.

where $\mathcal{M}_\gamma^\dagger$ and $\mathcal{M}_Z$ are the Born matrix elements for γ and Z^0 exchange respectively. The self-energy corrections, diagrams se1 and se2 from Fig. 3.1, are the same for both unpolarized and polarized cross-sections and they vanish for on-shell leptons in the on-shell renormalization scheme as was shown in Sec. 2.2.1. Therefore, the one-loop photonic corrections to the polarized cross-section are given by

$$\delta_{1-\text{loop}}^{(1P)} = \frac{\Re\left(\mathcal{M}_{\text{vert},\gamma}^\dagger \mathcal{M}_Z^P\right)}{\Re\left(\mathcal{M}_\gamma^\dagger \mathcal{M}_Z^P\right)} + \frac{\Re\left(\mathcal{M}_\gamma^\dagger \mathcal{M}_{\text{vert},Z}^P\right)}{\Re\left(\mathcal{M}_\gamma^\dagger \mathcal{M}_Z^P\right)}. \tag{3.20}$$

The vertex correction for γ exchange can be taken into account by replacing the tree-level on-shell vertex by

$$\gamma^\mu \longrightarrow F_1^\ell(Q_\ell^2)\gamma^\mu + \frac{i}{2m_\ell}\sigma_{\mu\nu}q^\nu F_2^\ell(Q_\ell^2), \tag{3.21}$$

where the expressions for $F_1^\ell(Q_\ell^2)$ and $F_2^\ell(Q_\ell^2)$ and the methods used for calculation were presented in Sec. 2.2. Analogous to Eq. (3.21), the tree-level on-shell vertex for Z^0 exchange can be take into account by the replacement

$$\gamma^\mu(g_V + g_A\gamma_5) \longrightarrow g_V\left[F_1^\ell(q^2)\gamma_\mu + \frac{i}{2m_\ell}\sigma_{\mu\nu}q^\nu F_2^\ell(q^2)\right] + g_A\left[F_A^\ell(q^2)\gamma_\mu\gamma_5 + \frac{q_\mu}{m_\ell}F_P^\ell\gamma_5\right], \tag{3.22}$$

where g_V and g_A are defined in Table 3.1. F_P, however, does not give any contribution to the polarized cross-section and can be ignored. As in the case of F_1^ℓ, F_A^ℓ is UV and IR divergent. The UV divergence is removed by renormalization, while the IR divergence cancels at the level of the cross-section, when we combine it with the soft-photon correction. The renormalized axial form-factor in the on-shell renormalization scheme is given by

$$F_A^{\ell(1,R)}(Q_\ell^2) = F_A^{\ell(1)}(Q_\ell^2) - F_A^{\ell(1)}(0) = F_A^{\ell(1)}(Q_\ell^2) + \delta Z_A, \tag{3.23}$$

where we introduced additional upper indices to display the loop-order and distinguish renormalized (with index R) from unrenormalized quantities. The counter-term δZ_A is given in the on-shell prescription by

$$\delta Z_A = -\frac{\alpha}{4\pi}\left(\Delta_\epsilon - \ln\frac{m_\ell^2}{\mu^2} + 2\ln\frac{\lambda^2}{m_\ell^2} + 2\right) = \delta Z_1 - \frac{\alpha}{2\pi}. \tag{3.24}$$

The difference between the renormalized form-factors F_1^ℓ and F_A^ℓ is given by

$$F_1^{\ell(1)} - F_A^{\ell(1)} = -\frac{\alpha}{2\pi}\left(1 - \frac{2m_\ell^2}{Q^2 v}\ln\frac{v+1}{v-1}\right), \tag{3.25}$$

where $v = \sqrt{1 + 4m_\ell^2/Q^2}$. It can be seen that for $Q^2 \gg m_\ell^2$ the difference between the two form-factors reduces to $-\frac{\alpha}{2\pi}$. Even though this difference is small, the exact result is included in our calculation at first order. This approximation becomes important at second order, for which the difference is proportional to α^2 and can be safely neglected (see Sec. 3.3). Since $F_1^{\ell(1)}$ is IR divergent, also $F_A^{\ell(1)}$ contains the same IR divergence, that cancels, in the same way as in the unpolarized scattering, with the inclusion of soft-photon radiation.

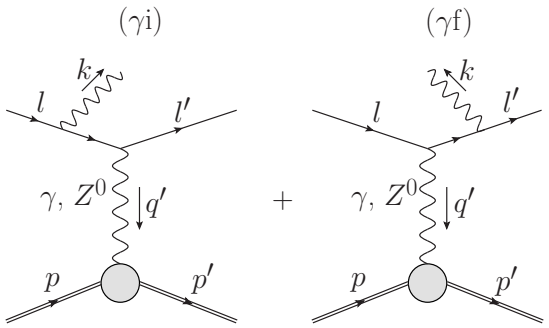

Figure 3.2: Feynman diagrams for first-order bremsstrahlung corrections.

The diagrams that contribute to the radiative process $ep \longrightarrow ep\gamma$ are given in Fig. 3.2 for both γ and Z^0 exchange. The matrix element is given then by

$$\mathcal{M}_{1\gamma} = \mathcal{M}^{\gamma}_{1\gamma\mathrm{i}} + \mathcal{M}^{\gamma}_{1\gamma\mathrm{f}} + \mathcal{M}^{Z}_{1\gamma\mathrm{i}} + \mathcal{M}^{Z}_{1\gamma\mathrm{f}}\,. \tag{3.26}$$

In the soft-photon approximation the matrix element for Z^0 exchange factorizes in the same way as for γ exchange as

$$\mathcal{M}^{Z}_{1\gamma} \longrightarrow \mathcal{M}^{Z}_{1s\gamma} = -e\mathcal{M}^{Z}_{0\gamma}\left(\frac{l\epsilon^*}{lk} - \frac{l'\epsilon^*}{l'k}\right) \tag{3.27}$$

where ϵ^{μ} is the photon polarization vector. The integration over the photon 4-momentum up to a cut-off Δ in the soft-photon approximation for the polarized cross-section can be performed in the same way as for the unpolarized cross-section (see Ref. [28]).

$$\int_{E_\gamma<\Delta} \mathrm{d}^4\sigma^{(1P)}_{1s\gamma} = \mathrm{d}\sigma^{(0P)}\left(-\frac{\alpha}{2\pi^2}\right)\int_{E_\gamma<\Delta}\frac{\mathrm{d}^3k}{2E_\gamma}\left(\frac{l}{lk} - \frac{l'}{l'k}\right)^2. \tag{3.28}$$

Therefore the relative one soft-photon correction to the polarized cross-section is the same with the unpolarized one and given by

$$\delta^{(1P)}_{1s\gamma}(\Delta) = \left(-\frac{\alpha}{2\pi^2}\right)\int_{E_\gamma<\Delta}\frac{\mathrm{d}^3k}{2E_\gamma}\left(\frac{l}{lk} - \frac{l'}{l'k}\right)^2 = \delta^{(1)}_{1s\gamma}(\Delta)\,. \tag{3.29}$$

The total first order non-radiative relative correction is IR finite and given by

$$\delta^{(1P)}_{\text{non-rad}}(\Delta) = \delta^{(1P)}_{1\text{-loop}} + \delta^{(1P)}_{1s\gamma}(\Delta)\,. \tag{3.30}$$

The polarized cross-section with one radiated photon in the final state is given by

$$\mathrm{d}^4\sigma^{(1P)}_{1h\gamma} = \frac{\mathrm{d}^4\Gamma_{1\gamma}}{4M|\vec{l}\,|}\overline{\Re\left(\mathcal{M}^{\dagger}_{1\gamma,\gamma}\mathcal{M}^{P}_{1\gamma,Z}\right)}\,, \tag{3.31}$$

where the flux factor is given for the fixed-target frame and the bar indicates that one has to average and sum over the polarization degrees of freedom in the initial and final state, respectively. Since the initial lepton is polarized, one has to average in the initial state only over the

polarization degrees of freedom of the initial proton. The matrix element that corresponds to the diagrams given in Fig. 3.2 for Z^0 exchange is given by

$$\begin{aligned}\mathcal{M}^P_{1\gamma,Z} =& \frac{eG_F}{2\sqrt{2}}\bar{u}(l')\left[\gamma_\mu(g_V+g_A\gamma_5)\frac{\not{l}-\not{k}+m_\ell}{-2lk}\not{\epsilon}^* + \not{\epsilon}^*\frac{\not{l}'+\not{k}+m_\ell}{2l'k}\gamma_\mu(g_V+g_A\gamma_5)\right]u(l,\lambda)\\ &\times\bar{u}(p')\left[\gamma^\mu(F_1^Z+F_2^Z)-\frac{(p'+p)^\mu}{2M}F_2^Z+\gamma^\mu\gamma_5 G_A^Z\right]u(p).\end{aligned} \tag{3.32}$$

The differential phase-space is the same as for the unpolarized cross-section and was given in Sec. 2.2.2. As in the leading order, for incident polarized electrons we can use the helicity projection operators from Eq. F.3 defined in App. F. The sum over final state electron spins leads to a calculation of a trace, which is calculated with the help of `FeynCalc` package and the final result is expressed in terms of invariant products of 4-momenta. The resulting expression is too large to be given here.

3.3 Second-order corrections

The asymmetry with $\mathcal{O}(\alpha^2)$ corrections is defined as

$$A_{PV}^{(0+1+2)} = \frac{\sigma_+^{(0+1+2)}-\sigma_-^{(0+1+2)}}{\sigma_+^{(0+1+2)}+\sigma_-^{(0+1+2)}} = \frac{\sigma_P^{(0)}+\sigma_P^{(1)}+\sigma_P^{(2)}}{\sigma^{(0)}+\sigma^{(1)}+\sigma^{(2)}}\,. \tag{3.33}$$

As in the first order we separate $\mathcal{O}(\alpha^2)$ corrections into non-radiative corrections, that include two-loop, one-loop, one soft-photon combined with one-loop and two soft-photons corrections, and hard photon corrections. The hard photon corrections include one hard photon combined with one-loop and one soft photon and two hard photons.

3.3.1 Non-radiative corrections

The Feynman diagrams for the two-loop correction are given in Fig. 3.3. The matrix elements that describe the contribution of these diagrams are denoted by $\mathcal{M}^P_{\text{2-loop},Z}$ for Z^0 exchange

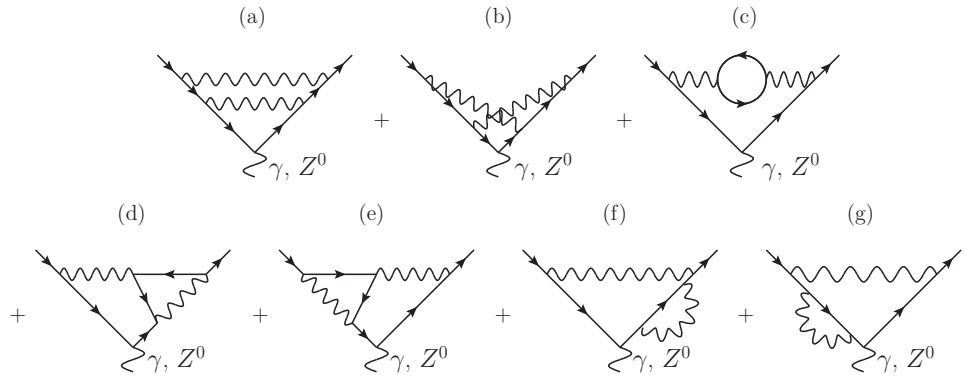

Figure 3.3: Feynman diagrams for two-loop vertex corrections.

and by $\mathcal{M}_{2\text{-loop},\gamma}$ for γ exchange. The relative second order loop correction includes the two-loop corrections to Z^0 exchange, the two-loop correction for γ exchange and additionally the square of the one-loop correction and is given by

$$\delta^{(2P)}_{2\text{-loop}} = \frac{\Re\left(\mathcal{M}^{\dagger}_{1\text{-loop},\gamma}\mathcal{M}^{P}_{1\text{-loop},Z}\right)}{\Re\left(\mathcal{M}^{\dagger}_{\gamma}\mathcal{M}^{P}_{Z}\right)} + \frac{\Re\left(\mathcal{M}^{\dagger}_{2\text{-loop},\gamma}\mathcal{M}^{P}_{Z}\right)}{\Re\left(\mathcal{M}^{\dagger}_{\gamma}\mathcal{M}^{P}_{Z}\right)} + \frac{\Re\left(\mathcal{M}^{\dagger}_{\gamma}\mathcal{M}^{P}_{2\text{-loop},Z}\right)}{\Re\left(\mathcal{M}^{\dagger}_{\gamma}\mathcal{M}^{P}_{Z}\right)}. \tag{3.34}$$

The square of one-loop corrections can be easily taken into account by using the parametrization from Eqs. (3.21) and (3.22) and is given by

$$\delta^{(2P)}_{1\text{-loop}} = \frac{\Re\left(\mathcal{M}^{\dagger}_{1\text{-loop},\gamma}\mathcal{M}^{P}_{1\text{-loop},Z}\right)}{\Re\left(\mathcal{M}^{\dagger}_{\gamma}\mathcal{M}^{P}_{Z}\right)}. \tag{3.35}$$

In Sec. 2.2 was stated, as a consequence of the Kinoshita-Lee-Nauenberg theorem, that the order of logarithms, $L \equiv \ln\left(Q^2/m^2\right)$, cannot be higher than the order of the coupling constant, such that the relative corrections have the form given in Eq. 2.61. This result implies that in the difference $F_1^{\ell(2)} - F_A^{\ell(2)}$ we cannot have logarithms with higher powers than 2. Assuming the coefficient of L^2 is of order $\mathcal{O}(1)$, for Q^2 relevant for the P2 experiment, the contribution of such a term is not higher than 10^{-4} and can be safely neglected. This allows us to conclude that the difference between the two-loop relative corrections for γ and Z^0 exchange are very small, of the order α^2, which allows us to make the following approximation

$$\frac{\Re\left(\mathcal{M}^{\dagger}_{2\text{-loop},\gamma}\mathcal{M}^{P}_{Z}\right)}{\Re\left(\mathcal{M}^{\dagger}_{\gamma}\mathcal{M}^{P}_{Z}\right)} + \frac{\Re\left(\mathcal{M}^{\dagger}_{\gamma}\mathcal{M}^{P}_{2\text{-loop},Z}\right)}{\Re\left(\mathcal{M}^{\dagger}_{\gamma}\mathcal{M}^{P}_{Z}\right)} \approx \frac{2\Re\left(\mathcal{M}^{\dagger}_{2\text{-loop},\gamma}\mathcal{M}^{P}_{Z}\right)}{\Re\left(\mathcal{M}^{\dagger}_{\gamma}\mathcal{M}^{P}_{Z}\right)} \approx 2F_1^{\ell(2)}. \tag{3.36}$$

A compact expression for $F_1^{\ell(2)}$, valid for $Q^2 \gg m_\ell^2$ was given in Eq. 2.133.

The diagrams for the process $ep \longrightarrow ep\gamma\gamma$ are given in Fig. 3.4. In the soft-photon approximation, if the photon energies are smaller than the cut-off Δ, it is possible to factorize the same eikonal factor, as was done in the unpolarized case (see Sec. 2.2.1). The relative corrections are then given by

$$\delta^{(2P)}_{2s\gamma} = \delta^{(2)}_{2s\gamma} = \frac{1}{2!}\left(\delta^{(1)}_{1s\gamma}\right)^2. \tag{3.37}$$

The diagrams for one-loop and one radiated photon correction are given in Fig. 3.5. If the radiated photon is soft we can approximate the contribution of this correction by considering the one-loop and soft-photon factorize as

$$\delta^{(2P)}_{1\text{-loop}+1s\gamma}(\Delta) = \delta^{(1P)}_{1\text{-loop}}\delta^{(1P)}_{1s\gamma}(\Delta). \tag{3.38}$$

Combining all non-radiative second order corrections at the level of the cross section we obtain an IR-finite result

$$\delta^{(2P)}_{\text{non-rad}}(\Delta) = \delta^{(2P)}_{2\text{-loop}} + \delta^{(1P)}_{1\text{-loop}}\delta^{(1P)}_{1s\gamma}(\Delta) + \delta^{(2P)}_{2s\gamma}(\Delta). \tag{3.39}$$

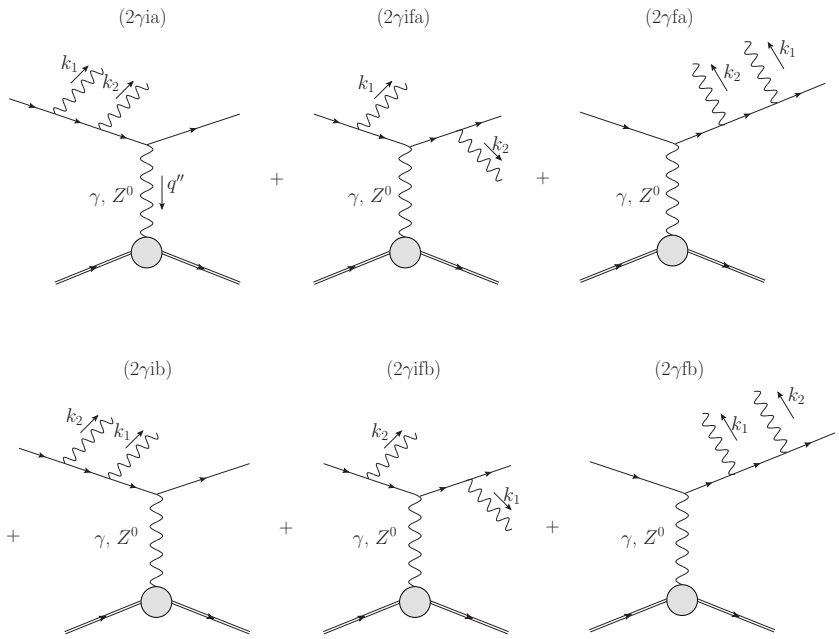

Figure 3.4: Feynman diagrams for two-photon bremsstrahlung.

3.3.2 Hard photon Corrections

$\mathcal{O}(\alpha^2)$ radiative corrections include one-loop corrections to $ep \longrightarrow ep\gamma$ process and two radiated photons in the final state, in which one is hard and the other one soft, or with both photons hard, i.e. with energies bigger than the cut-off Δ.

The diagrams for one-loop and one hard-photon correction are given in Fig. 3.5. The calculation of these diagrams goes along the same line as in Sec. 2.4.2 and is not given again here. The renormalization for the corrections that enter in the polarized cross-section is done in the on-shell scheme and differs from Sec. 2.4.2 only for $se1\gamma$ and $v2\gamma$ diagrams. In contrast

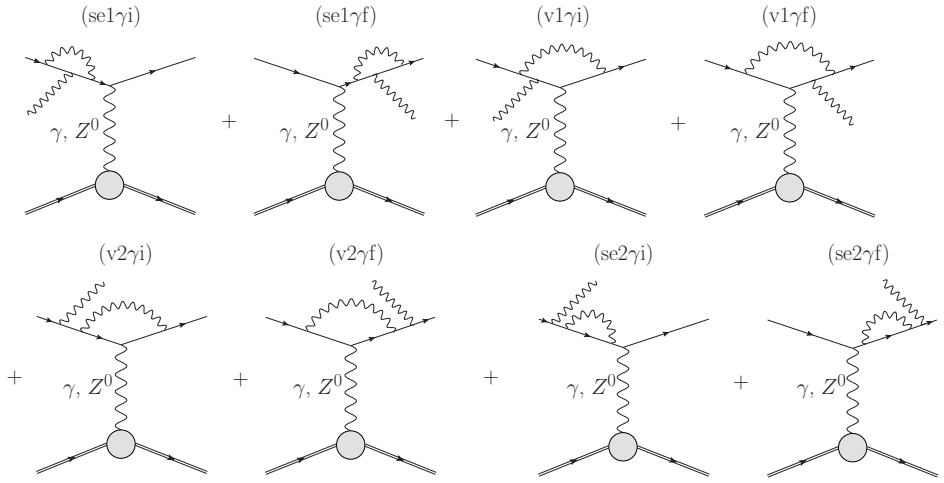

Figure 3.5: Feynman diagrams for one-loop corrections to one-photon bremsstrahlung.

with the unpolarized part, the UV divergence in the case of Z^0 exchange is removed for $se1\gamma$ and $v2\gamma$ diagrams by adding the vertex counter-terms δZ_1 for the vector part and δZ_A for the vector-axial part. The total renormalized polarized relative correction is given by the sum of the relative corrections as

$$\delta^{(2P)}_{1\text{-loop}+1h\gamma} = \delta^{P}_{\text{se}1\gamma} + \delta^{P}_{\text{v}1\gamma} + \delta^{P}_{\text{se}2\gamma} + \delta^{P}_{\text{v}2\gamma}\,, \tag{3.40}$$

and has the same IR structure with the unpolarized one, which cancels out at the level of the cross-section, when combined with the one hard-photon and one soft-photon correction. The relative corrections are given in this case by

$$\begin{aligned}
\delta^{P}_{\text{se}1\gamma} &= \frac{\Re\left(\mathcal{M}^{\dagger}_{\text{se}1\gamma,\gamma}\mathcal{M}^{P}_{1\gamma,Z}\right) + \Re\left(\mathcal{M}^{\dagger}_{1\gamma,\gamma}\mathcal{M}^{P}_{\text{se}1\gamma,Z}\right)}{\Re\left(\mathcal{M}^{\dagger}_{1\gamma,\gamma}\mathcal{M}^{P}_{1\gamma,Z}\right)} \\
\delta^{P}_{\text{v}1\gamma} &= \frac{\Re\left(\mathcal{M}^{\dagger}_{\text{v}1\gamma,\gamma}\mathcal{M}^{P}_{1\gamma,Z}\right) + \Re\left(\mathcal{M}^{\dagger}_{1\gamma,\gamma}\mathcal{M}^{P}_{\text{v}1\gamma,Z}\right)}{\Re\left(\mathcal{M}^{\dagger}_{1\gamma,\gamma}\mathcal{M}^{P}_{1\gamma,Z}\right)} \\
\delta^{P}_{\text{se}2\gamma} &= \frac{\Re\left(\mathcal{M}^{\dagger}_{\text{se}2\gamma,\gamma}\mathcal{M}^{P}_{1\gamma,Z}\right) + \Re\left(\mathcal{M}^{\dagger}_{1\gamma,\gamma}\mathcal{M}^{P}_{\text{se}2\gamma,Z}\right)}{\Re\left(\mathcal{M}^{\dagger}_{1\gamma,\gamma}\mathcal{M}^{P}_{1\gamma,Z}\right)} \\
\delta^{P}_{\text{v}2\gamma} &= \frac{\Re\left(\mathcal{M}^{\dagger}_{\text{v}2\gamma,\gamma}\mathcal{M}^{P}_{1\gamma,Z}\right) + \Re\left(\mathcal{M}^{\dagger}_{1\gamma,\gamma}\mathcal{M}^{P}_{\text{v}2\gamma,Z}\right)}{\Re\left(\mathcal{M}^{\dagger}_{1\gamma,\gamma}\mathcal{M}^{P}_{1\gamma,Z}\right)}\,.
\end{aligned}$$

The Feynman diagrams for one hard-photon and one soft-photon correction are given in Fig. 3.4. As was shown in [28], this correction consists of an IR divergent part, that factorizes in the soft-photon approximation, and an IR-finite part, that can be calculated numerically. The polarized cross-section for one hard-photon and one soft-photon is then given by

$$\sigma^{(2P)}_{1s\gamma+1h\gamma}(\Delta) = \delta^{(1P)}_{1s\gamma}(\Delta)\int_{\Delta}^{E_\gamma^{max}} \mathrm{d}^4\sigma^{P}_{1\gamma} + 2\int_{\Delta}^{E_\gamma^{max}}\int_{0}^{\Delta}\left(\mathrm{d}^7\sigma^{P}_{2\gamma}\right)^{\text{IR-finite}}_{1\gamma\to 0}\,. \tag{3.41}$$

Finally the polarized cross-section with two hard-photons in the final state is given by

$$\mathrm{d}^7\sigma^{(2P)}_{2h\gamma} = \frac{\mathrm{d}^7\Gamma_{2\gamma}}{4M|\vec{l}\,|}\overline{\Re\left(\mathcal{M}^{\dagger}_{2\gamma,\gamma}\mathcal{M}^{P}_{2\gamma,Z}\right)}\,, \tag{3.42}$$

where the 7-fold differential phase-space $\mathrm{d}^7\Gamma_{2\gamma}$ is the same as in the unpolarized cross-section and was treated in Sec. 2.4.4. The matrix element that corresponds to the Feynman diagrams from Fig. 3.4 for Z^0 exchange is given by

$$\begin{aligned}
\mathcal{M}^{P}_{2\gamma,Z} =& \frac{e^2 G_F}{2\sqrt{2}}\bar{u}(l')\Bigg[\gamma_\mu(g_V+g_A\gamma_5)\frac{\not{l}-\not{k}_1-\not{k}_2+m_e}{-2lk_1-2lk_2+2k_1k_2}\not{\epsilon}^{*}_2\frac{\not{l}-\not{k}_1+m_e}{-2lk_1}\not{\epsilon}^{*}_1 \\
&+\not{\epsilon}^{*}_2\frac{\not{l}'+\not{k}_2+m_e}{2l'k_2}\gamma_\mu(g_V+g_A\gamma_5)\frac{\not{l}-\not{k}_1+m_e}{-2lk_1}\not{\epsilon}^{*}_1 \\
&+\not{\epsilon}^{*}_1\frac{\not{l}'+\not{k}_1+m_e}{2l'k_1}\not{\epsilon}^{*}_2\frac{\not{l}'+\not{k}_1+\not{k}_2+m_e}{2l'k_1+2l'k_2+2k_1k_2}\gamma_\mu(g_V+g_A\gamma_5)+k_1\leftrightarrow k_2\Bigg]u(l,\lambda) \\
&\times\bar{u}(p')\left[\gamma^\mu(F_1^Z+F_2^Z)-\frac{(p'+p)^\mu}{2M}F_2^Z+\gamma^\mu\gamma_5 G_A^Z\right]u(p).
\end{aligned} \tag{3.43}$$

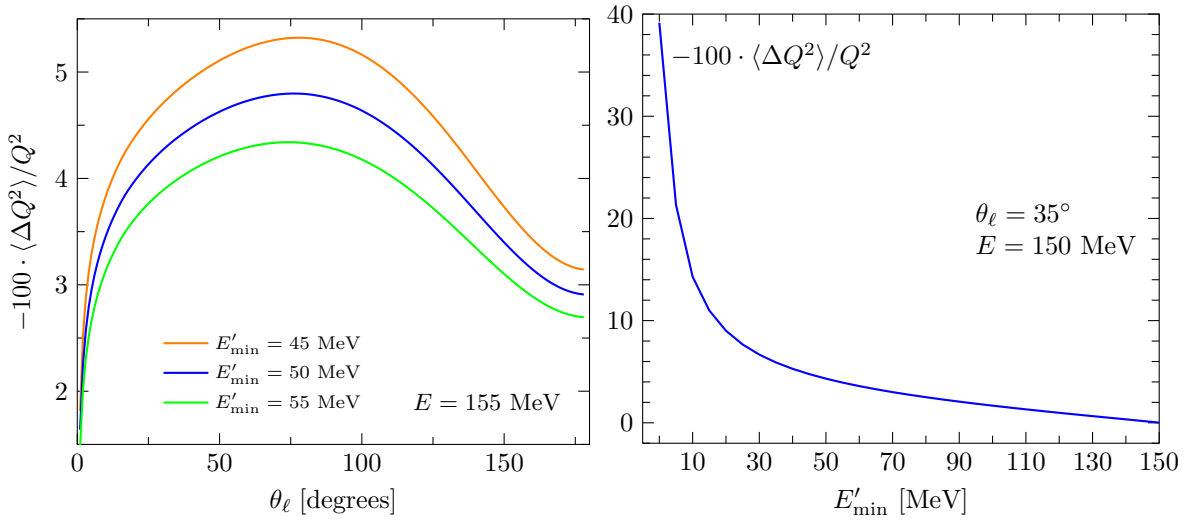

Figure 3.6: The average relative shift of the momentum transfer due to hard photon radiation as a function of the electron scattering angle and for different cuts on the energy of the scattered electron (left) and as a function of the minimum energy of the scattered electron (right). The beam energy is fixed at $E = 155$ MeV as expected for the Mainz P2 experiment.

The sum over final state electron spins leads to a calculation of a trace, which is calculated with the help of `FeynCalc` package and the final result is expressed in terms of invariant products of 4-momenta. The resulting expression is too large to be given here.

3.4 Numerical tests and results

3.4.1 The shift in Q^2 due to photon radiation

We define the average shift of the momentum transfer by

$$\langle \Delta Q^2 \rangle = \frac{1}{\sigma^{(0+1)}} \int \mathrm{d}^4\sigma^{(1)}_{1\gamma} \Delta Q^2 \,, \tag{3.44}$$

where $\sigma^{(0+1)}$ is the total unpolarized cross section with $\mathcal{O}(\alpha)$ corrections defined in Sec. 2.2, while $\mathrm{d}^4\sigma^{(1)}_{1\gamma}$ is the differential cross section for the process with one radiated photon in the final state. $\Delta Q^2 = Q^2 - Q^2_l$ is defined as the difference between the hadronic ("true") momentum transfer square Q^2 and the leptonic momentum transfer squared Q^2_ℓ. The integration in this expression can be performed numerically over the entire phase-space, since the product $\mathrm{d}^4\sigma^{(1)}_{1\gamma}\Delta Q^2$ is infra-red (IR) finite. Results for the kinematical conditions of the Mainz P2 experiment are shown in Fig. 3.6. We find that the average shift of the momentum transfer has a strong dependence on kinematic variables. In Fig. 3.6 we see the dependence on the scattering angle and we also find a strong dependence on the cut for the minimum value of the scattered electron's energy. This cut is related to the detector acceptance of the experiment. From Eq. 3.2 we see that the asymmetry is proportional to Q^2 and therefore we expect that a change in Q^2 will lead to a correction of similar size in the asymmetry when we include photon radiation. To show this effect we plot in Fig. 3.7 the shift in Q^2 at fixed angle, together

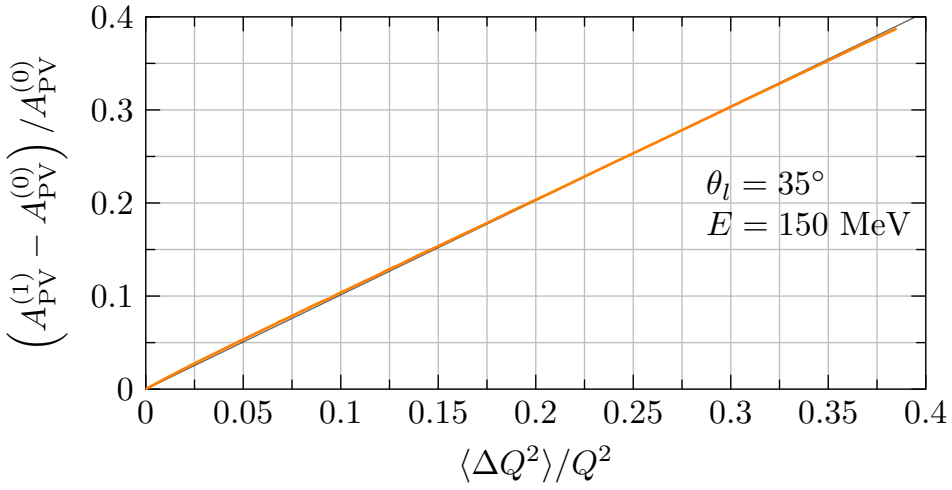

Figure 3.7: A comparison between the shift in Q^2 as a function of E'_{min} and the correction to the asymmetry due to first order QED radiative corrections for the same value of E'_{min}.

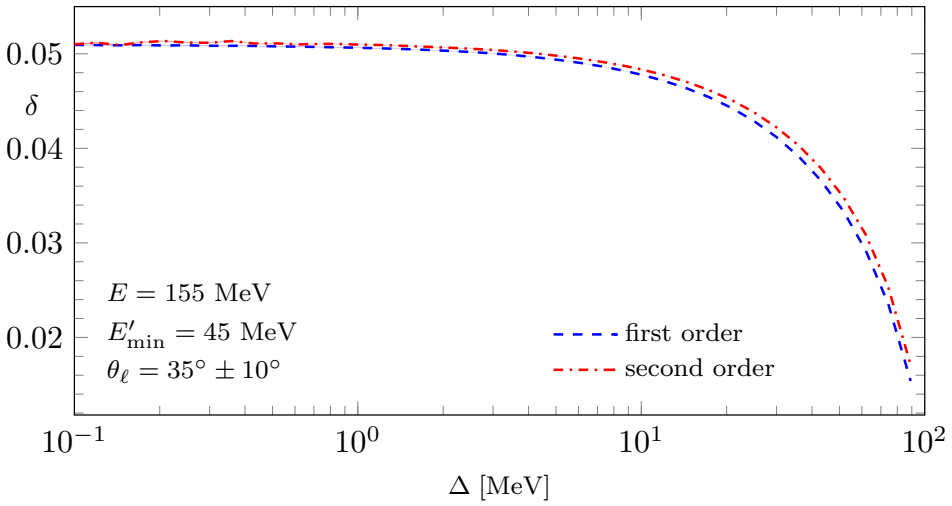

Figure 3.8: Test of the Δ-independence of the complete correction factors to the parity violating asymmetry A_{PV}, at first order $\delta = A_{PV}^{(1)}/A_{PV}^{(0)}$ and second order $\delta = A_{PV}^{(2)}/A_{PV}^{(0)}$. and including $\mathcal{O}(\alpha)$ and $\mathcal{O}(\alpha^2)$ QED corrections. Kinematic variables are chosen as relevant for the Mainz P2 experiment.

with the first order QED corrections to the asymmetry by varying the lower cut on the energy of the scattered electron as was done in the right plot of Fig. 3.6. We can see that at the same value of E'_{min} the change in the asymmetry, when including photon radiation, is of the same size with the shift in Q^2.

3.4.2 Results for the parity violating asymmetry

As was explained in the introduction, the weak mixing angle is running with Q^2. In our calculation the running of $\sin^2\theta_W$ is taken into account by using the implementation from

the `Fortran` code alphaQED (see Ref. [20]).

While a determination of the true momentum transfer is difficult or impossible, the dependence of the asymmetry on the electron scattering angle, θ_ℓ, is directly accessible in the experiment. We therefore study the effect of QED radiative corrections on the θ_ℓ-dependence of A_{PV}. The total asymmetry, with $\mathcal{O}(\alpha)$ and $\mathcal{O}(\alpha^2)$ corrections is independent of the cut-off Δ, as can be seen from Fig. 3.8. As in the study of the cross section (see Sec. **??**), we see that for bigger values of the cut-off, the soft photon approximation breaks down, while for smaller values the uncertainties become too large. However, we find that for 0.1 MeV $\lesssim \Delta \lesssim$ 5 MeV the asymmetry stays relatively constant and it is safe to choose any value of the the cut-off Δ in this range. The leading order asymmetry and the asymmetry with $\mathcal{O}(\alpha)$ corrections is found to be of the same size as the relative shift of Q^2. This is demonstrated by the numerical results shown in Fig. 3.9. A numerical calculation of the parity-violating asymmetry results in a very small second-order corrections. This can be seen in also in Fig. 3.9 where the curves for A_{PV} at first and at second order are almost indistinguishable. In fact, radiative corrections for the asymmetry are due to the shift of the momentum transfer Q^2. This kinematical effect is already fully present if there is one radiated photon and second-order corrections contribute indeed only at the expected level with an additional factor of α/π. Therefore, second-order QED corrections to the asymmetry have a negligibly small effect, as can be seen also from Fig. 3.10 where the relative corrections to the asymmetry are plotted as a function of the scattering angle.

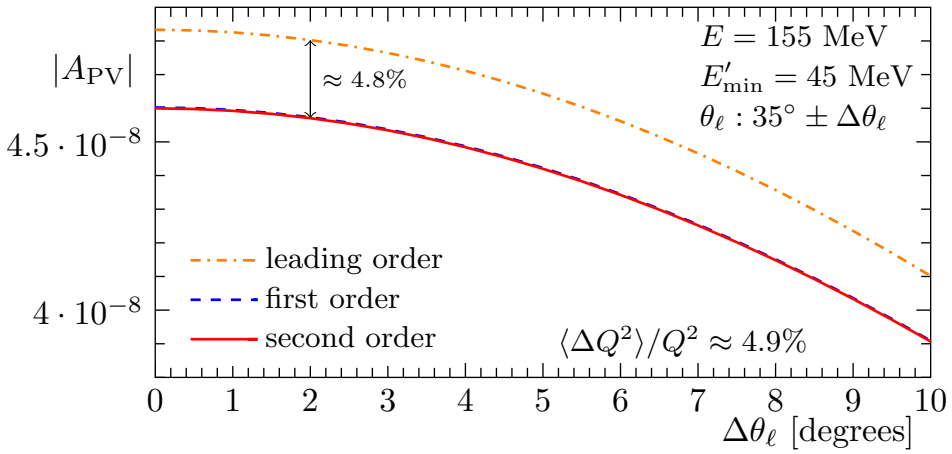

Figure 3.9: The parity violating asymmetry A_{PV} at leading order and including $\mathcal{O}(\alpha)$ and $\mathcal{O}(\alpha^2)$ QED corrections. Kinematic variables are again chosen as relevant for the Mainz P2 experiment. The asymmetry is shown as a function of the scattering angle acceptance $\Delta\theta_l$, i.e. cross sections are integrated over the electron scattering angle in the range $35^\circ - \Delta\theta_l \leq \theta_l \leq 35^\circ + \Delta\theta_l$.

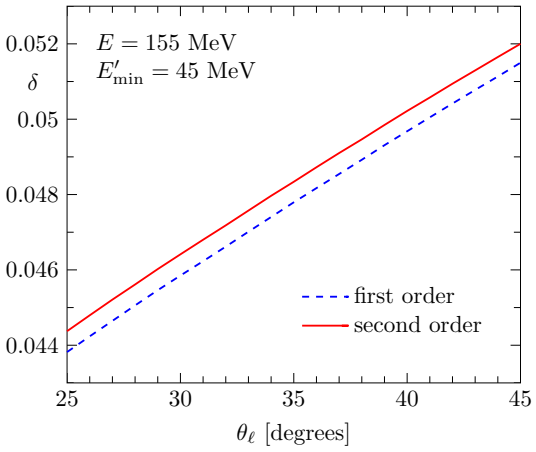

Figure 3.10: The correction factors dependence on the scattering angle for the parity violating asymmetry A_{PV}. They are defined at first order as $\delta = A_{PV}^{(1)}/A_{PV}^{(0)}$ and second order as $\delta = A_{PV}^{(2)}/A_{PV}^{(0)}$. and they include $\mathcal{O}(\alpha)$ and $\mathcal{O}(\alpha^2)$ QED corrections. Kinematic variables are chosen as relevant for the Mainz P2 experiment.

Chapter 4

Lepton-Carbon Scattering

4.1 Definitions and general remarks

The P2 experimental program at the MESA facility in Mainz (see Ref. [27]) includes a plan aiming also for a 0.3% determination of the weak charge of ^{12}C. There are several reasons for which this measurement is important. Apart from the extraction of the weak mixing angle, $\sin^2\theta_W$, which can be used to test the SM, electron scattering on heavier nuclei, like ^{12}C, allow the measurement of what is called the neutron skin, which is the measurement in the radii of the neutron and proton distributions. This can be done because the Z^0 boson, which is responsible for the parity violation, couples preferentially to neutrons. The goal of such a measurement is to constrain the equation of state of neutron rich matter. Recently, the lead (Pb) Radius EXperiment (PREX) has provided the first model-independent evidence in favor of a neutron-rich skin in ^{208}Pb (see Ref. [102]). Given this ambitious goal, a complete set of order-α radiative corrections should be included. An important effect in the determination of the weak charge of ^{12}C at order-α is given by Coulomb distortions, which scale as $Z\alpha$. This effect, together with effects due to nuclear structure, have been recently addressed in Ref. [103]. Here we study the effects of order-α leptonic radiation to the asymmetry between left- and right-handed electrons in electron-^{12}C scattering and in the extraction of the weak charge of ^{12}C.

As in the case of electron-proton scattering we choose a coordinate frame where the target nucleus is at rest and the z axis is directed along the momentum of the incident lepton. The notations for energies and angles of the particles that are involved in this scattering process were given in Fig. 2.1, except that now we denote the four momenta of the initial state and final state nucleus by c^μ and c'^μ. Unless explicitly stated, in this section we used the definitions given in Sec. 2.1 and Sec. 3.1.

We treat ^{12}C as a spin-0 particle. By doing so, the S-matrix element that describes the interaction between the virtual photon and the ^{12}C particle, is given by

$$C^\mu = Q_e^c \Gamma^\mu_{\gamma,c}\,, \tag{4.1}$$

where $Q_e^c = -Ze$ is the electric charge of the carbon nucleus. ^{12}C is made of 6 protons and 6 neutrons, such that $Z = 6$. The carbon vertex function that describes the interaction between the virtual photon and spin-0 particle with one-photon exchange is described by

$$\Gamma^\mu_{\gamma,c} = F_{\rm ch}(c + c')^\mu\,, \tag{4.2}$$

where $F_{\rm ch}$ is the carbon electromagnetic (or charge) form factor, which is normalized to 1 at $Q^2 = 0$. A parametrization of this form factor can be found in App. C.4. Other parametrizations of this form factor can be found in Ref. [104]. In case of Z^0 exchange the S-matrix element of ^{12}C is given by

$$\mathcal{C}^{\mu}_{Z} = g_Z Q^c_w \Gamma^{\mu}_{\gamma,c}\,, \tag{4.3}$$

where $g^2_Z = G_F M^2_Z/2\sqrt{2}$ and $Q^c_w = -4Z\sin^2\theta$ is the weak charge of ^{12}C. The carbon vertex function that describes the interaction of the virtual weak Z^0 boson with the spin-0 particle is given by

$$\Gamma^{\mu}_{Z,c} = F_{\rm wk}(c + c')^{\mu}\,, \tag{4.4}$$

where $F_{\rm wk}$ is the weak form factor, also normalized to 1 at $Q^2 = 0$. The weak form factor can be parametrized in the same way as the charge form factor, by using a symmetrized Fermi function (see App. C). In absence of experimental data, following Refs. [103] and [105], we choose the values of the parameters of the weak form factor to be the same with the charge form factor, i.e. $F_{\rm wk} = F_{\rm ch}$. In the Born approximation, the PV asymmetry for ^{12}C takes the following form (see Ref. [103])

$$A^{\rm PV}_c = \frac{\sigma^{(0)}_P}{\sigma^{(0)}} = -\frac{G_F Q^2}{4\sqrt{2}\pi\alpha}\frac{Q^c_w}{Z}\frac{F_{\rm wk}}{F_{\rm ch}}\,. \tag{4.5}$$

Since the weak charge of the carbon is negative the asymmetry is a positive number and not negative as in the case of the proton, for which the weak charge is a positive number.

Using the vertex rule from Eq. 4.2, the unpolarized Born cross section is given by

$$\frac{{\rm d}\sigma^{(0)}}{{\rm d}Q^2} = \frac{\overline{|\mathcal{M}_{\rm Born}|^2}}{16\pi\left[(s - m^2_\ell - M^2)^2 - 4m^2_\ell M^2\right]}\,, \tag{4.6}$$

where M is here the mass of the carbon-12 nucleus. The Born matrix element is given by

$$\mathcal{M}_{\rm Born} = \frac{1}{q^2}\mathcal{L}_\mu \mathcal{C}^\mu = -\frac{Ze^2}{q^2}\bar{u}(l')\gamma_\mu u(l)\Gamma^{\mu}_{\gamma,c}\,. \tag{4.7}$$

Averaging over initial state lepton polarizations and summing over the final ones as

$$\overline{|\mathcal{M}|^2} = \frac{1}{2}\sum_{\rm spins}|\mathcal{M}|^2\,, \tag{4.8}$$

we get the following expression for the differential Born cross section

$$\frac{{\rm d}\sigma^{(0)}}{{\rm d}Q^2} = \frac{4F^2_{\rm ch}Z^2\pi\alpha^2}{Q^4}\frac{\left[(s - m^2_\ell - M^2)^2 + Q^2(s - m^2_\ell)\right]}{\left[(s - m^2_\ell - M^2)^2 - 4m^2_\ell M^2\right]}\,, \tag{4.9}$$

where $s = (l + c)^2$ is the square of the energy in the center-of-mass frame.

The polarization dependent part of the differential cross section is given by

$$\frac{{\rm d}\sigma^{(0)}_P}{{\rm d}Q^2} = \frac{\overline{\Re\left(\mathcal{M}^{\dagger}_{{\rm Born},\gamma}\mathcal{M}^{P}_{{\rm Born},Z}\right)}}{16\pi\left[(s - m^2_\ell - M^2)^2 - 4m^2_\ell M^2\right]}\,. \tag{4.10}$$

Using vertex rule from Eq. 4.4, the Born matrix element for Z^0 exchange is given by

$$\mathcal{M}_{\text{Born,Z}} = \frac{1}{M_Z^2 - q^2}\mathcal{L}_{\mu,Z}C_Z^{\mu} = -\frac{G_F Q_w^c}{2\sqrt{2}}\bar{u}(l')\gamma_\mu(g_V + g_A\gamma_5)u(l,\lambda)\Gamma_Z^{\mu}\,. \tag{4.11}$$

However, in this case, the vector part of the leptonic current doesn't contribute. Using for the incident leptons the helicity projection operators from Eq. F.3 defined in App. F and summing over final state polarizations

$$\overline{\Re\left(\mathcal{M}^{\dagger}_{\text{Born},\gamma}\mathcal{M}^{P}_{\text{Born},Z}\right)} = \sum_{\text{spins}}\Re\left(\mathcal{M}^{\dagger}_{\text{Born},\gamma}\mathcal{M}^{P}_{\text{Born},Z}\right), \tag{4.12}$$

we get the following expression for the polarized Born cross section

$$\frac{\mathrm{d}\sigma_P^{(0)}}{\mathrm{d}Q^2} = -\frac{F_{\text{ch}}F_{\text{wk}}Q_w^c Z G_F\alpha}{\sqrt{2}}\frac{\left[(s - m_\ell^2 - M^2)^2 + Q^2(s - m_\ell^2)\right]}{\left[(s - m_\ell^2 - M^2)^2 - 4m_\ell^2 M^2\right]}\,. \tag{4.13}$$

To obtain this expression we have used instead of the helicity projection operators, the chirality projection operators defined in App. F. The difference between them is of the order of the lepton mass squared and can be ignored for electron scattering. It's easy to see that by using the expressions for the differential unpolarized and polarized cross sections we get the expression of the parity violating asymmetry from Eq. 4.5.

4.2 First order corrections

As in the case of electron-proton scattering we use a phase-space slicing method to deal with the IR divergences that appear in the calculation of the cross section for the $e^{12}C \longrightarrow e^{12}C\gamma$ process (for more details see the Chapter 2).

The order-α non-radiative leptonic corrections to the process $e^{12}C \longrightarrow e^{12}C$ consist of loop corrections, which include vertex and self-energy corrections and soft-photon corrections. The cross section which includes these corrections is given by

$$\sigma^{(1)}_{\text{non-rad}} = \sigma^{(1)}_{\text{1-loop}} + \sigma^{(1)}_{1s\gamma}\,, \tag{4.14}$$

where $\sigma^{(1)}_{\text{1-loop}}$ is the cross section with 1-loop corrections, while $\sigma^{(1)}_{1s\gamma}$ is the cross section with one radiated soft-photon in the final state. The loop and soft-photon corrections were treated in detail for both γ and Z^0 exchange in Sec. 2.2.1 and Sec. 3.3.1 respectively and we don't repeat them here.

In the case of order-α hard-photon leptonic bremsstrahlung the only difference is given by the matrix element squared, which for lepton-carbon unpolarized scattering is given by

$$\overline{|\mathcal{M}^{\ell}_{1\gamma}|^2} = -\frac{Z^2e^6}{2q'^4}\sum_{\text{spins}}\left|\bar{u}(l')\left[\gamma_\mu\frac{\not{l} - \not{k} + m_\ell}{-2lk}\not{\epsilon}^* + \not{\epsilon}^*\frac{\not{l}' + \not{k} + m_\ell}{2l'k}\gamma_\mu\right]u(l,\lambda)F_{\text{ch}}(c + c')^{\mu}\right|^2. \tag{4.15}$$

The expression for the matrix element squared is simpler for a spin-0 nucleon, like ^{12}C, and

we can give it's full expression here:

$$\begin{aligned}\overline{|\mathcal{M}^{\ell}_{1\gamma}|^2} =& \frac{4F_{\rm ch}^2 Z^2(4\pi\alpha)^3}{Q^4}\Bigg[\frac{m_\ell^2(M^2Q^2+U(Q^2-U))}{(lk)^2}+\frac{m_\ell^2(M^2Q^2+S(Q^2-S))}{(l'k)^2}\\ &+\frac{M^2(Q_\ell^2+Q^2)+Q^2S}{lk}+\frac{M^2(Q_\ell^2+Q^2)+Q^2U}{l'k}\\ &+\frac{Q^2\left(-2M^2Q^2-Q^2(S+U)+S^2+U^2\right)}{2(lk)(l'k)}\\ &-\frac{m_\ell^2\left(2M^2Q^2+Q^2-Q^2(S+U)+2SU\right)}{(lk)(l'k)}-4M^2\Bigg],\end{aligned} \tag{4.16}$$

where $S = 2lc$ and $U = -2l'c$. The 4-momenta product between the scattered electron and the final state photon can be expressed in terms of the other invariants as $l'k = lk + Q_\ell^2/2 - Q^2/2$. To simplify this expression we have used a partial fractioning technique implemented in an algorithm which is described in Ref. [95].

For lepton-carbon polarized scattering the matrix element that describes the Z^0 exchange for first order leptonic radiation is given by

$$\begin{aligned}\mathcal{M}^{P}_{1\gamma,Z} =& \frac{eG_F Q_w^c}{2\sqrt{2}}\bar{u}(l')\Big[\gamma_\mu(g_V+g_A\gamma_5)\frac{\not{l}-\not{k}+m_\ell}{-2lk}\not{\epsilon}^{*}+\not{\epsilon}^{*}\frac{\not{l}'+\not{k}+m_\ell}{2l'k}\gamma_\mu(g_V+g_A\gamma_5)\Big]\\ &\times u(l,\lambda)F_{\rm wk}(c+c')^\mu.\end{aligned} \tag{4.17}$$

Summing over initial state spins, the interference between the matrix element for photon exchange and the one for Z^0 exchange is given by

$$\begin{aligned}\overline{\Re\left(\mathcal{M}^{\dagger}_{1\gamma,\gamma}\mathcal{M}^{P}_{1\gamma,Z}\right)} =& \frac{4F_{\rm ch}F_{\rm wk}Z(4\pi\alpha)^2G_F m_\ell}{\sqrt{2}Q^2}\\ &\times\Bigg[\frac{m_\ell^2\left((4M^2+Q^2)(\zeta k+\zeta l')+(2U-Q^2)(\zeta p+\zeta p')\right)+2\zeta k(M^2Q^2+UQ^2-U^2)}{(lk)^2}\\ &+\frac{m_\ell^2\left(4M^2(\zeta k+\zeta l')+Q^2(\zeta k+\zeta l'+\zeta p+\zeta p')-2S(\zeta p_1+\zeta p_2)\right)}{(l'k)^2}\\ &-\frac{2\left(2M^2(2\zeta k+\zeta l')+U(2\zeta k+\zeta l'+\zeta p+\zeta p')\right)}{lk}\\ &+\frac{(Q_\ell^2+Q^2)(\zeta k+\zeta l'+\zeta p+\zeta p')-2\left(2M^2\zeta l'+S\zeta l'+U(2\zeta k+2\zeta l'+\zeta p+\zeta p')\right)}{l'k}\\ &-\frac{2m_\ell^2\left((4M^2+Q^2)(\zeta k+\zeta l')-(S-U)(\zeta p+\zeta p')\right)}{(lk)(l'k)}\\ &-\frac{2M^2Q^2(\zeta k+2\zeta l')+Q^2S(\zeta l'-\zeta p-\zeta p')+\ Q^2U(2\zeta k+3\zeta l'+\zeta p+\zeta p')}{(lk)(l'k)}\\ &+\frac{2U^2(\zeta k+\zeta l')+2SU\zeta l'}{(lk)(l'k)}\Bigg],\end{aligned} \tag{4.18}$$

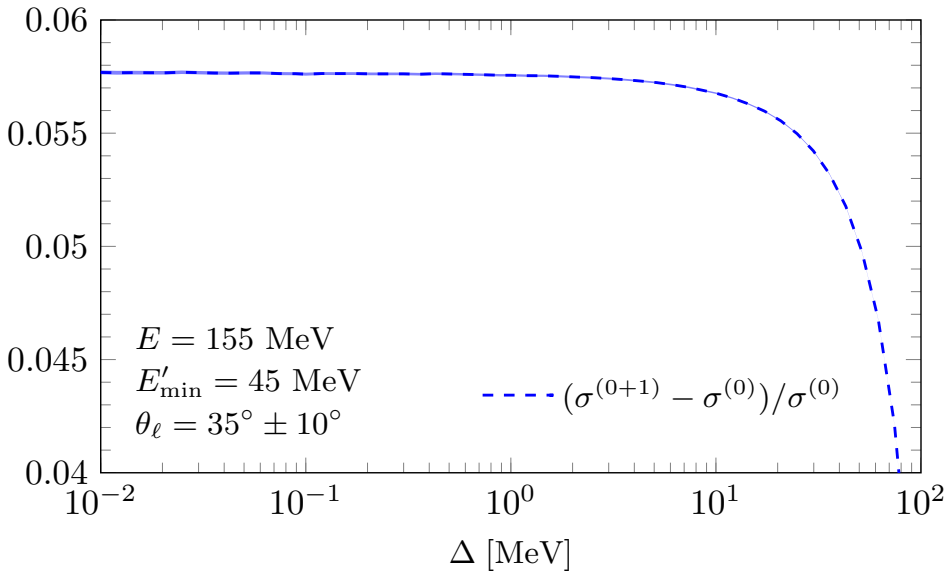

Figure 4.1: Test of the Δ-independence of the complete correction factors to the electron-^{12}C cross section. At order-α this correction factor is defined as $\delta = \sigma^{(1)}/\sigma^{(0)} - 1$. Kinematic variables are chosen as relevant for the Mainz P2 experiment. The numerical uncertainties are given by the thickness of the line.

where ζ^μ is the spin four-vector (see App. F). Although the difference between helicity projection operators and chirality projection operators is small, of the order of m_ℓ^2, in this case, these terms get enhanced by the collinear poles and can lead therefore to important effects. For P2 kinematics, for example, this can lead on average to a 1% effect.

4.3 Numerical tests and results

As was explained in detail in Sec. 2.2.1, the total result must be independent of the cut-off Δ. In practice, however, as can be seen from Fig. 4.1, if the cut-off is too large, the soft-photon approximation breaks down, while if it's too small, the uncertainties can become too large. The numerical uncertainties are however small at first order and, as can be seen from this figure, is safe to choose any value of the cut-off between 0.01 and 1 MeV.

The cross section for electron-carbon scattering with first order corrections, same as the one for electron-proton scattering (see Sec. 2.6), has a strong dependence on kinematic prescriptions. This behavior is shown in Fig. 4.2, where on the left side we see the dependence of the differential cross section on the scattering angle and on the right side the dependence of the correction factor to the minimum energy of the scattered electron, which is connected experimentally to the detector threshold.

It is worth mentioning here that one of first measurements of nuclear form factors was carried out at the Standford linear accelerator using electron-^{12}C scattering (see Ref. [106]). At the energies at which the measurement was performed ($E = 420$ MeV) the cross section features two minima, known as diffraction minima. These minima appear for certain values of Q^2, for which the charge form factor goes to 0, $F_{\text{ch}}(Q^2) \longrightarrow 0$. This behavior is shown in

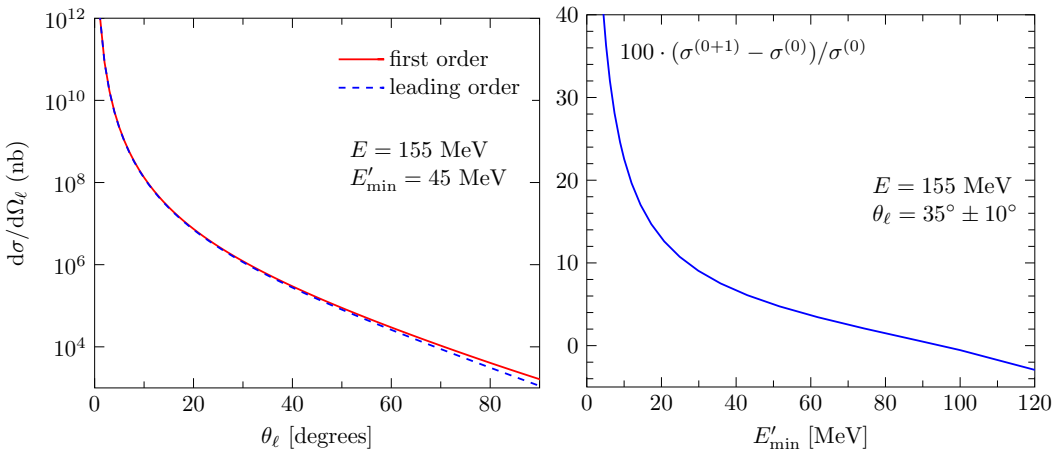

Figure 4.2: The dependence of the differential cross section for electron carbon scattering at first and leading order (on the left side) and the dependence of the correction factor on the minimum energy of the scattered electron (on the right side). The kinematics are chosen for the P2 experiment.

Fig. 4.3, where the leading order cross section is plotted together with the first order cross section at different values of the minimum of the scattered electron. As can be seen from this figure, when including photon radiation, the diffraction minima are washed out. Furthermore, the smaller the value of the minimum of the scattered electron's energy, the more significant the washing out effect. This effect can be explained by the fact that photon radiation leads to a shift in momentum transfer squared and the leptonic momentum transfer squared is replaced by the hadronic one as $Q^2 \longrightarrow Q'^2$ (see Sec. 3.4.1). Since the charge form factor is Q^2 dependent,

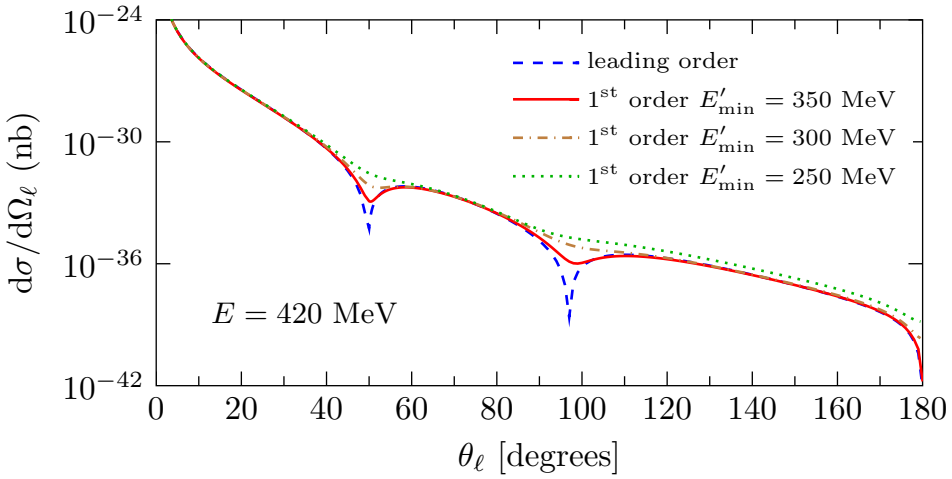

Figure 4.3: The differential cross section for electron-^{12}C scattering as a function of the scattering angle. The energy was chosen to match the one of the experiment that was performed at the Standford linear accelerator (see Ref. [106]). Two diffraction minima can be seen at this energy, that are washed out when photon radiation is included.

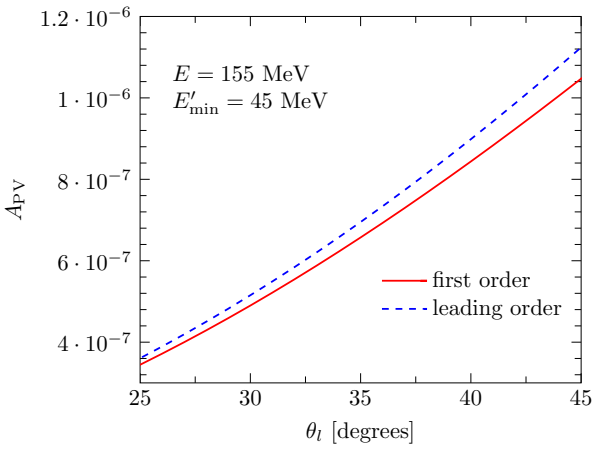

Figure 4.4: The parity violating asymmetry dependence on the scattering angle in electron-^{12}C scattering, at leading order and with $\mathcal{O}(\alpha)$ QED corrections.

the new hadronic momentum transfer square leads to shift in the minima of the form factor, because the form factor is now replaced with one that is Q'^2 dependent as $F_{ch}(Q^2) \longrightarrow F_{ch}(Q'^2)$. A smaller value of the energy of the scattered electron E'_{min} allows a bigger energy of the emitted photon. A bigger energy of the emitted photon leads to a bigger shift in Q^2, which in turn leads to a bigger washing out effect.

As can be seen from Eq. 4.5, the asymmetry is proportional to Q^2. Therefore we expect as well, as in the case of electron-proton scattering, a strong dependence on kinematical prescriptions. This effect can be seen for example in Fig. 4.4 where we can see the dependence on the scattering angle of the parity violating asymmetry at leading and at first order. Furthermore, at first order, the only QED effect that contributes is a kinematical effect coming from the shift of Q^2, which was studied in Sec. 3.4. As can be seen from Fig. 4.5, the difference

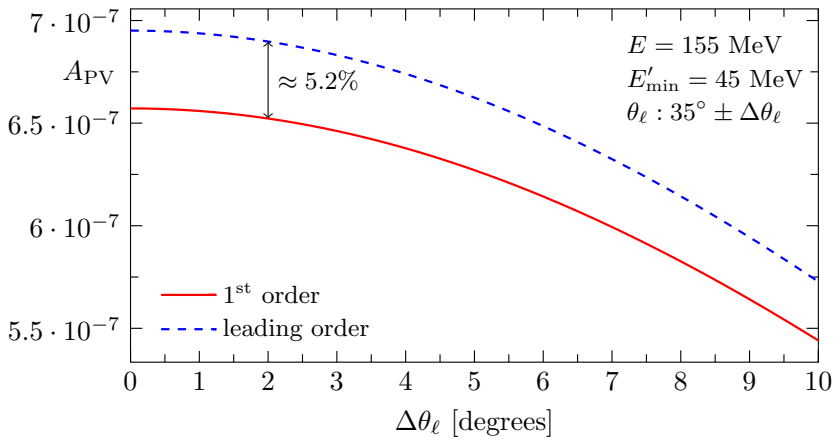

Figure 4.5: The parity violating asymmetry A_{PV} at leading order and including $\mathcal{O}(\alpha)$ QED corrections. Kinematic variables are again chosen as relevant for the Mainz P2 experiment. The asymmetry is shown as a function of the scattering angle acceptance $\Delta\theta_l$, i.e. cross sections are integrated over the electron scattering angle in the range $35^\circ - \Delta\theta_l \leq \theta_l \leq 35^\circ + \Delta\theta_l$.

between the leading order asymmetry and the one in which we include first order QED corrections is of the same size of the shift in Q^2, similar to the electron-proton asymmetry which was studied in Sec. 3.4. In this figure the asymmetry is plotted as a function of detector angle acceptance, from which we can also see that an important effect is given also by the separate integrations of the unpolarized and polarized cross sections over the scattering angle.

We conclude this section by noting that the effect from leptonic radiation is about 5% for the P2 experiment, similar with the effect in electron proton scattering. Therefore it is important to combine this correction with other order-α effects, like Coulomb distortions which were calculated in Ref. [103].

Chapter 5

POLARES — an event generator for polarized electron-proton scattering

5.1 Introduction

POLARES is a program for elastic electron-proton scattering with longitudinally polarized electron beams. It includes QED radiative corrections at first and second order in perturbation theory for the polarized, as well as for the unpolarized incident leptons. It can be used as an integrator to calculate cross sections and asymmetries for given kinematic conditions, as well as an event generator. The theory background was described in chapters 2 and 3. These chapters may also be consulted for more details, e.g. concerning the definition of kinematic variables, or of tests which have been performed to check the performance of the program. For tests concerning the event generator see sec. 5.4. POLARES is build as a library with C++ code. For the Monte Carlo integration it uses the Cuba library [63]. The Cuba library is contained in the POLARES package and doesn't need to be separately installed. A reference manual *refman.pdf* created by doxygen can also be found in the distribution, together with the *html* version. The manual with the instructions of how to install and use the the program can be found in App. H. The distribution can be found online at `https://github.com/razvanbucoveanu/POLARES`.

5.2 Description of the integrator

The integrals that usually appear in our calculations are multi-dimensional and the integrands are usually lengthy expressions that span many lines of code. For this reason, in order to calculate these integrals, we need to use a Monte Carlo (MC) approach.

The idea of MC integration (see [107] for more details) is to replace an integral (for illustration purposes we choose a 1-dimensional integral)

$$I = \int_0^1 f(x)\mathrm{d}x, \tag{5.1}$$

by an MC estimator defined as

$$I \approx \langle I \rangle = \frac{1}{N}\sum_{i=0}^{N} f(x_i),$$

where x_i is a random number uniformly distributed between 0 and 1 and N the number of points that are being sampled. As $N \longrightarrow \infty$ the MC estimator $\langle I \rangle$ converges to the value of I, i.e. $\lim_{N\to\infty} \langle I \rangle = I$. The error of the MC estimator is given by

$$\delta\langle I \rangle = \frac{\sigma}{\sqrt{N}}, \tag{5.2}$$

where the variance σ^2 can be estimated using

$$\sigma^2 = \frac{1}{N} \sum_{i=0}^{N} \left(f(x_i) - \langle I \rangle\right)^2 . \tag{5.3}$$

This method works well for uniform functions. However, for more complicated functions with high peaks, as the bremsstrahlung cross sections, this "naive" MC approach won't provide us with an accurate result. Since the error of the calculation is proportional to the variance of the result, we need to find a way to reduce the variance. The advantage of using the Cuba package for the numerical integration is that it includes different algorithms that can achieve this goal using different approaches. All algorithms use adaptive methods in order to reduce the variance, except Cuhre, which is a deterministic algorithm. The efficiency of Cuhre drops considerably with the number of dimensions however. One of these approaches, that is implemented in the Vegas algorithm (see Ref. [108] and Ref. [109] for a new version called Vegas+), is called importance sampling. This method changes the way we choose x_i such that more points are sampled where the contribution of the integrand is greater. Introducing a new function $g(x)$ we transform our integral I as

$$I = \int_0^1 \frac{f(x)}{g(x)} \mathrm{d}G(x), \tag{5.4}$$

where

$$G(x) = \int_0^x g(y)\mathrm{d}y. \tag{5.5}$$

Restricting g to be a positively-valued function, G(x) becomes a distribution function. Then, by sampling points from the distribution $G(x)$, the MC estimator becomes

$$\langle I \rangle = \frac{1}{N} \sum_{1}^{N} \frac{f(G^{-1}(r_i))}{g(G^{-1}(r_i))}, \tag{5.6}$$

where r_i is a random number uniformly distributed between 0 and 1. The variance of this MC estimator is given by

$$\sigma^2 = \frac{1}{N} \sum_{i=1}^{N} \frac{f^2(x_i)}{g^2(x_i)} - \left[\sum_{j=1}^{N} \frac{f(x_i)}{g(x_i)}\right]^2 , \tag{5.7}$$

which can be reduce by making an appropriate choice for $g(x)$ such that more points are generated where the contribution of the functions that is integrated is greater. This method can then be used to accurately integrate even functions with high peaks like the bremsstrahlung cross-sections.

Another algorithm that is included in the Cuba package is called Suave. Suave uses Vegas-like importance sampling combined with a globally adaptive subdivision strategy (see

Algorithm	Vegas	Suave	Cuhre
$\sigma^{(1)}_{1h\gamma}$ (nb)	4291.3 ± 0.9 (64 s)	4290.3 ± 0.8 (89 s)	4290.2 ± 97.3 (58 s)
$\sigma^{(2)}_{2h\gamma}$ (nb)	152.17 ± 0.04 (828 s)	151.91 ± 0.06 (978 s)	143.75 ± 97.5 (1975 s)

Table 5.1: Comparison of integration time required for different algorithms that are implemented in the Cuba package. We do the integration for P2 kinematics, i.e. $E = 155$ MeV, $\theta_\ell = 35^\circ \pm 10^\circ$ and $E' = 45$ MeV with the cut-off $\Delta = 10$ MeV. The integration is performed with $2 \cdot 10^8$ evaluations on a i7-7700 CPU @ 3.60 GHz and 16 GB of RAM memory, by using all available cores. For the Vegas algorithm we performed beforehand a "training" run with 10^8 evaluations by using the grid.

Ref. [110] for more details). Although Suave appears to have smaller uncertainties and reach convergence faster, a big disadvantage of this algorithm is that it uses the computer memory during the integration and the memory cost can be quite high if one requires a big number of evaluation to obtain an accurate result. For example, for 2×10^8 evaluations Suave needs approximately 15 GB of RAM memory. In Fig. 2.21 we showed a comparison between the two algorithms at different number of evaluations for the first order bremsstrahlung. As can be seen from this figure, at first order, 10^7 evaluations are enough for the numerical integration to reach convergence and Vegas and Suave agree very well, within the uncertainties, such that they can be used interchangeably. However, at second order, as can be seen from Fig. 2.22 and Fig. 2.23 a higher number of evaluations are required to reach convergence, typically more than 2×10^8, such that Suave cannot compete anymore with Vegas, which is not limited by the available RAM memory. A further advantage of the Vegas algorithm over Suave is that it uses a grid that can be stored and is refined after each integration. Using the grid allows us to use Vegas also as an event generator (see next section for more details).

5.3 Description of the event generator

The event generator consists of two steps. In the first step the program performs an initialization, in which the integrator, described in the previous section, is used to calculate the total cross section and to train the Vegas grid which will be used in the second step. The initialization is done using the `initialization()` function described in the manual (see App. H). After the initialization is finished the user can generate events using the `events()` function as is described in the manual. This function generates events by using the Vegas algorithm as a random number generator, but with numbers that are generated according to the previously trained grid. When using multiple threads the number of the child process has to be added to the seed using the `set_child_process(const int child_process)` function, on order to get different random numbers for each thread.

Schematically, a total cross section calculated by the program in the first step has the form

$$\sigma_{\text{tot}} = \int \mathrm{d}^n v f(\vec{v}), \tag{5.8}$$

where $\vec{v} = (v_1, \cdots, v_n)$ is a set of kinematic variables and $f(\vec{v}) = \mathrm{d}^n\sigma/\mathrm{d}v^n$. In the next step we

map the set of kinematic variables to a new set as

$$\vec{v} \longrightarrow \vec{x}(\vec{v}). \tag{5.9}$$

With the new set of variables the cross section is given by

$$\sigma_{\text{tot}} = \int \mathrm{d}^n x \omega(\vec{x}), \tag{5.10}$$

and we choose these new variables such that $\omega(\vec{x})$ is flat. The Vegas algorithm obtains $\omega(\vec{x})$ by using the method of importance sampling described in the previous section. Since the Vegas algorithm performs a MC integration, the cross section will be approximated by

$$\sigma_{\text{tot}} \approx \frac{1}{N} \sum_{i=1}^{N} \omega(\vec{x}_i) = W, \tag{5.11}$$

where $\omega(\vec{x}_i) \equiv \omega_i$ is called weight, while $\omega(\vec{x}_i)/W$ is called the average weight. Every event that is generated in the second step with the `events()` function comes therefore with an associated weight denoted by ω_i.

Usually we need to apply additional cuts to the total cross section σ_{tot}. This can be done by using θ functions in the integration, such that the new cross section to which the cuts were applied is given by

$$\sigma_i \equiv \Delta\sigma(y_i) = \int \mathrm{d}^n v f(\vec{v}) \Theta(y_i), \tag{5.12}$$

where $\Theta(y_i) = \theta(y(\vec{v}) - y_i)\theta(y_i + \Delta y - y(\vec{v}))$. These cuts can be applied also to the event generator, by generating events in a given bin defined by these cuts. For a given bin i, the cross section σ_i can then be approximated by

$$\sigma_i \approx \frac{1}{N} \sum_{i=1}^{N} \omega(\vec{x}_i) \Theta(y_i) \equiv W_i. \tag{5.13}$$

5.4 Results and tests of the event generator

In the previous section we discussed the possibility of applying certain cuts to the integration, such that instead of calculating a total cross section $\sigma = \sigma_{\text{tot}}$, we calculate a cross section σ_i for which we restrict the integration over the phase-space in a given interval. We saw that the cross section with these cuts σ_i can be obtained in two ways. One way is to apply the given cuts directly to the integration, while another way is to generate events in a bin i defined by these cuts, according to the initialized grid, which is part of the Vegas algorithm. By calculating the ratio, σ_i/σ, we find a distribution that shows the relative contribution of the different cross sections σ_i. Such a distribution is shown in Fig. 5.1, where the total cross section is given in this case by the first order bremsstrahlung cross section, $\sigma \equiv \sigma^{(1)}_{1h\gamma}$, to which the usual cuts for the P2 experiment are applied, while the cross sections σ_i's are obtained with the same P2 cuts and additionally cuts are applied to the emitted photon polar angle as $i < \theta_\gamma < i + 2^\circ$, where i takes values from 0° to 48° in steps of 2°. In this plot two peaks are visible, called collinear peaks, for initial state and final state radiation, respectively. For a discussion of these collinear peaks see Sec. **??**.

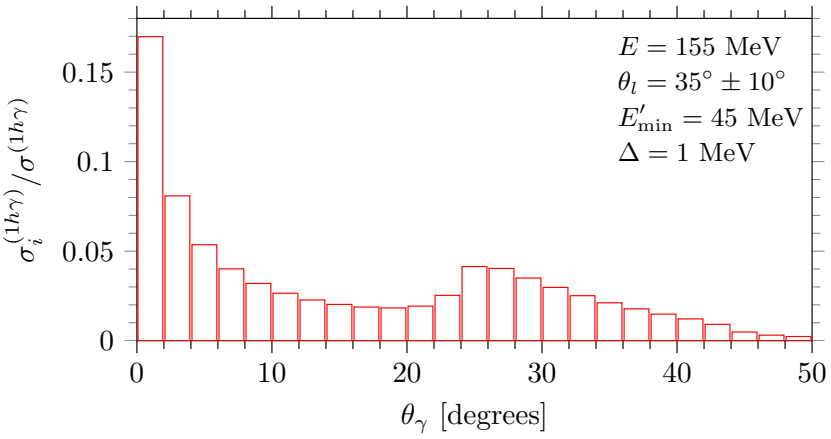

Figure 5.1: Histogram showing the distribution of the cross section σ_i, calculated with the integrator, relative to the total cross section σ. In this case σ is given by the first order bremsstrahlung cross section $\sigma^{(1)}_{1h\gamma}$. We used the kinematics that are relevant for the P2 experiment.

As was explained in the previous section, the value of the cross section in each bin defined by the applied cuts, can be approximated by the sum of all generated event weights, W_i, in that particular bin. Therefore, we expect that the distribution σ_i/σ obtained using the integrator, described in Sec. 5.2 can be approximated by the ratio of the weights W_i/W obtained with the event generator, described in Sec. 5.3. A comparison of these two ratios can be used as a test of the weights produced by the event generator, in order to make sure that the results obtained by the integrator are consistent with the results obtained by the event generator. The key here is that with the Vegas algorithm it is possible to store the grid which can be used later to generate events. With this test we showed that the grid can indeed reproduce the correct

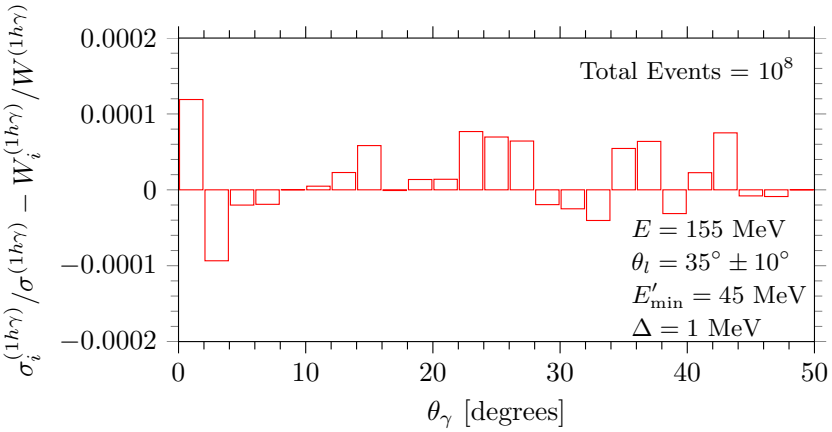

Figure 5.2: This figure shows the comparison between the ratio of the cross sections σ_i/σ for first order bremsstrahlung, obtained with the integrator, and the distribution of the event weights W_i/W, obtained with the event generator. The number of events that was used is 10^8. We used the kinematics that are relevant for the P2 experiment.

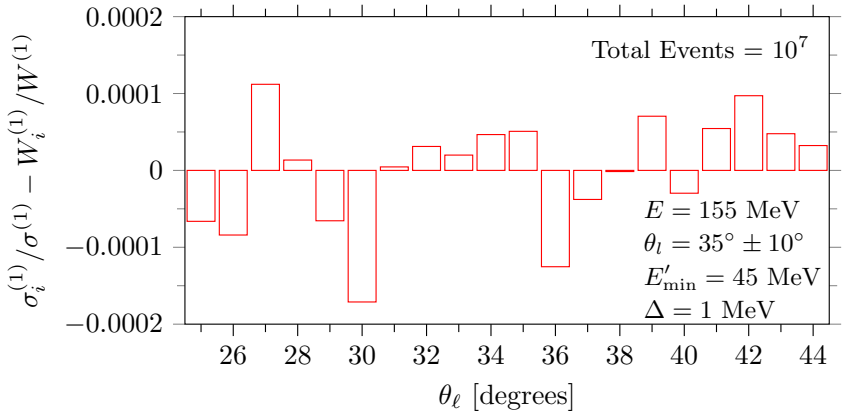

Figure 5.3: Histogram showing the comparison between the ratio of the first order cross sections $\sigma_i^{(1)}/\sigma^{(1)}$ obtained with the integrator, and the distribution of the event weights $W_i^{(1)}/W^{(1)}$, obtained with the event generator. The number of events that was used is 10^7. We used the kinematics that are relevant for the P2 experiment.

weights, that are consistent with the results of the integrator. The comparison $\sigma_i/\sigma - W_i/W$ is shown in Fig. 5.2, where we find a very good agreement of the two distributions, at the level of 10^{-4}, with random fluctuations, which lay inside in the statistical errors predicted by the Vegas algorithm. This result tells us that the event generator produces the correct weights ω_i, such that the averaged sum over these weights on a given bin is consistent with the result obtained with the integrator.

Using the same procedure, we can test the results of the event generator for the total cross sections with first and second order corrections. These tests are shown in Figs. 5.3 and 5.4. In the first figure, the cross section σ is given by the cross section with first order corrections $\sigma^{(0+1)}$ to which the P2 cuts are applied. For the cross sections σ_i we apply additionally a cut

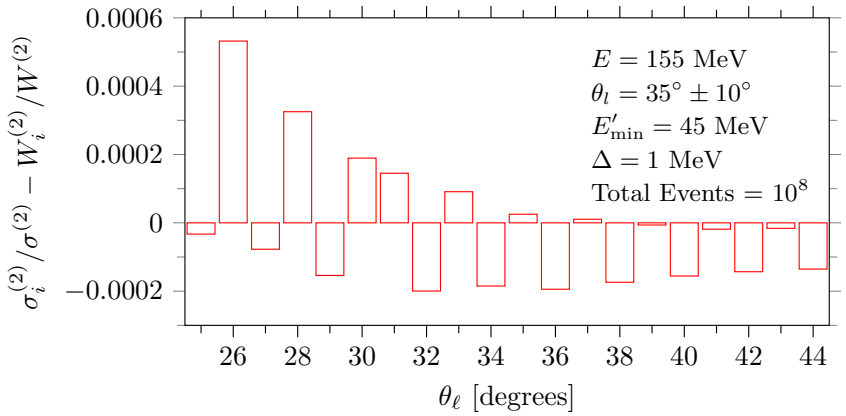

Figure 5.4: Figure showing the comparison between the ratio of the second order cross sections $\sigma_i^{(2)}/\sigma^{(2)}$ obtained with the integrator, and the distribution of the events weights $W_i^{(2)}/W^{(2)}$, obtained with the event generator. The number of events that was used is 10^8. We used the kinematics that are relevant for the P2 experiment.

on the scattering angle $i < \theta_\ell < i + 1^\circ$, where i takes values from 25° to 44°, in steps of 1°. Comparing the ratio σ_i/σ to the weights ratio W_i/W obtained with the event generator we find a good agreement with small fluctuations of the order of 10^{-4}, which tells us that the two methods are consistent and that the event generator performs well, within the numerical uncertainties of the Monte Carlo integration. The same comparison is done for the second figure, except that the total cross section σ is now given by the cross section with second order corrections $\sigma^{(0+1+2)}$. Although the agreement is a bit worse in this case, due to the higher uncertainties of the second order calculation, the fluctuations are still at the level of 10^{-4} and lie within the uncertainties of the numerical evaluation.

Chapter 6

Conclusions

In this work we have calculated leptonic QED corrections for elastic unpolarized and polarized lepton nucleon scattering at first and second order. This includes one- and two-loop QED virtual corrections and one and two photon real radiation.

In our study of numerical results, that were mostly done using the kinematics of the future P2 experiment in Mainz, we showed that a careful analysis of radiative correction is needed, that takes into account the experimental details which restricts the phase space for photon radiation. For this reason we have implemented these corrections in a Monte Carlo simulation called POLARES which is available on GitHub.

We have used various ways to test our results in Secs. 2.5 and and 3.4. As seen in Sec. 2.6 second-order corrections are generally small, but they become important for measurements at the per mill level. In Sec. 3.4 we showed that photon radiation at first order leads to a shift in the measured Q^2 of about 5% for P2 kinematics. We also showed that the effect of second order radiation to the shift in Q^2 is negligible, since this is only a kinematical effect given by the change in the scattered leptons energy. The P2 experiment plans to extract the weak charge of the proton by measuring the parity violating asymmtry between electron with positive and negative helicities. Since the parity violating asymmetry is proportional to Q^2 it becomes very important to have available a careful Monte Carlo treatment of QED radiative corrections. This goal was fulfilled with the implementation of our calculations in the POLARES library, that can be easily combined with the simulation of the P2 experiment.

At first order we have included also known treatments of hadronic corrections for the proton lines and we have presented a calculation of polarized and unpolarized lepton carbon scattering. The hadronic corrections, except for the two photon exchange correction, have a negligible effect. However, it is important to have a well defined separation of corrections that are contained in the effective nucleon form factors from the corrections that are subtracted during data analysis.

Appendix A

Cross-sections for $ep \longrightarrow ep$ and $ep \longrightarrow ep\gamma$

The matrix element squared for non-radiative ep scattering, averaged and summed over the spin degrees of freedom in the initial and final states, can be given in a compact form using the following form factor combinations:

$$G \equiv -2Q^2 \left(F_1^p + F_2^p\right)^2 , \qquad H \equiv 4 \left(F_1^p\right)^2 + \frac{Q^2}{M^2} \left(F_2^p\right)^2 . \tag{A.1}$$

We find

$$\frac{\mathrm{d}\sigma^{(0)}}{\mathrm{d}Q^2} = \frac{\overline{|\mathcal{M}_{\mathrm{Born}}|^2}}{16\pi \left[(s - m_\ell^2 - M^2)^2 - m_\ell^2 M^2\right]} \tag{A.2}$$

with

$$\overline{|\mathcal{M}_{\mathrm{Born}}|^2} = \frac{(4\pi\alpha)^2}{Q^4} \left\{ G(2m_\ell^2 - Q^2) - H \left[M^2 Q^2 + \left(s - m_\ell^2 - M^2\right)\left(Q^2 - s + m_\ell^2 + M^2\right)\right] \right\} , \tag{A.3}$$

and $s = (l + p)^2$. The expression of the cross section for the process $ep \longrightarrow ep\gamma$ was given in Eq. 2.62. For the matrix element squared of the radiative process with one additional photon, it is convenient to introduce also the variables $S = 2l \cdot p$ and $U = -2l' \cdot p$. Using a partial fractioning decomposition, to separate initial state and final state contributions and the interference between the two, we find for the matrix element squared for $ep \longrightarrow ep\gamma$, averaged and summed over initial and final state spin degrees of freedom the following expression:

$$
\begin{aligned}
\overline{\left|\mathcal{M}_{1\gamma}^{\ell}\right|^2} =& \frac{m_\ell^2\left[G(Q^2-2m_\ell^2)+H\left(M^2Q^2+U(Q^2-U)\right)\right]}{lk^2} \\
&+\frac{G(4m_\ell^2-Q_\ell^2-Q^2)-H\left(M^2(Q_\ell^2+Q^2)+Q^2S\right)}{lk} \\
&+\frac{4m_\ell^2\left[G(Q^2-2m_\ell^2)+H\left(M^2Q^2+S(Q^2-S)\right)\right]}{(2lk+Q_\ell^2-Q^2)^2} \\
&+\frac{2\left[G(-4m_\ell^2+Q_\ell^2+Q^2)+H\left(M^2(Q_\ell^2+Q^2)+Q^2U\right)\right]}{(2lk+Q_\ell^2-Q^2)} \\
&+\frac{G(8m_\ell^4-2Q^4)-H\left[2m_\ell^2\left(2M^2Q^2+Q^4-Q^2(S+U)+2SU\right)\right]}{lk(2lk+Q_\ell^2-Q^2)} \\
&-\frac{HQ^2\left(2M^2Q^2+Q^2(S+U)-S^2-U^2\right)}{lk(2lk+Q_\ell^2-Q^2)}-4(G+HM^2).
\end{aligned}
\tag{A.4}
$$

Appendix B

Renormalization and Regularization

A well known aspect of QFT is that it involves divergent quantities that have to be regularized. The infinities arise in fact because QFT was constructed as an idealized mathematical theory, which assumes infinitely extended fields (from where the infra-red (IR) divergence comes from) with infinite spatial resolution (that gives the ultra-violet (UV) divergence, see Ref. [111] for more details). The situation is somehow similar with what we know from electrostatics (see Ref. [112]) in the calculation of the electric field from an infinite line of charge for example. To get a meaningful, physical result for the electric field in this case we need to "regularize" the potential, for example by placing a cut-off on the length of the wire. So absorbing infinities in QFT is a mathematical trick from which we can obtain, from our idealized mathematical formulation, physical quantities that can be measured in a real experiment. The mechanism that makes this happen in QFT is called renormalization and it involves the absorption of IR and UV divergences.

In QED, the IR divergences originate from the coupling of a real photon with two on-shell lepton lines. In order to regularize these type of divergences we introduce a vanishing photon mass $\lambda \longrightarrow 0$. The calculation with a photon mass regulator gives rise to IR divergent terms that typically appear in the calculation of soft-photon radiation and vertex corrections. By including both soft-photon radiation and vertex corrections the IR divergent terms exactly cancel at the level of the cross-section. The other type of divergences that we encounter in our calculations are the UV divergences, which originate in virtual corrections involving loop diagrams. In order to regularize this type of divergences the dimensional regularization method (see Ref. [113] and Ref. [112]) was used, in which the calculation is done in an arbitrary dimension D. Such a regularization results in terms like $1/\epsilon_{\text{UV}}$, with $\epsilon_{\text{UV}} = D-4$, which becomes divergent for $D = 4$. The advantage of this type of regularization (see Ref. [114]), compared for example with a cut-off regularization, is that it automatically preserves symmetries, which is important for making the theory gauge invariant. However, the disadvantage of this type of regularization is that it forces us to introduce an auxiliary unphysical scale factor μ in order to keep the integral dimensionless. Dimensional regularization can be, of course, done also in the case of IR divergences. At one-loop order (NLO) we can switch between the two regularization schemes with the following replacement:

$$\ln\left(\frac{\lambda^2}{m^2}\right) \leftrightarrow \Delta_\epsilon, \tag{B.1}$$

where Δ_ϵ is defined as

$$\Delta_\epsilon = \frac{1}{\epsilon_{\rm IR}} - \gamma_E + \ln(4\pi), \tag{B.2}$$

with D the number of dimensions and γ_E is the Euler constant. Here $\epsilon_{\rm IR}$ is the singularity that corresponds in this case to the IR divergence. However, for reasons of simplicity we have used for the IR divergences the cut-off scheme.

The bare quantities, as the mass, charge and wave-function, that enter the Lagrangian contain the UV divergent terms that are left after regularization. These terms are removed by adding a counter-term Lagrangian, a process which is called renormalization. This subtraction can be done in different ways. The method which we used in this work, which is suitable for QED and for low energies is called the on-shell renormalization scheme.

The renormalized QED Lagrangian (see for example Ref. [42]) in this prescription is then given by

$$\mathcal{L}^R = \mathcal{L}^B - \mathcal{L}^{CT} = \bar{\psi}(i\gamma^\mu\partial_\mu - m)\psi - \frac{1}{4}F_{\mu\nu}F^{\mu\nu} - e\bar{\psi}\gamma^\mu\psi A_\mu, \tag{B.3}$$

where $\mathcal{L}^B$ is the bare Lagrangian and $\mathcal{L}^{CT}$ the counter-term Lagrangian that takes the form

$$\mathcal{L}^{CT} = (Z_2 - 1)\bar{\psi}i\gamma^\mu\partial_\mu\psi - (Z_2Z_m - 1)\bar{\psi}m\psi - (Z_3 - 1)\frac{1}{4}F_{\mu\nu}F^{\mu\nu} - (Z_1 - 1)e\bar{\psi}\gamma^\mu\psi A_\mu. \tag{B.4}$$

The counter-term renormalization constants are related to the renormalization constants derived in Sec. 2.2 by

$$\begin{aligned} Z_1 &= 1 + \delta Z_1, \\ Z_2 &= 1 + \delta Z_2, \\ Z_3 &= 1 + \delta Z_3, \\ \delta_m &= (1 - Z_m)Z_2 m. \end{aligned}$$

In the on-shell scheme we require, for example in the case of the lepton self-energy, that the pole of the propagator S corresponds to the physical mass that is being measured in an experiment (hence the name on-shell renormalization). The expressions of the renormalization constants for the lepton self-energy were found in Sec. 2.2 by requiring that the propagator S has a pole at $\not{l} - m_\ell = 0$ with residue 1. From this condition we found the expressions for the counter-terms δZ_2 and δ_m that were given in Eq. 2.30.

In the case of the vertex correction we can find the renormalization constant by requiring that in the limit $Q^2 \longrightarrow 0$ we recover the tree-level vertex. This condition leads to the expression of δZ_1 given in Eq. 2.42. As was shown in this section, as a consequence of the Ward identity, δZ_1 is the same with δZ_2.

Finally, the renormalized vacuum polarization is obtained by recovering the experimental value of the electric charge in the limit $q \longrightarrow 0$ of Coulomb scattering. This condition leads to the expression of δZ_3 given in Eq. 2.77.

It can be shown that the counter-term Lagrangian, which contains the renormalization constants determined at NLO, does in fact remove the UV divergences to all orders. The algorithm that is most commonly used to show that is the BPHZ algorithm (see for example Ref. [114]).

Appendix C

Form factors parametrizations

C.1 Proton Form Factors parametrization

We describe here briefly two parametrizations of the Sachs form factors defined in Sec. 2.1 that are included in our program. The first one, called "polynomial × dipole" (see Ref. [30]), is an extension of the dipole parametrization, which is combined with a polynomial of Q^2. It has the following form:

$$G^{E,M}_{\text{polynomial}\times\text{dipole}}(Q^2) = G_D(Q^2) \times \left(1 + \sum_{i=1}^{8} a_i^{E,M} Q^{2\cdot i}\right), \tag{C.1}$$

where the parameters a_i^E and a_i^M are given in table (C.1).

i	a_i^E	a_i^M
1	−0.4980	0.2472
2	5.45925	−4.9123
3	−34.7281	29.7509
4	124.3173	−84.0430
5	−262.9808	129.3256
6	329.1395	−111.1068
7	−227.3306	49.9753
8	66.6980	−9.1659

Table C.1: Polynomial × dipole parameters. The values can be found in Ref. [115], pp. 181.

The second parametrization presented here was derived by Friedrich and Walcher [116], who used the *ansatz* that the form factors are composed of a smooth part, which is identical to a double dipole description given by

$$G_s(Q^2) = s_0 \left(1 + \frac{Q^2}{s_1}\right)^{-2} + (1 - s_0)\left(1 + \frac{Q^2}{s_2}\right)^{-2}, \tag{C.2}$$

and a bump contribution, which consists of a Gaussian in Q^2 with an amplitude s_b at position Q_b and width σ_b. The bump contribution can be described therefore by

$$G_b(Q^2) = e^{-\frac{1}{2}\left(\frac{Q-Q_b}{\sigma_b}\right)^2} + e^{-\frac{1}{2}\left(\frac{Q+Q_b}{\sigma_b}\right)^2}. \tag{C.3}$$

By normalizing the bump contribution, i.e. by multiplying with Q^2, to be consistent with the smooth part, we get the complete model as

$$G^{E,M}_{\text{Friedrich-Walcher}}(Q^2) = G_s(Q^2, s^{E,M}_{0,1,3}) + s^{E,M}_b \cdot Q^2 \cdot G_b(Q^2, Q^{E,M}_b, \sigma^{E,M}_b), \tag{C.4}$$

where the parameters are given in table (C.2). For more details see Ref. [115].

Parameter	G_E	G_M
s_0	13.13613	0.99377
s_1	0.67183	0.71253
s_2	0.67186	−2.93647
s_b	−0.18245	−0.05312
σ_b	0.00636	−0.39067
Q_b	0.00636	−0.39067

Table C.2: Friedrich-Walcher parameters. The values can be found in [115], pp. 182.

C.2 Neutron Form Factors parametrization

The electric form factor G^n_E can be parametrized by following the model of Galster [117]

$$G^n_E = \frac{A\tau}{1 + B\tau} G_D(Q^2), \tag{C.5}$$

where G_D and τ are defined in chapter 2.4. The parameters A and B are given with the following values: $A = 2.28409$ and $B = 4.41942$. The magnetic form factor of the neutron can be described by a polynomial model, described in Ref. [118], as

$$G^n_M(Q^2) = \sum_0^9 a^n_i Q^{2i}, \tag{C.6}$$

where the parameters a^n_i are given in table C.3.

i	a^n_i	i	a^n_i
0	−1.9147	5	27.52359
1	6.47767	6	−12.81713
2	−17.32918	7	3.63457
3	31.80021	8	−0.57277
4	−37.18707	9	0.03843

Table C.3: Parameters for the magnetic neutron form factor. The values can be found in Ref. [118].

C.3 Strangeness Proton Form Factors

The electric proton form factor that describes the contribution of the strange quarks can be again parametrized as a Galster model

$$G^s_E = \frac{A^s\tau}{1 + B^s\tau} G_D(Q^2), \tag{C.7}$$

where G_D and τ are defined in chapter 2.4. The parameters A^s and B^s are given with the following values: $A^s = 0.32267$ and $B^s = 4.686$. The magnetic form factor can be parametrized with the help of a model determined by Young [119]

$$G_M^s = 0.044 + 0.93 \cdot Q^2. \tag{C.8}$$

C.4 ^{12}C form factors

The ^{12}C form factor can be described using a symmetrized Fermi function (see Ref. [104]) as

$$F_{\text{ch}} = \frac{3}{qc\Big((qc)^2 + (\pi qa)^2\Big)} \left(\frac{\pi qa}{\sinh(\pi qa)}\right) \left[\frac{\pi qa}{\tanh(\pi qa)} \sin(qc) - qc\cos(qc)\right], \tag{C.9}$$

where $q = \sqrt{Q^2}$, and a and c two constants given by

$$\begin{aligned} a &= 0.4506\text{fm}\,, \\ c &= 2.342\text{fm}\,. \end{aligned} \tag{C.10}$$

The weak form factor can be described by the same function. In absence of experimental data we take the parameters that describe this form factor identical as for the charge form factor, i.e $F_{\text{ch}} = F_{\text{wk}}$. In our program we allowed the possibility for a user defined form factor, that can be easily modified if new data becomes available.

Appendix D

Method for the calculation of one loop integrals and a list of scalar integrals

In order to perform the one-loop integrals we have used the `Mathematica` package `Feyncalc` [120]. We automatically used all the conventions defined in `Feyncalc` when performing the loop calculations. The most general one-loop integral can be written as

$$T_n^{\mu_1 \dots \mu_p} = \int \frac{\mathrm{d}^d k}{(2\pi)^d} \frac{k^{\mu_1} \cdots k^{\mu_p}}{D_0 D_1 \cdots D_{n-1}}, \tag{D.1}$$

where n are the number of external momenta p_i, d the number of dimensions and k_i the loop momenta. The quantities D_i are defined as:

$$D_i = (k + r_i)^2 - m_i^2 + i\epsilon\,, \tag{D.2}$$

where r_i are related to the external momenta as

$$\begin{aligned} r_j &= \sum_{i=1}^{j} p_i \quad \text{with } j = 1, \dots, n, \\ r_0 &= \sum_{i=1}^{n} p_i = 0 \end{aligned} \tag{D.3}$$

as indicated in Fig. D.1. The function `OneLoop` is used to perform the algebraic simplification of the amplitude into Passarino-Veltman integrals, while the function `PaVeReduce` is used

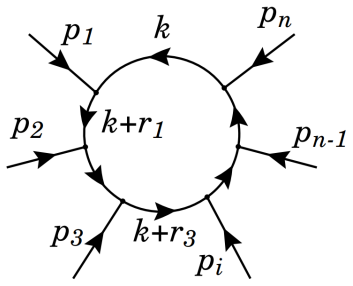

Figure D.1: Conventions for the loop momenta

to reduce the Passarino-Veltman integrals to the scalar integrals B_0, C_0 and D_0. Before using the `PaVeReduce` function, we perform the sum (or average) over spins and polarizations. For the calculation of the trace we used the function `Tr` from `Feyncalc` package. The final result is given in terms of scalar integrals and invariants. The scalar integrals, that have more complicated analytical expressions, were obtained by analytical continuation from the results given in Ref. [121]. The expressions for the simpler cases of the scalar integrals can be found in Ref. [122] and are given by

$$A_0(m^2) = m^2(\Delta_\epsilon + 1 - \log\frac{m^2}{\mu^2}), \tag{D.4}$$

$$B_0(0, m^2, m^2) = \Delta_\epsilon - \log\frac{m^2}{\mu^2}, \tag{D.5}$$

$$B_0(m^2, 0, m^2) = \Delta_\epsilon + 2 - \log\frac{m^2}{\mu^2}, \tag{D.6}$$

$$B_0(0, 0, m^2) = \Delta_\epsilon + 1 - \log\frac{m^2}{\mu^2}, \tag{D.7}$$

$$B_0(M^2, 0, m^2) = \begin{cases} \Delta_\epsilon + 2 + m^2\ln\left(\frac{m^2}{\mu^2}\right) - \frac{M^2}{M^2-m^2}\ln\left(\frac{M^2}{\mu^2}\right), & \text{for } M^2 > m^2, \\ \Delta_\epsilon + 2 + \frac{m^2-M^2}{M^2}\ln\left(1 - \frac{M^2}{\mu^2}\right), & \text{for } M^2 < m^2, \end{cases} \tag{D.8}$$

$$B_0(Q^2, m^2, m^2) = \Delta_\epsilon + 2 - v\ln\left(\frac{1}{x}\right) - \log\left(\frac{m^2}{\mu^2}\right), \tag{D.9}$$

$$B_0'(m^2, \lambda^2, m^2) = -\frac{1}{m^2} - \frac{1}{2m^2}\log\frac{\lambda^2}{m^2}, \tag{D.10}$$

$$B_0'(0, m^2, m^2) = \frac{1}{6m^2}, \tag{D.11}$$

$$C_0(m^2, m^2, 0, m^2, \lambda^2, m^2) = \frac{1}{2m^2}\log\frac{\lambda^2}{m^2}, \tag{D.12}$$

$$C_0(m^2, 0, M^2, 0, m^2, m^2) = -\frac{1}{m^2 - M^2}\left[\frac{\pi^2}{6} - \mathrm{Li}_2\left(\frac{M^2}{m^2}\right)\right], \tag{D.13}$$

$$C_0(m^2, m^2, Q^2, m^2, \lambda^2, m^2) = -\frac{1}{Q^2 v}\left[\ln\left(\frac{\lambda^2}{m^2}\right)\ln(x) - 2\mathrm{Li}_2(-x) - 2\ln(x)\ln(1+x) + \frac{\ln^2(x)}{2} - \frac{\pi^2}{6}\right], \tag{D.14}$$

$$C_0(0, Q_1^2, Q_2^2, m^2, m^2, m^2) = \frac{1}{2(Q_2^2 - Q_1^2)}\left[\ln^2(x_1) - \ln^2(x_2)\right], \tag{D.15}$$

where $Q_1 \neq Q_2$. In these expressions we have used he following notations:

$$\Delta_\epsilon \equiv \frac{2}{\epsilon} - \gamma_E + \log 4\pi,$$
$$v \equiv \sqrt{1 + \frac{4m^2}{Q^2}},$$
$$x \equiv \frac{v-1}{v+1},$$

with $Q^2 > 0$. For x_1 and x_2 Q^2 must be replaced with Q_1^2 and Q_2^2 respectively. Q_1^2 and Q_2^2 can represent different Q^2 definitions, e.g. the leptonic and the hadronic Q^2.

Appendix E

Phase-space parametrizations

E.1 One-photon bremsstrahlung, $ep \longrightarrow ep\gamma$

E.1.1 First parametrization

The phase-space for the radiative process was given in Eq. 2.63. After integrating out the final-state nucleon momentum to remove the δ-function for energy-momentum conservation, the phase space for $\ell p \longrightarrow \ell p \gamma$ is given by

$$\mathrm{d}^4\Gamma = \int \frac{1}{(2\pi)^5} \frac{\mathrm{d}^3 l'}{2E'} \frac{\mathrm{d}^3 k}{2E_\gamma} \delta\left[(l + p - l' - k)^2 - M^2\right] . \tag{E.1}$$

Using energies and angles as shown in Fig. 2.1 we write

$$\begin{aligned} \mathrm{d}^3 l' &= E' \, |\vec{l}\,'| \, \mathrm{d}\cos\theta_\ell \, \mathrm{d}\phi_\ell \, \mathrm{d}E' , \\ \mathrm{d}^3 k &= E_\gamma^2 \, \mathrm{d}\cos\theta_\gamma \, \mathrm{d}\phi_\gamma \, \mathrm{d}E_\gamma , \\ (l + p - l' - k)^2 - M^2 &= 2(A - B\cos\phi_\gamma) \end{aligned} \tag{E.2}$$

with

$$\begin{aligned} A =& M(E - E' - E_\gamma) - EE' + E'E_\gamma - EE_\gamma + |\vec{l}||\vec{l}\,'| \cos\theta_\ell \\ &+ |\vec{l}|E_\gamma \cos\theta_\gamma - E_\gamma |\vec{l}\,'| \cos\theta_\ell \cos\theta_\gamma + m_\ell^2 , \\ B =& E_\gamma |\vec{l}\,'| \sin\theta_\ell \sin\theta_\gamma . \end{aligned} \tag{E.3}$$

We can perform the integration over the azimuthal angle of the scattered lepton ϕ_ℓ and we find

$$\begin{aligned} \mathrm{d}\Gamma &= \int \frac{1}{4(2\pi)^4} E_\gamma |\vec{l}\,'| \, \mathrm{d}E' \, \mathrm{d}\cos\theta_\ell \, \mathrm{d}E_\gamma \, \mathrm{d}\cos\theta_\gamma \, \mathrm{d}\phi_\gamma \, \delta\left[2(A - B\cos\phi_\gamma)\right] \\ &= \frac{1}{8(2\pi)^4} \frac{\mathrm{d}E' \, \mathrm{d}\cos\theta_\ell \, \mathrm{d}E_\gamma \, \mathrm{d}\cos\theta_\gamma}{\sin\theta_\ell \sin\theta_\gamma \sin\phi_\gamma} \Theta\left(1 - \frac{A^2}{B^2}\right) , \end{aligned} \tag{E.4}$$

where $\sin\phi_\gamma = \sqrt{1 - A^2/B^2}$. Integration limits follow from the condition

$$\frac{A^2}{B^2} \leq 1 . \tag{E.5}$$

We find

$$
\begin{aligned}
& m_\ell < E' < E\,, \\
& \max\left(\frac{EE' - M(E-E') - m_\ell^2}{|\vec{l}||\vec{l}'|}, -1\right) < \cos\theta_\ell < 1\,, \\
& \frac{y}{a-x} < E_\gamma < -\frac{y}{a+x}\,, \\
& \frac{-F\sqrt{F^2+D^2-C^2} - DC}{D^2+F^2} < \cos\theta_\gamma < \frac{F\sqrt{F^2+D^2-C^2} - DC}{D^2+F^2}\,,
\end{aligned}
\tag{E.6}
$$

where we have used

$$
\begin{aligned}
C =& M(E - E' - E_\gamma) - EE' + E'E_\gamma - EE_\gamma + |\vec{l}||\vec{l}'|\cos\theta_\ell + m_\ell^2\,, \\
D =& E_\gamma(|\vec{l}| - |\vec{l}'|\cos\theta_\ell)\,, \\
F =& E_\gamma|\vec{l}'|\sin\theta_\ell\,, \\
a =& \sqrt{|\vec{l}|^2 + |\vec{l}'|^2 - 2|\vec{l}||\vec{l}'|\cos\theta_\ell}\,, \\
x =& E' - E - M\,, \\
y =& M(E - E') - EE' + |\vec{l}||\vec{l}'|\cos\theta_\ell + m_\ell^2\,.
\end{aligned}
$$

E.1.2 Second parametrization

An alternative choice is to fix the scattered electron's energy E' (see also [40]). From the equation

$$
(l + p - l' - k)^2 - M^2 = 0, \tag{E.7}
$$

we can express E' by solving the second order equation as

$$
E' = \frac{BC \pm A\sqrt{m_\ell^2(A^2 - B^2 + C^2)}}{A^2 - B^2}, \tag{E.8}
$$

where

$$
\begin{aligned}
A &= |\vec{l}|\cos\theta_\ell - E_\gamma\cos\psi, \\
B &= E + M - E_\gamma \\
C &= E_\gamma(E + M - |\vec{l}|\cos\theta_\gamma) - ME - m_\ell^2.
\end{aligned}
$$

The minus sign is in most cases the only physical solution. The plus sign can give a contribution only for a very large value of E_γ, close to the energy of the incident lepton E, and implicitly for very small values of E', which are typically much below a detector's threshold. The contribution from the plus sign in these cases is of the other of 10^{-10}, relative to the total cross section, and is much below the uncertainties of the numerical integration and therefore can be neglected.

Fixing E' the phase-space can then be expressed as

$$\mathrm{d}\Gamma = \frac{1}{4(2\pi)^4}\mathrm{d}E_\gamma \mathrm{d}\cos\theta_\ell \cos\theta_\gamma \mathrm{d}\phi_\gamma \frac{E_\gamma |\vec{l}'|^2}{\left|AE' - B|\vec{l}'|\right|}\Theta\left(m_\ell - E'\right)\Theta\left(E - E' - E_\gamma\right). \tag{E.9}$$

For the solution to be physical the value of E' have to satisfy the two Θ functions given in the previous equation. From $E' < E - E_\gamma$ we find that the photon energy has to satisfy

$$E_\gamma < \frac{M(E - m_\ell)}{M + E - |\vec{l}|\cos\theta_\gamma}.$$

The results obtained with the two phase-space parametrizations agree very well, within the uncertainties of the numerical integration, as can be seen also from Fig. 2.21. Although, in general, the second parametrization is faster than the first and can have smaller numerical uncertainties, the default choice, that was used also to obtain results, is the first parametrization. The reason for this choice is that for the first parametrization, since E' is one of the integration variables, it's possible to directly choose a limit for this energy, which is important for the P2 experiment. While for the second one E' can be only indirectly restricted after it was calculated as a function of the other variables, which can be inefficient and less numerical precise. If, on the other hand, one would like to set limits to ϕ_γ, then the use of the second parametrization would make more sense and it would be more efficient.

E.2 Two-photon bremsstrahlung, $ep \longrightarrow ep\gamma\gamma$

We use the same notation as shown in Fig. 2.1, but consider two photons in the final state, whose 4-momenta are denoted by k and k' with energies E_γ, E'_γ and angles θ_γ, θ'_γ, ϕ_γ, and ϕ'_γ, respectively. Using the δ function from energy-momentum conservation, the integration over the 4-particle phase space can be written as

$$\mathrm{d}^7\Gamma_{2\gamma} = \frac{E_\gamma E'_\gamma |\vec{l}'|}{16(2\pi)^7}\frac{\mathrm{d}E'\,\mathrm{d}\cos\theta_\ell\,\mathrm{d}E_\gamma\,\mathrm{d}E'_\gamma\,\mathrm{d}\cos\theta'_\gamma\,\mathrm{d}\phi'_\gamma\,\mathrm{d}\cos\theta_\gamma}{\left|\alpha_1\cos\phi_\gamma - \alpha_2\sin\phi_\gamma\right|} \tag{E.10}$$

where ϕ_γ can be expressed as a function of α_1, α_2 and α_3 by solving the equation

$$\alpha_1\sin\phi_\gamma + \alpha_2\cos\phi_\gamma = \alpha_3\,, \tag{E.11}$$

where

$$\begin{aligned}
\alpha_1 =& E_\gamma E'_\gamma \sin\theta_\gamma \sin\theta'_\gamma \sin\phi'_\gamma\,,\\
\alpha_2 =& |\vec{l}'|E_\gamma \sin\theta_\ell \sin\theta_\gamma + E_\gamma E'_\gamma \sin\theta_\gamma \sin\theta'_\gamma \cos\phi'_\gamma\,,\\
\alpha_3 =& m_\ell^2 + M(E - E' - E_\gamma - E'_\gamma) - E(E' + E_\gamma + E'_\gamma) + E'(E_\gamma + E'_\gamma) + |\vec{l}||\vec{l}'|\cos\theta_\ell\\
&+ |\vec{l}|E_\gamma\cos\theta_\gamma + |\vec{l}|E'_\gamma\cos\theta'_\gamma - |\vec{l}'|E'_\gamma(\sin\theta_\ell\sin\theta'_\gamma\cos\phi'_\gamma + \cos\theta_\ell\cos\theta'_\gamma)\\
&- |\vec{l}'|E_\gamma\cos\theta_\ell\cos\theta_\gamma - E_\gamma E'_\gamma\cos\theta_\gamma\cos\theta'_\gamma + E_\gamma E'_\gamma\,.
\end{aligned}$$

The solution of Eq. E.11 depends on the the signs of α_1 and α_2 and is expressed by

$$\phi_\gamma = \begin{cases} \arcsin \frac{\alpha_3}{\sqrt{\alpha_1^2+\alpha_2^2}} - \arctan \frac{\alpha_2}{\alpha_1} & \text{if } \alpha_1 > 0\,, \\ \arcsin \frac{\alpha_3}{\sqrt{\alpha_1^2+\alpha_2^2}} - \arctan \frac{\alpha_2}{\alpha_1} - \pi & \text{if } \alpha_1 < 0 \text{ and } \alpha_2 > 0\,, \\ \arcsin \frac{\alpha_3}{\sqrt{\alpha_1^2+\alpha_2^2}} - \arctan \frac{\alpha_2}{\alpha_1} + \pi & \text{if } \alpha_1 < 0 \text{ and } \alpha_2 < 0\,. \end{cases} \tag{E.12}$$

Integration limits for angles and energies follow from the condition that the arguments of the arcsin-functions in the expression for ϕ_γ in Eq. (E.12) have to be in the allowed range between −1 and +1. This is also our first condition and the most important one that has to be checked numerically and is given by

$$-1 \leq \frac{\alpha_3}{\sqrt{\alpha_1^2+\alpha_2^2}} \leq 1 \text{ (condition 0)}\,. \tag{E.13}$$

The required calculations that follow from this condition are straightforward, but tedious, and we write down only a few partial results in the following. From E.13 we find the following limits for θ_γ:

$$\frac{-\beta_2\beta_3 - \beta_1\sqrt{\beta}}{\beta_1^2+\beta_2^2} < \cos\theta_\gamma < \frac{-\beta_2\beta_3 + \beta_1\sqrt{\beta}}{\beta_1^2+\beta_2^2} \tag{E.14}$$

where

$$\begin{aligned} \beta_1 =& \sqrt{2E_\gamma^2|\vec{l}'|E'_\gamma \sin\theta_\ell \sin\theta'_\gamma \cos\phi'_\gamma + E_\gamma^2 E_\gamma'^2 \sin^2\theta'_\gamma + |\vec{l}'|^2 E_\gamma^2 \sin^2\theta_\ell}\,, \\ \beta_2 =& |\vec{l}|E_\gamma - |\vec{l}'|E_\gamma \cos\theta_\ell - E_\gamma E'_\gamma \cos\theta'_\gamma\,, \\ \beta_3 =& m_\ell^2 + M(E - E' - E_\gamma - E'_\gamma) - E(E' + E_\gamma + E'_\gamma) + E'(E_\gamma + E'_\gamma) + |\vec{l}||\vec{l}'|\cos\theta_\ell \\ & + |\vec{l}|E'_\gamma \cos\theta'_\gamma - |\vec{l}'|E'_\gamma(\sin\theta_\ell \sin\theta'_\gamma \cos\phi'_\gamma + \cos\theta_\ell \cos\theta'_\gamma) + E_\gamma E'_\gamma\,, \\ \beta =& \beta_1^2 + \beta_2^2 - \beta_3^2\,. \end{aligned}$$

Next we need to make sure that the square roots are real numbers. It is easy to see that the argument of β_1 is always positive. Therefore, the next condition that we find is given by

$$\beta \geq 0 \text{ (condition 1)}\,, \tag{E.15}$$

which we can use to determine the integration limits for ϕ'_γ as

$$\frac{E_\gamma^2 + \gamma_2 - E_\gamma\sqrt{\gamma}}{\gamma_1} < \cos\phi'_\gamma < \frac{E_\gamma^2 + \gamma_2 + E_\gamma\sqrt{\gamma}}{\gamma_1} \tag{E.16}$$

with

$$\gamma = 2\gamma_2 + \gamma_3 \tag{E.17}$$

and

$$\gamma_1 = |\vec{l}'|E'_\gamma \sin\theta_\ell \sin\theta'_\gamma\,, \tag{E.18}$$

$$\begin{aligned} \gamma_2 =& m_\ell^2 + M(E - E' - E_\gamma - E'_\gamma) - E(E' + E_\gamma + E'_\gamma) + E'(E_\gamma + E'_\gamma) \\ & + E_\gamma E'_\gamma + |\vec{l}||\vec{l}'|\cos\theta_\ell + E'_\gamma \cos\theta'_\gamma \left(|\vec{l}| - |\vec{l}'|\cos\theta_\ell\right)\,, \end{aligned} \tag{E.19}$$

$$\gamma_3 = |\vec{l}|^2 + |\vec{l}'|^2 + E_\gamma^2 + E_\gamma'^2 - 2E'_\gamma \cos\theta'_\gamma \left(|\vec{l}| - |\vec{l}'|\cos\theta_\ell\right) - 2|\vec{l}||\vec{l}'|\cos\theta_\ell\,. \tag{E.20}$$

For the square root to be real number we need the following condition

$$\gamma \geq 0 \text{ (condition 2)}, \tag{E.21}$$

which is always fulfilled provided that

$$E - E' - E_\gamma - E'_\gamma \geq 0\,. \tag{E.22}$$

It turns out that an explicit implementation of the kinematic limits given above in the numerical integration routine together with the partial fraction methods described in 2.4.4 is sufficient to render the efficiency of the Monte Carlo integration, which is defined by the number of accepted events at a level above 27 %. More specifically, condition 2, allows on average 86 % of events, while with condition 1, the allowed events drop considerably to 28 % and finally with condition 0 we get 27 % accepted events [1].

In our implementation of the numerical integration over the phase space we make sure that no kinematic limit is missed by reconstructing always complete events and checking the 4-momentum conservation.

[1] This test was perfomed with the Vegas algorithm with 10^9 evaluations.

Appendix F

Helicity projection operators

For the calculation of the polarized cross section we need to differentiate between electrons with positive and negative helicities. In order to achieve this we use helicity projection operators. We first define the spin four-vector (see Ref. [123]) as

$$\zeta^{\mu} = \frac{1}{m_{\ell}}(|\vec{l}|, E\hat{l}), \tag{F.1}$$

where $\vec{l}$ is the lepton 3-momentum, $\hat{l}$ its direction, E its energy and m_{ℓ} its mass, with the following properties

$$\zeta \cdot \zeta = -1 \quad \text{and} \quad \zeta \cdot l = 0. \tag{F.2}$$

With the help of the spin four-vector we can define the helicity projection operators for massive spin 1/2 particles as

$$u(l,\lambda)\bar{u}(l,\lambda) = \frac{1}{2}(1 + \lambda\gamma_5 \not{\zeta})(\not{l} + m_{\ell}), \tag{F.3}$$

where $\lambda = \pm 1$ for positive and negative helicities, respectively. The helicity spinors $u(l,\lambda)$ satisfy the Dirac equation and are eigenstates of $\gamma_5 \not{\zeta}$ with unit eigenvalue. In the ultrarelativistic limit, i.e. $E \gg m_{\ell}$, the spin four-vector reduces to $\zeta^{\mu} \longrightarrow l^{\mu}/m_{\ell}$ and we recover Eq. (3.2) in the low Q^2 limit. For $m_{\ell} \longrightarrow 0$ the helicity operators reduce to the chiral operators $(1 + \lambda\gamma_5)/2$.

Appendix G

Weak proton form factors

The weak proton Sachs form factors $G^Z_{E,M}$ can be related to the quark substructure of the proton by writing them as contributions from u, d and s quarks (see Ref. [124]). If the contribution from the heavy quarks (c, t and b) are neglected and each contribution of an individual quark is weighted by the appropriate quark charge (see Table 3.1), then the proton's electromagnetic and weak Sachs form factors become

$$\begin{aligned} G^\gamma_{E,M} =& \frac{2}{3} G^u_{E,M} - \frac{1}{3}\left(G^d_{E,M} + G^s_{E,M}\right), \\ G^Z_{E,M} =& \left(1 - \frac{8}{3}\sin^2\theta_W\right) G^u_{E,M} + \left(-1 + \frac{4}{3}\sin^2\theta_W\right)\left(G^d_{E,M} + G^s_{E,M}\right). \end{aligned} \tag{G.1}$$

Making the assumption of charge symmetry in the nucleon, which implies that $G^u_{E,M}$ and $G^d_{E,M}$ in the proton are simply interchanged in the neutron, we can write the Z^0 Sachs form factors in terms of the electromagnetic Sachs form factors of the proton (p) and neutron (n) and a contribution from the strange quarks as

$$G^Z_{E,M} = (1 - 4\sin^2\theta_W) G^{\gamma,p}_{E,M} - G^{\gamma,n}_{E,M} - G^s_{E,M}. \tag{G.2}$$

Some parametrizations for the neutron form factors and for the form factors of the strange quarks contribution can be found in App. C.2 and App. C.3. We note here that isospin violation, or charge symmetry breaking, invalidates the assumption that u-quark field is identical with the d-quark field in the neutron. The violation comes from mass difference and from electromagnetic effects. By using different theoretical models of the proton structure, the authors of Refs. [125], [126] and [127] all come to the conclusion that the contribution from isospin violation is of the order of 0.1%. The precision of the strange quark measurements would have to be better than this level, before charge symmetry breaking adds significant uncertainty to the determination.

The electroweak axial form factor of the nucleon can be similarly deconstructed to reveal the contribution of strange quarks, as described in Ref. [101].

Appendix H

Manual

H.1 Installation and general description

The code of the program can be found in this GitHub repository. The prerequisites for installing the POLARES library are a GNU C++ compiler that supports the C++11 standard (g++ version 1.6 or higher) and the GSL[1] library. The present version of POLARES was written and tested with GSL version 2.1 on Linux systems. The POLARES distribution comes in a coMessed tar archive *POLARES-x.y.tar.gz*, where *x.y* is the version number. Execute the usual sequence of commands to unpack and install the library:

```
gunzip -c POLARES-x.y.tar.gz | tar xvf -
cd POLARES-x.y
./configure
make
make install
make clean
```

This list of commands will install the library in the default path (*/usr/local*) which requires root permission. The `prefix`-option can be used to choose a different path:

```
./configure --prefix=/user/defined/path
```

In case the `gsl` library is not installed in the standard path it is possible to specify the path by:

```
./configure GSL_CONFIG_PATH=/path/to/folder/containing/gsl-config
```

or set the environment variable

[1] http://www.gnu.org/software/gsl/

```
  export GSL_CONFIG_PATH=/path/to/folder/containing/gsl-
config
```

If the POLARES library is not installed in the default path, one needs to set the environment variable

```
  export LD_LIBRARY_PATH=/user/defined/path/lib
```

so that the linker can find the shared library of the POLARES package.

The library contains a sub-folder called *examples*, in which few example programs with how to use the library are provided. The command `make examples` compiles all these example programs that are found in sub-folder *examples*. After running this command, if the compilation was successful, the user should be able to run any of the programs that were build in this folder. However, if the command `make clean` is executed the compilation of these programs will be deleted. This command can be of course omitted if the compilation of the example programs is not required.

H.2 General description

After installation the user can include *POLARES.h* into his or her own program and use the **`class`** `PES`, which is part of the **`namespace`** `POLARES` and contains all the necessary functions. An example of how this class can be used can be found in the file *examples/-main_example.cpp*. More examples with the functions from this class are found in the sub-folder *examples/*. In order to use the program, the user has to be careful specifying the paths to the source code and to the POLARES library. A sample makefile, called *Makefile_example*, can be found in the folder *examples*. Additionally, for the program to run, the working directory has to contain the folder named *share* which keeps additional input files, for example for the calculation of the hadronic part of the vacuum polarisation (see below).

The user can provide input to the program in a file, for which the default name is *POLARES.in*. The program looks for this file in the working directory. The name of the input file can be changed from the input class. The program will create also an output file with the same name as the input file and with the extension *.out*. A sample version of the input file comes with the distribution and contains all the possible input combinations.

In many cases, a complete specification of input data is not needed and default values defined in the library can be used. For this case, a basic input file, called *POLARES_basic.in*, is also provided and contains only the important input that a user requires to run the program. In addition to using a file to specify input options, one can also use the **`class`** `Input` in the main program, as described in the next section. However, input from the input file will overwrite input from the input class.

For complete functionality the data files *vp_Ignatov.dat*, *vp_Jeger.dat* and *vp_KNT18.dat* are also required to run the program. They contain tables needed for the calculation of the hadronic contribution to the vacuum polarization. The files are shipped with the distribution and can be found in the directory */user/defined/path/share/*.

Unless specified, all the energies and momenta are given in natural units of 1 GeV in the laboratory frame (see Sec. 2.1 for the definition of this reference frame). For convenience, the angles are given in degrees in the input, but in radians in the output.

H.3 How to use the library: description of the main functions

The POLARES **class** `PES` can be constructed explicitly by using

```
PES();
```

If values for parameters are defined in the input file they will overwrite the ones from **class** `Input`. A convenient way to start the calculations is by using the code

```
Input input;
// ...
// define input values as described below
// ...
PES my_pes_class;
my_pes_class.set_input(input);
my_pes_class.initialization();
```

and using functions of **class** `PES` to start event generation and analyze results. The most important public functions that can be found in **class** `PES` are:

- **void** `set_input(`**const** `Input& input);`

  This function is used to transfer values for input parameters defined in the main program to the **class** `PES`.

- **int** `initialization();`

  This function can be used to calculate total cross sections or asymmetries integrated over the phase space defined in the input. It is also needed to generate grids which are required for event generation. The output of this function is stored in two instances of the **class** `Output` (see below for a detailed description of the output):

  ```
  Output output;
  ```

  contains the actual results for total and partial cross sections, and

  ```
  Output errors;
  ```

  contains estimates of the numerical uncertainties of the results.

- **int** `sigma_diff_Omega_1(`**const double** `th1_deg);`

  This function calculates the differential cross section $d\sigma/d\Omega = d\sigma/(2\pi \sin\theta d\theta)$ and the corresponding asymmetries for a given scattering angle `th1_deg` (input value in degrees). The output is stored again in the objects `output` and `errors`. At next-to-leading order, this function performs an integration over the phase space for bremsstrahlung photons.

- **int** shiftQ2(**const double** thl_deg);

  This function calculates the average shift in Q^2 due to hard photon bremsstrahlung for a given scattering angle thl_deg (in degrees). The output is stored as in the case of the initialization in the objects output and errors.

- **int** events();

  This function generates events with a corresponding weight, which is stored in the final state class (see below). The function events() can be used after the grid initialization was completed successfully. Each call of this function generates one event and the user is free to choose the number of events to be generated. For each event the output is given in the object FS of the **class** Final_State (see below for a detailed description of its members).

- **bool** change_energy_initialization(**const double** E);

  With this function the user can change the energy of the incoming lepton beam after a first initialization. The input value for E is expected in units of GeV.

- **bool** change_energy_events(**const double** E);

  This function is useful in case the user wants to generate events for a range of energies. A sample program is provided in *examples/multiple_random_E_test.cpp*.

  change_energy_events returns **true** if the given energy is valid and the grid initialization was successful, **false** otherwise.

- **bool** set_child_process(**const int** child_process);

  This function must be used in case the user wants to generate events on multiple cores for creating different seeds for each child process.

H.4 Description of the input

All required input can be defined in the input file. A sample version with the name *POLARES.in* is contained in the distributed package. Each input item consists of a key word (possibly including spaces) and a value, separated by an equal sign, =. The order of input items in this file is arbitrary. Lines starting with # are comments. Passing the name of the input file to the program is done via **class** Input and giving this object as an argument to the function set_input. The variable in which the user can define the name of the input file is string input_file. For example, if the user wants to use the file *POLARES.in* as input the following code has to be used

```
Input input;
input.set_input("POLARES");
PES pes;
pes.set_input(input);
```

All the input can be inserted directly in **class** `Input`, which contains also all the default values, without the need of an input file. However, by providing the required values in the input file, the input from **class** `Input` is overwritten. Below we show a list of the variables contained in **class** `Input` with their corresponding names from the input file. All the flags can be accessed in **class** `Input` as `input.flag[input.name_of_flag]`, where `name_of_flag` is given below in square brackets after the corresponding name from the input file. For better readability the input file is structured in four sections as

1. `[General Input]`

   contains input required for the calculation of cross sections and asymmetries. Input given in this section is used for both the elastic process (including soft-photon and virtual corrections) and the radiative process with a hard photon in the final state.

2. `[E_gamma < Delta]`

   contains input required for the calculation of the non-radiative part of the cross section, including higher-order corrections.

3. `[E_gamma > Delta]`

   contains input required only for the radiative part with hard-photon emission.

4. `[Event Generator]`

   contains input required for the event generator.

The items contained in each section of the input file are the following (unless specified the default value for the flags is 0):

1. `[General Input]`

   - `Incident Lepton` [`lepton`] — a flag that specifies the type of lepton in the initial state. The options that are implemented in the current version are electron (0), positron (1), muon (2), anti-muon (3).
   - `Target Particle` [`target`] — a flag that specifies the type of target particle. The only options that are implemented in the current version are proton (0), carbon-12 (1) and electron (2). For carbon-12 only first order corrections are implemented.
   - `Incident Lepton Energy` [**double** `E`] — in units of GeV. The default value is 0.155 GeV.
   - `Polarization` [**double** `polarization`] — degree of the longitudinal polarization of the incident lepton beam ($-1 \leq P \leq 0$ for left-handed, $0 \leq P \leq 1$ for right-handed polarization). Default value is 1.
   - `Type of Cuts` [`cuts_born`] — a flag with which the user can choose to use cuts on the scattering angle θ_ℓ (0) or on Q^2 (1).
   - `theta_l min` [**double** `thl_min`] and `theta_l max` [**double** `thl_max`] — minimum and maximum values of the scattering angle in degrees. Default values are 25° and 45°.

- `Q^2 min` [**double** `Q2min`] and `Q^2 max` [**double** `Q2max`] — minimum and maximum values of Q^2 in GeV^2. Default values are 0.0044 GeV^2 and 0.0134 GeV^2.
- `Delta` [**double** `Delta`] — value of the photon energy cut-off in GeV to separate soft from hard photon radiation. Default value is 0.01 GeV.
- `Asymmetry` [`asymmetry`] — a flag which tells the initialization function whether to calculate (0) or not (1) the polarization-dependent part of the cross section and the resulting asymmetries. Default value is 1.
- `sin2thetaW` [**double** `sw2`] — value of the weak mixing angle, $\sin\theta_W^2(M_Z)$ in the $\bar{\text{MS}}$ scheme, where M_Z is the mass of the Z^0 boson. The default value is $\sin\theta_W^2(M_Z) = 0.23122$ (see the latest PDG review by J. Erler and A. Freitas [72]).
- LO [`LO`] — flag to suppress the calculation of the leading order (Born level) contribution to the cross section (for LO=0). The default, LO=1, is to include leading order.
- `Form Factors` [`form_factors`] — flag for the form factor parametrization of the proton. In the present version one can choose among the following options:
  - `Form Factors=0` — Simple dipole form factor with $M_D^2 = 0.71$ GeV^2 and the proton magnetic moment $\mu_p = 2.7928473$;
  - `Form Factors=1` — Dipole times polynomial taken from Bernauer's PhD thesis [115], pp. 181 (see also [30]);
  - `Form Factors=2` — Friedrich-Walcher parametrization [116];
  - `Form Factors=3` — Static limit, $G_E = 1$ and $G_M = \mu_p$;
  - `Form Factors=4` — User defined;
  - `Form Factors=5` — Symmetrized Fermi Form Factor for ^{12}C; (see Ref. [104]).
  - `Form Factors=6` — User defined form factor for ^{12}C.
- `Integration method` [`int_method`] — flag that specifies with witch algorithm is the integration over phase space performed. If the value is set to 0, the program uses Vegas Monte Carlo routine. This is required for event generation after initialization. Total cross sections can also be calculated with Suave (1) or with Cuhre (2). See the Cuba documentation [63] for details.
- `Maximum Number of Evaluations LO` [**int** `no_eval_LO`] — maximum number of evaluations of the integrand during the initialization for the leading order and elastic cross sections (default value is 10^7).
- `Maximum Number of Evaluations 1st` [**int** `no_eval_1st`] — maximum number of evaluations of the integrand during the initialization for the first order hard-photon bremsstrahlung (default value is 10^8).
- `Maximum Number of Evaluations gamma_loop` [**int** `no_eval_gamma_loop`] — maximum number of evaluations of the integrand during the initialization for one hard-photon bremsstrahlung combined with one-loop (default value is 10^8).
- `Maximum Number of Evaluations 2nd` [**int** `no_eval_2nd`] — maximum number of evaluations of the integrand during the initialization for the second order hard-photon bremsstrahlung (default value is 10^9).

- `Maximum Number of Evaluations 2nd sg finite` [**int** `no_eval_2nd_add`] — maximum number of evaluations of the integrand during the initialization for the finite part of one hard-photon and one soft-photon correction (default value is 10^8).
- `Minimum Number of Evaluations` [**int** `no_min_eval`] — minimum number of evaluations of the integrand during the initialization (default value is 10^5).
- `Relative Accuracy` [**double** `epsrel`] — required relative accuracy of the numerical integration (default value is 0).
- `Number of cores` [**int** `no_cores`] — number of cores to be used by the integration routines (default value is 4).
- `Echo input` [`echo_input`] — a flag to tell the initialization function whether to print the given input.
- `Output` [**char** `output_file`] — if any name is chosen here, a summary of input parameters and results of the numerical integration is written to the file *name-given.out*. If 0 is inserted the program doesn't create an output file.
- `Integration Output level` [`int_output`] — flag which tells the Cuba library to print details about the integration (see the Cuba documentation [63] for details, a copy of which is found in *doc/cuba.pdf*).
- NSTART [**int** `nstart`] — Vegas parameter: the number of points per iteration in the first iteration (see *cuba.doc*). Default value is 1000.
- NINCREASE [**int** `nincrease`] — Vegas parameter: increment for the number of points in subsequent iterations (see *cuba.doc*). Default value is 500.
- NBATCH [**int** `nbatch`] — Vegas parameter: the batch size for sampling (see *cuba.doc*). The default value is 1000.
- NNEW [**int** `nnew`] — Suave parameter: the number of new integrand evaluations in each subdivision (see *cuba.doc*). Default value is 100000.
- NMIN [**int** `nmin`] — Suave parameter: the minimum number of samples for subregions (see *cuba.doc*). Default value is 200.
- FLATNESS [**double** `flattness`] — Suave parameter to compute the fluctuation of a sample (see *cuba.doc*). Default value is 5.
- `Seed` [**double** `seed`] — seed for the pseudo-random-number generator. See *cuba.doc* for more details.

2. `[E_gamma < Delta]`

- `Order SP_loop` [`order`] — a flag to control inclusion of higher-order loop and soft-photon bremsstrahlung corrections. For hard-photon bremsstrahlung corrections see `Bremsstrahlung Type`. 0: include only leading order, i.e. Born- level cross section; 1: include first-order corrections, i.e. one-loop and one soft-photon bremsstrahlung corrections; 2: include second-order corrections, i.e.

two-loop, two soft-photon bremsstrahlung and one-loop + one soft-photon bremsstrahlung. If `Bremsstrahlung Type` 1 or 2 is selected, this option adds also one hard-photon bremsstrahlung + one-loop and one hard-photon bremsstrahlung + one soft-photon. Default value is 2.

- `Vacuum Polarization` [`vac_pol`] — flag for choosing the contribution from the vacuum polarization correction (running α).
  - `Vacuum Polarization=0` — vacuum polarization is not included;
  - `Vacuum Polarization=1` — only electron one-loop contribution;
  - `Vacuum Polarization=2` — full leptonic contribution;
  - `Vacuum Polarization=3` — including leptonic and hadronic contributions. The hadronic part is taken from [65];
  - `Vacuum Polarization=4` — including leptonic and hadronic contributions. The hadronic part is taken from [128];
  - `Vacuum Polarization=5` — including leptonic and hadronic contributions. The hadronic part is taken from [67].

  The default value is 3.
- `Hadronic corrections` [`hadr_corr`] — flag for choosing the contribution from corrections to the proton lines. 0: not included; 1: include only the interference between leptonic and hadronic corrections, i.e. the two-photon exchange and the interference between leptonic and hadronic radiation; 2: only purely hadronic terms, i.e. only corrections to the proton line; 3: total contribution, i.e. includes both the interference and the purely hadronic contributions. Option 1 and 2 have to be combined with `Two-photon exchange`>0 in order for the calculation to be consistent.
- `Two-photon exchange` [`tpe`] — flag for choosing the contribution of the two-photon exchange correction. The present version includes the Feshbach term (1), i.e. the calculation in which the proton is treated as a point-like particle and a calculation that includes both elastic and inelastic contributions (2) (see Ref. [74]). The latter is valid however only for forward angles and for energy of the incoming lepton of 155 MeV. The default value is 0, for which only the IR terms are included (according to Maximon and Tjon see Ref. [34]).
- `Kappa Form Factor` [`kappa_weak`] — flag that specifies if the correction factor responsible for the running of $\sin^2\theta_W$ is included (1) or not(1). If 1 is inserted the full contribution is included as described in Ref. [20] (the code is taken from [129]).

3. `[E_gamma > Delta]`

   - `Bremsstrahlung Type` [`brems`] — flag for choosing the type and the order of the leptonic bremstrahlung calculation. The default value is 2 for which first-order and second order hard-photon bremsstrahlung is included. If 1 is inserted only first order-bremsstrahlung is calculated and for 0 the program doesn't include at all hard-photon bremsstrahlung. For testing there are additional options that

are provided, including only second order (3) and various differential cross section (4-8). Use with care for testing! Wrong input can produce incomplete results.

- `Bremsstrahlung Add` [`brems_add`] — flag for specifying whether the remainder finite contribution to one hard photon and one soft photon, $\sigma^R_{1h\gamma+1s\gamma}$ (see Sec. 2.4.3 for details)is included (1), or not (0). This calculation is available only in combination with `Order SP_loop`=2 and with `Bremsstrahlung Type`=1 or 2.
- `Gamma Loop` [`GL`] — flag for specifying whether the exact calculation (0) or the approximation (1) is used for one hard photon and one-loop correction (see Sec. **??**). This calculation is available only in combination with `Order SP_loop`=2 and with `Bremsstrahlung Type`=1 or 2.
- `Hadronic Radiation` [`brems_hadr`] — flag for specifying the type of contribution coming from hadronic radiation. 0: the contribution is not included; 1: only the interference terms between leptonic and proton radiation are included; 2: only the squared terms from proton radiation are include; 3: the total contribution, i.e. the interference and squared terms, are included. In order for the calculation to be consistent this option has to be combined with the corresponding option from `Hadronic corrections`. This correction is available only at first order.
- `E_gamma max` [**`double`** `E_gamma_max`] — maximum value of the photon energy in GeV. The default value is $E - E'_{\text{min}}$, i.e. the energy of the incident lepton minus the minimum allowed energy for the scattered electron.
- `E' min` [**`double`** `E_prime_min`] and `E' max` [**`double`** `E_prime_max`] — minimum and maximum values of the scattered electron energy in GeV. The default values are the lepton mass m_ℓ and the energy of the incident lepton respectively E.
- `theta_gamma min` [**`double`** `thg_min`] and `theta_gamma max` [**`double`** `thg_max`] — minimum and maxium values of the photon polar angle in degrees. The default values are 0° and 180° respectively.
- `Phase Space Parametrization` [`ps`] — flag for choosing the type of phase space parametrization. It is valid only for the one hard-photon correction and can be useful depending on the experimental cuts that are needed. If 0 is inserted, the azimuthal angle ϕ_γ is expressed in terms of the remaining variables E', θ_ℓ, E_γ, θ_γ. If 1 is inserted, then the energy of the scattered lepton E' is expressed of the remaining variables θ_ℓ, E_γ, θ_γ ϕ_γ.

4. `[Event Generator]`

- `E min` [**`double`** `E_min`] and `E max` [**`double`** `E_max`] — minimum and maximum values for the energy of the incoming lepton. Maximum allowed range that is implemented in this version is between 0.01 GeV and 10 GeV.
- `Delta E` [**`double`** `Delta_E`] — step size for event generation with variable initial-state energy. Valid steps in the current version are 10^{-4}, 10^{-3} and 10^{-2} GeV.

H.5 Description of the output

For the functions `initialization()`, `sigma_diff_Omega_1(const double thl)` and `shiftQ2(const double thl)` the output is given in the objects `Output output` and `Output errors`. The object `output` contains the results of the numerical integration and the object `errors` the estimated uncertainties of these results. The output of the function `int events()` is given in the object `Final_State FS`. The detailed output for each function is:

1. `int initialization()`

   The members of `output` contain the values of partial cross sections, their uncertainties and asymmetries. Their names are structured as follows:

   $$\texttt{output.sigma\_}\begin{bmatrix}\texttt{unpol}\\ \texttt{pol}\end{bmatrix}\texttt{-}\begin{bmatrix}\texttt{elastic}\\ \texttt{inelastic}\end{bmatrix}\texttt{-}\begin{bmatrix}\texttt{born}\\ \texttt{1st}\\ \texttt{2nd}\\ \texttt{loop}\end{bmatrix}$$

   and similarly for `errors`. `unpol` and `pol` distinguish between unpolarized and polarized parts of the cross section while `inelastic` and `elastic` separate contributions to the cross section which have or have not a hard photon in the final state. `born`, `1st` and `2nd` denote contributions at leading, next-to-leading and next-to-next-to-leading order, i.e. the Born level cross section (Rosenbluth cross section, the contribution with one virtual or real photon, and contributions with two virtual or real photons. The one-loop correction to one-photon bremsstrahlung is denoted by the key word `loop` at the end of the name. For the hadronic contributions there is an additional index that is added after `1st` called `hadr`. All cross sections are given in units of nanobarns. In addition, the left-right asymmetries at Born level, as well as at first and second order are calculated and stored in the variables `output.asymm_born`, `output.asymm_1st` and `output.asymm_2nd`. Finally, there are vectors to store results for multiple energies:

   - `output.sigma_born_vect` — vector for storing the Rosenbluth cross section in case the initialization is done for multiple energies (nb).
   - `output.sigma_unpol_vect` — vector for storing the unpolarized total cross section in case the initialization is done for multiple energies (nb).
   - `output.sigma_pol_vect` — vector for storing the polarized total cross section in case the initialization is done for multiple energies (nb).
   - `output.ev_brems` — vector for storing the ratio between the inelastic and unpolarized total cross sections in case the initialization is done for multiple energies (nb).

2. `int shiftQ2()` The results for the shift in Q^2 are given in `output.shiftQ2`, while the uncertainties for this result in `errors.shiftQ2`, both in GeV^2.

3. **int** sigma_diff_Omega_l(**const double** thl_deg)

   The results of this function are stored in members of the output class as described above for total cross sections, but now for the differential cross section $\mathrm{d}\sigma/\mathrm{d}\Omega$ in units of nanobarns times sterad. Details can be found in the sample program *examples/sigma_Omega_l_test.cpp*.

4. **int** events()

   The results of the events function are stored in **class** FS as:

   - FS.E_l — energy of the scattered lepton E' (MeV).
   - FS.theta_l — lepton scattering (polar) angle θ_ℓ (rad).
   - FS.phi_l — lepton azimuthal angle ϕ_ℓ (rad).
   - FS.E_p — energy of the final proton (MeV).
   - FS.theta_p — final proton polar angle (rad).
   - FS.phi_p — final proton azimuthal angle (rad).
   - FS.E_gamma — emitted photon energy (MeV).
   - FS.theta_gamma — photon polar angle (rad).
   - FS.phi_gamma — photon azimuthal angle (rad).
   - FS.Q2 — leptonic momentum transfer squared (GeV^2).
   - FS.l_1[4] — momentum 4-vector of the incoming lepton.
   - FS.p_1[4] — momentum 4-vector of the incoming proton.
   - FS.l_2[4] — momentum 4-vector of the scattered lepton.
   - FS.p_2[4] — momentum 4-vector of the recoil proton.
   - FS.k[4] — momentum 4-vector of the bremsstrahlung photon.
   - weight — Event weight.
   - avg_weight — Averaged event weight.
   - FS.event_no — event number.
   - FS.event_type — 0 for elastic (non-radiative) and 1 for radiative events.

The function **int** events() will generate two types of events:

1. Elastic events characterized by the scattered lepton and the recoil proton in the final state. Event simulation follows the one-fold differential unpolarized and polarized cross sections in the scattering angle (in units of nb/rad),

$$\frac{\mathrm{d}\sigma_{\mathrm{unpol}}}{\mathrm{d}\theta_\ell} \quad \text{and} \quad \frac{\mathrm{d}\sigma_{\mathrm{pol}}}{\mathrm{d}\theta_\ell}.$$

   At first order, the cross sections include one-loop corrections and a soft-photon correction which was obtained analytically by integrating over photon momenta with energies $E_\gamma < \Delta$. The cut-off Δ must be chosen small enough so that the photon is soft and

cannot be detected. Elastic events can be recognized by the fact that the photon energy and angles in the final-state listing, `Final_State FS`, are exactly 0. At second order the cross sections include two-loop, one-loop and one soft photon and two soft photon corrections. The soft photon energies are taken to be separately smaller than the cut-off value, E_γ, $E'_\gamma < \Delta$.

2. Radiative events which contain an additional bremsstrahlung photon with energy $E_\gamma > \Delta$, or two bremsstrahlung photons with energies $E_\gamma > \Delta$ and $E'_\gamma > \Delta$. The photon is hard and can be detected, provided its energy is above a threshold and its angle within the acceptance range of the detector. Event simulation is performed according to the four-fold differential unpolarized and polarized cross sections (units nb/(GeV^{2}rad^2)) in case of one radiated hard photon as

$$\frac{\mathrm{d}^4\sigma_{\mathrm{unpol}}}{\mathrm{d}E'\mathrm{d}\theta_\ell\mathrm{d}E_\gamma\mathrm{d}\theta_\gamma} \quad \text{and} \quad \frac{\mathrm{d}^4\sigma_{\mathrm{pol}}}{\mathrm{d}E'\mathrm{d}\theta_\ell\mathrm{d}E_\gamma\mathrm{d}\theta_\gamma}.$$

or according to the seven-fold differential unpolarized and polarized cross sections (units nb/(GeV^{2}rad^2)) in case of two radiated hard photons as

$$\frac{\mathrm{d}^7\sigma_{\mathrm{unpol}}}{\mathrm{d}E'\mathrm{d}\theta_\ell\mathrm{d}E_\gamma\mathrm{d}E'_\gamma\mathrm{d}\theta_\gamma\mathrm{d}\theta'_\gamma\mathrm{d}\phi'_\gamma} \quad \text{and} \quad \frac{\mathrm{d}^7\sigma_{\mathrm{pol}}}{\mathrm{d}E'\mathrm{d}\theta_\ell\mathrm{d}E_\gamma\mathrm{d}E'_\gamma\mathrm{d}\theta_\gamma\mathrm{d}\theta'_\gamma\mathrm{d}\phi'_\gamma}.$$

H.6 Instructions of how to use the program

Typical running times can vary considerably, depending on the provided input options. The initialization of unpolarized and polarized cross sections at second order can take about 6 minutes on a 2.3 GHz Intel Core i7 processor and `Maximum Number of Evaluations 1st=100000` and `Maximum Number of Evaluations 2nd=1000000`. This setting may be acceptable for testing when only a modest 1% precision is required. High-precision results require much higher numbers of evaluations, in the order of several 10^8, or even 10^9 for second order bremsstrahlung. Note that the evaluation of the polarization asymmetry requires the separate evaluation of the unpolarized and polarized cross sections resulting in a factor of two increase in the run-time.
The program was designed for low energy precision experiments and has to be used with care for higher energies, typically above 10 GeV for the incoming lepton. The event generator also is designed to work for energies between 0.1 and 10 GeV. The initialization will work with energies outside this range, but not the events function.
The default input file is *POLARES.in* and has to be present in the folder from which the program is executed, unless the user chooses a different input file in the variable `input_file`. When generating events the user has to make sure that the initialization is done using Vegas. The other integration methods are just for calculation of the cross sections and do not work for event generation.

H.6.1 Event simulation for variable initial-state energy

Event simulation always requires information about the fully differential cross section which is stored in grids. This information is evaluated as a function of the energy of the incoming

electron (positron). The program allows to administer grids for a list of beam energies such that event generation can be performed with variable initial-state energy. The current version of the event generator works only with energies of the incoming lepton up 0.01 and 10 GeV with increments of 10^{-4}, 10^{-3}, or 10^{-2} GeV. The program will still work for energies outside these values, but grids will not be stored.

Before event generation the user has to call the initialization for a grid of energy values:

```
for (E = input.E_min; E <= input.E_max; E += input.Delta_E) {
if (my_pes_class.change_energy_initialization(E))
my_pes_class.initialization();
}
```

Subsequent event generation can be performed with the following function:

```
for (int i = 0; i < no_events; i++) {
double Ei=//take value from somewhere//;
if (my_pes_class.change_energy_events(Ei))
my_pes_class.events();
//write or analyze event listing//
}
```

The energy value `Ei` has to be inside the range `[E_min, E_max]`. If `Ei` in this example is not equal to one of the values in the list of energies for which the initialization was performed, event generation will be called for the closest value found in the grid. `my_pes_class.events()` will create an event listing and provide energies and scattering angles for all final-state particles in a class called FS. The members of this class have been described above in section H.5. A sample program is contained in *examples/multiple_random_E_test.cpp*.

H.7 File list

Fig. H.1 contains a map of all class dependencies of the main class, called `PES`. Each class is defined in a separate file, except for the smaller input/output classes, which are defined in the same file. Below we provide a list of these files and a short description of each class and how they depend on the other classes:

- `Polares.h` — the main header file that contains **`class`** `PES`. It defines all the main functions and it depends on all other classes.
- `IO_classes.h` — header file that contains the definitions of the input/output classes. The description of these classes can be found in Sec. H.4 and Sec. H.5.
- `parameters.h` — header file that contains the **`class`** `Parameters` which reads the input from the input file and sets all the parameters required by the program. It also makes sure the correct input is given and gives warnings and/or modifies it accordingly, otherwise. Most other classes depend on this class.

- `cuba_param.h` – header file that contains **class** `Cuba_parameters`, which defines all the parameters required by the cuba library (see [63]). Depends on the **class** `Parameters`.
- `gsl_rand.h` – header file that defines the **class** `Rand` which generates random numbers using the GSL library. `Class Integrands` and **class** `PES` depend on this class.
- `integrands.h` header file that contains **class** `Integrands` which defines all the integrands for numerical evaluation. **class** `PES` depends on this class.
- `cross_sections.h` header file that contains **class** `Cross_Setions` which defines all the expressions for the cross sections. `Class Integrands` depends on this class.
- `virtual_corrections.h` header file that contains **class** `Virtual_Corrections` which defines all the expressions for the non-radiative corrections. `Class Cross_Setions` depends on this class.
- `form_factors.h` header file that contains **class** `Form_Factors` which defines all form factors parametrizations. `Class Cross_Setions` depends on this class.
- `melem.h` header file that contains **class** `Melem` which defines second order unpolarized matrix elements. `Class Cross_Setions` depends on this class.
- `melem_pol.h` header file that contains **class** `Melem_pol` which defines second order polarized matrix elements. `Class Cross_Setions` depends on this class.
- `interpolation.h` header file that contains **class** `Interpolation` which defines the interpolation functions for hadronic vacuum polarization and two photon exchange corrections. `Class Cross_Setions`, **class** `Integrands` and **class** `PES` depend on this class.
- `gamma_looop.h` header file that contains **class** `Gamma_Loop` which defines the corrections for one loop and one hard-photon. `Class Virtual_Corrections` depends on this class.
- `scalar_integrals.h` header file that contains the `Scalar_Integrals` class which defines the expressions for the required scalar integrals. `Class Gamma_Loop` depends on this class.
- `const.h` header file that defines all the required constants. It is used by almost all other files.

Some examples of how the library can be used can be found in the folder `examples`. These files are

- `main_example.cpp` A program file that shows how to use the `initialization` and the `events` functions for a given energy of the incoming electron beam.

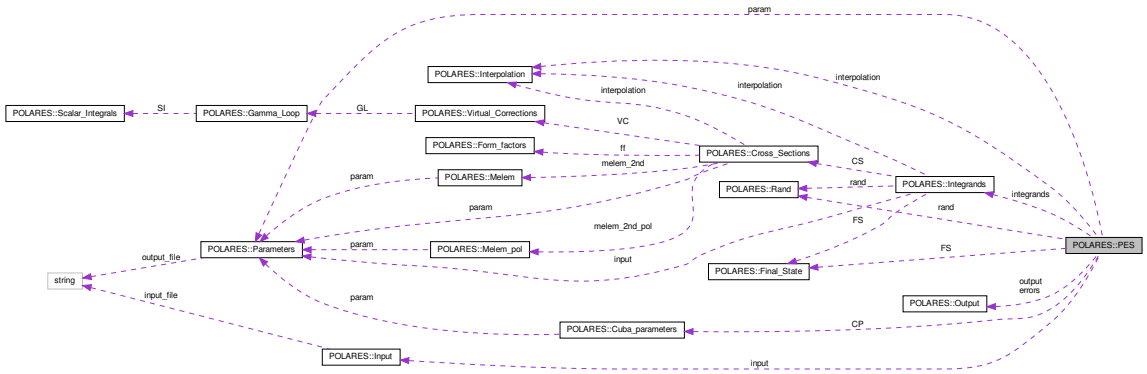

Figure H.1: Graph that shows the class dependencies of POLARES.

- `multiple_random_E_test.cpp` A program file that shows how to use the `initialization` and the `events` functions for a range of energies of the incoming electron beam.
- `sigma_diff_Omega_l_test.cpp` A program file that shows how to use the `sigma_diff_Omega_l` function to calculate the unpolarized and polarized differential cross section in respect to the solid angle of the scattered electron.

H.8 Examples

Here we reproduce the output generated from the program *main_example.cpp* using input from the file *POLARES.in*. It is contained in the file named *POLARES.out* and can be found in the package. This output is helpful for a user to test his/her new installation of POLARES.

```
##############################################################################
##                                POLARES 1.0
##
##     Radiative Corrections for Polarized Electron-Proton Scattering
##
##                                R.-D. Bucoveanu
##
##                            Tue Jun 15 12:27:09 2021
##
## If you use POLARES please cite R.-D. Bucoveanu and H. Spiesberger,
## Eur. Phys. J. A (2019) 55: 57, arXiv:1811.04970 [hep-ph].
## Copyright (c) Razvan Bucoveanu, 2019. E-mail: rabucove@uni-mainz.de
##############################################################################
##                                    Input
##
## [General Input]
## Type of incident lepton = electron
## Type of target particle = proton
## Incident lepton energy = 0.155 GeV
```

```
## Lower cut-off value for the photon energy (Delta) = 10 MeV
## Type of cuts for elastic scattering = Scattering angle (theta_l) cuts
## theta_l min = 25 degrees
## theta_l max = 45 degrees
## Form factor parametrization = Simple Dipole
## Calculate the asymmetry = yes
## Degree of Polarization = 100%
## sin2thetaW = 0.23122
## kappa form factor = 1 - full contribution for the running of sin2thetaW
## Maximum number of evaluations for 1st order bremsstrahlung = 200000000
##
## [E_gamma < Delta]
## Vacuum Polarization = Hadronic contributions (Jegerlehner))
## Two-photon exchange correction (TPE) = no contribution
##
## [E_gamma > Delta]
## Type of hard-photon bremsstrahlung = 1st order
## Hadronic Radiation = no hadronic radiation contribution
## E_gamma max = 0.11 GeV
## E' min = 0.045 GeV
## E' max = 0.155 GeV
## theta_gamma min = 0 degrees
## theta_gamma max = 180 degrees
#############################################################################
##                    Numerical integration results
##
## Sigma unpol Born = 34539.26 +- 0.0217144 nb
## Sigma unpol soft-photon 1st order = 31994.53 +- 0.02011958 nb
## Sigma unpol hard-photon 1st order = 4292.418 +- 0.9364307 nb
## Sigma unpol 1st order = 36286.95 +- 0.9366468 nb
## Sigma pol soft-photon 1st order = -0.001303486 +- 8.742848e-10 nb
## Sigma pol hard-photon 1st order = -0.0001071267 +- 1.940444e-08 nb
## Sigma pol 1st order = -0.001410613 +- 2.027873e-08 nb
## Sigma pol Born = -0.001416725 +- 9.49381e-10 nb
## Asymm 1st order = -3.887384e-08 +- -1.148546e-12
## Asymm Born = -4.101782e-08 +- -3.768986e-14
#############################################################################
```

Appendix I

Constants

In this appendix we list the value of the constants that were used in our calculation. The values are taken from the 2019 revision by C.G. Wohl (see Ref. [2]) and the 2018 CODATA recommended values (see Ref. [130]).

α	—	fine-structure constant (α = 1/137.035999084);
m_e	—	rest mass of the electron (m_e = 0.51099895 MeV);
m_μ	—	rest mass of the muon (m_μ = 105.658372 MeV);
m_τ	—	rest mass of the tau (m_μ = 1.77682 GeV);
M	—	proton rest mass (M = 938.27208816 MeV);
G_F	—	Fermi coupling constant (G_F = 1.1663787 GeV^{-2});
$\sin^2 \hat{\theta}_W(M_Z)$	—	weak mixing angle in the $\overline{\text{MS}}$ prescription ($\sin^2 \hat{\theta}_W(M_Z)$ = 0.23121);
m_W	—	mass of the $W^\pm$ boson (m_W = 80.379 GeV);
m_Z	—	mass of the Z^0 boson (m_Z = 91.1876 GeV).

Bibliography

[1] **MUSE** Collaboration, R. Gilman *et al.*, "Technical Design Report for the Paul Scherrer Institute Experiment R-12-01.1: Studying the Proton "Radius" Puzzle with μp Elastic Scattering," arXiv:1709.09753 [physics.ins-det].

[2] J. M. J. Erler (KPH and A. F. P. U.), "Electroweak Model and Constraints on New Physics." https://pdg.lbl.gov/2022/reviews/rpp2022-rev-standard-model.pdf, 2022.

[3] J. S. Schwinger, "A Theory of the Fundamental Interactions," *Annals Phys.* **2** (1957) 407–434.

[4] T. W. B. Kibble, "History of electroweak symmetry breaking," *J. Phys. Conf. Ser.* **626** no. 1, (2015) 012001, arXiv:1502.06276 [physics.hist-ph].

[5] S. L. Glashow, "The renormalizability of vector meson interactions," *Nucl. Phys.* **10** (1959) 107–117.

[6] S. Weinberg, "A Model of Leptons," *Phys. Rev. Lett.* **19** (1967) 1264–1266.

[7] S. Weinberg, "Physical Processes in a Convergent Theory of the Weak and Electromagnetic Interactions," *Phys. Rev. Lett.* **27** (1971) 1688–1691.

[8] S. Weinberg, "Recent progress in gauge theories of the weak, electromagnetic and strong interactions," *J. Phys. Colloq.* **34** no. C1, (1973) 45–67.

[9] F. Englert and R. Brout, "Broken Symmetry and the Mass of Gauge Vector Mesons," *Phys. Rev. Lett.* **13** (1964) 321–323.

[10] P. W. Higgs, "Broken Symmetries and the Masses of Gauge Bosons," *Phys. Rev. Lett.* **13** (1964) 508–509.

[11] G. S. Guralnik, C. R. Hagen, and T. W. B. Kibble, "Global Conservation Laws and Massless Particles," *Phys. Rev. Lett.* **13** (1964) 585–587.

[12] **ATLAS** Collaboration, G. Aad *et al.*, "Observation of a new particle in the search for the Standard Model Higgs boson with the ATLAS detector at the LHC," *Phys. Lett. B* **716** (2012) 1–29, arXiv:1207.7214 [hep-ex].

[13] Wikimedia, "Standard Model of Elementary Particles." https://en.wikipedia.org/wiki/File:Standard_Model_of_Elementary_Particles.svg#file, 2019.

[14] T. D. Lee and C.-N. Yang, "Question of Parity Conservation in Weak Interactions," *Phys. Rev.* **104** (1956) 254–258.

[15] C. S. Wu, E. Ambler, R. W. Hayward, D. D. Hoppes, and R. P. Hudson, "Experimental Test of Parity Conservation in β Decay," *Phys. Rev.* **105** (1957) 1413–1414.

[16] T. Morii, C. S. Lim, and S. N. Mukherjee, *The Physics of the Standard Model and Beyond*. WORLD SCIENTIFIC, 2004. https://www.worldscientific.com/doi/pdf/10.1142/4655. https://www.worldscientific.com/doi/abs/10.1142/4655.

[17] P. Langacker, *The standard model and beyond; 1st ed.* Series in high energy physics, cosmology, and gravitation. Taylor and Francis, Boca Raton, FL, 2010. https://cds.cern.ch/record/1226768.

[18] S. Weinberg, *The Quantum Theory of Fields*, vol. 1. Cambridge University Press, 1995.

[19] M. E. Peskin and D. V. Schröeder, *An Introduction to Quantum Field Theory*. Addison-Wesley, 1995.

[20] F. Jegerlehner, "Electroweak effective couplings for future precision experiments," *Nuovo Cim.* **C034S1** (2011) 31–40, arXiv:1107.4683 [hep-ph].

[21] A. Czarnecki and W. J. Marciano, "Electroweak radiative corrections to polarized Moller scattering asymmetries," *Phys. Rev.* **D53** (1996) 1066–1072, arXiv:hep-ph/9507420 [hep-ph].

[22] A. Czarnecki and W. J. Marciano, "Parity violating asymmetries at future lepton colliders," *Int. J. Mod. Phys.* **A13** (1998) 2235–2244, arXiv:hep-ph/9801394 [hep-ph].

[23] A. Czarnecki and W. J. Marciano, "Polarized Moller scattering asymmetries," *Int. J. Mod. Phys.* **A15** (2000) 2365–2376, arXiv:hep-ph/0003049 [hep-ph].

[24] J. Erler and R. Ferro-Hernández, "Weak Mixing Angle in the Thomson Limit," *JHEP* **03** (2018) 196, arXiv:1712.09146 [hep-ph].

[25] C. Wohl, "Physical Constants (a major revision)." https://pdg.lbl.gov/2021/reviews/rpp2020-rev-phys-constants.pdf, 2019.

[26] **Qweak** Collaboration, D. Androić *et al.*, "Precision measurement of the weak charge of the proton," *Nature* **557** no. 7704, (2018) 207–211, arXiv:1905.08283 [nucl-ex].

[27] D. Becker *et al.*, "The P2 experiment," *Eur. Phys. J. A* **54** no. 11, (2018) 208, arXiv:1802.04759 [nucl-ex].

[28] R. D. Bucoveanu and H. Spiesberger, "Second-Order Leptonic Radiative Corrections for Lepton-Proton Scattering," *Eur. Phys. J.* **A55** no. 4, (2019) 57, arXiv:1811.04970 [hep-ph].

[29] C. J. Horowitz *et al.*, "Weak charge form factor and radius of 208Pb through parity violation in electron scattering," *Phys. Rev. C* **85** (2012) 032501, arXiv:1202.1468 [nucl-ex].

[30] **A1** Collaboration, J. Bernauer *et al.*, "Electric and magnetic form factors of the proton," *Phys.Rev.* **C90** no. 1, (2014) 015206, arXiv:1307.6227 [nucl-ex].

[31] L. W. Mo and Y.-S. Tsai, "Radiative Corrections to Elastic and Inelastic e p and mu p Scattering," *Rev. Mod. Phys.* **41** (1969) 205–235.

[32] Y.-S. Tsai, "Radiative Corrections to Electron-Proton Scattering," *Phys. Rev.* **122** (1961) 1898–1907.

[33] C. de Calan, H. Navelet, and J. Picard, "Generalized radiative corrections for hadronic targets," *Nucl. Phys. B* **348** (1991) 47–65.

[34] L. C. Maximon and J. A. Tjon, "Radiative corrections to electron proton scattering," *Phys. Rev.* **C62** (2000) 054320, arXiv:nucl-th/0002058 [nucl-th].

[35] F. Weissbach, K. Hencken, D. Rohe, I. Sick, and D. Trautmann, "Radiative corrections for (e, e-prime p) experiments: Going beyond the peaking approximation," *Eur. Phys. J. A* **30** (2006) 477–487, arXiv:nucl-th/0411033.

[36] F. Weissbach, K. Hencken, D. Rohe, and D. Trautmann, "Improved radiative corrections to (e, e'p) experiments: Explicit treatment of kinematical corrections in multiphoton bremsstrahlung," *Phys. Rev. C* **80** (2009) 024602, arXiv:0805.1535 [nucl-th].

[37] I. Akushevich, H. Gao, A. Ilyichev, and M. Meziane, "Radiative corrections beyond the ultra relativistic limit in unpolarized ep elastic and Møller scatterings for the PRad Experiment at Jefferson Laboratory," *Eur. Phys. J. A* **51** no. 1, (2015) 1.

[38] A. B. Arbuzov and T. V. Kopylova, "On higher order radiative corrections to elastic electron–proton scattering," *Eur. Phys. J.* **C75** no. 12, (2015) 603, arXiv:1510.06497 [hep-ph].

[39] R. J. Hill, "Effective field theory for large logarithms in radiative corrections to electron proton scattering," arXiv:1605.02613 [hep-ph].

[40] A. V. Gramolin, V. S. Fadin, A. L. Feldman, R. E. Gerasimov, D. M. Nikolenko, I. A. Rachek, and D. K. Toporkov, "A new event generator for the elastic scattering of charged leptons on protons," *J. Phys.* **G41** no. 11, (2014) 115001, arXiv:1401.2959 [nucl-ex].

[41] I. Akushevich and A. Ilyichev, "Radiative effects in the processes of exclusive photon electroproduction from polarized protons," *Phys. Rev.* **D85** (2012) 053008, arXiv:1201.4065 [hep-ph].

[42] M. Vanderhaeghen, J. M. Friedrich, D. Lhuillier, *et al.*, "QED radiative corrections to virtual Compton scattering," *Phys. Rev.* **C62** (2000) 025501, arXiv:hep-ph/0001100 [hep-ph].

[43] V. V. Bytev, E. A. Kuraev, and E. Tomasi-Gustafsson, "Radiative corrections to the deeply virtual Compton scattering electron tensor," *Phys. Rev.* **C77** (2008) 055205, arXiv:hep-ph/0310226 [hep-ph].

[44] J. Arrington, P. Blunden, and W. Melnitchouk, "Review of two-photon exchange in electron scattering," *Prog.Part.Nucl.Phys.* **66** (2011) 782–833, arXiv:1105.0951 [nucl-th].

[45] E. Kuraev, A. Ahmadov, Y. M. Bystritskiy, and E. Tomasi-Gustafsson, "Radiative corrections for electron proton elastic scattering taking into account high orders and hard photon emission," *Phys.Rev.* **C89** no. 6, (2014) 065207, arXiv:1311.0370 [hep-ph].

[46] D. Borisyuk and A. Kobushkin, "Radiative corrections to polarization observables in electron-proton scattering," *Phys. Rev. C* **90** no. 2, (2014) 025209, arXiv:1405.2467 [hep-ph].

[47] R. Gerasimov and V. Fadin, "Contribution of Δ(1232) to real photon radiative corrections for elastic electron–proton scattering," *J. Phys. G* **43** no. 12, (2016) 125003, arXiv:1604.07960 [nucl-th].

[48] A. Kwiatkowski, H. Spiesberger, and H. J. Mohring, "Heracles: An Event Generator for *ep* Interactions at HERA Energies Including Radiative Processes: Version 1.0," *Comput. Phys. Commun.* **69** (1992) 155–172.

[49] K. Charchula, G. A. Schuler, and H. Spiesberger, "Combined QED and QCD radiative effects in deep inelastic lepton - proton scattering: The Monte Carlo generator DJANGO6," *Comput. Phys. Commun.* **81** (1994) 381–402.

[50] A. Arbuzov, D. Y. Bardin, J. Blumlein, L. Kalinovskaya, and T. Riemann, "Hector 1.00: A Program for the calculation of QED, QCD and electroweak corrections to e p and lepton+- N deep inelastic neutral and charged current scattering," *Comput. Phys. Commun.* **94** (1996) 128–184, arXiv:hep-ph/9511434.

[51] A. V. Afanasev, I. Akushevich, A. Ilyichev, and N. P. Merenkov, "QED radiative corrections to asymmetries of elastic e p scattering in hadronic variables," *Phys. Lett. B* **514** (2001) 269–278, arXiv:hep-ph/0105328.

[52] I. Akushevich, O. F. Filoti, A. N. Ilyichev, and N. Shumeiko, "Monte Carlo Generator ELRADGEN 2.0 for Simulation of Radiative events in Elastic ep-Scattering of Polarized

Particles," *Comput. Phys. Commun.* **183** (2012) 1448–1467, arXiv:1104.0039 [hep-ph].

[53] S. D. Drell and J. D. Walecka, "Electrodynamic Processes with Nuclear Targets," *Annals Phys.* **28** (1964) 18–33.

[54] D. Yu. Bardin and N. M. Shumeiko, "An Exact Calculation of the Lowest Order Electromagnetic Correction to the Elastic Scattering," *Nucl. Phys.* **B127** (1977) 242.

[55] B. Badelek, D. Yu. Bardin, K. Kurek, and C. Scholz, "Radiative correction schemes in deep inelastic muon scattering," *Z. Phys.* **C66** (1995) 591–600, arXiv:hep-ph/9403238 [hep-ph].

[56] I. Akushevich, H. Bottcher, and D. Ryckbosch, "RADGEN 1.0: Monte Carlo generator for radiative events in DIS on polarized and unpolarized targets," in *Monte Carlo generators for HERA physics. Proceedings, Workshop, Hamburg, Germany, 1998-1999*, pp. 554–565. 1998. arXiv:hep-ph/9906408 [hep-ph].

[57] V. Shtabovenko, R. Mertig, and F. Orellana, "New Developments in FeynCalc 9.0" *Comput. Phys. Commun.* **207** (2016) 432–444, arXiv:1601.01167 [hep-ph].

[58] M. D. Schwartz, *Quantum Field Theory and the Standard Model.* Cambridge University Press, 2014. http://www.cambridge.org/us/academic/subjects/physics/theoretical-physics-and-mathematical-physics/quantum-field-theory-and-standard-model.

[59] G. 't Hooft and M. J. G. Veltman, "Scalar One Loop Integrals," *Nucl. Phys.* **B153** (1979) 365–401.

[60] T. Kinoshita, "Mass singularities of Feynman amplitudes," *J. Math. Phys.* **3** (1962) 650–677.

[61] T. Lee and M. Nauenberg, "Degenerate Systems and Mass Singularities," *Phys. Rev.* **133** (1964) B1549–B1562.

[62] A. Arbuzov, "Leading and Next-to-Leading Logarithmic Approximations in Quantum Electrodynamics," *Phys. Part. Nucl.* **50** no. 6, (2019) 721–825.

[63] T. Hahn, "CUBA: A Library for multidimensional numerical integration," *Comput. Phys. Commun.* **168** (2005) 78–95, arXiv:hep-ph/0404043 [hep-ph].

[64] A. O. G. Kallen and A. Sabry, "Fourth order vacuum polarization," *Kong. Dan. Vid. Sel. Mat. Fys. Med.* **29** no. 17, (1955) 1–20.

[65] F. Ignatov, "Vacuum Polarization." http://cmd.inp.nsk.su/~ignatov/vpl/, 2008.

[66] **Working Group on Radiative Corrections and Monte Carlo Generators for Low Energies** Collaboration, S. Actis *et al.*, "Quest for precision in hadronic cross sections at low energy: Monte Carlo tools vs. experimental data," *Eur. Phys. J.* **C66** (2010) 585–686, arXiv:0912.0749 [hep-ph].

[67] A. Keshavarzi, D. Nomura, and T. Teubner, "Muon $g-2$ and $\alpha(M_Z^2)$: a new data-based analysis," *Phys. Rev.* **D97** no. 11, (2018) 114025, arXiv:1802.02995 [hep-ph].

[68] D. Drechsel and T. Walcher, "Hadron structure at low Q**2," *Rev. Mod. Phys.* **80** (2008) 731–785, arXiv:0711.3396 [hep-ph].

[69] S. Weinberg, "Phenomenological Lagrangians," *Physica A* **96** no. 1-2, (1979) 327–340.

[70] S. Scherer, "Introduction to chiral perturbation theory," *Adv. Nucl. Phys.* **27** (2003) 277, arXiv:hep-ph/0210398.

[71] V. Bernard, "Chiral Perturbation Theory and Baryon Properties," *Prog. Part. Nucl. Phys.* **60** (2008) 82–160, arXiv:0706.0312 [hep-ph].

[72] **Particle Data Group** Collaboration, P. Zyla *et al.*, "Review of Particle Physics," *PTEP* **2020** no. 8, (2020) 083C01.

[73] O. Tomalak and M. Vanderhaeghen, "Subtracted dispersion relation formalism for the two-photon exchange correction to elastic electron-proton scattering: comparison with data," *Eur. Phys. J. A* **51** no. 2, (2015) 24, arXiv:1408.5330 [hep-ph].

[74] O. Tomalak and M. Vanderhaeghen, "Two-photon exchange correction in elastic unpolarized electron-proton scattering at small momentum transfer," arXiv:1508.03759 [hep-ph].

[75] D. Borisyuk and A. Kobushkin, "Two-photon exchange at low Q**2," *Phys. Rev.* **C75** (2007) 038202, arXiv:nucl-th/0612104 [nucl-th].

[76] D. Borisyuk and A. Kobushkin, "TPEcalc: a program for calculation of two-photon exchange amplitudes," arXiv:1209.2746 [hep-ph].

[77] A. Afanasev, P. G. Blunden, D. Hasell, and B. A. Raue, "Two-photon exchange in elastic electron–proton scattering," *Prog. Part. Nucl. Phys.* **95** (2017) 245–278, arXiv:1703.03874 [nucl-ex].

[78] H. Fleurbaey, S. Galtier, S. Thomas, M. Bonnaud, L. Julien, F. Biraben, F. Nez, M. Abgrall, and J. Guéna, "New Measurement of the $1S-3S$ Transition Frequency of Hydrogen: Contribution to the Proton Charge Radius Puzzle," *Phys. Rev. Lett.* **120** no. 18, (2018) 183001, arXiv:1801.08816 [physics.atom-ph].

[79] W. Xiong *et al.*, "A small proton charge radius from an electron–proton scattering experiment," *Nature* **575** no. 7781, (2019) 147–150.

[80] **QWeak** Collaboration, D. Androić *et al.*, "Precision Measurement of the Beam-Normal Single-Spin Asymmetry in Forward-Angle Elastic Electron-Proton Scattering," *Phys. Rev. Lett.* **125** no. 11, (2020) 112502, arXiv:2006.12435 [nucl-ex].

[81] O. Koshchii and A. Afanasev, "Lepton mass effects for beam-normal single-spin asymmetry in elastic muon-proton scattering," *Phys. Rev. D* **100** no. 9, (2019) 096020, arXiv:1905.10217 [hep-ph].

[82] W. Beenakker and A. Denner, "Infrared Divergent Scalar Box Integrals With Applications in the Electroweak Standard Model," *Nucl. Phys. B* **338** (1990) 349–370.

[83] O. Koshchii and A. Afanasev, "Charge asymmetry in elastic scattering of massive leptons on protons," *Phys. Rev. D* **96** no. 1, (2017) 016005, arXiv:1705.00338 [nucl-th].

[84] W. A. McKinley and H. Feshbach, "The Coulomb Scattering of Relativistic Electrons by Nuclei," *Phys. Rev.* **74** (1948) 1759–1763.

[85] A. V. Afanasev, S. J. Brodsky, C. E. Carlson, Y.-C. Chen, and M. Vanderhaeghen, "The Two-photon exchange contribution to elastic electron-nucleon scattering at large momentum transfer," *Phys. Rev. D* **72** (2005) 013008, arXiv:hep-ph/0502013.

[86] D. Borisyuk and A. Kobushkin, "Two-photon exchange in dispersion approach," *Phys. Rev.* **C78** (2008) 025208, arXiv:0804.4128 [nucl-th].

[87] P. A. M. Guichon and M. Vanderhaeghen, "How to reconcile the Rosenbluth and the polarization transfer method in the measurement of the proton form-factors," *Phys. Rev. Lett.* **91** (2003) 142303, arXiv:hep-ph/0306007.

[88] P. Mastrolia and E. Remiddi, "Two loop form-factors in QED," *Nucl. Phys.* **B664** (2003) 341–356, arXiv:hep-ph/0302162 [hep-ph].

[89] T. van Ritbergen and R. G. Stuart, "Hadronic contributions to the muon lifetime," *Phys. Lett.* **B437** (1998) 201–208, arXiv:hep-ph/9802341 [hep-ph].

[90] A. I. Davydychev, K. Schilcher, and H. Spiesberger, "Hadronic corrections at O(alpha**2) to the energy spectrum of muon decay," *Eur. Phys. J.* **C19** (2001) 99–104, arXiv:hep-ph/0011221 [hep-ph].

[91] R. Bonciani, P. Mastrolia, and E. Remiddi, "QED vertex form-factors at two loops," *Nucl. Phys.* **B676** (2004) 399–452, arXiv:hep-ph/0307295 [hep-ph].

[92] G. J. H. Burgers, "On the Two Loop QED Vertex Correction in the High-energy Limit," *Phys. Lett.* **164B** (1985) 167–169.

[93] B. A. Kniehl, "Two Loop QED Vertex Correction From Virtual Heavy Fermions," *Phys. Lett.* **B237** (1990) 127–129.

[94] J. Boehm, M. Wittmann, Z. Wu, Y. Xu, and Y. Zhang, "IBP reduction coefficients made simple," *JHEP* **12** (2020) 054, arXiv:2008.13194 [hep-ph].

[95] M. Heller and A. von Manteuffel, "MultivariateApart: Generalized partial fractions," *Comput. Phys. Commun.* **271** (2022) 108174, arXiv:2101.08283 [cs.SC].

[96] P. Banerjee, T. Engel, A. Signer, and Y. Ulrich, "QED at NNLO with McMule," *SciPost Phys.* **9** (2020) 027, arXiv:2007.01654 [hep-ph].

[97] Y. Ulrich, "McMule – QED Corrections for Low-Energy Experiments," other thesis, 8, 2020.

[98] M. B. Barbaro, C. Maieron, and E. Voutier, "Lepton mass effects in the Bethe-Heitler process," *Phys. Lett.* **B726** no. 1-3, (2013) 505–511, arXiv:1305.3873 [hep-ph]. [Erratum: Phys. Lett.B727,no.4-5,573(2013)].

[99] P. Talukdar, F. Myhrer, and U. Raha, "Low-Energy Effective Field Theory of Lepton-Proton Bremsstrahlung," arXiv:1712.09963 [nucl-th].

[100] P. Talukdar, F. Myhrer, G. Meher, and U. Raha, "Low-Energy Lepton-Proton Bremsstrahlung via Effective Field Theory," *Eur. Phys. J.* **A54** no. 11, (2018) 195, arXiv:1810.04027 [nucl-th].

[101] E. Beise, M. Pitt, and D. Spayde, "The SAMPLE experiment and weak nucleon structure," *Prog.Part.Nucl.Phys.* **54** (2005) 289–350, arXiv:nucl-ex/0412054 [nucl-ex].

[102] D. Adhikari *et al.*, "An Accurate Determination of the Neutron Skin Thickness of ^{208}Pb through Parity-Violation in Electron Scattering," arXiv:2102.10767 [nucl-ex].

[103] O. Koshchii, J. Erler, M. Gorchtein, C. J. Horowitz, J. Piekarewicz, X. Roca-Maza, C.-Y. Seng, and H. Spiesberger, "Weak charge and weak radius of ^{12}C," *Phys. Rev. C* **102** no. 2, (2020) 022501, arXiv:2005.00479 [nucl-th].

[104] J. Piekarewicz, A. R. Linero, P. Giuliani, and E. Chicken, "Power of two: Assessing the impact of a second measurement of the weak-charge form factor of ^{208}Pb," *Phys. Rev. C* **94** no. 3, (2016) 034316, arXiv:1604.07799 [nucl-th].

[105] C. J. Horowitz, "Parity violating elastic electron scattering and Coulomb distortions," *Phys. Rev. C* **57** (1998) 3430–3436, arXiv:nucl-th/9801011.

[106] R. Hofstadter, "Electron scattering and nuclear structure," *Rev. Mod. Phys.* **28** (1956) 214–254.

[107] J. M. Hammersley and D. C. Handscomb, *Monte Carlo Methods.* Springer, Dordrecht, 1964.

[108] G. Lepage, "Vegas Documentation." http://www.acsu.buffalo.edu/~phygons/cp2/topic6/vegas.pdf, 2014.

[109] G. P. Lepage, "Adaptive Multidimensional Integration: VEGAS Enhanced," arXiv:2009.05112 [physics.comp-ph].

[110] T. Hahn, "CUBA: A Library for multidimensional numerical integration," *Comput.Phys.Commun.* **168** (2005) 78–95, arXiv:hep-ph/0404043 [hep-ph].

[111] N. Beisert, "Lecture notes on QFT." https://people.phys.ethz.ch/~nbeisert/lectures/QFT1-19HS-Notes.pdf, 2020.

[112] F. Olness and R. Scalise, "Regularization, Renormalization, and Dimensional Analysis: *Dimensional Regularization meets Freshman E&M*," *Am. J. Phys.* **79** (2011) 306, arXiv:0812.3578 [hep-ph].

[113] G. 't Hooft and M. J. G. Veltman, "Regularization and Renormalization of Gauge Fields," *Nucl. Phys.* **B44** (1972) 189–213.

[114] J. C. Collins, *Renormalization: An Introduction to Renormalization, the Renormalization Group and the Operator-Product Expansion*. Cambridge Monographs on Mathematical Physics. Cambridge University Press, 1984.

[115] J. C. Bernauer, *Measurement of the elastic electron-proton cross section and separation of the electric and magnetic form factor in the Q^2 range from 0.004 to 1 GeV^2*. PhD thesis, Johannes Gutenberg University Mainz, 2010.

[116] J. Friedrich and T. Walcher, "A Coherent interpretation of the form-factors of the nucleon in terms of a pion cloud and constituent quarks," *Eur. Phys. J.* **A17** (2003) 607–623, arXiv:hep-ph/0303054 [hep-ph].

[117] S. Galster, H. Klein, J. Moritz, K. H. Schmidt, D. Wegener, and J. Bleckwenn, "Elastic electron-deuteron scattering and the electric neutron form factor at four-momentum transfers 5fm^{-2} < q^2 < 14fm^{-2}," *Nucl. Phys.* **B32** (1971) 221–237.

[118] M. A. El Yakoubi, *Contribution of the strange quark to the nucleon electromagnetic structure : The results of the A4 experiment at Q^2 = 0.23 (GeV/c)^2*. Theses, Université Paris Sud - Paris XI, Mar., 2007. https://tel.archives-ouvertes.fr/tel-00151260.

[119] P. Wang, D. B. Leinweber, A. W. Thomas, and R. D. Young, "Strange magnetic form factor of the proton at Q**2 = 0.23- GeV**2," *Phys. Rev.* **C79** (2009) 065202, arXiv:0807.0944 [hep-ph].

[120] V. Shtabovenko, R. Mertig, and F. Orellana, "New Developments in FeynCalc 9.0" *Comput. Phys. Commun.* **207** (2016) 432–444, arXiv:1601.01167 [hep-ph].

[121] M. Heller, O. Tomalak, M. Vanderhaeghen, and S. Wu, "Leading Order Corrections to the Bethe-Heitler Process in the $\gamma p \to l^+ l^- p$ Reaction," *Phys. Rev. D* **100** no. 7, (2019) 076013, arXiv:1906.02706 [hep-ph].

[122] R. K. Ellis and G. Zanderighi, "Scalar one-loop integrals for QCD," *JHEP* **02** (2008) 002, arXiv:0712.1851 [hep-ph].

[123] H. E. Haber, "Spin formalism and applications to new physics searches," in *Spin structure in high-energy processes: Proceedings, 21st SLAC Summer Institute on Particle Physics, 26 Jul - 6 Aug 1993, Stanford, CA*, pp. 231–272. 4, 1994. arXiv:hep-ph/9405376.

[124] D. Beck and R. McKeown, "Parity violating electron scattering and nucleon structure," *Ann. Rev. Nucl. Part. Sci.* **51** (2001) 189–217, arXiv:hep-ph/0102334.

[125] V. Dmitrasinovic and S. Pollock, "Isospin breaking corrections to nucleon electroweak form-factors in the constituent quark model," *Phys. Rev. C* **52** (1995) 1061–1072, arXiv:hep-ph/9504414.

[126] G. A. Miller, "Charge Symmetry Breaking in the Nucleon and Parity Violating Elastic Electron-Proton Scattering," in *6th International Workshop on From Parity Violation to Hadronic Structure and More*. 10, 2014. arXiv:1410.8599 [nucl-th].

[127] R. Lewis and N. Mobed, "Isospin violation and the proton's neutral weak magnetic form-factor," *Phys. Rev. D* **59** (1999) 073002, arXiv:hep-ph/9810254.

[128] F. Jegerlehner, "Hadronic contributions to the photon vacuum polarization and their role in precision physics," *J.Phys.* **G29** (2003) 101–110, arXiv:hep-ph/0104304 [hep-ph].

[129] F. Jegerlehner. http://www-com.physik.hu-berlin.de/~fjeger/software.html.

[130] CODATA, "Fundamental Physical Constants." https://physics.nist.gov/cuu/pdf/all.pdf, 2018.

Acknowledgments

I would like to thank my wife, my grandmother and my friends for all their love, support and encouragements. I couldn't have done it without you!

I am very grateful to my supervisor, who first of all gave me the chance to work on this interesting project and who supported me all these years, even when I had more difficult times. His door was always open when I had questions and his constructive criticism helped me a lot to improve the quality of my work. He helped me to improve not only my technical skills, but also to improve as a scientist and as a person.

Finally, I would like to thank also my colleagues for all their help, interesting discussions and all the nice coffee breaks we had together.